Lagrangian coherent structures and physical processes of coastal upwelling

Anass El Aouni

JOINT PHD

IN PARTIAL FULFILLMENT OF REQUIREMENTS OF THE DEGREE OF

Doctor of Philosophy

IN APPLIED MATHEMATICS AND SCIENTIFIC COMPUTING

UNIVERSITY OF BORDEAUX

AND UNIVERSITY MOHAMMED-V IN RABAT

DOCTORAL SCHOOL MATHEMATICS AND COMPUTER SCIENCE OF BORDEAUX

AND

FACULTY OF SCIENCES OF RABAT

By **Anass El Aouni**

Lagrangian coherent structures and physical processes of coastal upwelling

Under the direction of Dr. Hussein Yahia and Pr. Khalid Minaoui

September 24th, 2019

Jury members:

Dr. Véronique Garçon	Laboratory of Geophysical Studies and Spatial Oceanography, France	Jury president
Pr. Emilio Hernández-García	Institute for Cross-Disciplinary Physics and Complex Systems, Spain	Reviewer
Dr. Guillaume Charria	French Research Institute for Exploitation of the Sea, France	Reviewer
Dr. Khalid Daoudi	Inria Bordeaux, France	Examiner
Dr. Hussein Yahia	Inria Bordeaux, France	Advisor
Dr. Abdelali El Moussaoui	Mercator Ocean, France	Examiner
Pr. Khalid Minaoui	Mohammed V University in Rabat, Morocco	Advisor
Pr. Mohamed Ouadou	Mohammed V University in Rabat, Morocco	Examiner

THÈSE EN COTUTELLE PRÉSENTÉE

POUR OBTENIR LE GRADE DE

DOCTEUR DE

L'UNIVERSITÉ DE BORDEAUX

ET DE L'UNIVERSITÉ MOHAMMED-V DE RABAT

ÉCOLE DOCTORALE MATHÉMATIQUES ET INFORMATIQUE DE BORDEAUX

ET

LA FACULTÉ DES SCIENCE DE RABAT

SPÉCIALITÉ Mathématiques Appliquées et Calcul Scientifique

Par **Anass El Aouni**

Lagrangian coherent structures and physical processes of coastal upwelling

Sous la direction de Dr. Hussein Yahia et de Pr. Khalid Minaoui

Soutenue le 24/09/2019

Membres du jury:

Veronique Garcon	DR HDR LEGOS-CNRS, France	Présidente
Emilio Hernández-García	PES IFISC, Espagne	Rapporteur
Guillaume Charria	CR HDR Ifremer, France	Rapporteur
Khalid Daoudi	CR Inria Bordeaux, France	Examinateur
Hussein Yahia	CR HDR Inria Bordeaux, France	Directeur de thèse
Abdelali El Moussaoui	CR HDR Mercator Ocean, France	Examinateur
Khalid Minaoui	PH Université Mohammed-V de Rabat	Directeur de thèse
Mohamed Ouadou	PES Université Mohammed-V de Rabat	Examinateur

Lagrangian coherent structures and physical processes of coastal upwelling

by

Anass El Aouni

Submitted to the ECOLE DOCTORALE DE MATHEMATIQUES ET INFORMATIQUE DE BORDEAUX & ECOLE DOCTORALE DE LA FACULTE DES SCIENCES DE RABAT
on September 24, 2019, in partial fulfillment of the
requirements for the degree of
Doctor of Philosophy

Résumé

L'étude des processus physiques d'un système d'upwelling est essentielle pour comprendre sa variabilité actuelle et ses changements passés et futurs. Cette thèse présente une étude interdisciplinaire du système d'upwelling côtier à partir de différentes données acquises par satellite, l'accent étant mis principalement sur le système d'upwelling d'Afrique du Nord-Ouest (NWA). Cette étude interdisciplinaire aborde (1) le problème de l'identification et de l'extraction automatiques du phénomène d'upwelling à partir d'observations satellitaires biologiques et physiques. (2) Une étude statistique de la variation spatio-temporelle de l'upwelling de la NWA tout au long de son extension et de ses différents indices d'upwelling. (3) Une étude des relations non linéaires entre le mélange de surface et l'activité biologique dans les régions d'upwelling. (4) études lagrangiennes de tourbillons cohérents; leurs propriétés physiques et identification automatique. (5) L'étude des transports effectués par les tourbillons lagrangiens de la NWA Upwelling et leur impact sur l'océan.

Mots-clés: Upwelling d'Afrique du Nord-Ouest, segmentation d'upwelling, exposants de singularité, filament d'upwelling, tourbillons de moyenne échelle, dynamique des fluides non linéaire, structures cohérentes lagrangiennes, advection chaotique.

Lagrangian coherent structures and physical processes of coastal upwelling

by

Anass El Aouni

Submitted to the ECOLE DOCTORALE DE MATHEMATIQUES ET INFORMATIQUE DE BORDEAUX & ECOLE DOCTORALE DE LA FACULTE DES SCIENCES DE RABAT
on September 24, 2019, in partial fulfillment of the
requirements for the degree of
Doctor of Philosophy

Abstract

Studying physical processes of an upwelling system is essential to understand its present variability and its past and future changes. This thesis presents an interdisciplinary study of the coastal upwelling system from different satellite acquired data, with the main focus placed on the North-West African (NWA) upwelling system. This interdisciplinary study covers (1) the problem of the automatic identification and extraction of the upwelling phenomenon from biological and physical satellite observations. (2) A statistical study of the spatio-temporal variation of the NWA upwelling throughout its extension and different upwelling indices. (3) A Study of the nonlinear relationships between the surface mixing and biological activity in the upwelling regions. (4) Lagrangian studies of coherent eddies; their physical properties and automatic identification. (5) The study of transport made by Lagrangian eddies off the NWA Upwelling and their impact on the open ocean.

The proposed upwelling identification approaches are based on the combination of the physical process triggering the upwelling event along with different methods in image processing, computer vision and signal processing. Two upwelling identification methods were proposed, the first one uses the Fuzzy c-mean clustering algorithm along with the Ekman transport theory to identify and extract the upwelling regions from Sea Surface Temperature (SST) images. The second method uses a region-based approach to not only successfully delineate upwelling regions from SST images but also extract upwelling region from CHLa images.

A novel upwelling index is proposed based on the upwelling segmentation methods. This index has several advantages over state-of-the-art ones: simplicity, computational efficiency and accuracy. This index is used along with different upwelling indices to carry on a statistical analysis of the spatio-temporal variability of the NWA upwelling dynamics. This statistical variability of upwelling focuses on its relationship to atmospheric variables (10m-wind, wind stress). The relationship between upwelling spatial extension and the atmospheric variables differ somewhat in the two

regions. However, the pattern of its intensity generally reflects the common atmospheric pattern favoring upwelling: southward wind/wind stress, Cross-shore Ekman transport.

In these regards, a computational software system for the calculation of the upwelling index is made available for users in order to extract and monitor the intensity and extension of upwelling along the NWA margin. This C-code allows providing users continually by space synthetic products informing about environmental parameters and permitting the evaluation and monitoring of the coastal upwelling dynamic in space and time.

The relationship between physical structures of oceanic fronts and the biological activity is explored. In this regard, a new concept of studying the nonlinear relationship between surface mixing/stirring and chlorophyll concentration is proposed. The surface mixing/stirring is computed based on a recent geodesic theory of Lagrangian coherent structures (LCSs). These LCSs are used to study the link between surface mixing/stirring and chlorophyll-a (CHL_a) fronts concentration extracted through the calculation of singularity exponents in a microcanonical formulation of singularity exponents associated to gradient measure, with a geometric computation of the Most Singular Manifold (MSM). The results shed new light on the previous studies, addressing mixing using Finite-size Lyapunov exponents (FSLEs).

Two objective definitions of Lagrangian coherent vortex are introduced along with their automatic detection. The First method is based on a decomposition of particle trajectory into two parts: closed curves which give information about uniformly rotating flow, and one that describes the mean displacement. The former part yields an objective measure of material rotation. The proposed method defines a Lagrangian coherent vortex as closed material lines in which fluid particles complete the same polar rotation. The second method is based on frequency-domain representation of Lagrangian trajectories. The method identifies and extracts coherent vortices as tubular level surfaces along which particles' trajectories share similar frequencies. Both methods identify all coherent vortices in an automatic manner, showing high vortices' monitoring capacity. Moreover, they are suitable to applications to float data as they define vortices based on their observed trajectories.

The impact of NWA upwelling over the open ocean is explored throughout the roles played by mesoscale eddies off the Canary archipelago. These eddies carry coherent waters from upwelling regions and pour them into the open ocean. A yearly up to 4 coherent mesoscale eddies characterized by diameters varying from 25 to 140 km are detected. An overall of 63 coherent eddies of about 40 kms in diameter among about 59% of their contents resides in the Upwelling and its transition. These mesoscale eddies were used to compute coherent fluid transport off Canary Islands, which proved to be lower (by about one order of magnitude) than previous transport estimates.

Keywords: North-West African upwelling, upwelling segmentation, singularity exponents, upwelling filament, mesoscale eddies, nonlinear fluid dynamics, Lagrangian coherent structures, chaotic advection.

Unité de recherche

Equipe GEOSTAT, centre de recherche INRIA Bordeaux Sud-Ouest,
200 Avenue de la Vieille Tour, 33405 Talence, France.

Laboratoire de Recherche en Informatique et Télécommunications (LRIT-URAC 29),
Facult des Sciences de Rabat - Avenue Ibn Batouta, Rabat, Maroc.

Résumé substantiel

Dans le cadre de l'étude des phénomènes océanographiques, une meilleure connaissance de la dynamique et de la circulation océanique passe par une meilleure compréhension des nombreux mécanismes mis en jeu dans l'océan. Une des tâches importantes dévolues aux océanographes est notamment l'analyse des systèmes d'upwelling des bordures côtières des océans. L'upwelling côtier est défini comme une remontée d'eaux profondes sur le plateau continental, qui compense la dérive des eaux de surface vers le large (Transport d'Ekman) sous les actions combinées d'un vent favorable et de la rotation de la Terre (Force de Coriolis). Les eaux froides remontant le long de ces côtes, sont généralement riches en nutriments ce qui a pour effet de "doper" naturellement le processus de photosynthèse dans la couche euphotique. Ces systèmes sont à l'origine de fortes structures océaniques susceptibles d'engendrer de fortes altérations dans la distribution de la couche euphotique, favorisant une grande fluctuation des ressources halieutiques. En effet, 25% du stock mondial de poissons est capturé dans les quatre principaux courants d'écosystèmes d'upwelling (le courant des Canaries, le courant du Benguela, le courant du Humboldt et le courant de la Californie), représentant plus de 5% de la surface totale des océans.

Ma thèse porte sur la dynamique de l'upwelling d'Afrique du Nord-Ouest. Elle présente donc une étude interdisciplinaire de ce système d'upwelling côtier à partir de différentes données acquises par satellite. Cette thèse aborde:

1. Le problème de l'identification et de l'extraction automatiques du phénomène d'upwelling à partir d'observations satellitaires biologiques et physiques.

2. Une étude statistique de la variation spatio-temporelle de l'upwelling de la NWA

tout au long de son extension et de ses différents indices d'upwelling.

3. Une étude des relations non linéaires entre le mélange de surface et l'activité biologique dans les régions d'upwelling.

4. Des études lagrangiennes de tourbillons cohérents; leurs propriétés physiques et identification automatique.

5. L'étude des transports effectués par les tourbillons lagrangiens de la NWA Upwelling et leur impact sur l'océan.

La détection et l'analyse de l'upwelling constitue un enjeu économique majeur dans la mesure où il est la principale source d'enrichissement des écosystèmes côtiers. A cet égard, et à l'insuffisance et la discontinuité des mesures in-situ, l'imagerie satellitaire constitue une source d'information fondamentalle permettant la mise en lumière des structures méso-échelles composant les zones d'upwelling. Cette thèse commence par présenter différentes méthodes classiques de traitement des images couramment utilisées dans la segmentation des régions d'upwelling à partir des images SST et de concentration de chlorophylle. Elle décrit les méthodes précédentes proposées pour la détection d'upwelling marocain, discute de leurs résultats et propose deux méthodes efficaces d'identification de l'upwelling marocain à partir d'observations satellitaires physiques et biologiques. Les approches d'identification d'upwelling proposées reposent sur la combinaison du processus physique déclenchant le phénomène d'upwelling et de différentes méthodes de traitement d'image, de vision par ordinateur et de traitement du signal. Deux méthodes d'identification de l'upwelling ont été proposées. La première utilise l'algorithme de classification Fuzzy c-mean avec la théorie de transport d'Ekman pour identifier et extraire les régions d'upwelling à partir d'images de température de surface de la mer (SST). La seconde méthode utilise une approche par région non seulement pour délimiter avec succès les régions d'upwelling à partir des images SST, mais également pour extraire la région d'upwelling à partir des images CHLa.

Le suivi de l'évolution temporelle du phénomène d'upwelling à partir de mesures satellitaires est une opération fastidieuse et difficile à effectuer basée sur l'analyse

systématique d'images quotidiennes ou même hebdomadaires. Afin de rendre cette surveillance opérationnelle et efficace, des méthodes simples ou complexes ont été développées pour synthétiser la localisation de l'upwelling le long de la côte pendant une période donnée. La plupart de ces méthodes utilisent des indices basés sur une différence thermique entre les eaux côtières et les eaux du large. Les indices existants utilisés dans la littérature pour quantifier et analyser les variations saisonnières et interannuelles de la dynamique de l'upwelling sont décrits. Ensuite, un nouvel indice d'upwelling est proposé basé sur les méthodes de segmentation d'upwelling. Cet index présente plusieurs avantages par rapport aux précédents: simplicité, efficacité et précision des calculs. Cet indice est utilisé avec différents indicateurs d'upwelling pour effectuer une analyse statistique de la variabilité spatio-temporelle de la dynamique d'upwelling dans la marge NWA. Cette variabilité statistique de l'upwelling est axée sur sa relation avec les variables atmosphériques (vent à 10 m, stress du vent). La relation entre l'extension spatiale des remontées d'eau et les variables atmosphériques diffère quelque peu dans deux régions. Cependant, le schéma de son intensité reflète généralement le schéma atmosphérique commun qui favorise l'upwelling: vent du sud / stress du vent, transport d'Ekman transfrontière.

À cet égard, un système informatique permettant de calculer l'indice de l'upwelling est mis à la disposition des utilisateurs afin d'extraire et de surveiller l'intensité et l'extension de la remontée le long de la côte marocaine. Ce code C permet de fournir aux utilisateurs des produits synthétiques spatiaux en continu, informant sur les paramètres environnementaux et permettant l'évaluation et la surveillance de la dynamique de l'upwelling côtier dans l'espace et dans le temps.

La relation entre les structures physiques des fronts océaniques et l'activité biologique est explorée. On s'est intéressé à étudier les structures physiques des fronts océaniques associés avec l'upwelling et leur impact sur la production primaire. À cet égard, un nouveau concept d'étude de la relation non linéaire entre le mélange en surface et la concentration en chlorophylle est proposé. Le but de cette partie est d'étudier le processus de mélange dans différentes régions de l'Afrique du nord-ouest en utilisant les structures cohérentes lagrangiennes (LCS) obtenues à partir du tenseur

Cauchy-green. Le mélange de surface est calculé sur la base d'une théorie géodésique récente des structures cohérentes lagrangiennes (LCS). Ces LCS sont utilisés pour étudier le lien existant entre le mélange de surface et la concentration de fronts de chlorophylle-a (en tant que proxy pour les processus biologiques) extraits par le calcul d'exposants de singularité avec un calcul géométrique du plus singulier (MSM). Les résultats ont apporté un nouvel éclairage sur les études précédentes, abordant le mélange à l'aide d'exposants de Lyapunov de taille finie (FSLE).

Deux définitions objectives du vortex cohérent lagrangien sont introduites avec leur détection automatique. La première méthode est basée sur une décomposition de la trajectoire des particules en deux parties: des courbes fermées qui donnent des informations sur un écoulement tournant uniformément et une qui décrit le déplacement moyen. La première partie fournit une mesure objective de la rotation des matériaux. La méthode proposée définit un vortex cohérent lagrangien comme des lignes de matière fermées dans lesquelles des particules de fluide effectuent la même rotation polaire. La seconde méthode est basée sur la représentation dans le domaine fréquentiel des trajectoires lagrangiennes. Le procédé identifie et extrait des tourbillons cohérents sous forme de surfaces de niveau tubulaire le long desquelles les trajectoires des particules partagent des fréquences similaires. Les deux méthodes identifient tous les tourbillons cohérents de manière automatique, en montrant une capacité de surveillance élevée. De plus, ils conviennent aux applications sur des données des bouées car ils définissent des vortex en fonction de leurs trajectoires observées.

Les zones d'upwelling de bord Est (EBUZ) comprennent certains des écosystèmes les plus productifs du monde, en particulier le système d'upwelling du courant des Canaries (CCUS) qui constitue l'une des principales régions d'upwelling du monde. Contrairement à l'autre (EBUZ), CCUS inclut une source de tourbillons de moyenne échelle; l'existence de l'archipel des îles Canaries, qui agit comme une barrière perturbant le courant des Canaries allant vers le sud-ouest, ainsi que le mécanisme joué par le cisaillement du vent dans le sillage des îles, qui permet la formation des tourbillons à des intensités relativement faibles du courant des Canaries. Ainsi, en plus des

eaux profondes froides et riches en nutriments, une quantité importante d'énergie est transférée dans des tourbillons océaniques de moyenne échelle, qui sont presque continuellement créés par l'archipel. Cela peut jouer un rôle important dans le transfert des propriétés de l'eau de l'upwelling froid et riche en nutriments vers l'océan, ce qui peut avoir un impact significatif sur la répartition régionale des propriétés biologiques et physiques de l'eau.

Ces tourbillons océaniques générés aux îles Canaries ont fait l'objet de recherches approfondies au cours des deux dernières décennies. Leurs premières observations provenaient de la télédétection . Ils ont été identifiés comme des tourbillons cycloniques (anticycloniques) à cœur froid (chaud) à partir d'images thermiques. Plus tard, leurs caractéristiques principales telles que le diamètre et la profondeur ont été révélées à partir de données in situ. Les chercheurs se sont ensuite intéressés à la compréhension de leurs effets biologiques et à la détermination de leurs mécanismes de génération, et enfin étudier leur évolution et impact sur l'offshore.

Cependant, ils ont été principalement étudiés dans la perspective eulérienne, où des corrélations persistantes entre les quantités d'écoulement sont recherchées dans un domaine spatial fixe. Cependant, en ne suivant pas le mouvement des fluides, les techniques eulériennes sont limitées car elles omettent un aspect important de la cohérence: le transport de la même masse fluide par un mouvement cohérent. Cela crée un problème conceptuel car le transport de matériaux par tourbillons doit être indépendant de l'observateur, comme l'exigent les axiomes de base de la mécanique du continuum, et surtout du point de vue du transport, de tels tourbillons sont matériellement incohérents dans une large mesure; sous advection lagrangienne, les limites supposées des tourbillons deviennent rapidement tendues et filamenteuses, ce qui implique que l'eau fuit de manière significative à travers les limites de la structure.

Ces approches eulériennes du suivi des tourbillons souffrent de plusieurs inconvénients.

- Les structures ainsi identifiées ne sont pas matérielles; les algorithmes de suivi eulériens associent des caractéristiques spatiales proximales identifiées à des instantanés voisins avec un seul objet, mais ces caractéristiques ne représentent

pas nécessairement le même fluide.

- les structures ne sont pas objectives; différents observateurs dans des cadres qui se translatent et se font pivoter l'un par rapport à l'autre identifient différentes régions d'écoulement comme étant cohérentes. Le point de vue lagrangien, au contraire, suit le fluide en mouvement et est donc plus approprié pour examiner les mouvements de structure cohérents.

La perspective de structure cohérente (SC) tente d'identifier des "tourbillons" spécifiques et discrets et de les suivre à travers l'océan.

Dans la dernière partie de cette thèse, le rôle des tourbillons de méso-échelle au large de l'archipel des Canaries est étudié à l'aide de la méthode Lagrangienne que j'ai développé tout en utilisant une base de données de 24 ans des champs de vitesse de surface de la mer dérivé de l'altimétrie de surface satellite sous l'approximation géostrophique. Je décris le processus physique qui crée ces tourbillons, calcule leur diamètre, leur durée de vie, leur vitesse et utilise toutes ces informations pour calculer le transport par voie d'eau cohérente au large des îles Canaries, qui s'est avéré plus petit (d'environ un ordre de grandeur) que les estimations de transport précédentes.

Acknowledgments

This Joint PhD thesis has been prepared within Geostat team at Bordeaux's INRIA under the direction of Dr. Hussein Yahia and the laboratory of research in computer science and telecommunications at Mohammed V University under the direction of Pr. Khalid Minaoui.

First, I would like to express my sincere gratitude to my thesis advisors Dr. Hussein Yahia and Pr. Khalid Minaoui for giving me the opportunity of conducting my PhD study on a very exciting research topic. I am very grateful to Khalid Daoudi and my advisor Hussein for welcoming me in GEOSTAT team. I am grateful to Minaoui for being supportive and encouraging me during my PhD.

Perhaps, what I enjoyed the most during my PhD is exploring fields which were new for me, and for that I am very grateful to my advisors Hussein and Minaoui for trusting me and giving me the freedom to pursue various projects and to conduct an independent and interdisciplinary research project.

I would like to express my gratitude to all the jury members who honoured me with their presence and feedback: Dr. Véronique Garçon, research director at *Laboratoire d'études en géophysique et océanographie spatiales, CNRS*; Pr. Emilio Hernández-García, Professor at *Institute for Cross-Disciplinary Physics and Complex Systems, Spain*; Dr. Guillaume Charria, Senior researcher at *Laboratoire d'Océanographie Physique et Spatiale, Ifremer*; Dr. Abdelali El Moussaoui, Senior researcher at *Mercator Ocean*; Pr. Mohammed Ouadou, Professor at *Mohammed V University in Rabat.*

I am also very grateful to all my friends and colleagues who have supported me during the last few years: Stophe, Badr, Mehdi, Francis, Mohammed, Safae, Ekaterina, Guillaume, Biswajit, Arash, Gongfeng and Ayoub.

Finally, I would not have made it this far without the support of my family, and for that, I will be always grateful to them. Thank you mom, dad, Youness, Meryem and Bibisha.

This work was funded by PHC-Toubkal Project n° TBK/16-24 and PPR2-6.

Acronyms

AVHRR	Advanced Very High Resolution Radiometer
CCUS	Current Upwelling System
CHLa	Chlorophyll-a
CSET	Cross-Shore Ekman Transport
CTZ	Coastal Transition Zone
CUC	Canary Upwelling Current
CUI	Coastal Upwelling Index
EBCUS	Eastern Boundary Current upwelling Systems
EBUZ	Eastern Boundary Upwelling Zones
EKE	Eddy Kinetic Energy
FCM	Fuzzy c-means
FSLE	Finite-size Lyapunov Exponent
FTLE	Finite-time Lyapunov Exponent
GDP	Gross Domestic Product
LACCL	Lagrangian Averaged Closed Curve Length
LAVD	Lagrangian Averaged vorticity Deviation

LCS	Lagrangian Coherent Structure
MODIS	Moderate Resolution Imaging Spectroradiometer
MSM	Most Singular Manifold
NAO	North Atlantic Oscillation
NWA	North-West African
PDE	Partial Differential Equations
PSO	Particle Swarm Optimization
SST	Sea Surface Temperature
SSH	Sea Surface height

Contents

List of Figures

List of Tables

Chapter 1

Introduction

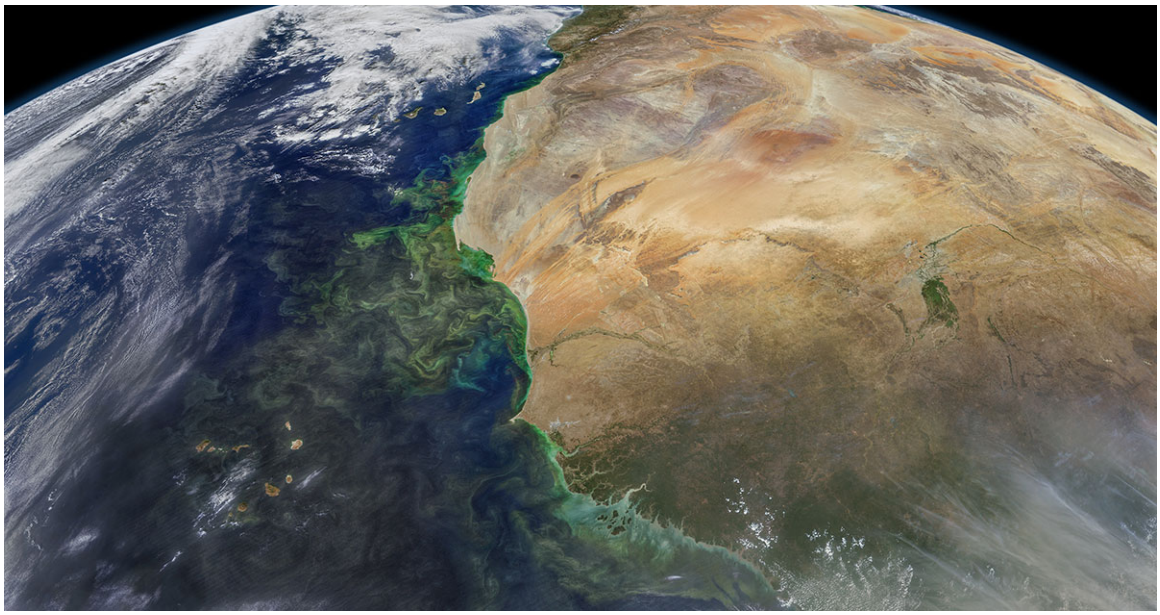

Abstract

The present chapter is dedicated to describe the general physics driving coastal upwelling, numerous upwelling mechanisms and indicators, the ecological response to coastal upwelling events, the location of major upwelling ecosystem, to present different data used throughout this thesis, and to present the objective and organization of this thesis.

1.1 Upwelling

In general terms, the National oceanic and Atmospheric Administration defines upwelling as *"a process in which deep, cold water rises toward the surface"*. According to the processes in play, we can distinguish different types of upwelling:

- **Wind-driven upwelling:**
  - **Coastal upwelling:** The most known type of upwelling, and the most closely related to human activities. It is generated by the wind blowing parallel to a coastline in a favorable direction and for a sufficient period of time [Huyer, 1983, Feely et al., 2008, Andrews and Hutchings, 1980, Bakun, 1990] (more details in the next subsection).
  - **Upwelling at the Equator:** It occurs close to the Equator where the Southern Hemisphere trade winds reach into the northern hemisphere, giving uniform wind direction on either side of the equator. This causes a divergence at the surface at the equator, which drags up nutrient-rich water from below [Wyrtki, 1981, Picaut, 1983].
  - **Upwelling in the Southern ocean:** This is actually a type of coastal upwelling, it is generated due to strong eastward winds blowing around Antarctica all year round. Since there are no continents in a band of open latitudes between South America and the tip of the Antarctic Peninsula, this upwelling provides a pathway for the deep water masses of the global ocean to return to the surface [Anderson et al., 2009].
- **Other sources**
  - **Sub-mesoscale Eddies edge:** They are those that show a negative Sea Surface Height (SSH) (water colder than the surrounding areas) that can upwell cooler and nutrient-rich water towards the ocean surface. Those with a positive SSH (warm eddies) have a downwell effect of warm surface waters. However, the net impact of these eddies on the biological activity

in the global ocean is still not fully understood, and it is a subject of very active research [Klein and Lapeyre, 2009, Mahadevan and Tandon, 2006].

– **Current interactions:** interaction between two currents can cause upwelling. For example, interaction between the warm poleward Brazil Current and the cold equatorward Malvinas Current causes upwelling with interesting phytoplankton blooms [Matano et al., 2010, Olson et al., 1988].

1.1.1 Coastal upwelling

The coastal upwelling phenomenon can be defined as "a wind-driven near-shore circulation induced into stratified rotating ocean." Several important items can be pointed out from this definition:

- **Wind:** Wind force plays a dominant role in the dynamics of coastal upwelling.
- **Near-shore:** this phenomenon takes place in coastal zones.
- **Stratification:** the fluid presents vertical water masses with different properties (density, temperature, salinity...)
- **Rotation:** Coriolis effect caused by the Earth's rotation plays important roles in the dynamics of upwelling phenomenon.

1.1.2 The physics of coastal upwelling

The simplest explanation of the coastal upwelling [Stewart, 2000] is summarized in Fig.1-1: When the wind blows across the sea surface during sufficiently long time and in a particular direction, it causes wind-water interaction which provokes mean transverse transport of the water [Ekman, 1905]. This is called *Ekman transport*, and it can produce a net movement of the ekman layer 90° to the right (left) of the wind in the northern (southern) hemisphere.

[1] `https://www.nwfsc.noaa.gov/research/divisions/fe/estuarine/oeip/db-coastal-upwelling-index.cfm`

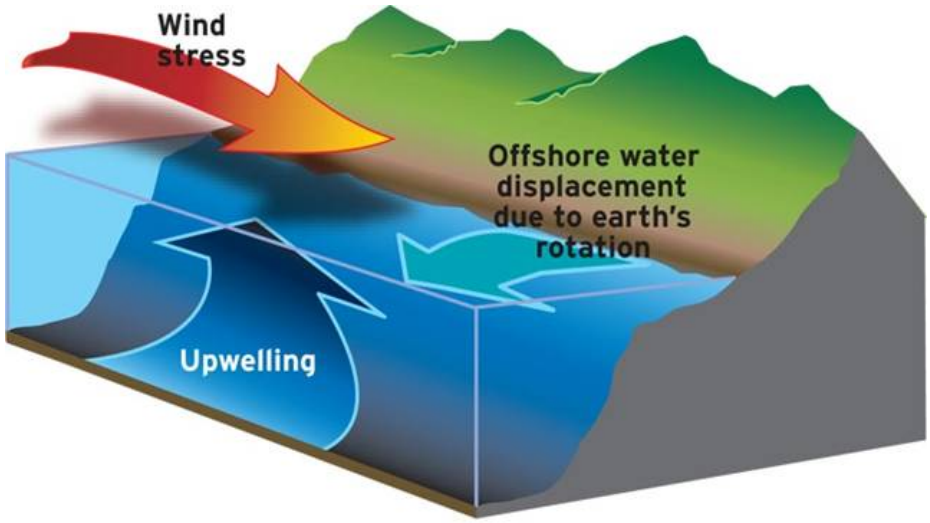

Figure 1-1: Scheme of coastal upwelling in the northern hemisphere. It shows winds blowing southward and causing a net movement of surface water 90° to the right. This water movement is replaced with deep water, a process called upwelling[1].

In the case of the northern hemisphere, if the wind blows southward along a meridional-oriented coastline, then offshore Ekman transport is created at the surface. The associated lowering of the sea surface near the coast produces a pressure gradient which is directed normal to the shore and drives a geostrophic current along the coast, with the same direction as the wind, called *upwelling jet* [Allen, 1973]. Flow field related to upwelling is directed at an angle away from the coast near the surface, parallel to the coast at mid-depth (below the Ekman layer but above the bottom boundary layer) and at an angle towards the coast in the frictional boundary layer at the bottom [Csanady, 1967]. Thus, the effective water movement is the result not only of the wind but also the geostrophic flow arising from the water depletion along the coast.

To better understand the upwelling phenomenon, we must address several processes related to it. These are surface, deep circulation and the processes responsible for the vertical movement. The Sun is the main source of energy which drives ocean currents [Ellabban et al., 2014]. Earth receives uneven solar energy, the tropics absorb more heat than they lose, and the poles lose more heat than they absorb [Pvamanarhan et al., 1989] as shown in the world map of average annual sunshine

(see Fig.1-2). The imbalance between poles and equator drives the planetary heat

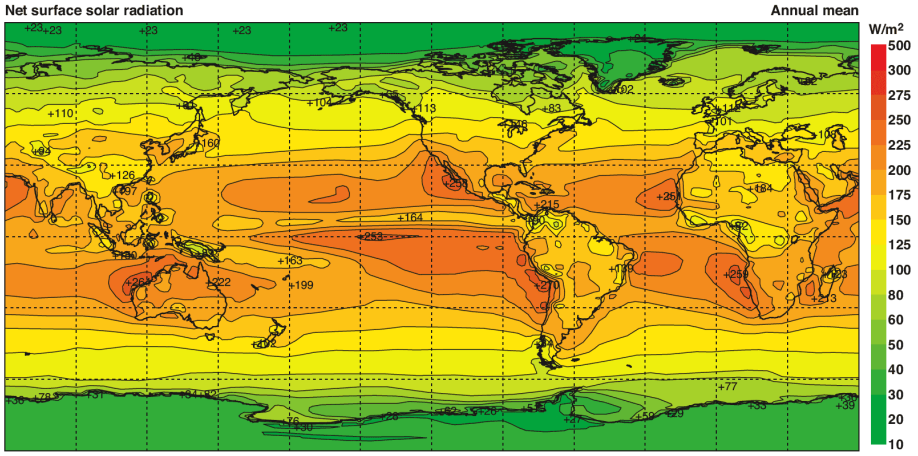

Figure 1-2: Heating of earth's surface by solar radiation, in W/m2, calculated from the ECMWF 40-year reanalysis of atmospheric data. The tropics absorb more heat than they lose, while the poles lose more heat than they absorb. This imbalance drives the planetary heat engine[2].

engine. Heat is redistributed around Earth and to various parts of the climate system through various processes, including ocean processes, atmospheric processes, and interactions between the two [Loubere, 2012]. About half the heat transported to the poles is carried by the ocean currents. The other half is transported by winds [Loubere, 2012].

Wind-induced circulation

The main driver of surface currents is the wind [Lagerloef et al., 1999]. The winds are governed by an alternation of low and high pressures according to the latitude. The large-scale global wind field consists of dominating westerly winds at latitudes between 30 and 60 degrees in the northern and southern hemispheres (the Westerlies) and dominating easterly winds in the tropical/subtropical zone (the Trade winds) [Hadley et al., 1735]. This wind field pattern results from the low atmospheric pressure in the tropics (warm ascending air) and high atmospheric pressure in the subtropics (cooled descending air)[Sverdrup, 1947]. Wind stress generates strong currents (up to several m/s) in the ocean surface layer. The thickness of the surface layer which is triggered

[2] `http://www.personal.kent.edu/~mkeatts/oceansandclimate.html`

by wind is of the order of 500 meters [Charnock, 1955]. Due to earth rotation (Coriolis effect), ocean currents tend to be deflected to the right in the northern hemisphere and to the left in the southern hemisphere [Kundu, 1976], hence creating the five major gyres: the North Atlantic, the South Atlantic, the North Pacific, the South Pacific and the Indian Ocean Gyre [Rhines and Young, 1982], see Fig.1-3 (clockwise rotating in the northern hemisphere and anticlockwise in the southern hemisphere).

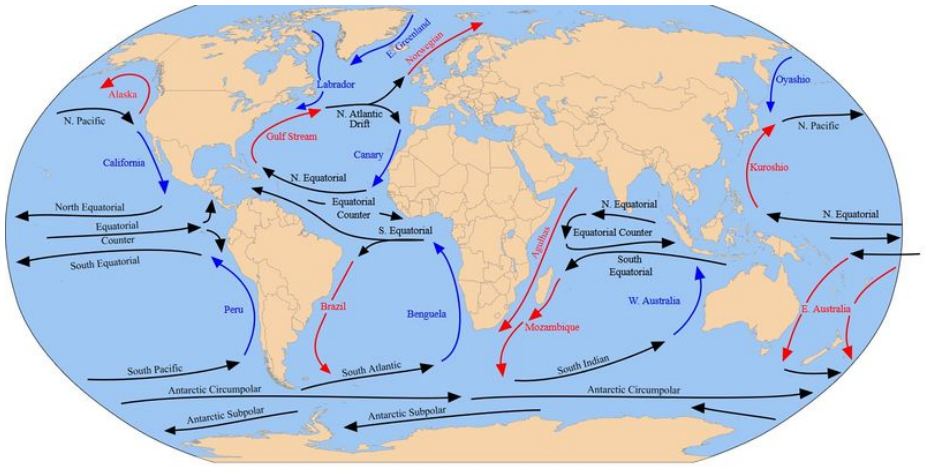

Figure 1-3: World's map showing the main ocean current system which consists of large anticyclonic gyres. Warm currents are shown in red and cold currents are shown in blue[3].

Deep ocean circulation

The winds have no more influence after 800m of depth, thus, they can not be the engines of the deep ocean circulations [Price et al., 1987]. Those currents are primarily driven by density differences [Fairbanks, 1989]. This is called the thermohaline circulation, because it is based on temperature differences (cold water is denser than hot water) and salinity differences (salt water is denser than fresh water). The thermohaline circulation is mainly driven by the formation of deep water masses in the North Atlantic and the Southern ocean caused by differences in temperature and salinity of the water [Aagaard et al., 1985]. The great quantities of dense water sinking at high latitudes must be offset by equal quantities of water rising elsewhere. Note that

[3] `https://earthhow.com/`

cold water in polar zones sink relatively rapidly over a small area, while warm water in temperate and tropical zones rise more gradually across a much larger area (see Fig.1-4 for summary of the thermohaline circulation's path). Then they slowly return poleward near the surface to repeat the cycle [Stommel and Arons, 1959]. However, the water masses moving around by thermohaline circulation are huge (water fluxes are of the of 20 sverdrup ($10^6 m^3 s^{-1}$). Density gradients alone are not sufficient for sustaining the deep ocean circulation. Upwelling and mixing processes, to bring deep ocean water back to the surface, are required too [Elias, 2006].

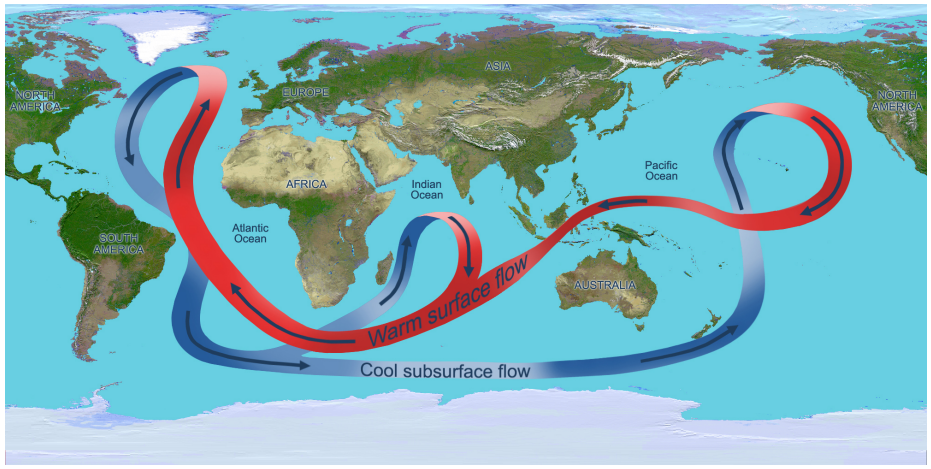

Figure 1-4: World's map showing the thermohaline circulation. Blue paths represent cool deep-water currents, while red paths represent warm surface currents[4].

Ekman transport

Upwellings are due to the effect of wind over the sea surface. The physical processes associated with the oceanic response to the wind have been known for a long time. It was Vagn Walfrid Ekman, a Swedish oceanographer, who laid the foundations of the theory of upwellings. As wind blows over the ocean a surface current develops due to the drag at the wind-water interface [Ekman, 1905]. The surface current, under the Coriolis effect is deflected to the right (northern hemisphere). When surface water particles are moved by the wind, they drag deeper layers of water molecules

[4] `https://earthhow.com/`
[5] `http://pordlabs.ucsd.edu/`

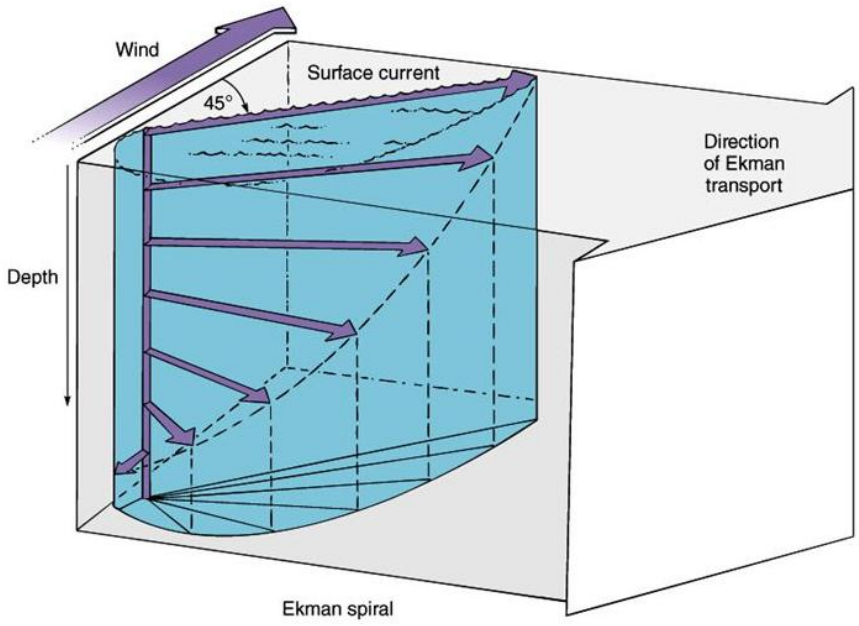

Figure 1-5: The Ekman spiral pattern under ideal conditions in the Northern Hemisphere. Each successive layer of water is deflected to the right of surface wind. The lengths of the arrows correspond to the strength and direction of the current[5].

below them. Like surface water, the deeper water is deflected by the Coriolis effect to the right of the wind in the Northern Hemisphere and to the left in the Southern Hemisphere [Ekman, 1905]. As a result, each successively deeper layer of water moves more slowly to the right or left, creating a spiral effect as shown in Fig.1-5. This is called the Ekman spiral [Knauss and Garfield, 2016]. The layer of water from the surface to the point of dissipation of this spiral is known as the Ekman layer. If all flow over the Ekman layer is integrated, the net transportation is at 90° to the right (left) of the surface wind in the northern (southern) hemisphere.

1.1.3 Identification

According to the national oceanic and atmospheric administration *"Upwelling is a process in which deep, cold water rises toward the surface."*

According to this description, deep water that surfaces in upwelling regions is cold, thus, upwelling events are easily identified using Sea Surface Temperature (SST) images. Fig.1-6 was obtained by combining all the SST measurements made by

the Moderate Resolution Imaging Spectroradiometer sensor (MODIS) aboard Aqua satellite, from February 1, 2002, to January 29, 2008. These data are obtained through the ocean Color web page `https://oceancolor.gsfc.nasa.gov`.

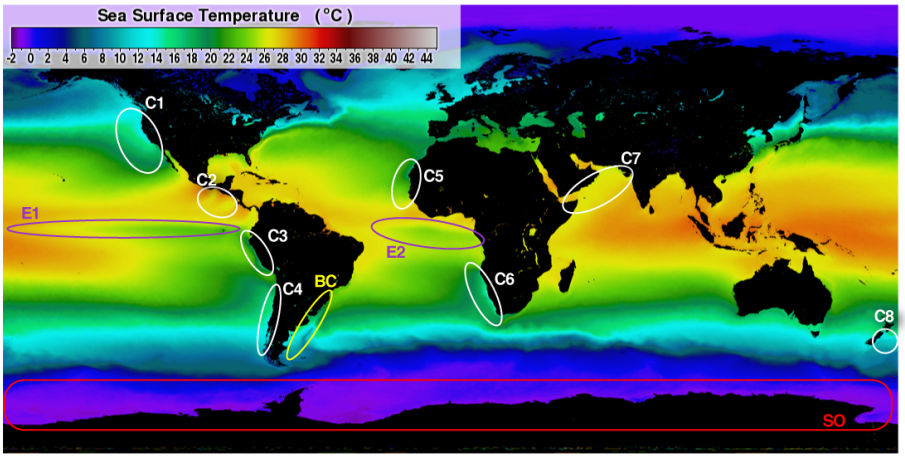

Figure 1-6: Climatology of sea surface temperature, computed for the period of time between Feb 1, 2002 to Jan 29 2008. $C_{1..8}$ delineate different coastal upwellings in the globe. E_1 and E_2 present equatorial upwellings.

Upwelled water also contains nutrients and dissolved gases that are not been used at depth because of a lack of sunlight [Bakun, 1990]. Once on the surface, these nutrients and gasses help to fuel photosynthesis by small algae called phytoplankton [Margalef, 1978]. Phytoplankton contains a photosynthetic pigment called chlorophyll that lends them a greenish color [Pottier, 2006]. When phytoplankton grows in large numbers, they make the ocean appear green in color. Thus, ocean color images can also be used to identify upwelling regions. We show in Fig.1-7 an example of chlorophyll-a ($\mathrm{CHL_a}$) concentration map obtained as the combination of all $\mathrm{CHL_a}$ images made my MODIS from February 1, 2002, to January 29, 2008. Upwelling regions can be identified from these maps as coastal areas with high $\mathrm{CHL_a}$ concentration.

From the global view of the surface temperature and $\mathrm{CHL_a}$, we can detect four regions of coastal upwelling, often referred to as upwelling systems:

- The Canary Current, located off northwest Africa.
- The Benguela upwelling, located along the coasts of Namibia and South Africa.

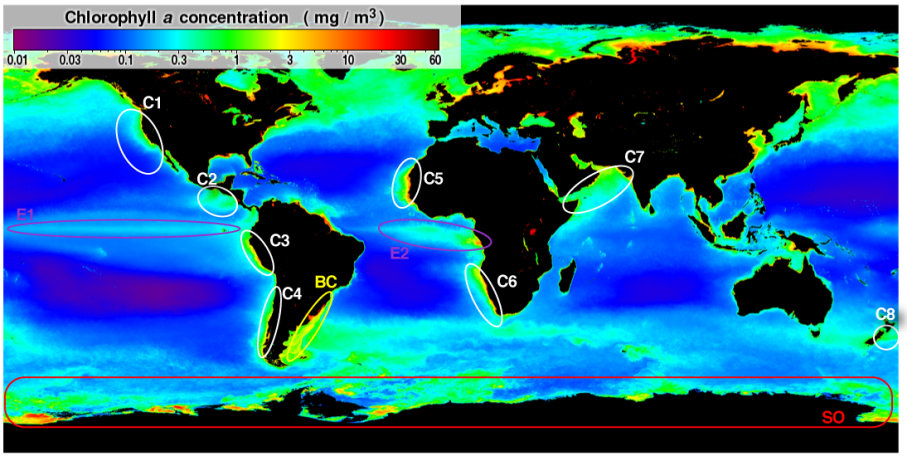

Figure 1-7: Climatology of Chlorophyll-a concentration, computed for the period of time between Feb 1, 2002 to Jan 29 2008. $C_{1..8}$ delineate different coastal upwellings in the globe. E_1 and E_2 present equatorial upwellings.

- The Peru-Chile upwelling system, also known by the Humboldt Current.
- The California upwelling system, located along the west coast of north America.

All these regions are located in the eastern part of the main subtropical gyres. Thus, they are known as *Eastern Boundary upwelling Systems (EBUS).*

1.1.4 Why upwelling systems are important?

By injecting nutrients into the surface water, upwelling systems play an important role in the marine ecosystems [Strass, 1992]. Hundreds of species at different trophic levels are attracted to upwelling region creating interesting biological life and diversity [Cury and Roy, 1989, Marlow et al., 2000]. Even though upwelling areas represent only 0.1% of the total ocean surface, they are home to the largest contribution of ocean biological productivity. Their mean productivity is estimated around 6 times of the mean productivity in the open ocean [Ryther, 1969]. Coupled with the vast coastal human populations, these regions play key biological and socio-economical roles. [Durand et al., 1998] stated that approximately 30% of marine fish catches is provided by the four major upwelling systems, while [Jennings et al., 2009] estimated that the five major upwelling systems can provide 25% of the global fishery.

In this work we are interested in the Canary upwelling Ecosystem, particularly the central part located in the North-West African margin. The winds responsible for the Canary upwelling System are called *trades* [Barton et al., 1998]. They are caused by the atmospheric pressure gradient. They are due to the regular alternation of bands of high pressure (or tropical ones) and low pressure (equatorial). Trade winds reach their maximal intensity in summer, when the Azores high pressure system is at its northernmost position [Wooster et al., 1976].

Fisheries play an important role in the socio-economy of coastal states of the Canary current upwelling system [Arístegui et al., 2006, Binet et al., 1998]. In this region, a population of about 58 million of which 70% are related to the Canary Current ecosystem [Heileman and Tanstad, 2008], this population is distributed over many countries: Morocco, Canary islands (Spain), Mauritania, Guinea, Gambia, Cape Verde and Senegal. As for example in 2006, Morocco's fisheries contributed 3% to the country's GDP (Gross Domestic Product) and $500,000$ opportunities between direct and indirect jobs. For Senegal the fisheries contributed 11% to the country's GDP and about $700,000$ jobs were associated to it [Kämpf and Chapman, 2016].

1.2 Remote sensing and satellite images

1.2.1 Remote sensing

Remote sensing is the science that makes it possible to observe earth, ocean and atmosphere systems, at a distance, without any physical contact [Lillesand et al., 2014]. It works by exploiting the electromagnetic radiation from a source that interacts with targets on the earth's surface in a unique manner, depending on its physical, chemical, and biological properties to be reflected, emitted, or backscattered towards a sensor [Boyd, 2005]. It may be split into "active" remote sensing (when a signal is emitted by a satellite or aircraft and its reflection by the object is detected by the sensor) and "passive" remote sensing (when the reflection of sunlight is detected by the sensor) [Schowengerdt, 2006].

There are four types of resolution when discussing satellite imagery in remote sensing: spatial, spectral, temporal, and radiometric:

Spatial resolution

Satellite image consists of an array of pixels. Each pixel contains measurement about a small area on the land surface, which is considered as a single object [Jensen and Lulla, 1987]. Spatial resolution is a measure of the area of the smallest dimension on the Earth's surface over which an independent measurement can be made by the sensor. It is not only determined by sensor specifics, but also the height of the sensor above the Earth's surface. Fig.1-8 gives an example of the same object acquired in different spatial resolutions. A high spatial resolution corresponds to a small pixel size.

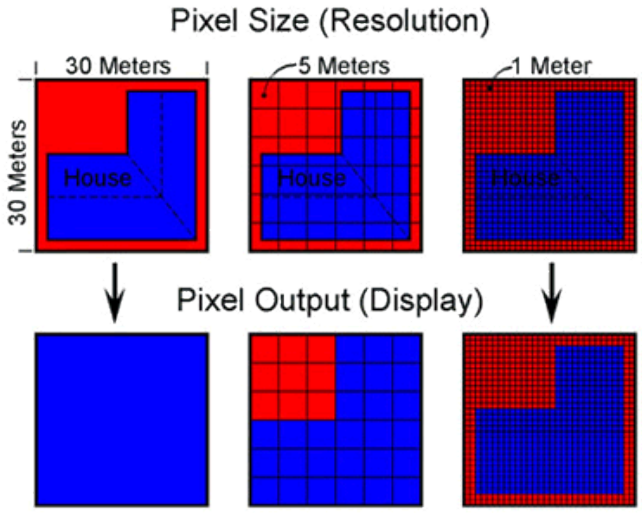

Figure 1-8: Raster with low and high spatial resolution, low resolution may lead to sub-sampling.

Spectral resolution

Our universe is filled with electromagnetic radiation spread over a range of wavelengths ranging from gamma rays of small wavelengths $\mathcal{O}(1010\,\mu\text{m})$ to long wave radio waves $\mathcal{O}(1010\,\text{nm})$ (see Fig.1-9). Different classes of features and details in an image can often be distinguished by comparing their responses over distinct wavelength

ranges [Jensen and Lulla, 1987]. Spectral resolution, or more generally frequency spectrum, is a complex attribute referring to the number and spectral width of the bands in a given sensor [Steininger and Horning, 2007]. Higher spectral resolution refers to large number of bands and narrow spectral widths.

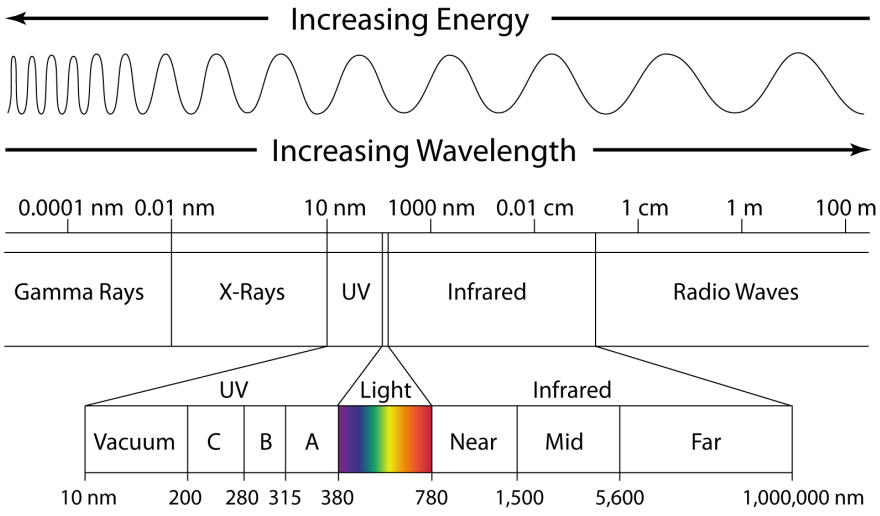

Figure 1-9: A diagram of the electromagnetic spectrum, showing various properties across the range of wavelengths and energies.

Radiometric resolution

While the arrangement of pixels describes the spatial resolution of an image, the radiometric resolution describes the actual information content in an image [Tsang et al., 1985]. Every time an image is acquired on film or by a sensor, its sensitivity to the magnitude of the electromagnetic energy determines the radiometric resolution. The radiometric resolution of an imaging system describes its ability to discriminate very slight differences in energy. The finer the radiometric resolution of a sensor [Lillesand et al., 2014], the more sensitive it is to detecting small differences in reflected or emitted energy. In other words, the radiometric resolution refers to the dynamics of the acquired signal.

Temporal resolution

In addition to spatial, spectral, and radiometric resolution, the concept of temporal resolution is also important to consider in a remote sensing system. Temporal resolution refers to the precision of a measurement with respect to time. It is considered as the minimum time scale during which a particular feature can be recorded twice. The absolute temporal resolution of a remote sensing system to image the same area at the same viewing angle a second time is equal to the *repeat cycle* of a satellite.

The ability to collect imagery of the same area of the Earth's surface at different periods of time is one of the most important elements for applying remote sensing data [Lillesand et al., 2014]. Spectral characteristics of features may change over time and these changes can be detected by collecting and comparing multi-temporal imagery.

1.2.2 Satellite images

Sea Surface Temperature

Sea surface temperature (SST) provides a synoptic view of the temperature distribution of the skin (first micrometers of the surface layer) of the surface ocean [Rayner et al., 2003]. The satellite-measured SST provides both a synoptic view of the ocean and a high frequency of repeat views [Alexander and Fairbridge, 1999], allowing the examination of basin-wide upper ocean dynamics not possible with ships or buoys. In this thesis, we consider NASA's (National Aeronautic and Space Administration) Moderate Resolution Imaging Spectroradiometer (MODIS). MODIS satellites have been providing global SST data since 2000 [Minnett et al., 2004].

MODIS captures data in 36 spectral bands ranging in wavelength from 0.4 µm to 14.4 µm and at varying spatial resolutions (2 bands at 250 m, 5 bands at 500 m and 29 bands at 1 km; see Tab.1.1 for more details), providing complete global coverage of the Earth every 1 to 2 days [Savtchenko et al., 2004]. MODIS Aqua Global Level 3 Mapped Thermal SST products consists of SST data derived from the 11 and 12 µm thermal IR infrared (IR) bands (MODIS channels 31 and 32). Daily, weekly (8 day)

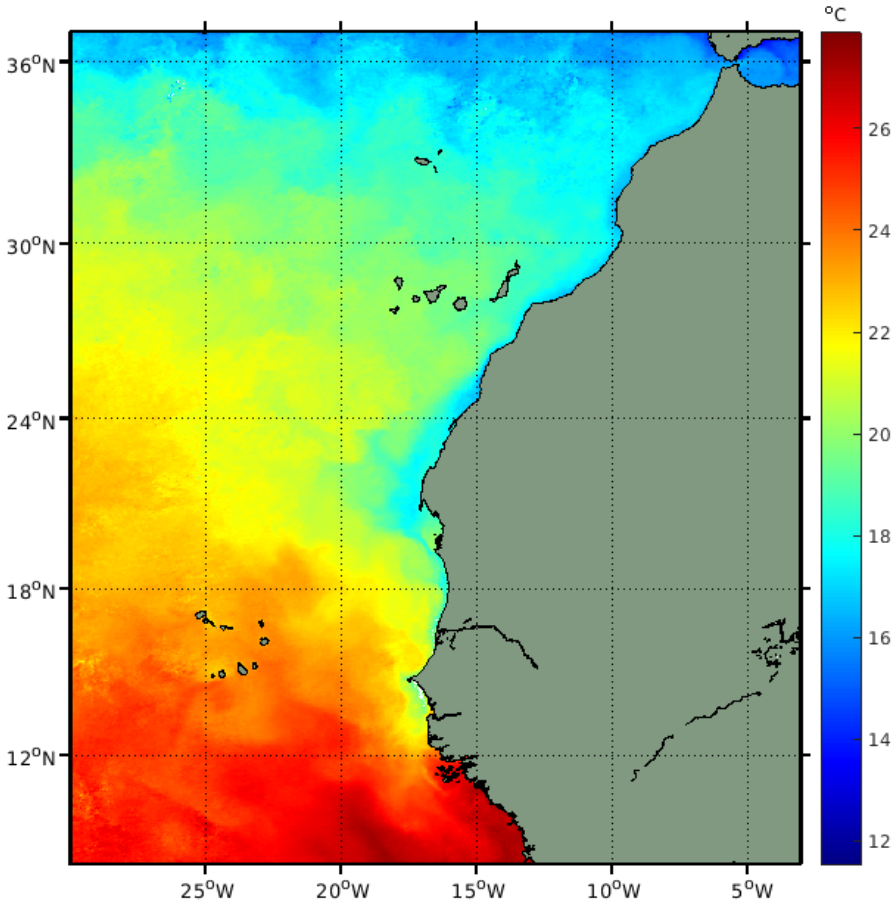

Figure 1-10: Modis 30-day SST image over the North-West African margin. Each pixel presents temperature in $°C$. This image is obtained on the first week of January 2001 and it is showing a typical upwelling scenario over the studied area.

and monthly images are available at both 4.63 and 9.26 km spatial resolution and for both daytime and nighttime passes [Justice et al., 2002]. Fig.1-10 shows an example of MODIS 8-day SST image over the North-West African upwelling.

Ocean color

Unlike Sea Surface Temperature data (which comes directly from the ocean's proper radiation in the infrared), ocean color is determined by the interactions between visible solar radiation as well as the constituents that are in suspension in the ocean [Pottier, 2006]. Consequently, phytoplankton as well dissolved organic matter will have their proper spectral characteristics, and ocean color data can be calibrated to

provide datasets of CHL_a concentration (CHL_a) in proper units (mg/m^3) [Carder et al., 2004]. CHL_a concentration data provide an estimate of the live phytoplankton biomass in the surface layer [Pottier, 2006]. The MODIS Aqua instrument provides quantitative data on global ocean bio-optical properties to examine oceanic factors that affect global change and to assess the oceans' role in the global carbon cycle, as well as other biogeochemical cycles.

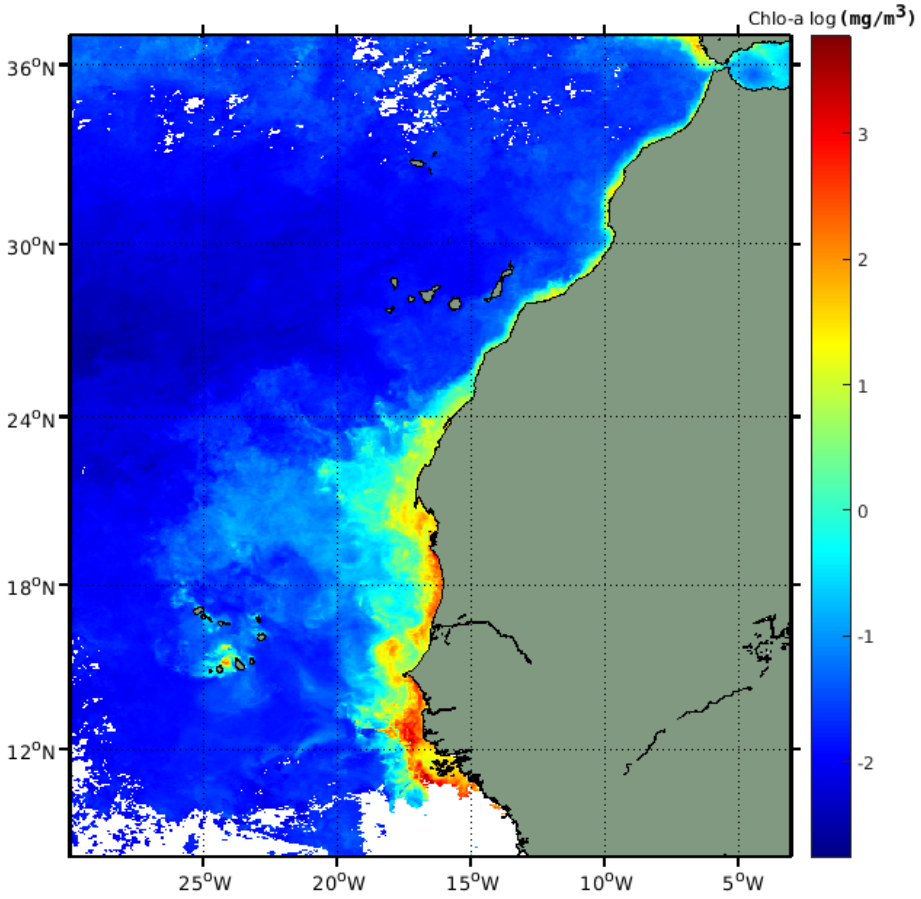

Figure 1-11: MODIS 30-day CHL_a concentration image over the North-West African margin. Each pixel presents CHL_a concentration in ($log(mg/m^3)$). This image is obtained on the first week of January 2001 and it is showing a typical upwelling scenario over the studied area.

The MODIS CHL_a products are derived using a 3-band ocean color algorithm (OC3) with the NOAA-MSL12 software [Wang et al., 2014, Carder et al., 2004]. Atmospheric correction is performed using the NOAA NIR-SWIR combined approach developed by the NOAA/NESDIS Center for Satellite Applications and Research

(STAR). The Level 3 standard mapped image (SMI) CHL_a dataset has daily, weekly (8 day) and monthly temporal resolution and 4.6 km (at the equator) spatial resolution. Fig.1-11 shows and example of MODIS 8-day image over the North-West African upwelling.

Wind speed and direction

Ocean wind is defined as the motion of the atmosphere relative to the surface of the ocean [Trenberth et al., 1990]. Typically, ocean winds are measured very close to the ocean surface by buoys, platforms, and ships. The most common reference height for near-surface ocean wind measurements is 10 meters above sea level [Yelland and Taylor, 1996]. Ocean wind is measured using either in situ (i.e., on site) or remote sensing (i.e., from a distance) instruments and techniques [Wentz et al., 1992]. Here we consider those measured by satellite. Two types of microwave instruments measure ocean surface winds, the passive microwave radiometer and the active microwave scatterometer. The ocean surface responds quickly to the motion of the air above, which provides a distinct roughness pattern depending on the relative speed and direction of the wind with respect to the ocean surface [Risien and Chelton, 2008]. The roughness of the ocean surface provides a specific "brightness". With the right combination of specific microwave wavelengths and processing algorithms, the brightness of the ocean surface can be accurately translated to a near-surface wind speed [Liu, 2002]. We must note that the brightness provided by the roughness of the ocean surface can only be observed using passive microwave radiometers. On the other hand, the scatterometer is an active instrument and sends a signal to the Earth's surface which reflects off the ocean Bragg waves on the surface of the larger scale ocean waves [Ebuchi et al., 2002]. The reflected energy measured by the scatterometer is translated using a geophysical model function into a 10-meter neutral wind speed and direction [Stoffelen and Anderson, 1997].

In this thesis we consider data from Quick Scatterometer (launched in June 1999 and operated until November 2009). The Level 3 wind speed and direction dataset is available at daily, weekly and monthly temporal resolution and 0.25° of spatial

Primary Use	Band	Bandwidth	Spectral Radiance	Required SNR
Land/Cloud/Aerosols Boundaries	1	620 - 670	21.8	12
	2	841 - 876	24.7	201
Land/Cloud/Aerosols Properties	3	459 - 479	35.3	243
	4	545 - 565	29.0	228
	5	1230 - 1250	5.4	74
	6	1628 - 1652	7.3	275
	7	2105 - 2155	1.0	110
Ocean Color/ Phytoplankton/ Biogeochemistry	8	405 - 420	44.9	880
	9	438 - 448	41.9	838
	10	483 - 493	32.1	802
	11	526 - 536	27.9	754
	12	546 - 556	21.0	750
	13	662 - 672	9.5	910
	14	673 - 683	8.7	1087
	15	743 - 753	10.2	586
	16	862 - 877	6.2	516
Atmospheric Water Vapor	17	890 - 920	10.0	167
	18	931 - 941	3.6	57
	19	915 - 965	15.0	250
Surface/Cloud Temperature	20	3.660 - 3.840	0.45(300K)	0.05
	21	3.929 - 3.989	2.38(335K)	2.00
	22	3.929 - 3.989	0.67(300K)	0.07
	23	4.020 - 4.080	0.79(300K)	0.07
Atmospheric Temperature	24	4.433 - 4.498	0.17(250K)	0.25
	25	4.482 - 4.549	0.59(275K)	0.25
Cirrus Clouds Water Vapor	26	1.360 - 1.390	6.00	150(SNR)
	27	6.535 - 6.895	1.16(240K)	0.25
	28	7.175 - 7.475	2.18(250K)	0.25
Cloud Properties	29	8.400 - 8.700	9.58(300K)	0.05
Ozone	30	9.580 - 9.880	3.69(250K)	0.25
Surface/Cloud Temperature	31	10.780 - 11.280	9.55(300K)	0.05
	32	11.770 - 12.270	8.94(300K)	0.05
Cloud Top Altitude	33	13.185 - 13.485	4.52(260K)	0.25
	34	13.485 - 13.785	3.76(250K)	0.25
	35	13.785 - 14.085	3.11(240K)	0.25
	36	14.085 - 14.385	2.08(220K)	0.35

Table 1.1: Characteristics of MODIS. Bands 1 to 19 are in nm, Bands 20 to 36 are in µm, Spectral Radiance values are $(W/m^2 - \mu m - sr)$, SNR = Signal-to-noise ratio, $NE(\Delta)T$ = Noise equivalent temperature difference.

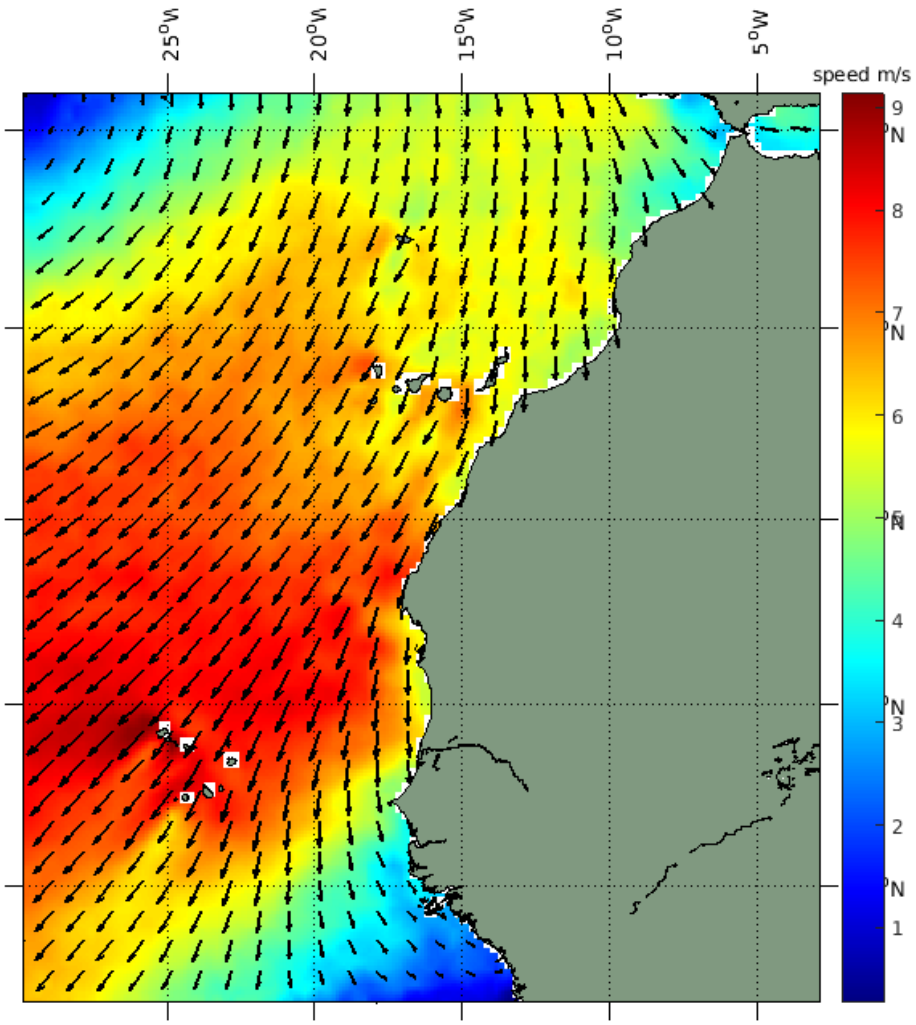

Figure 1-12: Quikscat wind speed (ms^{-1}) for the first week of January 2001. Black arrows highlight different wind direction which are the main driver of the upwelling phenomenon over the North-West African margin.

resolution. Fig.1-12 shows QuikScat wind speed and direction over the North-West African upwelling.

Sea Surface Height

Sea Surface Height (SSH) is the sea surface height with respect to the Reference ellipsoid (an arbitrary reference surface that is a rough approximation of the Earth's shape). SSH measurement includes dynamic contributions from ocean circulation and variations in the geoid with respect to the reference ellipsoid. The sea surface height (SSH) is calculated through altimetry satellites [Glazman et al., 1996], which

determine the distance from the satellite to a target surface by measuring the satellite-to-surface round-trip time of a radar pulse [Chelton et al., 2001]. The satellites then measure the distance between their orbit altitude and the surface of the water. Due to the difference in depths of the ocean, an approximation is made.

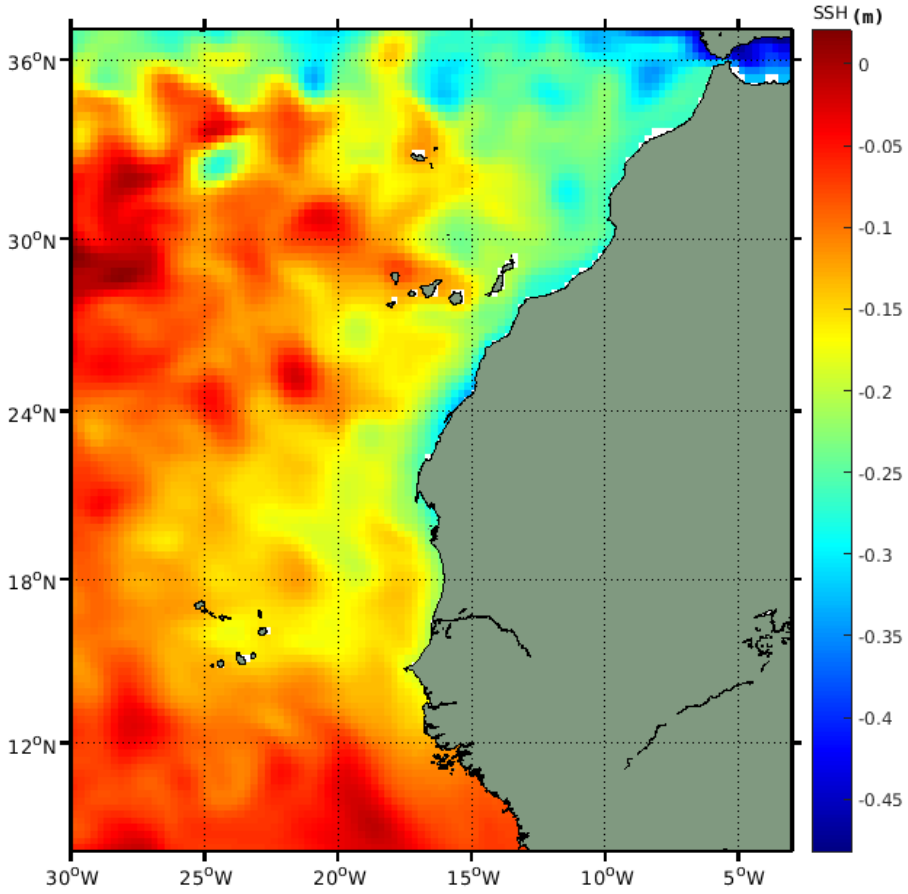

Figure 1-13: 8-day Sea Surface Height (SSH) composite above mean geoid. Each pixel presents information in meter. This AVISO data is obtained in the first week of January 2001 over the North-West African margin.

The satellite's altitude then has to be calculated with respect to the reference ellipsoid. It is calculated using the orbital parameters of the satellite and various positioning instruments. The sea surface height is then the difference between the satellite's altitude relative to the reference ellipsoid and the altimeter range. The satellite sends microwave pulses to the ocean surface. In this thesis we consider SSALTO/DUACS multi-satellite products. The daily data is obtained from the Copernicus Marine Environment Monitoring Service (CMEMS) with spatial resolution of $25km$. Fig.1-13

shows Aviso SSH over the North-West African upwelling.

1.3 Operational oceanography and model data

Operational oceanography can be defined as the activity of systematic and long-term routine measurements of the seas and oceans and atmosphere, and their rapid interpretation and dissemination. It can provide estimates of essential ocean variables (e.g. sea level, temperature and currents) for the present and the future, as well as for the past [Flather, 2000]. Operational oceanography depends on availability of ocean observations and super-computer facilities, and uses computer models and mathematical models that have been developed over several decades [Flather, 2000]. Ocean observations are required in real-time and near-real-time, thus it is usually proceeded by the rapid transmission of observational data to data assimilation centers [Ide et al., 1997].

1.3.1 Mercator ocean and GLORYS2V4

Mercator ocean is a privately-owned non-profit company, funded by five major French institutions involved in operational oceanography, CNRS (National Center of Scientific Research), Ifremer (French Research Institute for Exploitation of the Sea), IRD (Institute of Research for Development), Meteo-France and Shom (Hydrographic and oceanographic Service of the French Navy), whose goal is to deliver comprehensive, worldwide information on the oceans' physical state from surface to bottom, using ocean modeling and data assimilation. To this end, Mercator-ocean operates a large range of operational systems [ocean forecast system (OFS)] that can analyze and forecast the three-dimensional ocean state, including temperature, salinity, and currents at various resolutions.

Important products provided by Mercator ocean are:

- nowcasts providing the most usefully accurate description of the present state of the sea including living resources.

- forecasts providing continuous forecasts of the future condition of the sea for as far ahead as possible.

- Reanalyses assembling long term data sets which will provide data for description of past states, and time series showing trends and changes,

Mercator ocean uses the general-circulation model, in the global and regional case, based on the Nucleus for European Modelling of the ocean (NEMO) [Madec et al., 2015]. Daily surface atmospheric conditions are given by the analyses and forecasts of the European Center for Medium Range Weather Forecast (ECMWF).

Another component of the Operational forecasting system is the assimilation system. It was developed to assimilate satellite sea-level anomaly (SLA) data coming from the SSALTO/DUACS data center gathering all available missions (JASON, ENVISAT, and GFO), as well as SST and vertical profiles of in situ temperature and salinity measurements from the CORIOLIS center (ARGO profiling floats, XBT, CTD, TAO/PIRATA/TRITON moorings) [Vidard et al., 2009].

The weekly process of analyses/forecast run for day D begin with two successive 1-week analyses, starting at day D 14. Then, from day D, the system performs 2 weeks of forecasts, driven at the surface by the ECMWF atmospheric forecast [Garric and Parent, 2013]. Weekly runs provide daily mean analysis and forecast fields of temperature, salinity, and currents among other fields.

Here in this thesis we consider the Global Reanalysis GLORYS2V4 which contains 3D potential temperature, salinity and currents information from top to bottom global ocean and 2D sea surface level, sea ice thickness, sea ice fraction and sea ice velocities information [Garric et al., 2017]. This product is global with a spatial resolution of $1/4^\circ$ released on the ORCA025 tri-polar grid, and 75 vertical levels. More details are given bellow:

Table 1.2: Characteristics of GLORYS2V4

Geographical coverage	Global ocean ($180°W - 180°E; 77°S - 90°N$)
Grid and Resolutions :	ORCA025 [1/4°; 75 levels]
Grid size :	1442x1021x50 (partial steps)
Code et Version :	Nemo3.1
Data assimilation :	Yes
Sea Ice Modeling :	LIM2 EVP Sea Ice Model
Tides :	No
Bathymetry :	ETOPO1 for deep ocean and GEBCO8 on coast and continental shelf.
Time step :	1080 s

Table 1.3: Forcing and Data Assimilation

Data assimilation	yes
Data assimilation scheme:	SAM2v1 (Kalman filter with SEEK formulation) with Incremental Analysis Update and bias correction
Data assimilated	SST (Reynolds AVHRR-AMSR 1/4°), - Reprocessing of Sea Surface Height (Jason1, Jason2, Envisat, T/P, GFO, ERS1-2), -Reprocessing of InSituprofilesand "NASA team" for sea-ice -Elephant seals database - HybridMSSH - Sea ice concentration (IFREMER/Cersat)
Atmospheric forcings	- 3-Hourly ERA-interim ECMWF forcings; - Bulk CORE Formulation with radiative flux correction and diurnal cycle
Runoff	Dai and Trenberth(2002)Monthly Climatology/ 109rivers/ total rivers runoff 1.3Sv
Open Boundary Conditions	no

Table 1.4: Initial Conditions and Relaxation

Initial conditions	- T and S Levitus (1998) and PHC2.1 in the Arctic ocean and Medatlas for Mediterranean Sea. - NSIDC Bootstrap for Sea ice concentration and thickness.
Surface relaxation	No
Water column (3D) relaxation	Relaxation toward deep Antarctic waters
Convection	By intensication of vertical mixing (diffusion term)

Table 1.5: Parameterisation

Surface physics parametrisation :	Free Surface (explicit + filtering)
Bottom friction :	Non linear (constant bottom drag)
Lateral friction :	Partial slip (shlat = 0.5)
Vertical mixing :	TKE 1.5 closure scheme
Advection :	TVD advection scheme
Tracer diusion :	Isopycnal laplacian e11 m^2/s
Momentum diusion :	Horizontal bilaplacian + laplacian ($2000m^2/s$) in Ob and Ienisseï estuaries
Horizontal diusion coecient for tracers and momentum :	Ahm0 = -1.8 aht0 = 300 m^2/s

1.4 Thesis objectives

This thesis is conducted within the second phase of the Partenariats Hubert Curien Project, automatic detection of the Moroccan upwelling system from SST images, funded by Campus France. The first phase ran from February 2009 to May 2012. The subsequent second phase ended in December 2018 and had the topic: Multi-satellite study of upwelling along the Moroccan coast. This interdisciplinary project was carried out by several French and Moroccan research institutions covering atmospheric and oceanic science, physical, biological and computational aspects of the Moroccan upwelling system. This project had the goal to automatically identify and extract the Moroccan upwelling from SST and CHL_a images, to propose a new improved upwelling index, and to explore its spatio-temporal dynamics. To address the aims of the project, I raised the following questions and tried to answer them in my thesis. The first two questions focus on the automatic detection of the Moroccan upwelling system, whereas the last three cover its spatio-temporal dynamics.

- Why do previous automatic upwelling detection methods only work on the southern part of the system?
- What are the atmospheric drivers of the Moroccan upwelling system?
- How to automatically delineating the upwelling can serve us to study its spatio-temporal dynamics?
- How do physical and biological processes interact with each other in the Moroccan upwelling system?
- How does the Moroccan upwelling system contribute and impact the open ocean?

1.5 Thesis outline

The thesis contains six main chapters, chapter 2 to chapter 7. Most of them have been published or submitted for peer-reviewed publication. A short presentation of

the chapters content is given in the following.

In chapter 2, I present different classical methods of image processing commonly used in the segmentation of Upwelling regions from SST images and CHL_a concentration. I review previous methods proposed for the Moroccan upwelling detection, discuss their results and propose two efficient methods for the Moroccan upwelling identification from biological physical satellite observations.

In chapter 3, I make use of the upwelling extraction methods proposed in the previous chapter to introduce a simple and intuitive algorithm to quantify the Upwelling intensity. The newly introduced index improves the way the thermal difference is defined, taking into account the spatial structure of the upwelling, and its link with the Ekman transport. Later in this chapter, I use this proposed index, the upwelling extraction methods along with several other biological and physical indices to study the spatio-temporal variation of Moroccan upwelling dynamics.

In chapter 4, I motivate the importance of transport in fluids in many natural systems, then I introduce the phenomenon of *chaotic advection* and show methods from the theory of dynamical systems that allow the determination of the geometry of mixing in chaotic flows.

In chapter 5, I focus my interests in studying the relationship between physical structures of oceanic fronts and the biological productivity in upwelling regions. I study the horizontal stirring and mixing in different upwelling areas using Lagrangian coherent structures (LCSs). I compute these using the recent geodesic theory of LCSs. I use these LCSs to study the link between the CHL_a fronts concentrations and surface mixing, based on 10 years of satellite data. These LCSs move with the flow as material lines, thus I calculate the horizontal mixing from the intersection of these LCSs with the finite time Lyapunov exponents (FTLEs) maps. I compare my results with those of a recent study conducted over the same area, but based on Finite Size Lyapunov Exponents (FSLEs) whose output is a plot of scalar distributions. I discuss the differences between FSLE and geodesic theory of LCS. The latter yields analytical solutions of LCSs, while FSLEs can only provide LCSs for sharp enough ridges of nearly constant height

In chapter 6 and 7, my focus shifted toward studying the transport properties of mesoscale eddies (i.e. vortices of $100 \sim 200$ kms in diameter) over a finite time duration. While these oceanic structures are well known to stir and mix surrounding water masses by their swirling motion, they can also carry and transport organic matter as coherent structures. In these two chapters, I am interested in dynamic transport properties of these coherent structures, which have chaotic and mixing properties on large time scales. Present techniques to analyze fluid coherent vortices rely on classical geometric theory of the Cauchy-Green's invariants; vortices are related to closed orbits of their field. Others define coherent vortices from vorticity, by calculating its averaged deviation. In these chapters, I take two different approaches to identify coherent vortices and their centers in automatic manner. The first is based on a rigorous analysis of particles trajectories. The second method is based on the frequency-domain representation of Lagrangian trajectories. I illustrate the new methods by identifying and extracting Lagrangian coherent vortices in different two- and three-dimensional flows.

In chapter 8, I explore the impact of the Moroccan upwelling system over the open ocean. I do this by exploring the role played by mesoscale eddies off the Canary archipelago in carrying coherent waters from the upwelling region and pouring them into the open ocean. I use the method I proposed in the previous chapter to extract coherent mesoscale eddies from a 24 years dataset of sea surface velocity field derived from satellite surface altimetry. I investigate their lifespan, create a sequence of consistent fluid transport, and assess the significance of the achieved transport estimations. I use these mesoscale eddies to compute coherent fluid transport off Canary Islands, which I prove to be lower (by about one order of magnitude) than previous transport estimates.

Chapter 2

Upwelling segmentation from biological and physical satellite images

Abstract

In this chapter I am interested in classical methods commonly used in image processing to segment upwelling regions from SST images and CHL_a concentration. The objective of this chapter is to review previous methods proposed for the problem of upwelling detection in the studied area, highlight their advantages and limitations, then improve some of them to efficiently identify and extract the north-west African upwelling from biological physical satellite observations.

2.1 Segmentation methods

2.1.1 Segmentation methods

Segmentation is a widely studied topic in computer vision. Image segmentation is the process of partitioning a digital image into multiple sets of pixels (segments). The goal of this process is to change the presentation of a given image into a more meaningful image which it easier to analyze [Shapiro and Stockman, 2001, Barghout and Lee, 2004]. Thus, a good segmentation method must be one that leads to a good

interpretation without reducing too much the content. Image segmentation is the process of labeling every pixel in an image such that pixels with the same label share certain characteristics computed properties, such as color, intensity, or texture. It is usually used to identify objects and boundaries in images.

There are three general approaches to segmentation, region-based methods, edge-based methods and thresholding

- **Region-based** segmentation methods operate directly on the regions by looking for areas R_i in the image that have pixels with common properties.
- **Edge-based** segmentation methods transform original images into edge images based on the localization of important variations of a gray level image and the detection of the physical and geometrical properties of objects of the scene
- **Thresholding** is the simplest method of image segmentation. It is yet an effective way of partitioning an image into a foreground and background. Thresholding technique is a type of image segmentation that isolates objects by creating binary images.

2.1.2 Edge-based segmentation

Contour detection segmentation is a fundamental step in image processing field [Chan and Vese, 2001]. It includes a variety of mathematical methods that aim at identifying points in a digital image at which the image intensity changes sharply. The purpose of edge segmentation is to capture events and changes in properties of the images, these properties changes are most likely to correspond to [Barrow and Tenenbaum, 1981, Lindeberg, 2001]:

- discontinuities in depth,
- discontinuities in surface orientation,
- changes in material properties and,
- variations in scene illumination.

The result of edge-based segmentation may lead to a set of connected curves that indicate the boundaries of objects as well as curves that correspond to discontinuities in surface orientation. Thus, edge-based segmentation might significantly reduce the amount of data to be processed and may therefore filter out information that may be regarded as less relevant, while preserving the important structural properties of an image.

There are many methods for edge detection, but most of them can be grouped into two categories:

- Differential approaches.
- Optimal edge detector.

Gradient edge detection

The most common type of edge detection process uses a gradient operator, of which there have been several variations [Maini and Aggarwal, 2009, Gonzalez et al., 2004]. Mathematically, for an image function, $f(x, y)$, the gradient $G(f(x, y))$ and the gradient direction, $\theta(x, y)$ are computed as:

$$\nabla f = G[f(x, y)] = \begin{bmatrix} G_x \\ G_y \end{bmatrix} = \begin{pmatrix} \frac{\partial f}{\partial x} \\ \frac{\partial f}{\partial y} \end{pmatrix} \tag{2.1}$$

$$\theta = tan^{-1} \left(\frac{G_y}{G_x} \right) \tag{2.2}$$

where,

$$G_x = f(x + 1, y) - f(x - 1, y) \tag{2.3}$$

$$G_y = f(x, y + 1) - f(x, y - 1) \tag{2.4}$$

The gradient edge detection properties are:

- The magnitude of gradient $M(x, y) = \sqrt{G_x^2 + G_y^2}$ provides information about the strength of the edge.
- The direction of gradient is always perpendicular to the direction of the edge.

In general, these derivatives are computed by convolution of the image with a mask of differences [Acharya and Ray, 2005]. In this subject, several convolution masks have been proposed in the literature to estimate the modulus of the gradient: Roberts, Prewitt, Sobel and Kirsch. The main disadvantage of these operators is their high sensitivity to noise (clouds) due to the implementation of the derivation which results in a high-pass filtering. Also, the quality of the segmentation strongly depends on the size of the masks; to enlarge it means to increase the quality of the results obtained and consequently to increase the calculation time.

The zero-crossing based methods search for zero crossings in a second-order derivative expression computed from the image in order to find edges. Such methods are very useful because the 2nd derivative is very sentient of noise and this is helpful in the filtering of noise from the image. In this subject we can cite the Laplacian of Gaussian also referred as LoG [Al-Amri et al., 2010]. In this approach the image is convolved with Gaussian filter to reduce the noise. Pixels that have locally maximum gradient, are examined as edges in which the zero crossing is found [Hueckel, 1973, Torre and Poggio, 1986].

Optimal edge detector

It is based on the definition of an optimality criteria for localization and detection; these criteria are based on optimal smoothing filters. In this category, Canny's filter (Canny, 1986) is made by convoluting the signal by a finite impulse response filter; it proposes an approximation by the 1st derivative of Gaussian. For this, it mathematically defines three optimality criteria:

- Detection: the contour must be well detected by minimizing false responses.
- Location: the contour must be located with certainty by optimizing the precision with which the contour is detected.

- Single response: the contour must cause a single response for a single contour avoiding edge effects.

2.1.3 Region-based segmentation

Methods belonging to the region-based segmentation operate directly on the regions by looking for areas R_i in the image that have pixels with common properties. There are mainly two types of segmentation methods that adopt this approach: splitting/merging methods and clustering methods.

Splitting/merging methods

Split/merge algorithms seek to merge regions (or pixels) with similar characteristics. Indeed, the Region Growing method is a common technique in this category [Chang and Li, 1994] whose principle is to examine neighboring pixels of initial seed points and determines whether the pixel neighbors should be added to the region. The use of this type of method on SST images makes it possible to roughly detect upwelling zones [Tamim et al., 2014b]. However, the prior knowledge of criteria that vary greatly from one image to another is a very strong constraint. Indeed, the segmentation is made very difficult by the influence of the initial position of the seed points, the choice of the stopping conditions, the important calculation time, and the sensitivity related to the noise.

Clustering methods

Clustering methods consist of dividing a set of pixels of an image I into a number C clusters (i.e class). A class represents a family of pixels with common properties and thus identifies one or more regions with physical characteristics (e.i, upwelling regions, non-upwelling, earth, clouds in SST images). The quality of the results obtained depends largely on the robustness of the classes.

Clustering algorithms have experienced a very significant interest, especially in the context of the automatic segmentation of SST images. In this category several

methods have been developed, the most popular being k-means, it owes its popularity to its simplicity and its ability to handle large sets of data.

The difficulty of clustering algorithms lies in the priority knowledge of the number of classes present in the image as well as the gray levels delimiting each class [Tamim et al., 2013]. In particular, SST images present upwelling regions with a very weak dynamic: the maximum temperature difference between the upwelling regions is of the order of $2°C$. We will return with more detail in the second part of this chapter on the automatic classification methods of SST images.

Mathematical morphology

Mathematical morphology [Matheron, 1975, Serra, 1983] finds an immense field of application, particularly in the detection of thermal structures in SST images [Holyer and Peckinpaugh, 1989, Marcello et al., 2005]. Mathematical morphology is a collection of operators based on set theory and defined on an abstract structure known as an infinite lattice. It is intended to analyze and recognize the geometrical properties and structure of the objects. It includes techniques such as erosion, dilation, opening, closing.

Dilation Dilation generally increases the sizes of objects. It is a process that translates the origin of the structuring element B throughout the domain of the image I and checks to see whether it overlaps with one valued pixels. Dilation of I by structuring element B is denoted by $I \oplus B$.

Erosion Erosion generally decreases the sizes of objects and removes small anomalies. As in dilation, the manner and extent of shrinking is controlled by the structuring element. Erosion of I by structuring element B is denoted by $I \ominus B$

Opening The opening operator is the composition of a morphological dilation with erosion using the same structuring element B. This operator makes it possible to

isolate surfaces present in the image I and to smooth out the contours.

$$(I \ominus B) \oplus \bar{B} \tag{2.5}$$

With $\bar{B}$ denoting the transpose of B.

Closing The closing operator is realized by using a dilation by B then an erosion by $\bar{B}$. It helps to remove small objects, while closing removes small holes.

$$(I \oplus B) \ominus \bar{B} \tag{2.6}$$

Gradient morphology The morphological gradient is defined as the difference between the dilated I by the structuring element B and the eroded I by B:

$$\nabla I = \frac{1}{2}(I \oplus B) - (I \ominus B) \tag{2.7}$$

It measures in each point of the image the difference between the maximum and the minimum of the gray levels on the neighborhood defined by the structuring element B.

All these morphological operators have comparable or even superior performances to those based on the combination of filters and linear gradients [Van Vliet et al., 1989] and require fewer operations. However, these operators are made more robust if a usual filtering precedes their use. In the case of SST images, it is widely recognized that the results obtained are very insignificant [Cayula et al., 1991].

2.1.4 Discussion

In this first part, we present results obtained with different segmentation methods. The results evoked suggest the limitations of conventional segmentation techniques for the detection of structures of interest in SST images. These limitations are mainly related to the nature of the images to be processed. Indeed, SST images present irregular contours with a very weak dynamics on the zones of upwelling. However,

region-based segmentation methods: the k-means method, generally provide interesting results and have been very successful in oceanographic image analysis. It therefore seems useful to propose a method that takes into account the region-based information in the analysis of SST images. In the continuation of this chapter, we will focus on region-based segmentation approaches, more specifically, we will analyze the methods of automatic classification of satellite images.

2.2 Automatic extraction upwelling regions from SST images

As we pointed-out earlier (first part of this chapter), the clustering-based segmentation of SST images for the purpose of identifying upwelling regions is very important task in oceanography. It has contributed in many studies on the analysis of thermal structures [Nieto et al., 2012, Tamim et al., 2015, Tamim et al., 2013, Sousa et al., 2008, El Aouni et al., 2015, El Aouni et al., 2018f]. Clustering algorithm seeks to identify groups with similar pixels in order to better discover the distribution and the correlation between the objects of the image. It consists in defining descriptive attributes of the image and then using a classification technique from these attributes to extract distinct and homogeneous regions [Jain and Dubes, 1978]. The use of this approach in the detection of upwelling zones is very promising in the case where it is considered that coastal upwelling is characterized by a cold and homogeneous zone compared to warm and heterogeneous offshore waters.

2.2.1 Clustering Methods

In clustering [Richards, 2013] one tries to identify groups of pixels based on a similarity criterion, when the only data available are unlabeled, and no structural information about it is available. Depending on the nature of the data and the purpose for which clustering is being used, different measures of similarity may be used to place items into classes. The existing clustering methods can be grouped into two categories,

fuzzy [Looney, 1999] and hard [Jain and Dubes, 1988]. In hard clustering, data is divided into distinct clusters, where each data element belongs to exactly one cluster. In fuzzy clustering, data elements can belong to more than one cluster simultaneously, with different degrees of membership.

In the context of upwelling segmentation several techniques and algorithms have addressed the problem of automated identification of upwelling regions in SST images. For instance, [Cayula and Cornillon, 1992] proposed an unsupervised classification method in which neural network is trained based on the k-means clustering. In [Nieto et al., 2012], authors proposed a histogram-based separation method, where the bi-modality of SST histogram is interpreted to represent two types of water. In [Sousa et al., 2008], authors propose an algorithm to extract upwelling regions in the coastal ocean of Portugal. Their algorithm is based on fuzzy c-means (FCM) and yields good segmentation accuracy in that particular area. Other upwelling detection technique based on FCM were proposed for that particular areas we cite [Nascimento and Franco, 2009b, Nascimento and Franco, 2009a].

For the north-west african upwelling, several upwelling segmentation were proposed. Ostu's algorithm is applied on SST images in the southern part of Morocco to separate cold upwelling from the warmer water in the offshore [Tamim et al., 2013]. Another approach based on the use of the FCM algorithm with an adaptive cluster merging was proposed for the same area [Tamim et al., 2014b]. Another fuzzy approach was applied on that area, which was based on the use of Gustafson-Kessel clustering algorithm [Tamim et al., 2014a]. On the same area, another combination of Otsu's and region growing algorithms were proposed to extract upwelling regions from SST images [Tamim et al., 2015]. In a comparison between the application of these methods over that area, the FCM algorithm seems to be the one which gives satisfying results in term of upwelling identification [Tamim, 2015]. FCM algorithm attempts to partition a finite collection of n pixels $X = \{x_1, ..., x_n\}$ into a collection of c fuzzy clusters with respect to some given criterion. Given a finite set of pixels, the algorithm returns a list of c cluster centers $C = \{c_1, ..., c_c\}$ and a fuzzy partition matrix, which presents the degree of belonging for each pixel x_k to a given cluster

c_i. The FCM algorithm is applied to minimize an objective function called c-means functional:

$$J_m(X;U,V) = \sum_{k=1}^{n}\sum_{i=1}^{c}(\mu_{ik})^m \left\|x_k - v_i\right\|^2 \tag{2.8}$$

where n is the length of the vector X presenting pixels of a given SST image. $V = \{v_1, v_2, ..., v_n\}$ is the vector of cluster prototypes and $U = [\mu_{ik}]$ is the fuzzy partition matrix which presents the degree of belonging for each pixel x_k to a given cluster c_i. The weighting exponent m controls the fuzziness of membership values, which vary in the interval $[1, \infty[$. An increase of m lead to an increase of fuzziness partitions. In our work, $m = 2$.

The objective function (Eq.A.7) can be seen as a measure of the total variance of x_k from v_i. The minimization of the objective function (Eq.A.7) represents a nonlinear optimization problem that can be solved by using respectively the following cluster centroids and membership functions:

$$v_i = \frac{\sum_{k=1}^{n}(\mu_{ik}^m)x_k}{\sum_{k=1}^{n}(\mu_{ik}^m)}, 1 \leq i \leq c \tag{2.9}$$

$$\mu_{ik} = \frac{1}{\sum_{j=1}^{c}(\frac{\left\|x_k - v_i\right\|}{\left\|x_k - v_j\right\|})^{\frac{2}{(m-1)}}}, 1 \leq i \leq c, 1 \leq k \leq n \tag{2.10}$$

The goal here is to iteratively improve a sequence of sets of fuzzy clusters through those equations until no further improvement is possible for the objective function.

Optimal number of clusters In unsupervised classification, the number of clusters is rarely known a priori, and in order to have the optimal number of classes it must be chosen with great care. Several methods have been proposed to automatically determine the number of clusters which better fit the data [Griffa et al., 2007]. In [Tamim et al., 2014a], authors used validity indices for several values of c and then

evaluates the goodness of the obtained c-partition. Results show that $c = 2$ is better fit for their studied area. Due to the nature of the studied area which is characterized by a strong and variable upwelling throughout the year, and based on its scientific and technical knowledge, [Tamim et al., 2015, Tamim et al., 2013] set $c = 2$ in order to separate the cold water near the coast from the warmer in the offshore direction.

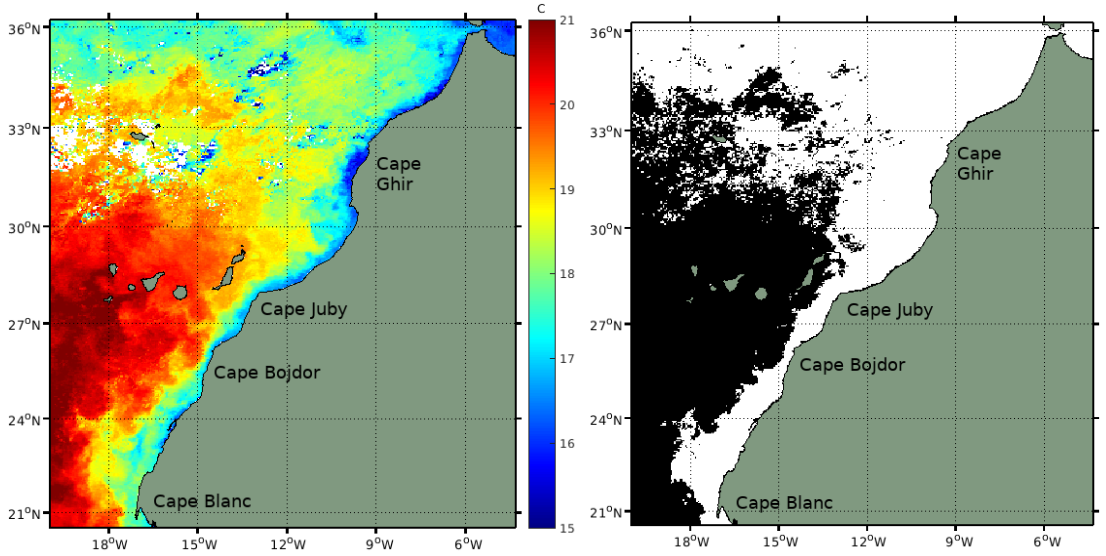

(a) (b)

Figure 2-1: a) 8-day SST images obtained on the first week of January 2007, b) the result of the method developed in [Tamim et al., 2015] applied on the SST image from Fig.2-2(a). White color refers to upwelling water while black color refers to offshore water.

Fig.2-1(b) shows results of the method developed in [Tamim et al., 2014a] applied on the SST images in Fig.2-1(a). However, while it yields accurate segmentation in the southern part of the Moroccan Atlantic coast, it fails however to provide good segmentation on the whole Moroccan upwelling system (including center and north). The white color refers to the upwelling region, one can clearly see that the method completely overestimates the contouring of the upwelling regions in the northern part. The main reason behind this failure is the high variability of the latitudinal distribution of temperatures. Hence, for example, offshore temperatures in north (while they are higher than coastal north temperatures) can be close to upwelling temperatures in south. An example of such phenomena is shown in Fig.2-2. To bypass

this problem, we propose a latitudinal normalization by offshore temperatures, thus is, we consider "region-dependent" difference of temperatures rather the temperatures themselves. The procedure is described in the following.

2.3 Upwelling extraction based on nonlinear transformation of SST images.

2.3.1 Latitudinal normalization of SST images

As described in [Ekman, 1905], if the wind blows parallel to the coast in the Northern hemisphere (such as along the coast of Morocco, where the wind blows South), Ekman transport can produce a net movement of surface water 90° to the left of the winds which might result in coastal upwelling. Thus, in order to identify the upwelling, it is natural to compare the temperature of the inshore water with offshore water within a perpendicular direction to the coast. The idea here is very similar to the coastal upwelling index, which is widely used to characterize the upwelling spatio-temporal dynamics from SST [Van Camp et al., 1991, Nykjær and Van Camp, 1994, Demarcq and FAURE, 2000, Santos et al., 2005, Marcello et al., 2011]. However, the coastal upwelling index is usually calculated as a difference between the minimal temperature recorded in the upwelling region and its reference in the offshore water. Here, we consider normalizing each SST image based on this principal; instead of calculating the index over the minimal temperature, we compute it over the whole pixels belonging to the same radial. In this work [El Aouni et al., 2018e, El Aouni et al., 2018a], we thus partition each image into R radials which are perpendicular to the coast, as shown in Fig.2-3, where R are pixel of width and 3000 km of length starting from the coast line.

All the radials present the same angle to the coast line in order to cover all the pixel of the image as follows:

We first define the general orientation of the Moroccan coast as a virtual line (see

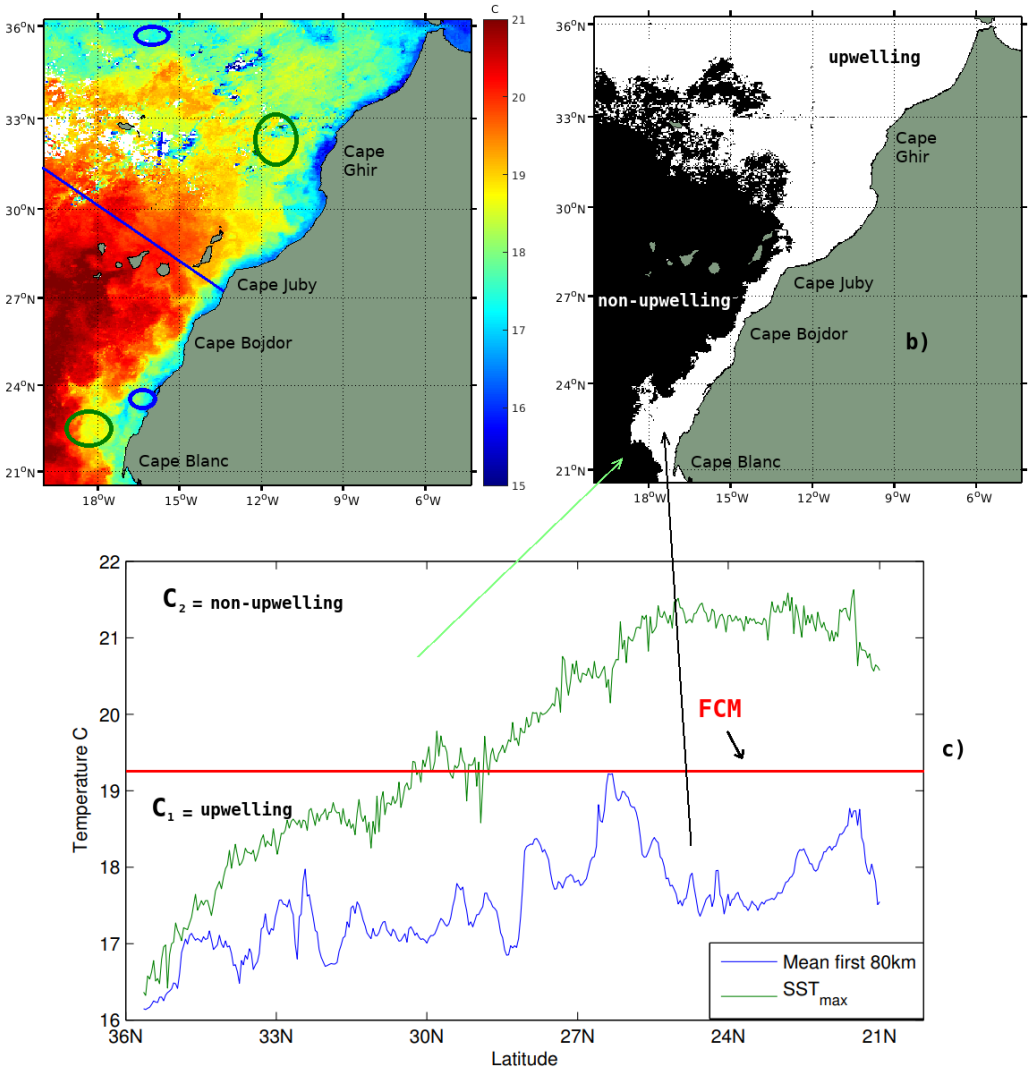

Figure 2-2: a) 8-day SST images obtained on the first week of January 2007, with thermal comparison between the inshore and offshore waters (circles with same the color highlight similar temperature caught in the offshore and the upwelling waters), b) the result of the method developed in [Tamim et al., 2015] applied on the SST image from Fig.2-2(a). White color refers to upwelling water while black color refers to offshore water. c) latitudinal comparison between the upwelling and the offshore temperature; green curve represents the maximal temperature on each latitudinal step of the SST image in Fig.2-2(a), blue curve represents the mean temperature over the first 80km of each latitudinal step.

black line in Fig.2-3)

$$L_{lat,lon} = (P_{n,n}, ..P_{s,s}) \tag{2.11}$$

where starting from the northern $(P_{n,n})$ till the southern point $(P_{n,n})$ of Morocco.

This line will serve to define the perpendicular radials as:

$$\begin{aligned} \langle R^1_{northernLat,northernLon}, L\rangle &= 0 \\ &\vdots \\ \langle R^r_{southernLat,southernLon}, L\rangle &= 0 \end{aligned} \tag{2.12}$$

On each radial we first define the maximal offshore temperature. To do so, we need to consider offshore waters where the influence of the upwelling is expected to be insignificant. To do so, we use bathymetry data and define offshore waters as the ones which have a balthymetry less than $-500m$. Fig 2-3 shows an example of a radial in which the maximal offshore temperature is sought.

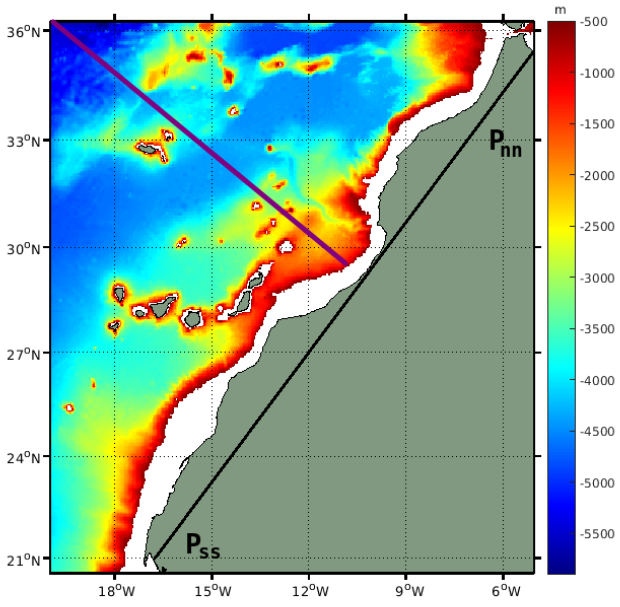

Figure 2-3: GEBCO bathymetry over the studied areas. The purple line shows an example of radial in which SST_{max} is sought. The black line presents the orientation of the coastline.

Fig 2-2 illustrates the phenomenon of latitudinal high variability of temperature. The green curve represents the maximal temperature on each radial of the SST image in Fig.2-2(a). The blue curve represents the mean temperature over the first 80

km of each radial. As stated above, north and central maximal temperatures can be much lower than minimal temperatures in the south. This is the main reason behind the failure of segmentation methods proposed in [Tamim, 2015, Tamim et al., 2015, Tamim et al., 2014a, Tamim et al., 2014b, Tamim et al., 2013]. As they are all considered as linear methods, and they do not take into account the spatial information of the upwelling phenomenon. Let's take for example the FCM algorithm which showed to be the best segmentation method all over the ones presented for that area [Tamim, 2015]. Fig.2-2(a) shows the synthetic presentation of the FCM algorithm applied on the SST images. The red line present the FCM algorithm, while the green and blue present temperature of upwelling and offshore waters. This Figure makes it very clear why the FCM fails to separate these two classes, both green and blue curves are spatially distributed in nonlinear way, which makes it impossible for the FCM to properly separate them.

Consider now a radial $r \in \{1, ..., R\}$ composed of temperature pixels $r = \{T_i^r; i = 1, ..., R\}$. Let T^r be the maximal temperature on radial r:

$$T^r = \max_i T_i^r \tag{2.13}$$

We now define the offshore gradient of temperature as:

$$\delta T_i^r = T^r - T_i^r \tag{2.14}$$

Fig.2-4(a) displays the image of Fig.2-1(a) after this normalization. As we can see this image keeps the same thermal structures in the SST image. Moreover, the upwelling area, which corresponds now to high gradient intensities, is visually more clear than in the original SST image. However, there exists some unnatural lines due to some maximal temperatures which are not presenting the right thermal references. Fig.2-4(c) shows T^r vector (red line) used to generate Fig.2-4(a). This vector contains many fluctuations which causes the unnatural lines. To overcome this problem a moving average algorithm with a window size of 5 is used to smooth out the vector of the thermal references (Fig.2-4(c) blue line). Fig.2-4(b) shows the final normalized

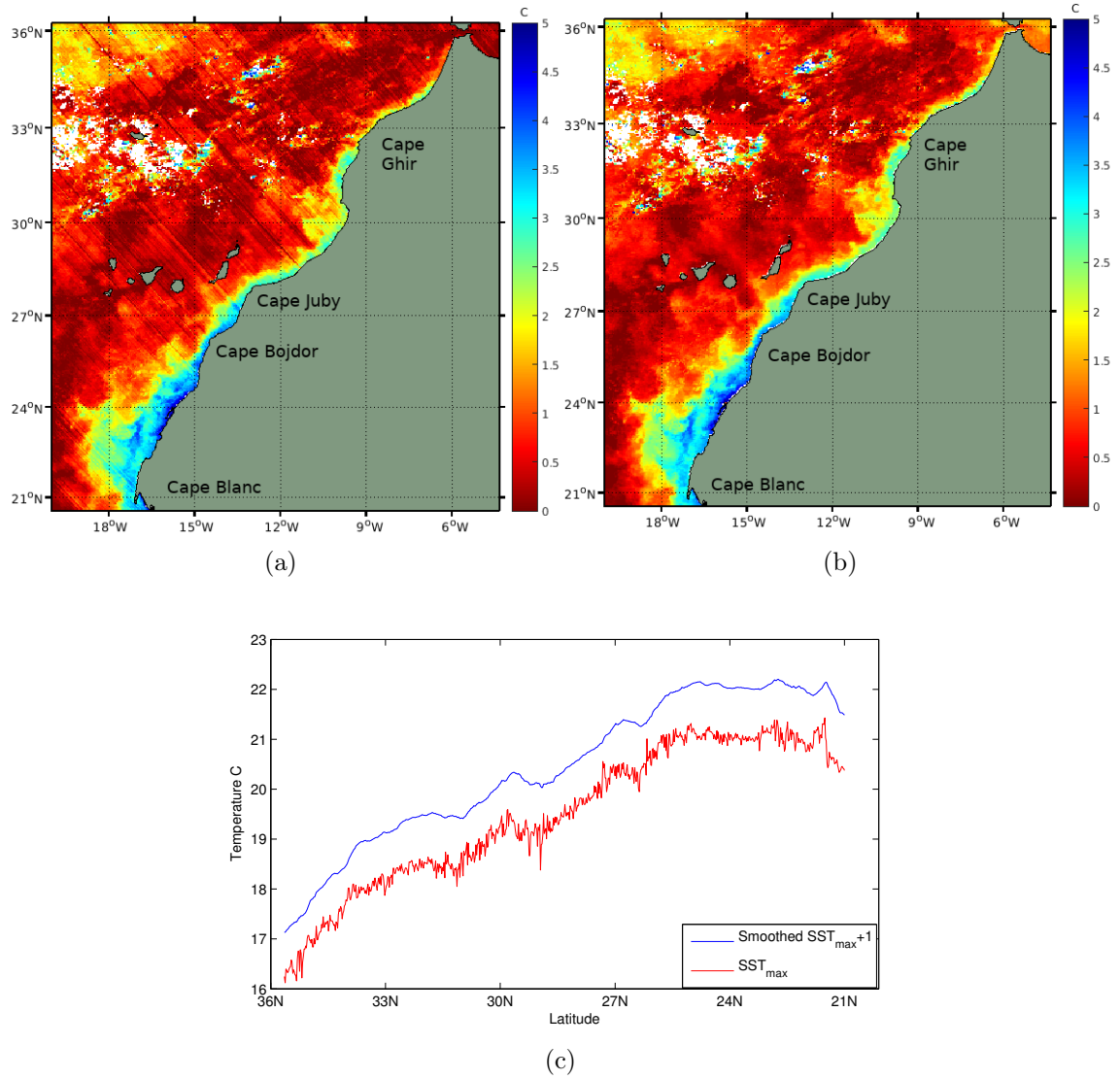

Figure 2-4: a) Normalization of the SST image in Fig.2-2(a). b) Smoothed normalized SST image, c) SST_{max} vector before (red) and after (blue) being smoothed.

image computed using the smoothed T^r vector.

Fig 2-5 displays the "dual" information of Fig.2-2 where the green curve represents now the minimal gradient in each radial and the purple cure represents the mean gradient over the first 80 km of each radial. One can see that offshore information (green curve) is now normalized over the whole coast and is clearly discriminated from the inshore information (purple curve). Bringing back the synthetic presentation of the FCM algorithm applied on this image. Again red line presents the FCM algorithm while both green and blue curves present the temperature gradient in the upwelling

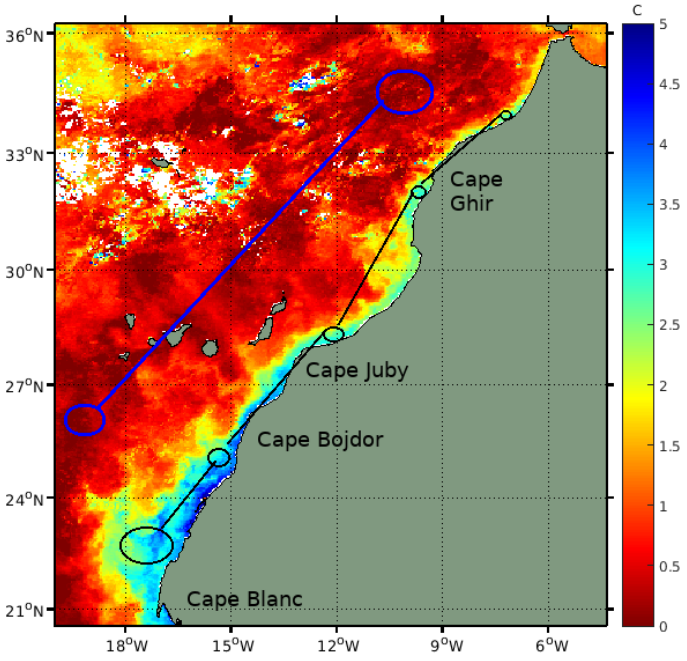

(a)

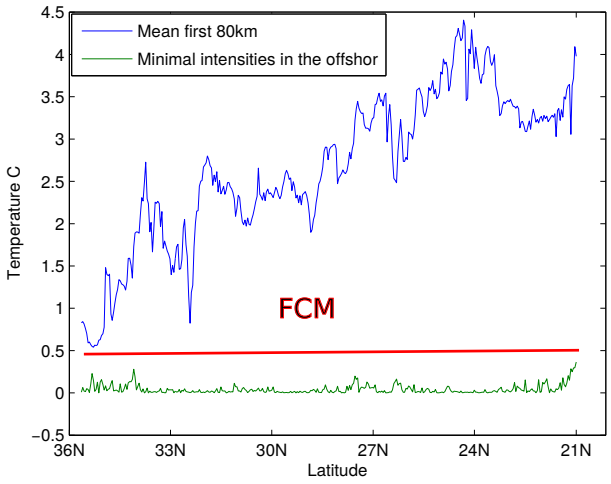

(b)

Figure 2-5: a) Normalization of the SST image in Fig.2-2(a), with thermal comparison between the inshore and offshore water, b) latitudinal comparison between the upwelling and the offshore pixel values.

and the offshore water. Now there is no doubt that both classes are linearly separable.

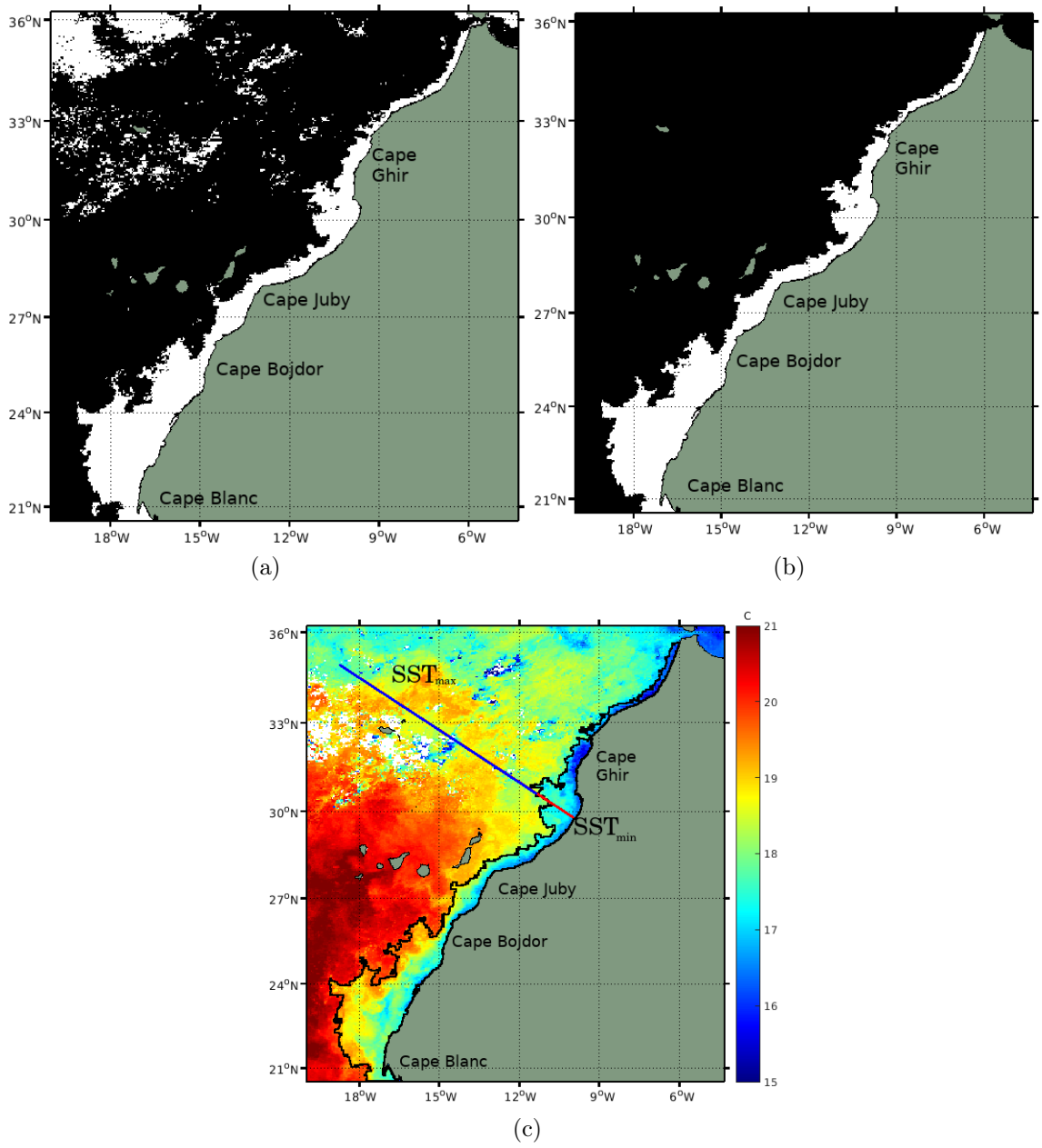

Figure 2-6: a) binary result of FCM applied on the normalized SST image, b) binary result after the application of the region-groing algorithm on the image (b). c) Final segmentation achieved by the proposed method.

Upwelling segmentation

Once the normalization is applied on an SST image, an image with gradient temperature intensities is obtained. The upwelling area corresponds to the region(s) with the lowest intensities. Segmentation of this area goes back to separate the latter from

pixels with the highest intensities. To do so, we apply the FCM on each normalized images to provide labeled clusters sharing the similar statistical properties 2-6a).

In addition to the upwelling area, the FCM's output include some additional noise structures far away from the coast, not belonging to the upwelling region. For that reason and based on the fact that all pixels pertaining to the upwelling must have connectivity with the coastline, a segmentation procedure is required consisting on the application of the Region-growing algorithm to remove those isolated pixels in the offshore direction.

Fig.2-1 displays the segmentation obtained with the method we developed in [Tamim et al., 2015]. As stated above, this method fails to provide a good segmentation along the whole coast. Fig.2-6(b) shows the segmentation obtained after the normalization we developed here. Our new method yields a very accurate segmentation on the whole coast and is even able to track the filaments.

Oceanographer evaluation

We evaluate the accuracy of our upwelling segmentation method by testing it over a subset of 131 SST images covering the Moroccan Atlantic coast during the years 2007, 2008 and 2009. As commonly done, validation is carried out independently by a professional oceanographer. Throughout this evaluation, we used 4 grades: Bad, Poor, Good and Excellent. The grade Bad is attributed when the upwelling region is not well delineated by the proposed algorithm. Excellent is assigned when the area is correctly identified in each SST image.

The results of the oceanographer's evaluation are presented in Fig.2-7. This figure shows that 53% and 44% of the dataset are "Good" and "Excellent", respectively. The grade "Poor" is attributed to only 3% of the data while the grade "Bad" is not attributed at all. Overall the 131 SST images used in this study, the segmentation of 97% of the images is considered as Good or Excellent, showing the high accuracy of our approach.

In this part, we proposed a novel method for segmentation of upwelling areas along the Moroccan coast which is based on a thermal nonlinear normalization of

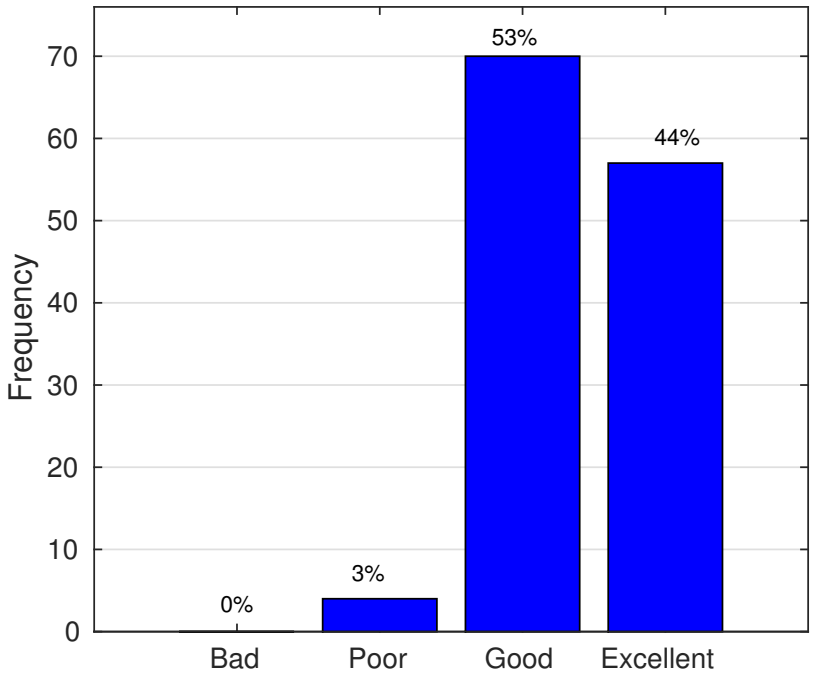

Figure 2-7: Qualitative evaluation made by the oceanographer of segmentation results produced by the proposed method.

SST images. This method showed to be very accurate and more robust than a recent sate of the art method. The segmentation method we developed here will serve as a framework to define a novel upwelling index which will be used in the next chapter to characterize the spatio-temporal dynamics of the north-west African upwelling. However, the upwelling phenomenon has both physical and biological characteristics associated with it. And for a better understanding, we need to characterize the upwelling dynamics from both physical and biological observations. Thus, the next part of this chapter will be dedicated to the development of a segmentation method for the detection and extraction of the upwelling areas from both SST and CHL_a images along the central part of the Canary upwelling Ecosystems.

2.4 Upwelling extraction simultaneously from SST and CHL_a images

In this part [El Aouni et al., 2019b], we present a novel simple and intuitive method to identify and segment upwelling areas of the North-west African upwelling. This method is capable of extracting upwelling areas from both SST and CHL_a images. As shown in the previous part of this chapter, offshore temperatures in north can be close to upwelling temperatures in south parts. Thus, a possible way to identify upwelling regions over this area is to consider a sub-regions approach, where one has to meridionally divide the whole system to sub-regions with homogeneous latitudinal variation of SST. Based upon this suggestion, and to better understand spatial distribution of temperatures over upwelling regions of North-West Africa, we carry out a statistical analysis study of the spatial distribution of upwelling, its latitudinal and longitudinal temperature variation.

2.5 Data and area of interest

This study focuses on the northern part of the North-West African part of the Canary upwelling Ecosystem, between $20°N$ to $36°N$ and $4°W$ to $19°W$. This zone is depicted in Figure 2-8 which shows two acquisitions (one SST and one CHL_a) of the same area. MODIS-T SST and CHL_a datasets are processed to provide images at spatial resolution of 4×4 km, leading to images of size 378×378 pixels. SST and CHL_a data are obtained from NASA's oceancolor website `http://oceancolor.gsfc.nasa.gov/`. We use datasets consisting of 644 8-day SST and 644 8-day CHL_a images, covering the period between 2003 and 2016. The images display typical upwelling conditions with a well-defined upwelling main front in term of sharpness all over the studied area visible on the CHL_a image. The SST image presents a well defined upwelling main front only south of $28°N$, the thermal front being not clearly identified north of $28°N$. Moreover, the temperature distribution varies both meridionally and zonally, whereas the CHL_a distribution shows only clear longitudinal variation. Both images are acquired at the

same date (first week of January 2007). The CHL_a image shows more cloudiness than what is present in the thermal observation. This is due to different wavelengths and algorithms used to provide such data. We consider 8-day SST and CHL_a images because they constitute a good compromise between the variability of the pixel values and the necessity to provide a continuous spatio-temporal coverage. SST and CHL_a images are included in the database if they have at least 25% of valid information in the area between the coast and 200 km offshore. We also consider monthly SST and CHL_a images to describe the interannual variability of the upwelling dynamics. We also use the daily global 1/4° resolution product GEKCO (Geostrophic and Ekman Current Observatory) of surface currents developed by [Sudre et al., 2013] to compute the eddy kinetic energy and the cross-shore Ekman Transport index. The surface currents are calculated from a combination of wind-driven Ekman currents, at 15 m depth, derived from Quickscat and ASCAT wind estimates, and geostrophic currents computed from Sea Surface Heights.

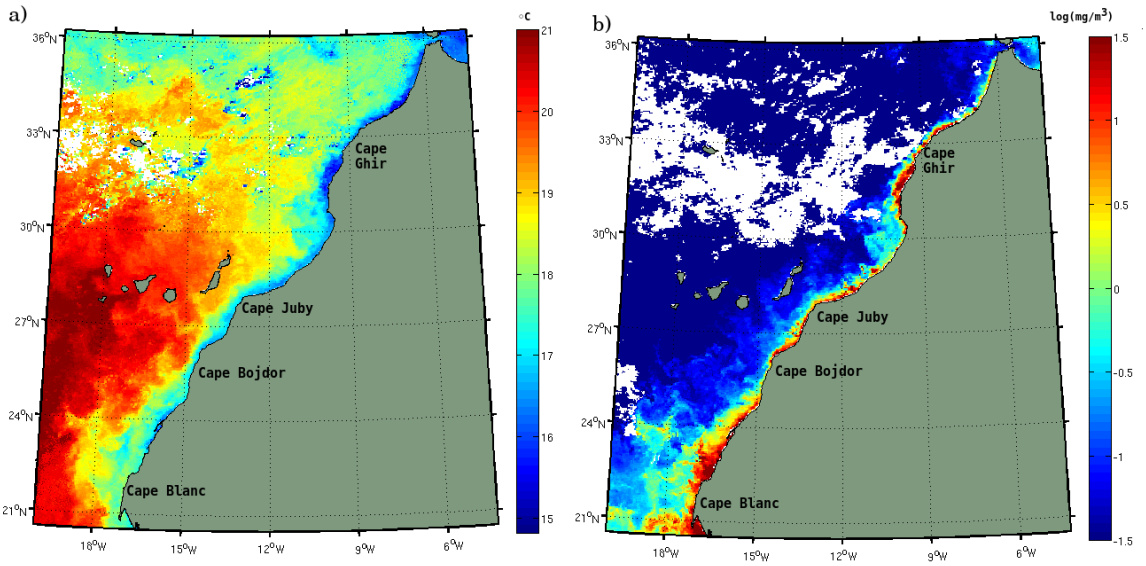

Figure 2-8: (a) 8-day SST image ($°C$), (b) CHL_a concentration ($log(mg/m^3)$) image obtained on the first week of January 2007, showing typical upwelling scenario from physical and biological observations; similar oceanic structures appear in both images.

2.6 Upwelling identification and segmentation

Our goal is to develop an upwelling segmentation method which allows the identification of the upwelling areas from SST and CHL_a images. We first seek to overcome the problems encountered when applying the method developed in [Tamim et al., 2015] over SST images, and to provide an upwelling segmentation from biological observations.

As stated in the previous part, north and central maximal temperatures can be much lower than minimal temperatures in the south. Thus, a possible way to identify upwelling regions over this upwelling system is to consider a sub-region approach, where one has to divide "zonally" the whole system into sub-regions and apply the method developed here [Tamim et al., 2015] over each sub-region, then merge all the regions later on. An example is given in Fig 2-9(d), where the green curve represents the maximal temperature on each latitudinal step of the SST image in Fig 2-9(a). In order to fully separate the green curve from the blue one, we divided our system into 4 sub-regions. We clearly see that the sub-regions have different sizes. The problem is how to define these sub-regions, knowing that the upwelling itself varies seasonally. For each SST image we will have a different number of sub-regions. The solution to this is to:

- Zonally divide the system into sub-regions characterized by low latitudinal variation of temperature.
- Over each one of the sub-regions, we would apply the technique developed in [Tamim et al., 2015].
- Later on, merge the results of each sub-region to have a final delineation of the upwelling limit.

However, this could result in a discontinuity of the main upwelling contour (knowing that upwelling waters in each sub-region will have its own centroid). To overcome this:

- First apply clustering algorithm with maximal number of clusters over the whole system.
- Zonally divide the system into sub-regions.
- In each sub-region identify upwelling water.
- Later on merge upwelling region from the sub-region to reproduce the main upwelling contour.

2.6.1 Extraction of the upwelling areas

In the unsupervised clustering, the number of clusters is rarely known a priori and it must be chosen with great care. In fact, if the cardinality (number of pixels belonging to a given cluster) of a cluster is larger, one or more good compact clusters should be broken due to the variations in the similarity, or if it is smaller, one separate cluster may be merged [Kaymak and Setnes, 2002, Frigui and Krishnapuram, 1996, Backer and Jain, 1981]. In the literature two main approaches for determining the good number of clusters in data can be distinguished:

- Use the clusters validity functions to extract the good number of clusters which best describe the data.
- Start with large number of clusters, and successively reduce this number by merging clusters that are similar, according to some predefined criteria.

In this work we use the second approach, but instead of using the similarity-based cluster merging approach, we developed an upwelling special algorithm that merges parts of clusters which best reproduce the shape of upwelling. Our method is based on a rigorous analysis of the spatial distribution of the upwelling; we applied particle swarm optimization clustering algorithm (PSO) [Kennedy, 2011, Kennedy et al., 2001] with a maximal number of clusters $C_{max} = 6$ over one year of SST images. Then, we analyzed the meridional and zonal distribution of the clusters. Results show that:

- The cardinality of the clusters gets smaller in the south direction, which results in upwelling with more clusters in the southern part as compared to the northern one.

- The same cluster presents the upwelling water in the southern region and offshore water in the northern region.

- The same cluster shows smaller cardinality in the upwelling water, and larger one in offshore water.

- Starting from the coastline, the cardinality of the clusters gets larger in the offshore direction (the upwelling waters present a small portion compared to the waters in the open ocean).

Based on this analysis we developed an algorithm that iteratively breaks and merges parts of clusters to create the upwelling pattern of the studied area. The algorithm initializes the PSO clustering algorithm with a number of clusters $C_{max} = 6$. (Fig 2-10(a) (upper panel) shows results from the PSO clustering algorithm applied on the SST image from Fig.2-8). Then the algorithm starts by zonally dividing the whole system into equally small sub-regions of $90km$: for each sub-region from North to South, it starts from the coastline, and calculates the cardinality of the first cluster and labels it as upwelling if it presents less than 15% of cardinality of the sub-region, then goes to the next one, and includes it only if the cardinality of the current cluster is less or equal to the sum of the previous ones as described by the Algorithm 2 (Appendix). Each sub-region is characterized by the number of clusters it includes. Fig.2-10(b) shows the result of Algorithm 2. Lines with the gray color mean that only one cluster is considered, for the brown lines two clusters are considered, 3 for the green and 4 for the white.

The second part of the algorithm consists of merging connected sub-regions of similar number of clusters in order to create the different upwelling regions with different number of clusters (isolated sub-regions add or remove one cluster depending on their surrounding). We finally defined 4 regions (Fig.2-10(c)), the first one contains

only one cluster, the second contains 2, 3 for the third and 4 for the last one. Fig.2-10(d) illustrates the final segmentation obtained for the upwelling regions. Finally, these regions are merged to create the upwelling area as shown in Fig.2-10(e). One can see that our new method yields a very accurate segmentation on the whole coast.

2.7 Conclusion

The present chapter was dedicated to reviewing existing method for the purpose of the automatic segmentation of upwelling regions. We showed how region-based segmentation methods are more adapted to the upwelling identification problem. The reviewed methods give very satisfying results on their corresponding studied regions. Then, the reviewed methods were tested over our studied area, which is an extension of the latter's methods' region, which includes the central and northern part of the Moroccan upwelling. However, results show that these methods fail to properly extract the upwelling over the whole Moroccan coast. By analyzing the meridional distribution of the upwelling temperature, the physical process that creates the upwelling, the results of the previous methods and the way their algorithms function; we first managed to bypass all the problem faced by these methods. This has been done by considering a latitudinal normalization by offshore temperatures, which could be interpreted in other term as considering a "region-dependent" difference of temperatures rather the temperatures themselves. Latter in this chapter, we explained that the upwelling phenomenon involves cooler and usually nutrient-rich water, and that is important to consider both physical and biological observation in order to better characterize its spatio-temporal dynamics. That it is needed to develop a segmentation method that works simultaneously on both SST and CHL_a images. Thus, in last part of this chapter, we developed a method that does so. The method does not consider the pixels values but rather their spatial distribution. The methods developed here are going to be used in the next chapter to quantify the spatio-temporal dynamics of the north-west African upwelling.

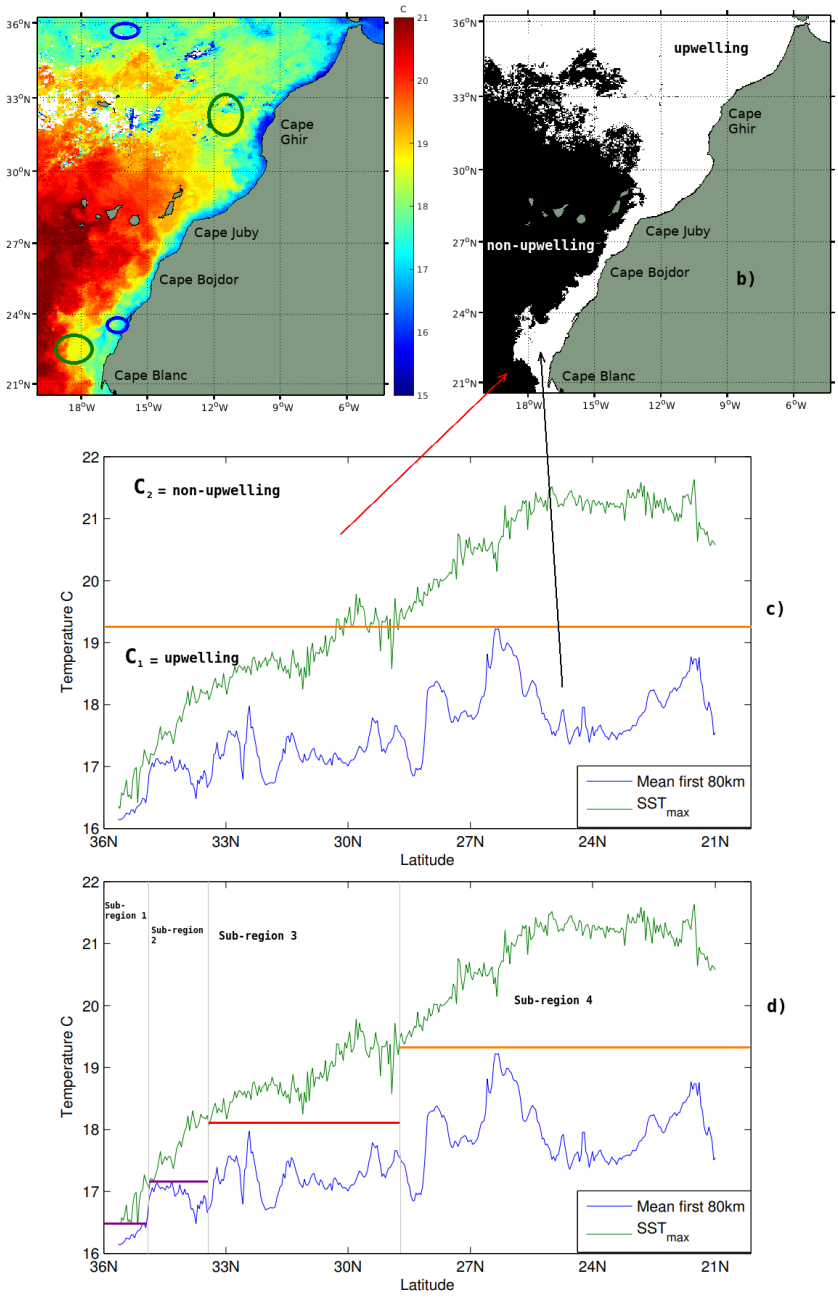

Figure 2-9: a) 8-day SST images obtained on the first week of January 2007, with thermal comparison between the inshore and offshore waters (circles with same the color highlight similar temperature caught in the offshore and the upwelling waters), b) the result of the method developed in [Tamim et al., 2015] applied on the SST image from Fig 2-9(a). White color refers to upwelling water while black color refers to offshore water. The latter method gives results in the southern part, but it fails to properly identify the upwelling regions in the northern part. c) and d) latitudinal comparison between the upwelling and the offshore temperature; green curve represents the maximal temperature on each latitudinal step of the SST image in Fig 2-9(a), blue curve represents the mean temperature over the first 80 km of each latitudinal step.

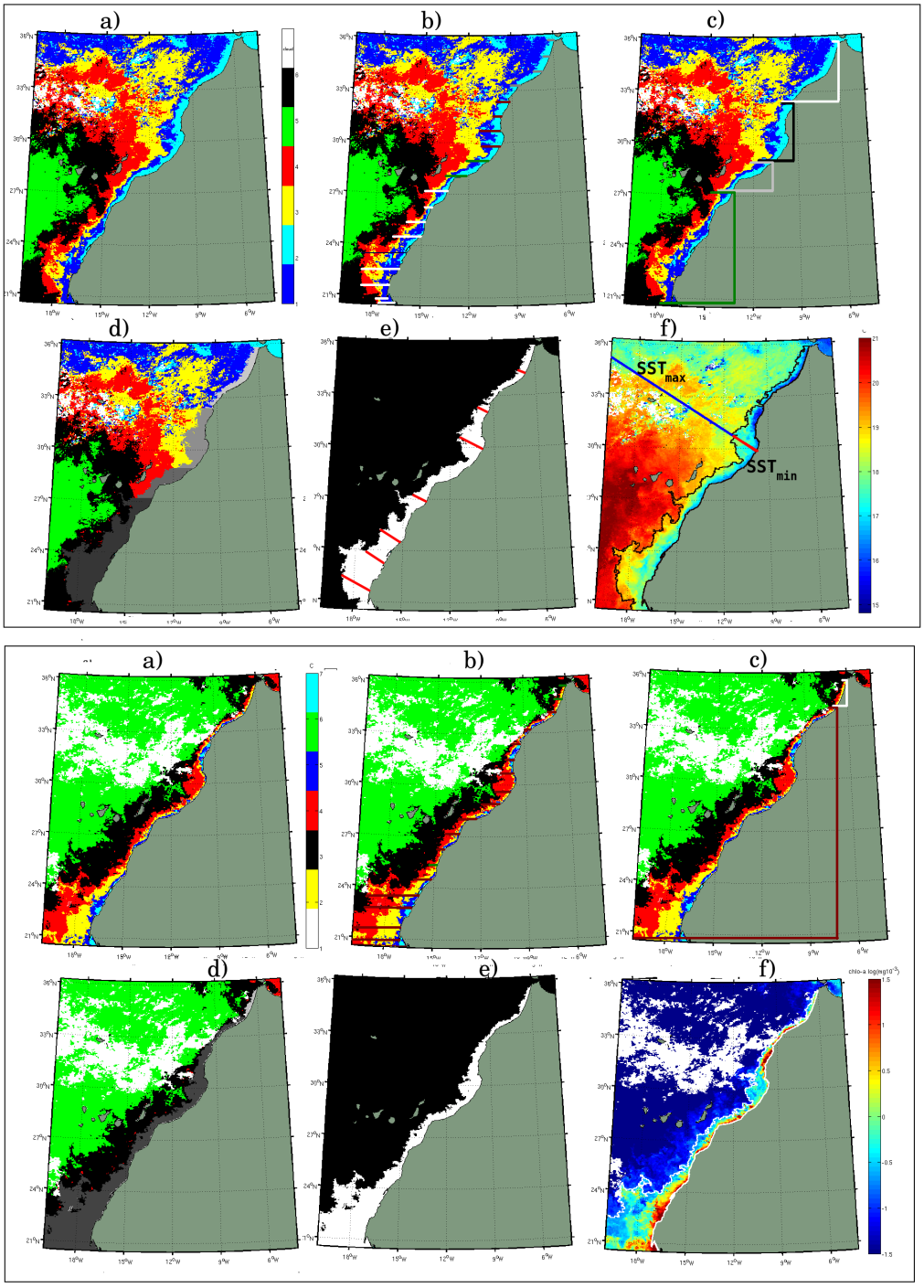

Figure 2-10: (a) PSO clustering applied on SST (upper panel) CHL_a (lower panel). (b) Result of algorithm 2. (c) sub-Regions of connected groups of pixels with same number of candidate clusters. (d) different upwelling regions, (e) Binary image of the proposed method. (f) The final segmentation achieved by the proposed method. The line (black for SST, white for chla) shows the delimitation of the upwelling area.

Chapter 3

Upwelling Dynamics from Biological and Physical satellite Observations

Abstract

In this chapter, I first review existing indices used in the literature to quantify and analyze the seasonal and interannual variation of the upwelling dynamics. Then, I use the upwelling extraction methods which I proposed in the previous chapter to develop a novel simple and intuitive method to quantify the upwelling intensity. The newly introduced index improves the way the thermal difference is defined, taking into account the spatial structure of the upwelling, and its link with the Ekman transport. Later on in this chapter, I use this proposed index, the upwelling extraction methods along with several other biological and physical indices to study the spatio-temporal variation of Moroccan upwelling dynamics.

The characterization and analysis of the spatial and temporal variability of the upwelling phenomenon is of crucial importance to understand the process of the productivity of the marine ecosystem and the influence of this phenomenon on fluctuations in fisheries resources. Indeed, the spatial and temporal evolution of these resources is in close interaction with the dynamics of their marine environment, especially that of upwelling.

Nevertheless, monitoring the temporal evolution of the upwelling phenomenon from satellite measurements is a tedious and difficult operation to perform based on the systematic analysis of daily or even weekly images. In order make this monitoring operational and effective, simple or complex methods have been developed to

synthesize the location of upwelling along the coast for a given period.

Most of these methods use indices based on a thermal difference between coastal and offshore waters. Indeed, the temperature distribution along longitude direction, is supposed to be more or less the same both in offshore waters and in coastal waters. Unlike coastal upwelling with low temperatures in near-shore waters, this horizontal thermal homogenization breaks down by creating thermal differences between coastal and warmer offshore waters. In this case, the isotherms take frankly meridian pace more or less parallel to the coast. As a result, thermal difference between inshore and offshore water, negative in case of upwelling, is a very good indicator not only of the presence of upwelling for each latitude, but it also gives the intensity and strength of this phenomenon. On this basis, several upwelling index calculation methods have been developed and put in the form of applications that make it possible to generate synthetic data providing information on the situation of upwelling covering a given period [Nykjaer and Vancamp, 1992, Nykjær and Van Camp, 1994, Demarcq and FAURE, 2000]:

- **The Cross-Shore Ekman Transport** (CSET) is calculated as the water flux theoretically transported offshore by the wind stress (from satellite data) from the coastal upward flux of colder water [Ekman, 1905]. Under the assumption of alongshore balance between Coriolis force and alongshore wind stress, the offshore Ekman transport per unit length (υ, in the x direction) is given by:

$$\upsilon = \frac{\tau_y}{\rho f} \tag{3.1}$$

  This index estimates the volume of upwelled flow and it is presented in $(m^3 s^{-1} m^{-1})$. This transport depends on latitude and wind stress, where τ_y is the alongshore (in the y direction) surface wind stress in Pascal units, ρ is the surface water density (g/cm^3), and f is the Coriolis parameter in Newton units. The drag coefficient of the wind on the sea surface is computed from the nonlinear formula proposed by [Trenberth et al., 1990].

- **Upwelling index** is based on the thermal difference between coastal and off-

shore waters on the same radial. This index is extracted exclusively from satellite data of sea surface temperature [Nykjær and Van Camp, 1994, Demarcq and FAURE, 2000, Benazzouz et al., 2014b].

In the literature, several indices use SST images to characterize the intensity of upwelling. The first method was proposed by [Nykjaer and Vancamp, 1992] and [Nykjær and Van Camp, 1994] on the entire West African coastline which computes a simple thermal difference between the maximum value SST_{max} (representing warm offshore waters) and the minimum value SST_{min} (representing the upwelling waters) encountered along the same radial:

$$CUI = SST_{max} - SST_{min} \tag{3.2}$$

The results of this index are largely correlated with those obtained by the Cross-Shore Ekman Transport.

Another normalized coastal upwelling index have been developed by [Demarcq and FAURE, 2000].

$$CUI = \frac{SST_{max} - SST_{min}}{SST_{max} - SST_{up}} \tag{3.3}$$

However, this index is difficult to define for the latitudinally changing patterns of the west African region, where different water masses occur, the SACW and NACW, respectively the South and North Atlantic Central Waters. Without a very clear measure of SST_{up} (the original temperature of the upwelled water before it reaches the sea surface) this normalization is difficult to apply to the Moroccan region and introduces a seasonal bias. Probably the most accurate and robust method to compute an upwelling index which has been developed so far is the one proposed in [Benazzouz et al., 2014b]. The strength of this method stems in a large statistical study over a 30 years history of SST data.

3.1 A novel SST-based upwelling index

Upwelling indices have been widely used for the characterization and the identification of spatial and temporal structures of upwelling. In this section we propose a novel and intuitive method to define a latitudinal upwelling index, based on the segmentation we proposed in the previous subsection.

The most commonly used concept to define these indices is simply to compute thermal difference between coastal and offshore temperatures at the same latitude [Demarcq and FAURE, 2000, Van Camp et al., 1991]. [Benazzouz et al., 2014b] showed that this kind of index is the most suitable for Moroccan upwelling. That is, if r is a given latitude, T^r_{max} and T^r_{min} are the maximal offshore and minimal inshore temperatures respectively, then the upwelling index at latitude r is:

$$I^r = T^r_{max} - T^r_{min}. \tag{3.4}$$

Obviously, we consider latitudes as radials r which are perpendicular to the coast line. We now proceed to define T^r_{max} and T^r_{min}.

3.1.1 Computation of T^r_{min}

In most of the methods in the literature, T^r_{min} is defined as the minimum temperature recorded in the coastal band from the coast up to the continental slope [Van Camp et al., 1991, Nykjær and Van Camp, 1994, Demarcq and FAURE, 2000, Santos et al., 2005]. For the Moroccan coast, the latter is generally chosen to be 500 km. In the recent work [Benazzouz et al., 2014b], an involved and large statistical study over a 30 years history of SST data have been used to determine T^r_{min}. To the best of our knowledge, this is the most accurate and robust technique that has been proposed so far.

On the other hand, note that by definition, T^r_{min} necessarily belongs to the upwelling region. Thus, given that we have developed an upwelling segmentation method which shows a very good accuracy, we naturally define T^r_{min} as the minimal temperature recorded within the extracted upwelling area. That is, let S be the segmented

upwelling area, then given a radial $r \in \{1, ..., R\}$ composed of temperature pixels $r = \{T_i^r; i = 1, ..., R\}$, T_{min}^r is defined as:

$$T_{min}^r = \min_{i \in S} T_i^r \tag{3.5}$$

3.1.2 Computation of T_{max}^r

T_{max}^r should be chosen as the offshore temperature where the influence of the upwelling is expected to be negligible. In the literature, T_{max}^r has been chosen from various locations at different distances from the coast. For instance, [Nykjær and Van Camp, 1994] choose the offshore position at 500 km from the coast. [Santos et al., 2005] found that the general patterns of the spatio-temporal variability of their SST-based index were similar within the range 400-1000 km offshore. [Lathuilière et al., 2008] choose the SST average in the band located within 500-700 km from the coast. In our work, we define T_{max}^r in similar manner as in [Benazzouz et al., 2014b]. That is, it is defined as the maximum temperature outside the upwelling area we extract up to 3000 km in the offshore direction.

Fig.3-1 shows an example of a radial and the areas where T_{min}^r and T_{max}^r are sought. The blue line represents the area where T_{max}^r is sought, while the red one is used to identify T_{min}^r.

As we mentioned above, we consider that the upwelling index introduced in [Benazzouz et al., 2014b] as the state of the art and the most accurate method developed so far. We now stretch the advantage of our upwelling index as compared to the one of [Benazzouz et al., 2014b]:

- Our index is simple, very intuitive and computationally much more efficient.
- Given that T_{min}^r in [Benazzouz et al., 2014b] is sought in a fixed band from the coast, some low temperatures may be neglected in the estimation. Our index insures that all the (necessary) low temperatures are considered in the calculation.
- The choice of our radials (90°) is theoretically more appropriate and is indirectly

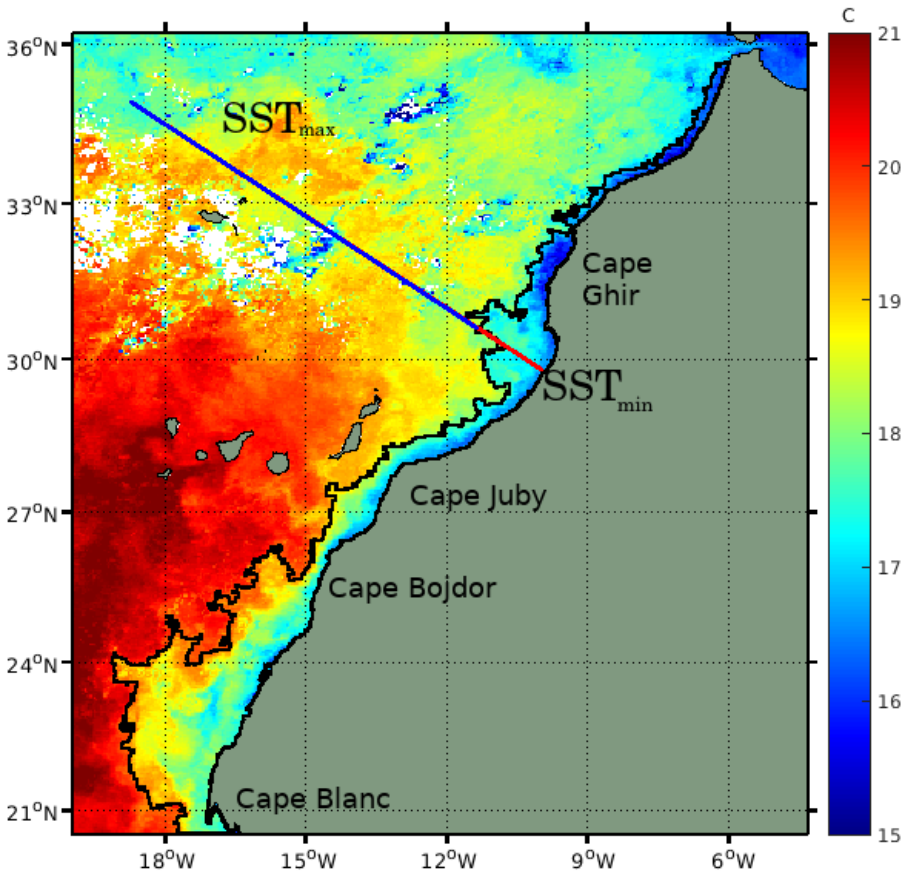

Figure 3-1: Example of the SST_{min} and SST_{max} calculation.

confirmed by the good segmentation results.

- More importantly, the major advantage of our technique is its "online" nature. Indeed, the index of [Benazzouz et al., 2014b] is *static* in the sense that it was developed for the purpose of a fixed period historical study. If one wants to analyze new data (in present or future), the whole (relatively complicated) statistical analysis has to be carried out again. Our index, in turn, is *dynamic* in the sense that it can be really used for both historical studies at any period of time as well as for new data at any temporal resolution, including one single acquisition. Online upwelling analysis can be thus easily performed.

In order to evaluate the effectiveness of our index as compared to [Benazzouz et al., 2014b], in the remaining of this chapter we follow the same (historical) analysis carried out in [Benazzouz et al., 2014b] and compare the results of the two approaches.

3.2 Upwelling intensity from SST images

In this section, we analyze the seasonal and inter-annual variability of the Moroccan upwelling activity. In [Benazzouz et al., 2014b], a study of spatio-temporal variability of the upwelling intensity in the Canary Current upwelling system has been established over a period of 30 years, from 1982 to 2011. An improved SST-based index based on a rigorous statistical analysis of satellite SST fields and their variability was used. Here we follow the main steps of that study but using our upwelling index instead.

3.2.1 Seasonal variability of upwelling intensity

In this subsection, we analyze the seasonal variability of the upwelling intensity via a space-time Hovmoller (stH) diagram (Fig.3-2) at 4km/8-day spatio-temporal resolution, from $21°N$ to $36°N$ and over the same period used in [Benazzouz et al., 2014b], from 1982 to 2011 (for a fair comparison). We compare the spatio-temporal variability of our index I^r with the index I_{AB} of [Benazzouz et al., 2014b] as well as with their Ekman equivalent, the cross-shore Ekman transport index I_{CSET}. Note however that the latter is computed over the period 2000-2009 because QuickSCAT/SeaWinds data are available only for this period.

Fig.3-2-a) and Fig.3-2-b) show the stH obtained by I_{AB} and our index I^r, respectively. Fig.3-2-d) shows the stH of the Ekman index I_{CSET}.

First, Fig.3-2-a) and Fig.3-2-b) show that the results obtained by I_{AB} and I^r are *globally* similar. Indeed, the range of both indices is the same and with both approaches the main patterns of variability can be synthesized into the three characteristic regions:

- The northern region between $33°N$ to $36°N$ where the upwelling is weak/inexistent. This is consistent with the fact of weaker winds and an unfavorable orientation of the coast line in this region

- The central region between $27°N$ ($26°N$ in [Benazzouz et al., 2014b]) and $33°N$.

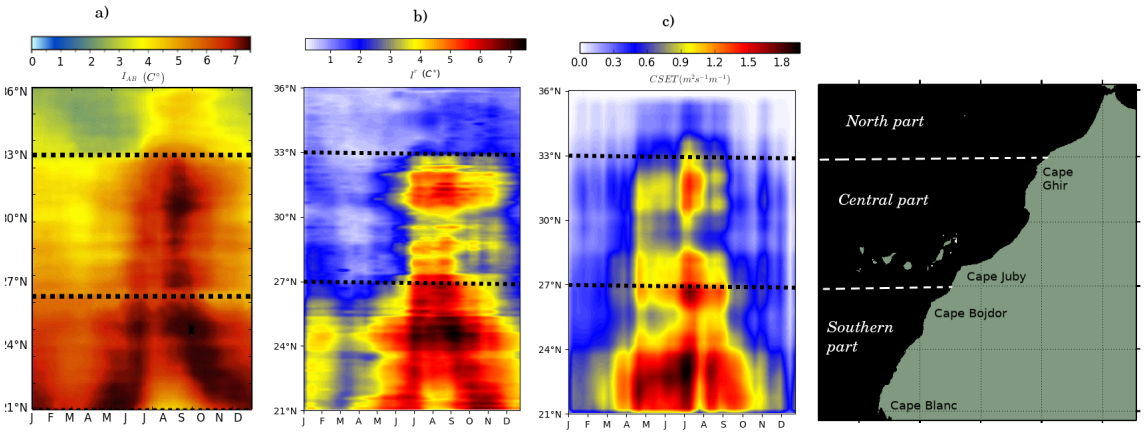

Figure 3-2: Space-time Hovmoller plot of upwelling seasonal variability using : a) I_{AB} index, b) our index I^r and c) the Ekman index I_{CSET} (for the period 2000 - 2009).

Here, the upwelling is stronger in summer and autumn, with the highest values around the locations where prominent upwelling filaments are developed, Cape Juby ($27°N$) and Cape Ghir ($31°N$).

- The southern Moroccan region between $21°N$ to $27°N$ where the upwelling is intense throughout the year with a maximum from spring to autumn. This region is characterized by the giant filament of Cape Blanc with an extension up to 450 km [Marcello et al., 2011].

This *global* similarity shows the effectiveness of assessing upwelling intensity as radial thermal difference when inshore and offshore temperature are correctly estimated.

On the other hand, local comparison between Fig.3-2-a) and Fig.3-2-b) presents many differences. In order to analyze these differences and to assess the accuracy of our method (w.r.t. [Benazzouz et al., 2014b]), we use the CSET index I_{CSET} as a vehicle for comparison. Note that [Benazzouz et al., 2014b] have used I_{CSET} to evaluate the accuracy of their method and that it is exactly the same index we compute here (Fig.3-2-c).

At large scale, it is clear that our I^r is much more similar to I_{CSET} than I_{AB}, with a time lag spatially varying meridionaly between 4 to 6 week. Moreover, I^r and I_{CSET} span almost the same seasons on the 3 regions with nearly coincident maxima

and minima proportionally. At lower scales, I_{AB} displays a high intensity through the whole year in the southern region between $21°N$ and $27°N$. I^r and I_{CSET} show in turn much weaker intensity in winter and spring. In the central region between $27°N$ and $33°N$, I_{AB} displays a medium intensity during winter and spring while I^r and I_{CSET} both show a very weak intensity. The difference in intensities is more remarkable in the northern region between $33°N$ and $36°N$. Indeed, I_{AB} is relatively high which contradicts the well known quasi-absence of upwelling in this region. On the opposite I^r and I_{CSET} show an absence of intensity as expected.

The meridionaly averaged upwelling index can be plotted in 2D (one axis describes the monthly change while the other present the annual variations) to obtain a clearer image about the upwelling dynamics Fig.3-3. When looking at this figure, the similarity between I^r and I_{CSET} is even better highlighted, showing a strong correlation between both indices. The difference in the temporal variability of both variables reflects the different inertia between the atmosphere and ocean systems, these differences mostly concern the duration of the upwelling seasons.

In summary, these results suggest that our method is more accurate than [Benazzouz et al., 2014b] in assessing the spatio-temporal seasonal variability of the Moroccan coastal upwelling, with all the other computational advantages presented in the previous section.

3.2.2 Interannual variability of upwelling intensity

In this subsection we analyze the inter-annual variability of the upwelling intensity. In order to show/confirm the effectiveness of our index, we start first by comparing its annual variability to the Ekman index I_{CSET}. The latter is displayed in Fig.3-4 a) over the period 2000-2009. Fig.3-4 b) shows our index I^r over the same period. It can be seen that I^r is highly correlated with the Ekman index where both indices present a very similar pattern and variation with proportional intensities in the 3 regions. This is further confirmed when analyzing the meridionaly averaged indices in Fig.3-5. It is indeed even more clear that both indices are very similar when looking at each region separately. On the other hand, Fig.3-4 c) shows the variability of the

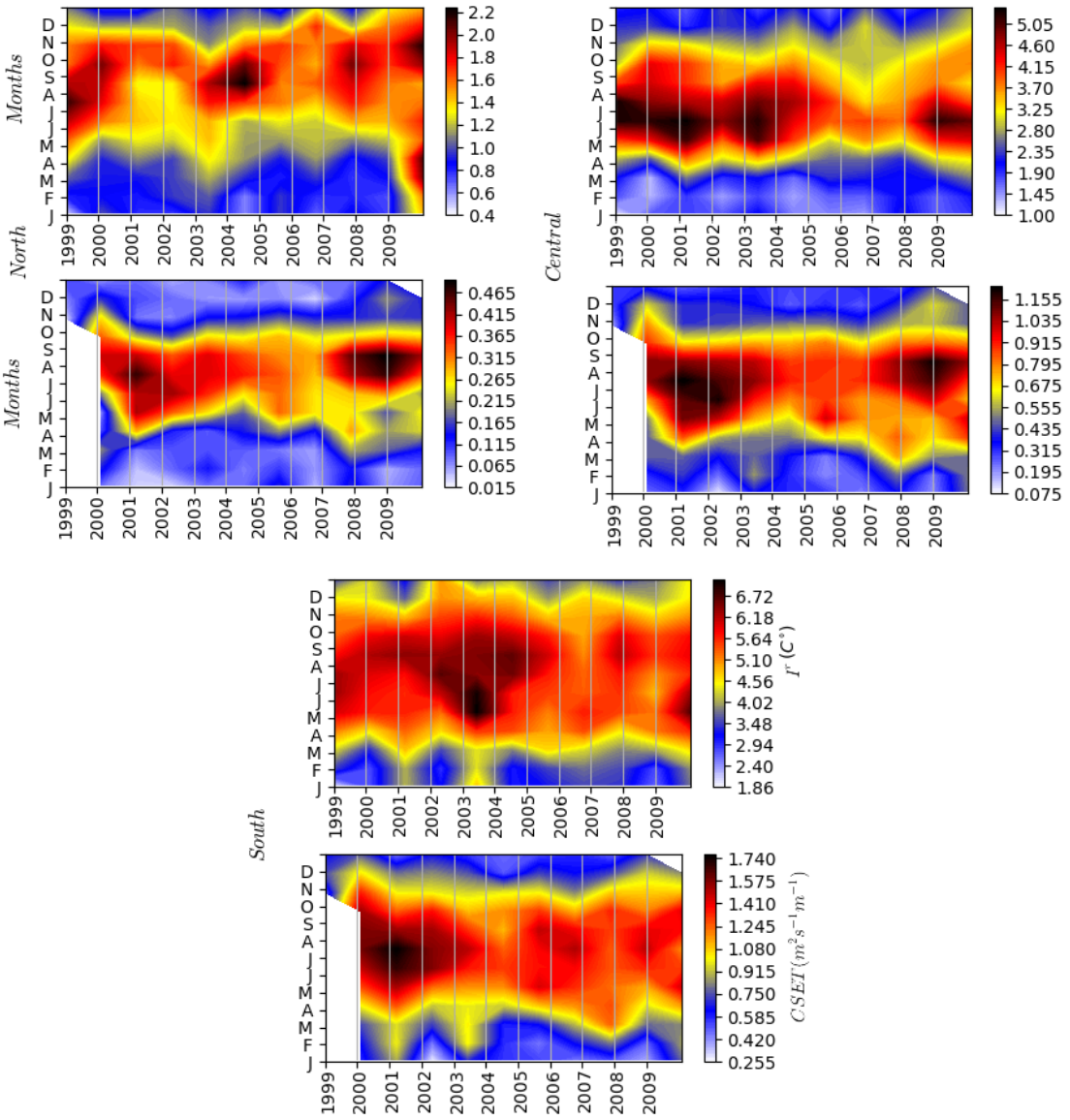

Figure 3-3: Hovmoller plot of the meridionally averaged I^r (upper panel) and I_{CSET} (lower panel) from 2000 to 2009.

index I_{AB}. It is again obvious that the latter yields much less accurate description of the upwelling variability. These observations show and confirm the accuracy and robustness of our index.

We now analyze the inter-annual variability of the upwelling intensity over the full period from January 1982 to December 2015 (Fig.3-6) using weekly 8-day SST data. We recall that the period covered in [Benazzouz et al., 2014b] is from 1982 to 2011.

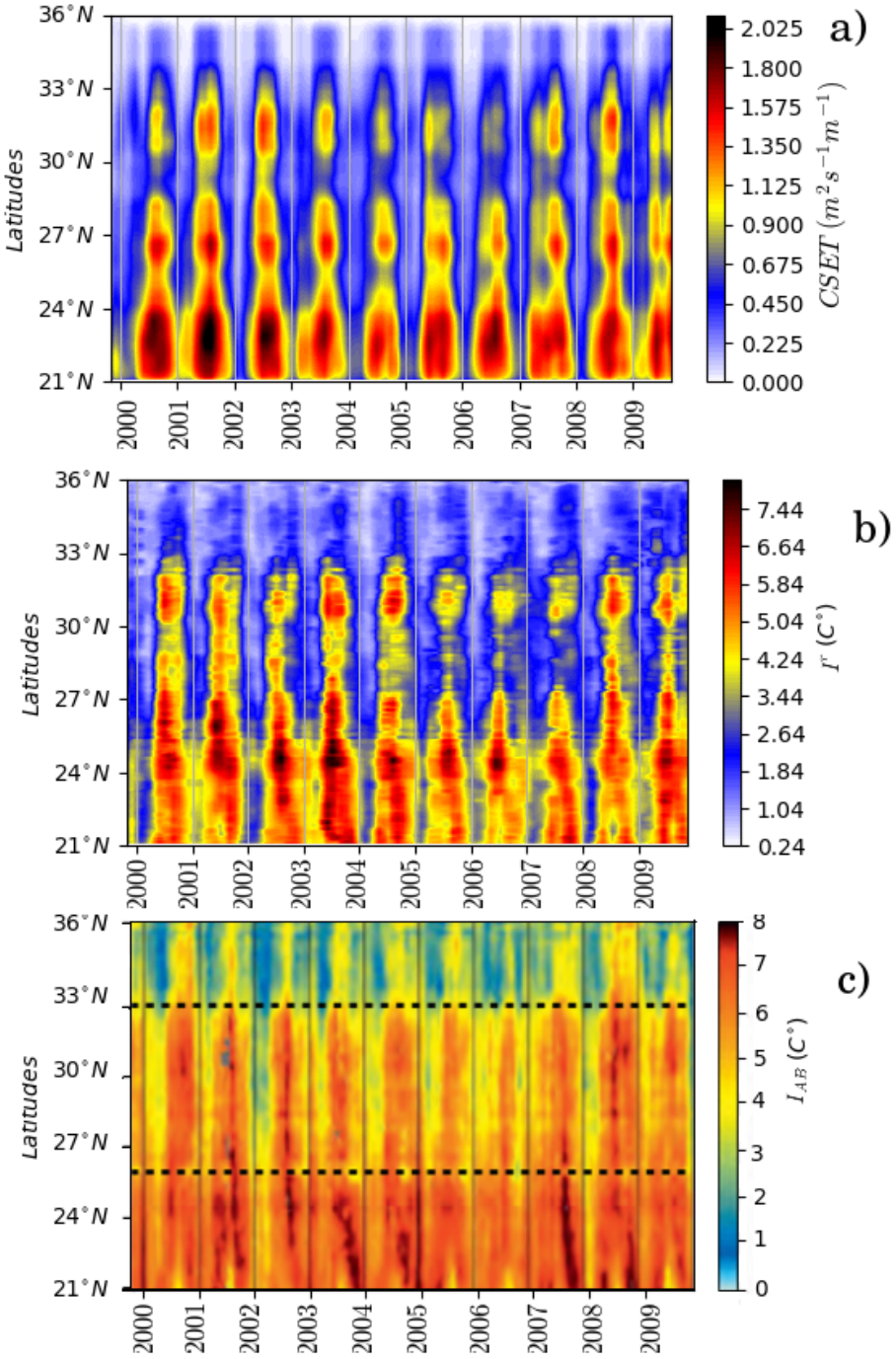

Figure 3-4: Space-time Hovmoller plot of the seasonal and interannual variability of: a) I_{CSET} b) I^r index and c) I_{AB} index between 2000 and 2009.

Fig.3-6 a) shows that the 3 regions defined previously are still very distinct. It also shows that the interannual variability provided by our index I^r is quite different

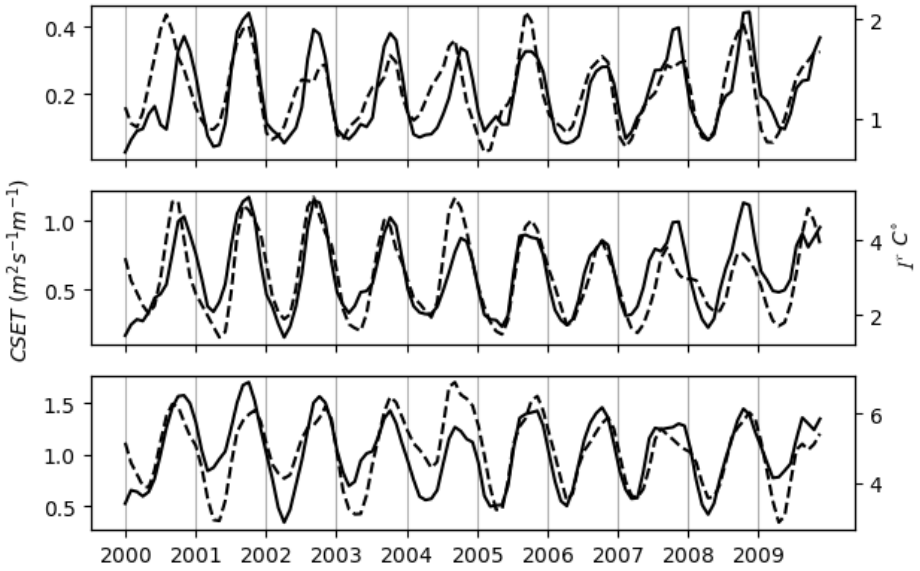

Figure 3-5: Comparative seasonal and interannual variability of the I^r (doted lines) and the I_{CSET} from the Quikscat wind (plain lines) of the three characteristic areas previously identified (a)North, b)Central, d)South).

from [Benazzouz et al., 2014b] in several aspects:

- The southern part: In [Benazzouz et al., 2014b] the upwelling is strong and quasi permanent all over the years and seasons. Our analysis shows that while upwelling is generally stronger in this region it is not however neither quasi permanent nor strong in all seasons. Indeed, it is absent or week (sometimes medium) in all winters. It is generally strong in spring and summer but a decrease in intensity occur some years, such as 1996, 1997, when El Nino took place [Williamson et al., 2000, Chandra et al., 1998, McPhaden, 1999, Ulloa et al., 2001] and 2010 where the North Atlantic Oscillation reach extreme negative values [Osborn, 2011, Seager et al., 2010, Cohen et al., 2010].

- The central part: In [Benazzouz et al., 2014b] a regular and quasi periodic pattern is observed, ranging from medium to strong except in 1996 and 1997. [Benazzouz et al., 2014b] associate these anomalies to a quasi absence of juveniles in 1996 and 1998 and the collapse of the regional sardine stock between 1996 and 1997 [Machu et al., 2009]. Our analysis, on the opposite, highlights first an absence of upwelling in winter. Second, in spring and summer, it high-

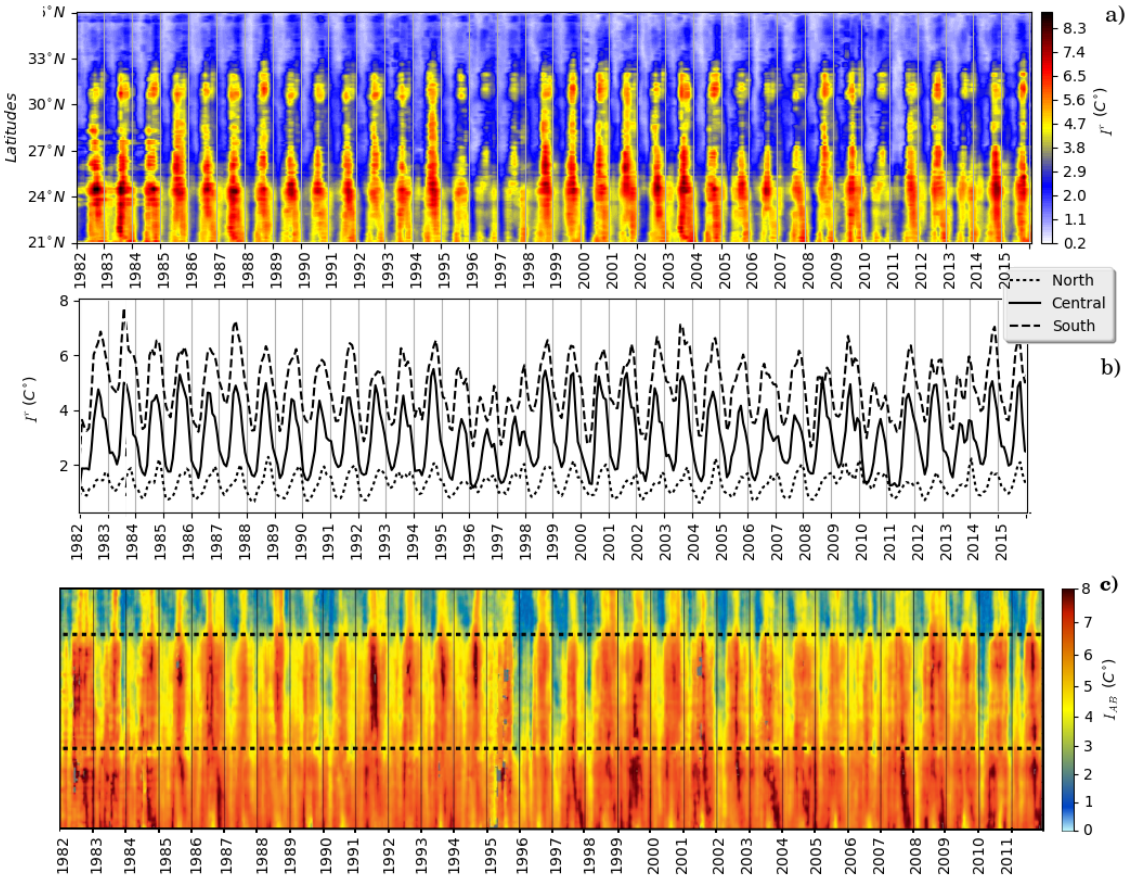

Figure 3-6: a) Space-time Hovmoller plot of the seasonal and interannual variability of the I^r from 1982 to 2015, b) monthly time series of the three characteristic areas previously identified, c) I_{AB} Index.

lights the presence of periods where the upwelling is not present, such as between 1995 and 1997, between 2005 and 2007, 2010 and 2013.

- The northern part: Our analysis shows a total absence of upwelling over all years, as opposed to [Benazzouz et al., 2014b].

These observations are confirmed by Fig.3-6 b) which displays the meridionaly averaged intensity over the 3 regions. Indeed, the upwelling intensity is always (every month) decreasing from south to north where intensities vary roughly between $4°C$ and $8°C$ in the south, $2°C$ and $6°C$ in the center, and below $2°C$ in the north. Moreover, there is a clear periodicity in the seasonal variability showing a weak/absent upwelling in winter which increases through the year to reach its highest value in

summer.

Fig.3-7 presents the Hovmoller plot of the meridionaly averaged I^r. The upper, middle and lower panels correspond to the north, centeral and southern part of Morocco. This figure shows clearly the upwelling seasonality and the monthly variation of its dynamics. In particular, it shows weak upwelling in the beginning of all years till June over the Southern/Central regions and an absence till April in the North part. Furthermore, periods of abnormal upwelling decreasing such as in 1996/1997 and the end of 2010 are highlighted, where the upwelling seasonality decreases by $3°C$ in the summer/autumn seasons, and no major change in the winter/spring.

3.3 Upwelling intensity from model data

In this part, we replicate the same previous interannual study of the upwelling index but this time using temperature from model data. Fig. 3-8 shows the stH of the upwelling intensity calculted from SST and GLORYS2V4 without and with assimilation. In general CUI from both satellite and model shows the same annual variation with the same upwelling duration. The CUI from GLORYS2V4 without assimilation has slightly two different regimes in the southern part from around $21°N$ to $26°N$, which is not the case in the CUI from satellite data that shows only one homogeneous regime. In terms of intensity both CUI are intense with nearly coincidence maxima and minima, leading to global positive correlation. On the other hand, CUI from GLORYS2V4 with assimilation shows very similar pattern to the one from SST images, similar regime in the southern region, the 3 regions defined previously are still very distinct. However, a decrease of the upwelling intensity is remarked in the model data. This slight difference in the upwelling intensity can be due to the spatial resolution of the model data which is $25km$.

Fig.3-9 shows CUI calculated at different depth, we observe important changes in the upwelling seasonality pattern and intensity. At $50m$ of depths, the CUI has slightly two different regimes in the southern part from around $21°N$ to $26°N$, it slightly loses the homogeneity recorded in first level (0.5). The 3 regions defined

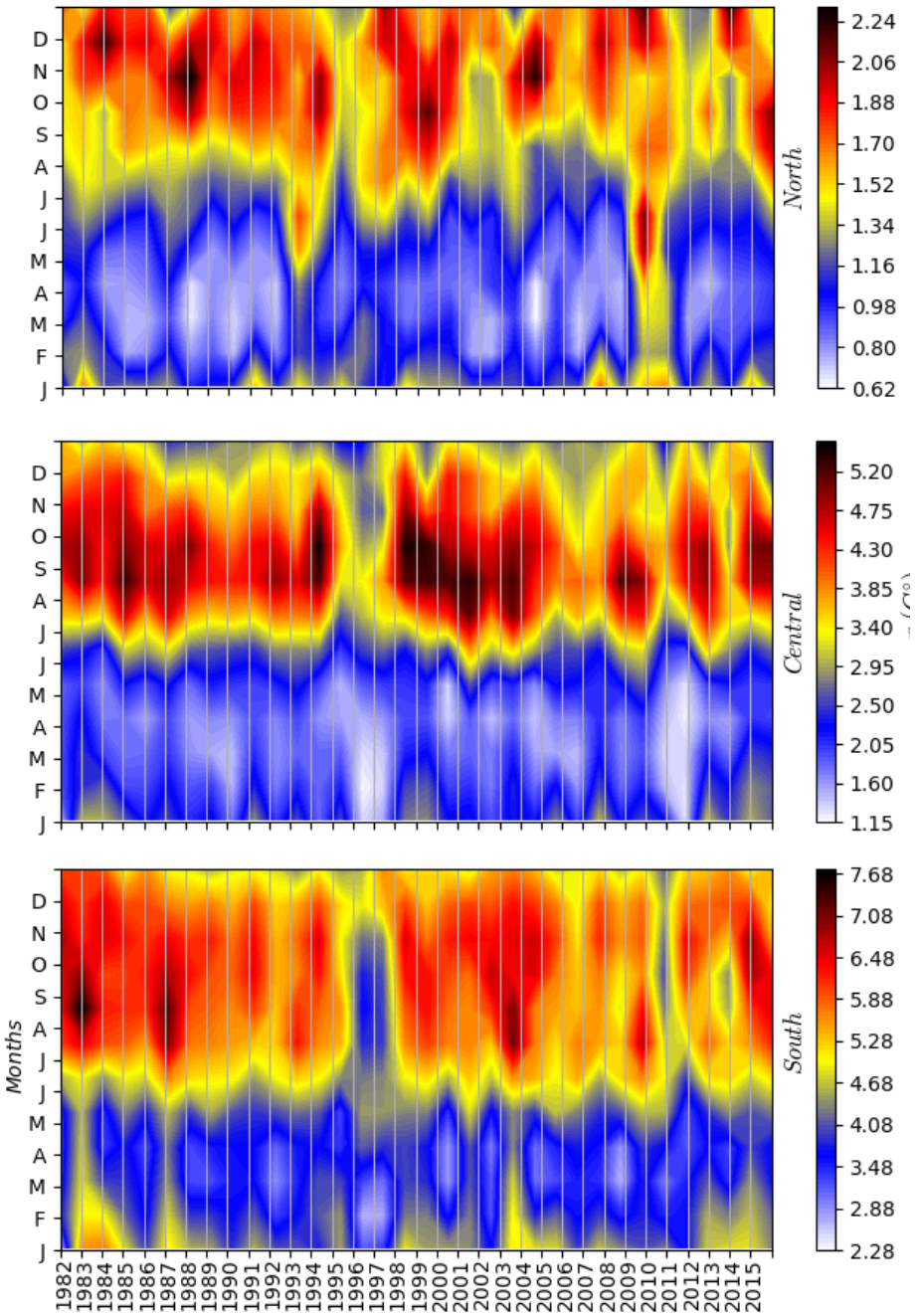

Figure 3-7: Hovmoller plot of the meridionally averaged I^r from 1982 to 2015.

previously are no longer present. The northern region of the system could be merged with the central one since they have very similar variation. At this level the upwelling is more intense, this can mainly be explained in term of the SST_{min}; water layers are thicker if the offshore compared to upwelling areas. Fig.3-10 shows monthly

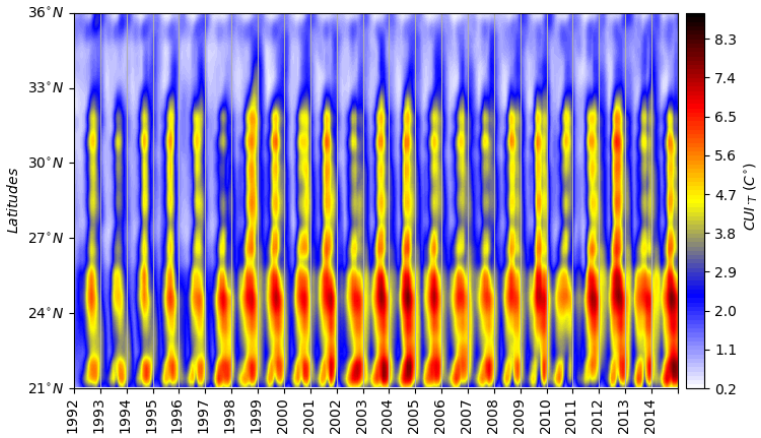

(a)

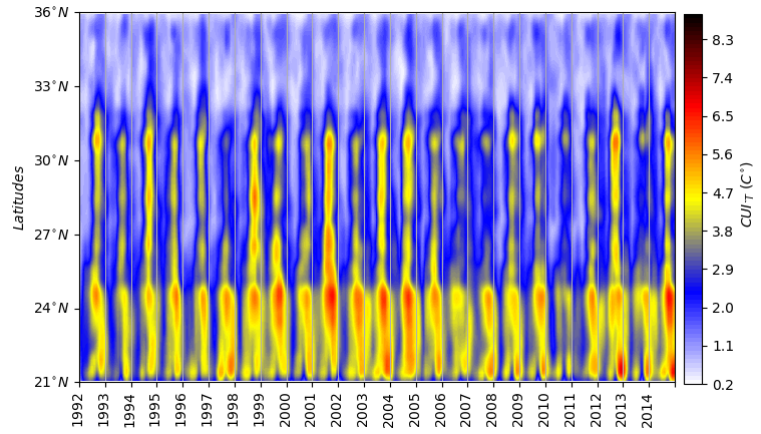

(b)

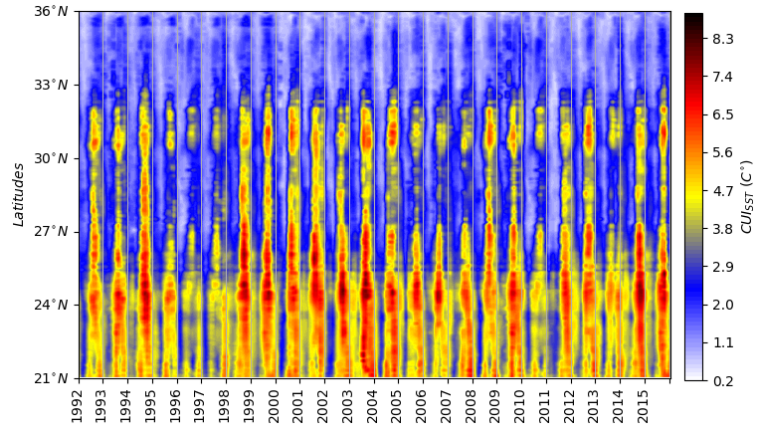

(c)

Figure 3-8: Space-time Hovmoller plot of the seasonal and interannual variability of the I^r: a) GLORYS2V4 without assimilation, b) GLORYS2V4 with assimilation, c) SST images.

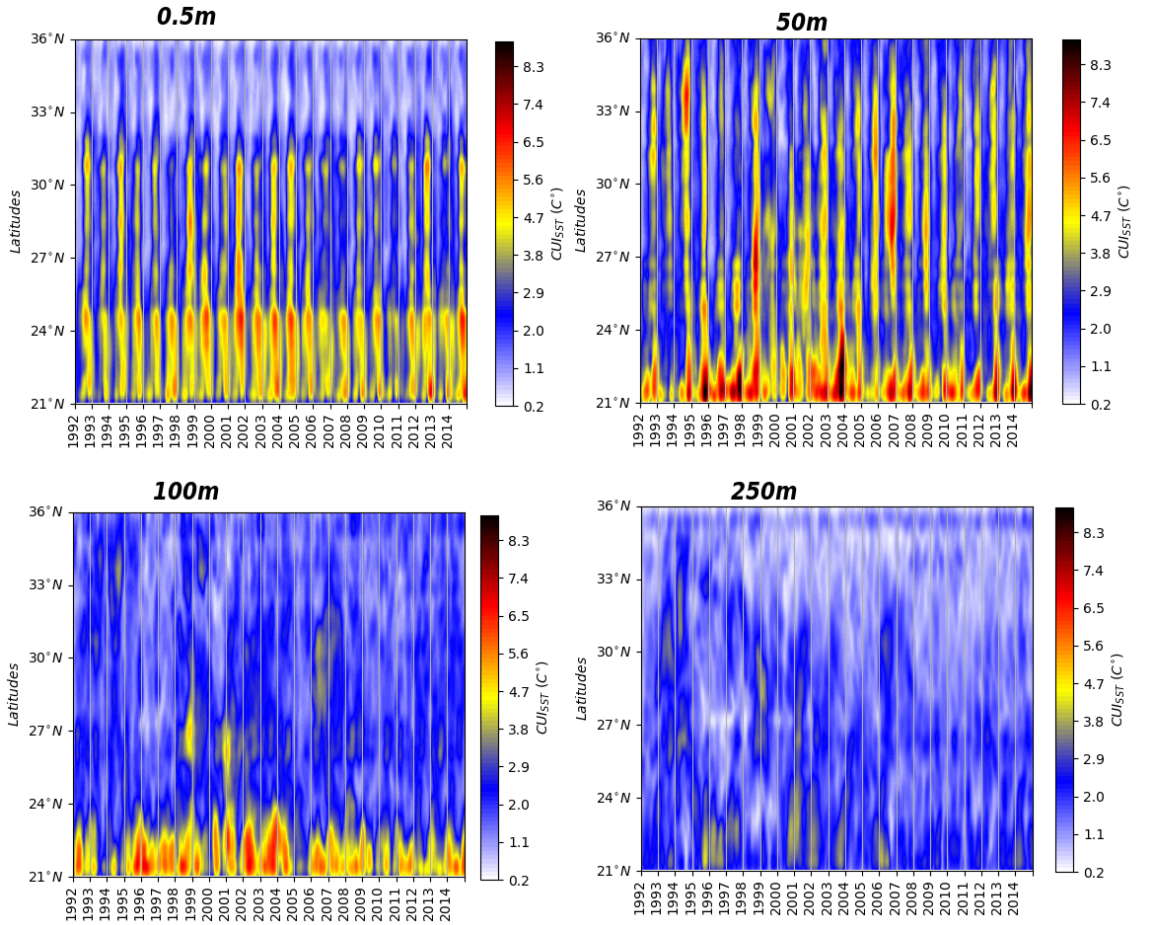

Figure 3-9: Space-time Hovmoller plot of the seasonal and interannual variability of the I^r at different depths.

Temperature V-section of the year 2010 around Cape Blanc, we clearly see how layers lose their thickness in the inshore regions. At $100m$ of depth, CUI in the region between $21°N$ to $24°N$ remain intense. In this region, water is upwelled from very deep layers compared to other regions of this upwelling system and creating a very interesting thermal gradient at such depth.

In the remaining depth levels, no interesting thermal gradient is for the whole system and over all the period of time (see Fig.3-11).

3.3.1 Conclusion

Based on the segmentation method we defined in the previous chapter we developed a novel upwelling index which is more effective than previous indices. We then carried

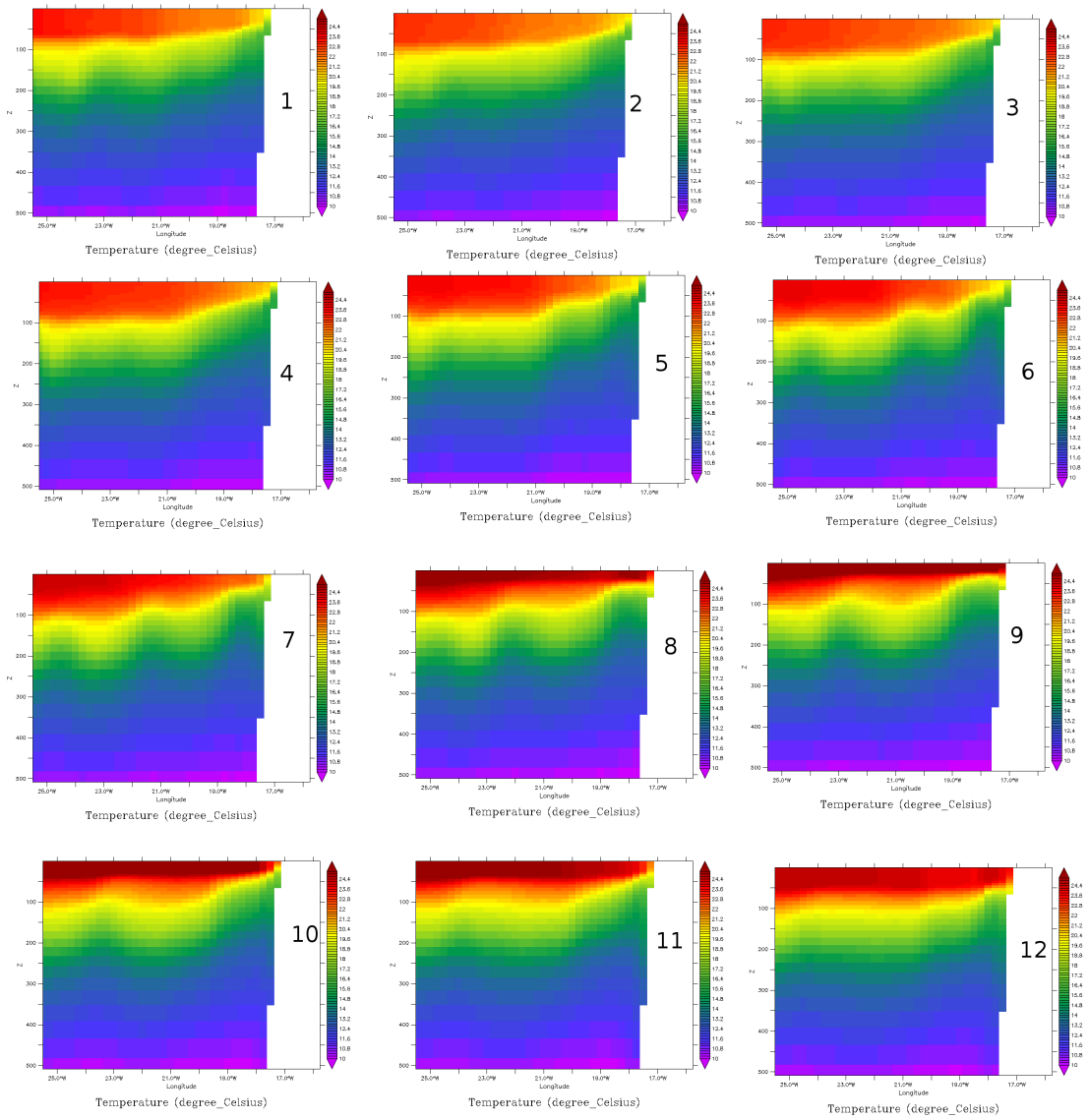

Figure 3-10: GLORYS2V4: monthly Temperature V-section of the year 2010 in the point (lat $=21.42°N$ lon $=-18.51°N$)

out the same historical study of spatio-temporal dynamics of Moroccan upwelling as in [12]. By comparing the two indices (ours and the one developed in [12]) to the Ekman transport index, we showed that ours allows a significantly more accurate description of the dynamics. Moreover, as opposed to the other index, ours allows more efficient upwelling analysis and at any temporal resolution. Furthermore, the methodology we developed in this part can be easily adapted to other upwelling

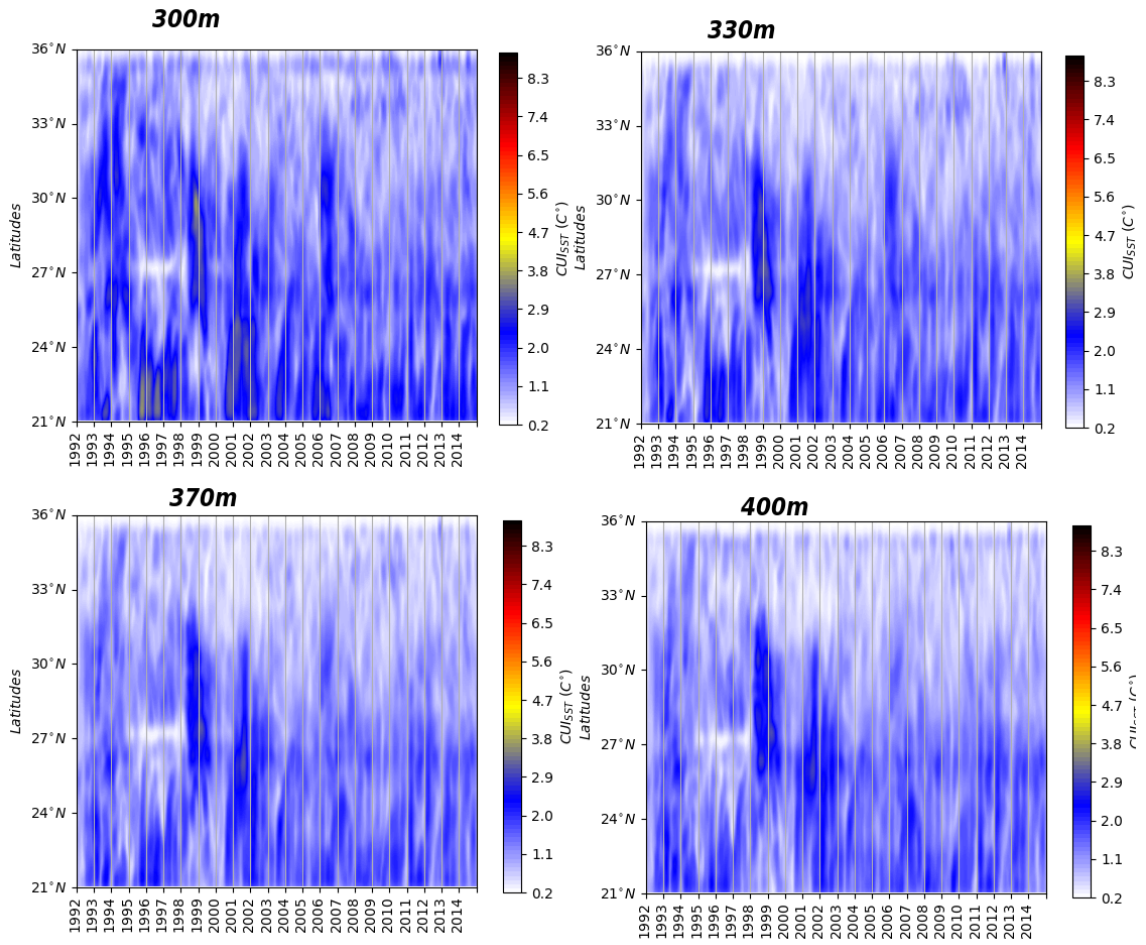

Figure 3-11: Space-time Hovmoller plot of the seasonal and interannual variability of the I^r at different depths.

regions of the globe. We then applied our CUI using temperature from model data and over different levels of depth, showing the effectiveness of our method on different data and different spatial resolution.

In the next part of this chapter, we use the algorithm we proposed for the problem of the upwelling identification from biological and physical satellite observation to study this upwelling system through its spatial distribution from both physical and biological observation. Moreover, we explore the upwelling dynamics in interplay between its spatio-temporal extensions and different upwelling indices.

3.4 Seasonal and interannual upwelling variability

In this part, we use the upwelling identification method we proposed in the previous chapter to provide a seasonal climatology and document the interannual variability of the African upwelling extension from SST and CHL_a imagery. For each latitudinal step, the upwelling extension is calculated as the length of the radial starting from the coastline end ending in the extracted contour of upwelling.

3.4.1 Spatio-temporal variability of the upwelling extension from SST and chlorophyll-a imagery.

We discuss the seasonal variability of the upwelling extension from SST and CHL_a images, based on Hövmoller diagrams at 4km/8-day spatio-temporal resolution. Fig.3-12 shows the Hövmoller diagram of the seasonal climatology of the upwelling extension from SST and CHL_a images, computed for the period $2003 - 2016$.

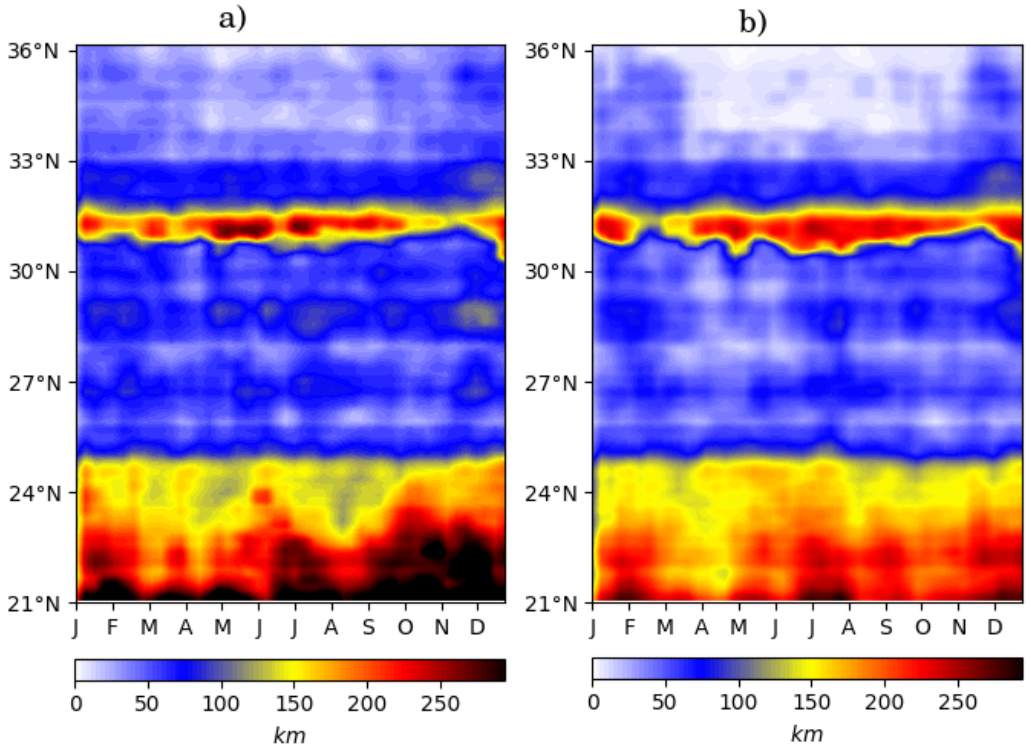

Figure 3-12: Space-time Hövmoller plots of upwelling seasonal variability of: (a) CHL_a extension, (b) SST extension for the period 2003-2016

The main patterns of variability are synthesized into four specific regions; region south of $25°N$ with maximal extension, followed by the region of cape Ghir ($31°N$) with maximal extension occurring during summer. Region between $31°N-25°N$ with minimal extension and north of $33°N$ with weak extension during summer and absent in winter. Both upwelling extensions from SST and CHL_a images show slightly similar patterns, with a general increase in the upwelling extension deduced from chlorophyll-a south of $25°N$. Both parameters are mostly driven by the same process which is the wind stress applied at the sea surface but the spatio-temporal evolution can be controlled by other mechanisms. The thermal ocean response can be instantaneous to the wind stress, but the biological response in term of CHL_a richness can be timely lagged. Also, the CHL_a extension can potentially lead to the importance of filaments in transporting water masses offshore and their physical and biological characteristics across the shelf break. In the southern part of the system (south of $23°N$), [Kostianoy and Zatsepin, 1996] estimated that half of the upwelled waters flow across the upwelling front in filaments. To investigate the possible role of mesoscale dynamics, the alongshore variations of eddy kinetic energy were examined. Fig.3-13(e) shows the log of the eddy kinetic energy computed along the studied area. Progressing south, the EKE clearly increases alongshore. The CHL_a extension width may increase southward due to an increase of the horizontal mixing induced by mesoscale processes. Note that the nature of mesoscale processes can be various, as for instance baroclinic instabilities of the upwelling jet, coastal and planetary waves and that mesoscale dynamics and wind stress are interlinked and cannot be considered as separate processes.

3.4.2 Interannual variability of the upwelling dynamics

In this section, we explore the spatio-temporal dynamics of the north-west African upwelling throughout various physical and biological upwelling descriptors.

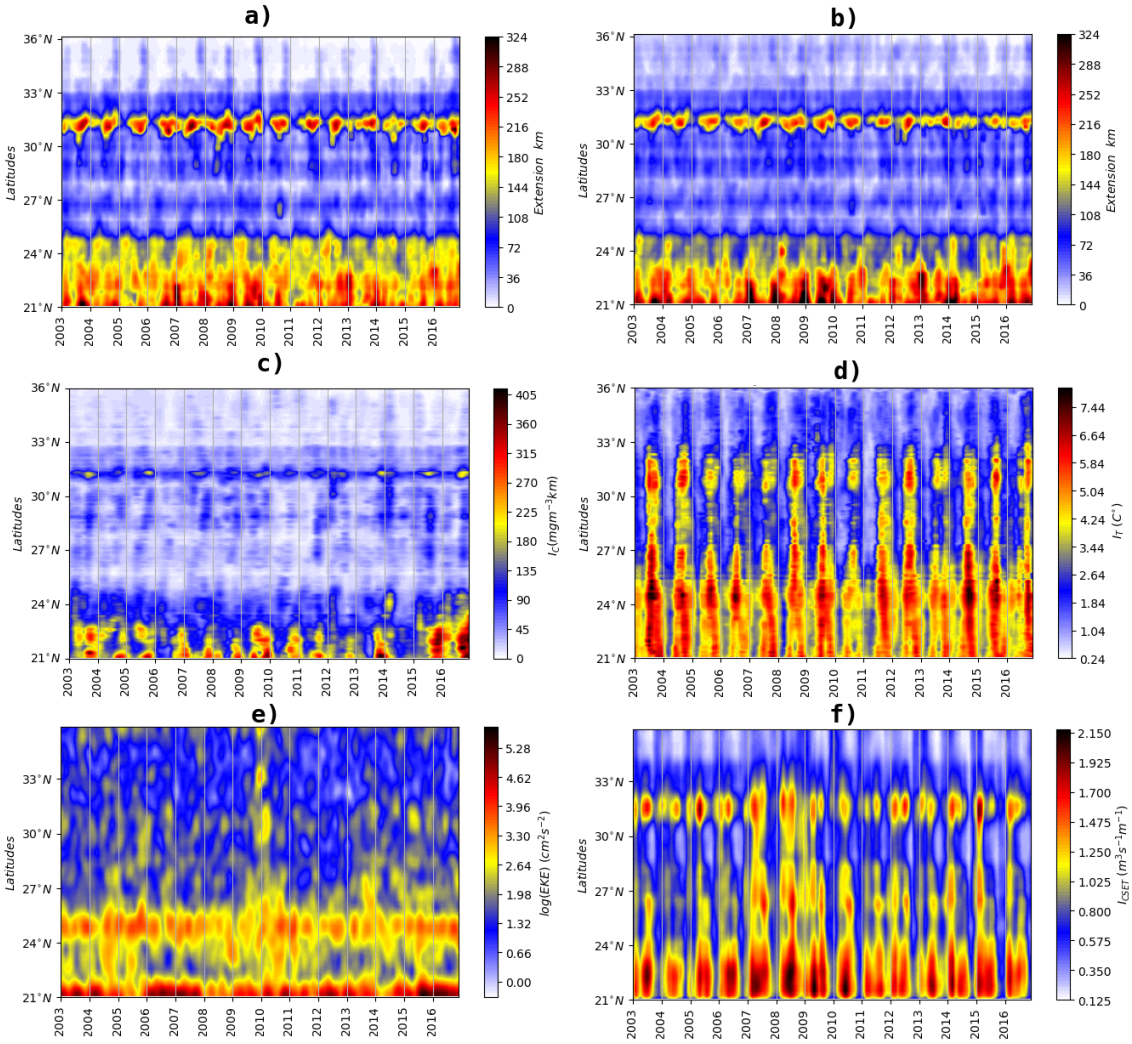

Figure 3-13: Space-time Hövmoller diagram of: a) upwelling extension from SST, b) upwelling extension from CHL_a, c) upwelling index (I_c) computed as the CHL_a average multiplied by its extension, d) upwelling intensity I_T, e) eddy kinetic energy (cm^2s^{-2}) estimated from geostrophic velocities derived from satellite-derived sea level anomalies, f) Cross-shore Ekman Transport (I_{CSET}), over the 2003-2016 archive period.

Upwelling extension

Figs.3-13(a,b) show a Hövmoller diagrams at 4km/30-day spatio-temporal resolution of the upwelling extension from SST and CHL_a images, while Fig.3-14(a,b) show their anomalies.

The offshore extent of the upwelling, as determined from the SST images (Fig.3-13b), displays high variability both in space and time, with quasi-permanent greater

extensions ($> 150km$) in the region between Cape Bojdor and Cape Blanc ($21°N - 25°N$) in summer around $31°N$ (Cape Ghir) during most years. The region between $31°N - 25°N$ is characterized by a very moderate average offshore extension of the upwelling ($< 80km$). Finally, the northern part of the system (north of $33°N$) records the lowest upwelling extension not exceeding 50 km in summer and absent in winter. On the other hand, the upwelling extension as determined from CHL_a concentrations shows a very similar pattern to the one from SST, with a large extension in the biological observations, suggesting that the response of the phytoplankton to upwelling processes may extend beyond the main physical frontal zone. The CHL_a front extended up to 400 km, compared with 300 km for the SST front in the south between $24°N$ and $21°N$. However, both fronts were closer to the coast and also closer to each other in the central region between $25°N$ and $33°N$. For the region north of $33°N$ the extent of the upwelling from biological observation is more pronounced compared to the thermal one which is absent during winter during most years. The greater offshore extent of the CHL_a front in the southern region could be explained by the flow pattern of the Canary Current. The current flows closer to the coast in the north but moves farther offshore south of $24°N$ along with mesoscale processes which possibly advect phytoplankton beyond the SST front to considerable distances offshore in the south. In terms of interannual variability, the whole period of time is characterized by a considerable year to year variability and oscillations between periods of strong and weaker upwelling extension. Nevertheless, such separation is very area dependent (see Fig.3-14).

Upwelling indices

Along with the upwelling extension, we use three upwelling indices for our analysis, which are computed at every latitude and each time step of the interannual variability:

- Thermal-based upwelling index I_T which we proposed in the first part of this chapter.

- The CHL_a index I_C is defined as the integration of the CHL_a concentration from

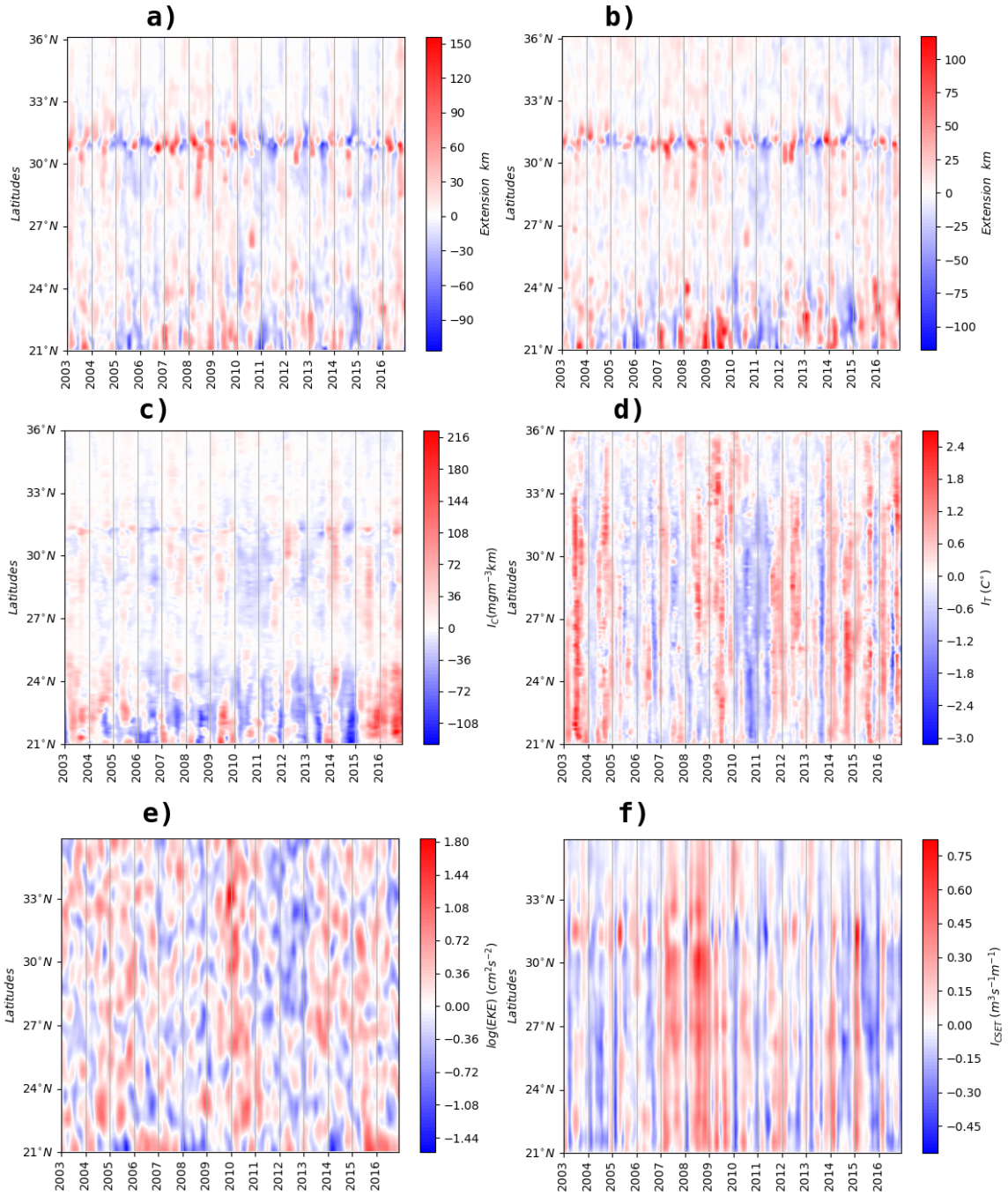

Figure 3-14: Space-time Hövmoller diagram presenting anomalies of: a) upwelling extension from SST, b) upwelling extension from CHL_a, c) upwelling index (I_c) computed as the CHL_a average multiplied by its extension, d) upwelling intensity I_T, e) eddy kinetic energy (cm^2s^{-2}) estimated from geostrophic velocities derived from satellite-derived sea level anomalies, f) Cross-shore Ekman Transport (I_{CSET}), over the 2003-2016 archive period.

the coast to the limit of the extracted upwelling contour. This is equivalent to the product of the upwelling extension (upwelling limit) and the average CHL_a concentration over the same radial and can be expressed in $mgm^{-3} \times km$.

- The Cross-shore Ekman Transport (I_{CSET}). It is computed using daily wind measurements from QuickSCAT and ASCAT winds at $1/4°$ resolution.

We now analyze the interannual variability of the upwelling intensity. Fig.3-13(d) shows a Hövmoller diagram at 4km/30-day spatio-temporal resolution of upwelling intensity I_T produced following the method developed in [Benazzouz et al., 2014b]. The main patterns of variability can be synthesized into the three characteristic regions:

- The northern region between $33°N$ to $36°N$ where the upwelling is weak/inexistent. This is consistent with the presence of weaker and unfavorable orientation of the winds in this region (winds are not parallel to the coast line).

- The central region between $27°N$ and $33°N$. Here, the upwelling is stronger in summer and autumn, with the highest values around the locations where prominent upwelling filaments are developed at Cape Juby ($27°N$) and Cape Ghir ($31°N$).

- The southern Moroccan region between $21°N$ to $27°N$ where the upwelling is intense throughout the year with a maximum from spring to autumn but a decrease in intensity occurs some years, such as in 2010 where the North Atlantic Oscillation reaches extreme negative values (see Fig.3-15).

Indeed, the upwelling intensity I_T is always (every month) decreasing from south to north where intensities vary roughly between $4°C$ and $8°C$ in the south, $2°C$ and $6°C$ in the center, and below $2°C$ in the north. Moreover, there is a clear periodicity in the seasonal variability showing a weak/absent upwelling in winter which increases through the year to reach its highest value in summer.

In order to interpret the seasonal variability of the upwelling intensity I_T, we now focus on another proxy of the upwelling index, the Cross-shore Ekman Transport I_{CSET} (Fig.3-13f). It shows that the main pattern of upwelling-favorable winds

occurred during the period January-October for the region south of $24°N$ with a minimum marked in at the end of each year. Such winds occur north of $24°N$ mostly during the period March-July and marked a minimum mostly between August-December for most years. Latitudinal variations are clearly identified: I_{CSET} peaks around $31°N$ and between $27°N$ and $21°N$. These peaks are located off capes, suggesting that orographic effects accelerate the wind locally. At large scale, I_{CSET} and upwelling intensity I_T show similar patterns, with a time lag spatially varying meridionally between 4 and 6 weeks. Moreover, upwelling intensity and I_{CSET} span almost the same seasons on the 3 regions with nearly coincident maxima and minima proportionally clearly suggesting that the seasonal and latitudinal variability of I_T is driven by the trade winds' variability.

The other upwelling index, related to the $\mathrm{CHL_a}$ concentration I_C, gives another perspective on the upwelling conditions. Fig.3-13c shows a Hövmoller diagram at 4km/30-day spatio-temporal resolution of $\mathrm{CHL_a}$ index I_c. We observe a considerable interannual and seasonal variability in the $\mathrm{CHL_a}$ index I_c along the Moroccan coast, indicating lower phytoplankton biomass during some years (2006) and higher biomass in others (2015, 2016). Latitudinal differences are very noticeable and low I_c is generally featured during all years north $33°N$. Some seasonal signals are evident where very moderate indices were observed in summer between $31°N$ and $27°N$. In contrast, the region between $21°N$ and $24°N$ displayed elevated index I_c during most years and seasons and some of the highest values of the $\mathrm{CHL_a}$ index I_c along with noticeable seasonal variation compared with the other regions. This is the largest spatial region along the Moroccan coast that appears to contain the highest contents of phytoplankton in the surface waters with the interannual variability revealing that 2016 was a particularly anomalous year.

We used different upwelling indices to characterize the interannual variation of the upwelling dynamics. Each of the indices allows us to synthesize the studied area into different regions. However, this division is different from each index to another. Here, we divide our studied area based on the combination of the upwelling extensions and the previous upwelling indices:

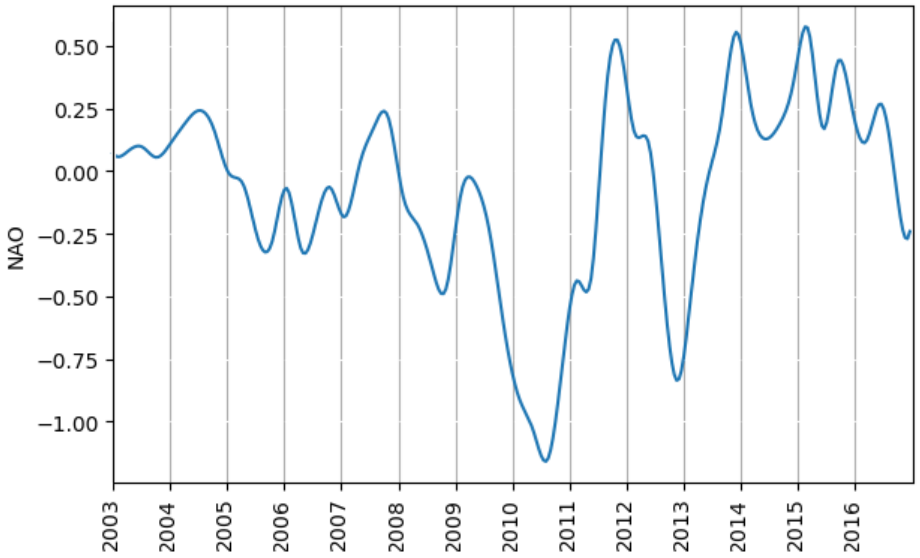

Figure 3-15: North Atlantic Oscillation index from 2003 to 2016.

- In the region north of $33°N$, all the indices suggest that this region is characterized by a weak/inexistent upwelling.

- Cape Ghir around $31°N$ is characterized by the presence of a submarine plateau, which extends offshore (150 km). This allows the generation of permanent coastal upwelling extent during summer and autumn (Fig.3-13(a,b)). This is associated with variations of water column stratification which influence the structure of phytoplankton communities (Fig.3-13c) and a strengthening of the upwelling favorable wind (Fig.3-13f) which results in a stronger thermal gradient (Fig.3-13d).

- Region between $26°N$ and $31°N$, both the upwelling extension and intensity I_T show different properties. The upwelling is intense but does not extend too much. Moreover, the upwelling seasonality is more pronounced in its intensity I_T while no clear seasonality is recorded in its spatial distribution. The difference between the upwelling extension and intensity is due to two different physical processes: the upwelling intensity quantifies the coastal cooling effect created by the Cross-shore Ekman transport I_{CSET} which shares a very similar pattern with the upwelling intensity I_T in the present region (Fig.3-13(d,f)). On the

other hand, the upwelling extension of the upwelled water is due to instabilities generated in the upwelling jet.

- The southern region (between $25°N$ and $21°N$) is characterized by a permanent intense upwelling activity throughout the year with a wind maximum in summer and thermal peak from spring to autumn. This region shows high $\mathrm{CHL_a}$ index I_c, with clear seasonality similar to the thermal index I_T reaching its high values around the end for most years. Instabilities generated in the upwelling jet over this region are spatially structured into filaments and eddies that remain coherent, relatively persistent and recurrent for several weeks, resulting in high upwelling extension, penetrating up to 400 km offshore Cape Blanc and transporting biologically important materials far into the ocean interior.

3.5 Conclusion

Based on our previously defined segmentation method, we provided a seasonal and interannual variability of the upwelling activity using SST and $\mathrm{CHL_a}$ images. The results show that the upwelling spatial extension patterns computed from SST and $\mathrm{CHL_a}$ display substantially the same pattern. Hence, it is very interesting to consider the importance of the connections between adjacent coastal regions and between the coastal and offshore oceans. We thus show that the accuracy/robustness in the prediction of the evolution of the coastal upwelling is better achieved when adequately using both sensors. Moreover, we explored the upwelling dynamics in interplay between its spatio-temporal extensions and intensity for the period between 2003 and 2016. This led us to define regions with different upwelling properties in term of the upwelling extension and intensity.

Chapter 4

Transport and Coherent Structures in Unsteady Flows

Abstract

In this chapter we motivate the importance of transport in fluids in many natural systems. Then we introduce the phenomenon of *chaotic advection* and show methods from dynamical systems' theory that allow to determine the geometry of mixing in chaotic flows: Lagrangian Coherent Structures (LCSs).

4.1 Transport and Mixing

Fluids are ubiquitous in both nature and technological applications, and their dynamics is ranging from the largest known length scales in galactic flows, to medium scale flows in oceans, rivers and planetary atmospheres, to the smallest scales in human cells. The study of fluid dynamics is interesting not only to understand physical phenomena, but also in designing technological devices and industrial processes. In nature, oceanic and atmospheric flows, for instance, play a key role on the global scale transporting heat from the tropics towards the poles. This plays a key role in distributing local climate in many regions of the globe. In geoscience, most transport process are related to moving fluid, e.g., the dispersion of dust, moisture, and volcanic ashes [Haszpra and Tél, 2011] in the atmosphere, the transport of nutrients, marine

wildlife, dissolved gases [Olascoaga and Haller, 2012] in the ocean. In biological sciences, the blood flow in veins is crucial to supply cells with all necessary substances, while it transports water and nutrients from the ground into the leaves in case of plants. In industrial domain, the development of motors includes flows of combustion processes in engines. Transportation by cars, ships and plane is largely affected by the surrounding flow which pushes the engineering industries to develop solutions to the problems of propulsion through air and water. In the contrast approach, geophysical flows as wind, ocean currents or rivers play important roles extracting renewable energy. Flows in tubes and pipes transport gas and oil over large distances and allow to providing whole cities with fresh water and dispose of the waste water. Fluids tend to lose its stability while increasing velocity. This fundamental property of fluid motion is responsible for most of the introductory flows being time-dependent. Contrary to steady flows, time-dependent flows efficiently mix the fluid, i.e., the properties of the fluid, as the concentration of a physical or chemical quantity or also discrete solid particles, are transported by the fluid in irregular way.

4.2 Transport process

In principle, the motion of a fluid could be described by the time-dependent velocities, or equally, by the trajectories of fluid parcels. However, this is not convenient and most fluid flows are macroscopic and have length scales much larger than the parcels scale. Therefore, the fluid is described as a continuum. In this fluid continuum, two conceptually different basic processes are practical to describe transport. In the following, a short definition of the basic two transport mechanisms, diffusion and advection is given.

4.2.1 Diffusion

Diffusion is a transport process that is induced by random motion, or more specifically, motion that can be described by statistical means. Molecular diffusion is the typical case, which is the thermal motion of all (liquid or gas) particles at temperatures

above absolute zero, where the thermal Brownian motion of molecules or atoms is in principle deterministic. However, due to the large number of collisions involved, it can be described as a stochastic random walk. The displacements of the molecules are then stochastic variables and obey certain probability distributions. In the absence of concentration (or chemical potential) gradient in the medium there is no net flux, as diffusive transport in one direction is exactly balanced by transport in the opposite direction. These change if a concentration is not homogeneously distributed. The diffusive flux J from regions of high concentrations to low concentrations driven by random movements is described by Fick's first law:

$$\mathbf{J} = -D\frac{\partial \varphi}{\partial x} \tag{4.1}$$

where D is the diffusion coefficient that depends linearly on temperature, φ is the concentration and x the position. In two or more dimensions we must use ∇, the gradient operator, which generalizes the first derivative, then obtaining

$$\mathbf{J} = -D\nabla\varphi \tag{4.2}$$

Assuming a continuity equation for the concentration without source terms on the right-hand side

$$\nabla.\mathbf{J} + \frac{\partial \varphi}{\partial t} = 0 \tag{4.3}$$

and a constant, isotropic, homogeneous diffusion coefficient D, we get Fick's second law, the diffusion equation

$$\frac{\partial \varphi}{\partial t} = D\nabla^2\varphi \tag{4.4}$$

This states that under diffusion, the concentration increases at positive curvature of the concentration field and decreases at negative curvature of the concentration field. Therefore, this process tends to bring into equilibrium concentration differences and finally leads to a constant concentration, which is the most probable state of

distribution. The diffusion coefficient in water has a magnitude of $D \approx 10^{-9} m^2 s^{-1}$, thus, diffusive transport over a length of $1mm$ takes about $103s$.

4.2.2 Advection

Unlike the diffusion, which is the statistical description of irregular motion, advection process is the deterministic motion given by the partial differential equation that governs the motion of a conserved scalar field as it is advected by a known velocity vector field. Let $\varphi(x,t)$ be the concentration field of a passive tracer. Then, the concentration field evolves under a flow as

$$\frac{\partial \varphi(x,t)}{\partial t} = -v \nabla \varphi(x,t) \tag{4.5}$$

The motion of fluid can be described in two fundamental reference systems: the Eulerian and the Lagrangian frame. In the Eulerian presentation, we use a Cartesian coordinate system fixed in space, which is more convenient for the representation of fields. In the Lagrangian presentation, we fix our coordinate system to the moving fluid particles and evaluate the processes that act on a fluid particle to obtain differential equations for its behavior. Differential equations in both frames are related by the material derivative

$$\frac{d}{dt} = \frac{\partial}{\partial t} + v \nabla \varphi(x,t) \tag{4.6}$$

This states that a rate of change of a property in the Lagrangian presentation $\frac{d}{dt}$ translates to two terms in the Eulerian one. At a fixed point in space, a field changes due to inherent rates of change $\frac{\partial}{\partial t}$, and because the field is advected over the fixed point, represented by the term $v\nabla$. In the Lagrangian frame the advection equation. 4.5 for a passive tracer is simply

$$\frac{d}{dt}\varphi = 0 \tag{4.7}$$

which express that the concentration in a fluid parcel is constant in time.

Flow measurements are possible in both, the Eulerian and Lagrangian presentation. In Eulerian measurements, the flow is measured at fixed points and seems more natural. Measurement devices can be installed in a certain place and deliver velocity data at a well defined position. Lagrangian measurements with drifting particles can give a much better insight into transport. For this purpose, drifters on the sea surface can use GPS system. Or based on the use of imaging techniques to track position of particles.

4.3 Chaotic Advection

Mixing and transport processes are extremely important topics in physical oceanography. In fluid dynamics and chaos theory, mixing is the process by which flow tracers develop into complex fractals under the action of a fluid flow. Two basic mechanisms are responsible for fluid mixing: diffusion and advection. In liquids, molecular diffusion alone is hardly efficient for mixing. Advection, that is the transport of matter by a flow, is required for better mixing. The flow is very regular, as it consists solely of a rotational motion, and transport seems to be predictable. However, when the action of the vortices is continuously switched on and off, particles in the flow undergo chaotic trajectories and mixing is significantly enhanced. Generally, chaotic advection refers to irregular motion of particle trajectories in a simple deterministic time-dependent flow that is given by an advective velocity field. The term chaotic advection was introduced in a paper by Aref [Aref, 1984] where he numerically studies the mixing of particles in a flow induced by two point vortices. Since that paper, various studies has applied ideas from dynamical systems to the problem of mixing in fluids [Aref, 1990, Aref, 2002, Ottino, 1989, Pierrehumbert, 1994]. Here, we are mainly interested in the spatial distribution of fluid volumes that are alternatively separated and merged by the flow. In order to unveil the geometry of mixing in time-dependent fluid flows, one need to consider the Lagrangian approach and analyze trajectories of infinitesimal fluid parcels. Their trajectories are solutions of the

dynamical system:

$$\dot{\mathbf{x}} = \mathbf{v}(\mathbf{x}, t), \quad \mathbf{x} \in \mathbb{R}^2, \quad t \in [\alpha, \beta] \tag{4.8}$$

the velocity field $v(x,t)$ here can present experimental measurements from a numerical hydrodynamic model solving the governing equations for fluid motion, or from an analytical kinematic model flow, or from satellite measurement of sea surface current. Thus, the velocity field is given as a data set in a fixed Eulerian frame, and we obtain particle trajectories by integrating Eq.4.8. This dynamical system is numerically solved using a simple 4th order Runge-Kutta scheme and a cubic interpolation in time and space. A trajectory that starts from the initial condition x_0 at time t_0 and evolves to its position at time t is denoted by $x(x_0, t_0, t)$. In a chaotic flow, the trajectories of particles highly depend on the initial conditions (x_0, t_0). Thus, initially close trajectories may rapidly diverge. Typically, the distance between both trajectories grows exponentially in chaotic flows.

The mixing patterns which appear in chaotic fluid flows are solely determined by the dynamical system 4.8 that governs the advection. These patterns can be extracted from trajectories that solve equation. 4.8 by applying methods from dynamical systems' theory. In particular, dynamical system theory deals with the analysis of the phase space which is the space of the dynamic variables of the system. Here, the phase space is the real space in two dimensions (x, y). The topology of the phase space determines the dynamics of the trajectories. We seek to separate regions of different dynamics in the fluid by analyzing the portrait of the phase space of the flow.

In the following, we choose a simple steady flow to introduce the basic dynamical systems' concept of a hyperbolic fix point and its stable and unstable manifolds. We shortly present how these manifolds can be estimated also in unsteady flows for a finite time, and we give the definition of the finite-time Lyapunov exponent. Then, we present the similar finite-size Lyapunov exponent in a short paragraph. Finally, we give an outlook on the very recent development of a new theory to extract transport

barriers from time-dependent flows.

4.4 Lagrangian Coherent Structures (LCSs)

We seek to extract flow structures that organize fluid trajectories in a time-dependent flow. In the geophysical fluid dynamics community these structures are referred to as Lagrangian coherent structures or LCS [Peacock and Dabiri, 2010]. According to Haller, Lagrangian coherent structures (LCSs) are distinguished surfaces of trajectories in a dynamical system that exert a major influence on nearby trajectories over a time interval of interest [Haller and Yuan, 2000]. LCSs associated with hyperbolic trajectories are directly connected with the concept of stable and unstable manifolds of hyperbolic fix points. Thus, we introduce this concept and explain how LCSs can be estimated from finite-time stretching fields of the fluid flow.

4.4.1 Stable and Unstable Manifolds in a Steady Linear Strain Flow

We consider a simple linear strain flow (Fig.4-1) that defines a time-independent or autonomous dynamical system [Branicki and Wiggins, 2009, Samelson and Wiggins, 2006]

$$\dot{\mathbf{x}} = \mathbf{v}(\mathbf{x}) = b\begin{pmatrix} -x \\ y \end{pmatrix} \tag{4.9}$$

where b is the strain amplitude. This flow field has a hyperbolic fix point $x_f = (0,0)$ satisfying $v(x_f) = 0$. A small perturbation $\delta x(t)$ to this fix point evolves as:

$$\begin{aligned} \delta\dot{\mathbf{x}} &= v(x_f + \delta x) - v(x_f) \\ &\approx v(x_f) + \nabla v(x_f)\delta x - v(x_f) \\ &= \nabla v(x_f)\delta x \end{aligned} \tag{4.10}$$

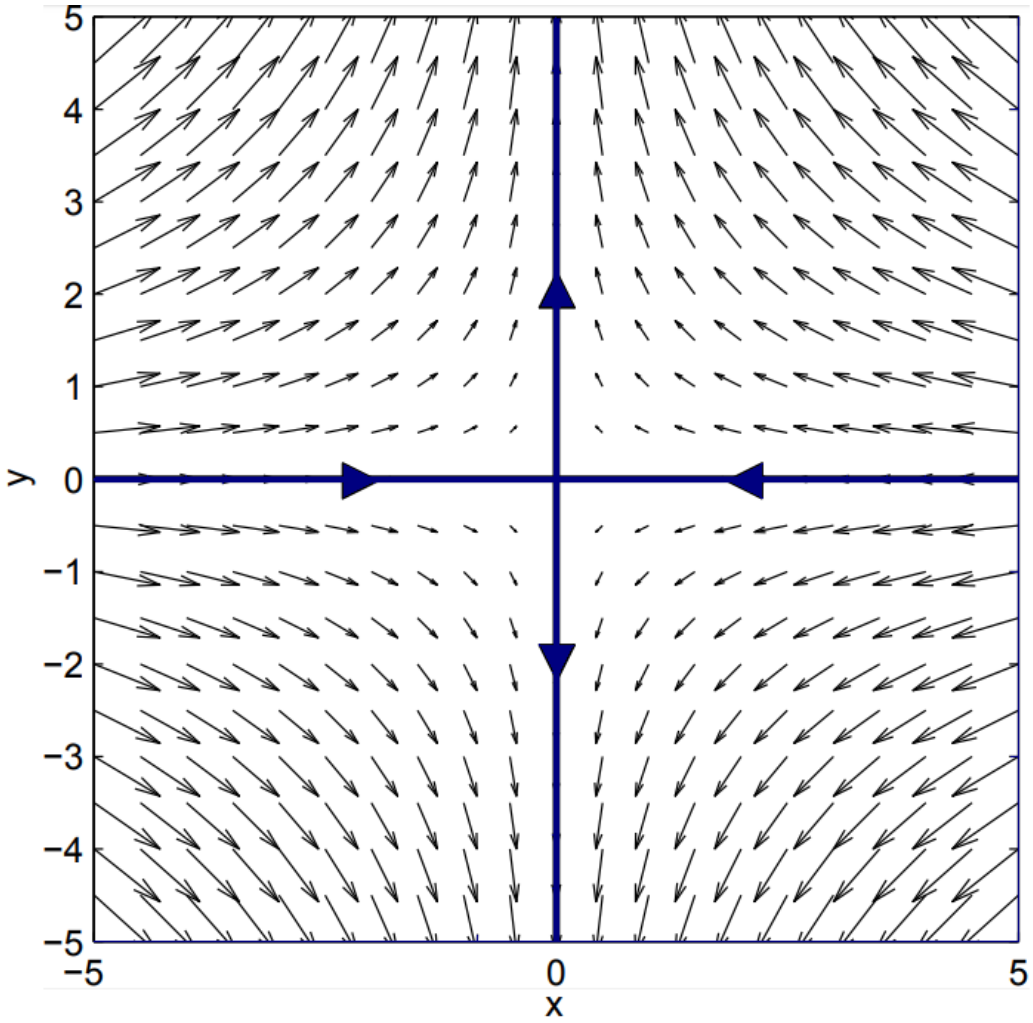

Figure 4-1: Linear strain flow defining a dynamical system with a hyperbolic fixed point $x_f = (0, 0)$. The x-axis and y-axis are the stable and unstable invariant manifolds of the hyperbolic fix point. Fluid parcels in each quadrant are confined to the respective quadrant by the hyperbolic manifolds.

The gradient matrix of the velocity field is

$$\delta v(x_f) = \begin{pmatrix} \partial_x v_x & \partial_y v_x \\ \partial_x v_y & \partial_y v_y \end{pmatrix} = b \begin{pmatrix} -1 & 0 \\ 0 & 1 \end{pmatrix} \tag{4.11}$$

Hence, the perturbation is stretched exponentially in time as given by the eigenvalues of ∇v as

$$\begin{pmatrix} \delta x(t) \\ \delta y(t) \end{pmatrix} = \begin{pmatrix} e^{-bt}\delta x_0 \\ e^{bt}\delta y_0 \end{pmatrix} \tag{4.12}$$

The stable and unstable directions of the hyperbolic fix point are aligned with

the x-direction and y-direction respectively. All points on the x-axis asymptotically converge to the fix point while they always stay on the x-axis. Thus, the x-axis is the stable invariant manifold of the hyperbolic point x_f. In the opposite side, all points on the y-axis asymptotically diverge away from the fix point while they always stay on the y-axis. This characterizes the y-axis as the unstable invariant manifold. These stable and unstable manifolds separate regions in the phase space with different dynamics. As they are material lines, they cannot be crossed by fluid and act as transport barrier. In the present case, these material lines completely separate the fluid into four regions that do not exchange fluid. However, in time-dependent flows, fluid exchange between separated regions is possible. The stable and unstable manifolds determine the geometry of this exchange and are therefore of high interest to obtain the geometry of mixing in the fluid.

4.4.2 LCS in Unsteady Flows

As pointed in the previous section, stable and unstable manifolds of hyperbolic fix points are asymptotic concepts. However, in geophysical flows such as the atmosphere or the ocean, we are interested in chaotic transport on relatively short time scales, while the asymptotic mixing is irrelevant Therefore, various theoretical and applied studies present different definitions of stable and unstable manifolds for finite-time dynamical systems [Haller and Yuan, 2000, Huhn et al., 2012, Mancho et al., 2006, Shadden et al., 2005, Wiggins, 2005]. It turns out that in many practical applications, the manifolds can be estimated as lines of maximal stretching in the flow. For example, if we compute the exponential separation rate of nearby trajectories in the flow we therefore expect the stable manifold to appear as a line of high stretching values. Similarly, on unstable manifolds, nearby trajectories separate exponentially fast if the flow is integrated in backward time. Hence, the separation rate of nearby trajectories, can be used to estimate the positions of stable and unstable manifolds in unsteady flows.

4.5 Finite-time Lyapunov Exponents

The Lyapunov exponent is a classical measure to quantify the sensibility of a dynamical system to initial conditions [Arrowsmith and Place, 1990, Baker et al., 1996, Ott, 2002]. A simple definition is

$$\lambda = \lim_{t\to\inf} \lim_{\delta(0)\to 0} \frac{1}{t} \log \frac{\delta(t)}{\delta(0)} \tag{4.13}$$

Here $\delta(0)$ is the initial perturbation to a given trajectory and $\delta(t)$ is the grown perturbation at time t. The orientation of the initial perturbation rapidly aligns with the direction of maximum stretching. In chaotic flows initially close trajectories separate exponentially fast, such that a positive Lyapunov exponent indicates chaotic behavior, while in regular flows the Lyapunov exponent is zero.

The Lyapunov exponent is an asymptotic measure. In order to quantify the stretching of fluid parcels during a finite time interval, the Lyapunov exponent is modified to a finite-time version, the finite-time Lyapunov exponent (FTLE):

$$\lambda(t_0, \tau) = \frac{1}{\tau} \log \frac{\delta(t_0 + \tau)}{\delta(t_0)} \tag{4.14}$$

This quantity measures the average exponential separation rate of trajectories with an initial distance $\delta(t_0)$ over a time period τ, assuming that the distance grows as:

$$\delta(t) = \delta(t_0) e^{(\lambda t)} \tag{4.15}$$

This is a rather intuitive definition of FTLEs. A definition related to the deformation of the fluid is given in the following paragraph, this later is useful to compute FTLE fields in a flow.

FTLE computation from flow map As the FTLE is sensitive to initial conditions, we integrate trajectories in a velocity field starting from a grid of initial positions $x_0(t_0)$ at time t_0. After the finite-time τ, the trajectories reach the positions

$x(t_0+\tau)$. The initial positions x_0 can be mapped to the final positions $x(t+\tau)$ by the operator $F_{t_0}^{t_0+\tau}$, called the flow map, such that

$$x(t_0+\tau) = F_{t_0}^{t_0+\tau}(x_0(t_0)) \tag{4.16}$$

In linear approximation, an infinitesimal perturbation vector $\delta x_0(t)$ to a trajectory starting at x_0 is deformed by the flow as

$$\begin{aligned} x(t_0+\tau) &\approx \nabla[F_{t_0}^{t_0+\tau}(x_0)]\delta x_0(t) \\ &= \nabla[x(t_0+\tau)]\delta x_0(t) \end{aligned} \tag{4.17}$$

Hence, we have to differentiate the final positions $x(t_0+\tau)$ with respect to x_0 to obtain the deformation tensor

$$\nabla F_{t_0}^{t_0+\tau}(x_0) = \nabla[x(t_0+\tau)] = \begin{bmatrix} \frac{\partial x}{\partial x_0} & \frac{\partial x}{\partial y_0} \\ \frac{\partial y}{\partial x_0} & \frac{\partial y}{\partial y_0} \end{bmatrix} \tag{4.18}$$

We are interested in the stretching of the perturbation vector. Its norm is given by the inner product

$$\begin{aligned} \|\delta x(t_0+\tau)\| &= \langle\, \delta x_0, \nabla F(x_0)^T \nabla F(x_0)\delta x_0 \rangle^{\frac{1}{2}} \\ &= \langle\, \delta x_0, C(x_0)\delta x_0 \rangle^{\frac{1}{2}} \end{aligned} \tag{4.19}$$

with the right Cauchy-Green deformation tensor $C(x_0)$. By definition $C(x_0)$ is a symmetric tensor and has real eigenvalues. The factor of maximal stretching $S(x_0)$ of the length of the perturbation $\delta x_0(t)$ under the flow map $F_{t_0}^{t_0+\tau}$ is given by

$$S(x_0) = \left[\max_{i=1,N} \lambda_i(C(x_0))\right]^{\frac{1}{2}} \tag{4.20}$$

where λ_i are the eigenvalues of $C(x_0)$. Finally, the field of finite-time Lyapunov exponents (FTLE) depending on initial conditions (x_0, t_0) and on the finite integration

time τ is then

$$\sigma(x_0, t_0, \tau) = \frac{1}{\tau} \log(S(x_0)) \tag{4.21}$$

We obtain the forward FTLE field by taking $\tau > 0$ and integrating the velocity forward in time, while for the backward FTLE field the negative velocity field is integrated backward in time with $\tau < 0$. The backward FTLE field is denoted by $\sigma^-(x_0, t_0, \tau)$ and the forward FTLE field is denoted by $\sigma^+(x_0, t_0, \tau)$. The forward FTLE field reveals the strong stretching along stable hyperbolic manifolds and the backward FTLE field reveals the unstable manifolds, where fluid converges in forward time.

Choice of the Finite Integration Time For the computation of FTLE fields the integration time τ must be predefined. Basically, the time τ has to be long enough to allow trajectories to explore the Lagrangian coherent structures present in the flow. A typical time scale in the flow is the eddy turnover time. If a multiple of the eddy turnover time is used as an integration time, clear linear structures will appear in the FTLEs field. However, a small increase of the integration time above typical time scales in the flow would generate new detailed structures in the FTLEs field, nevertheless, the main structures in the FTLE field remain the same.

LCS as Ridges in the FTLE Field [Shadden et al., 2005] defines LCSs as ridges of high values in the FTLE fields. Ridges are given by lines of local maxima of the FTLE field and a criterion can be formulated using the Hessian matrix and the gradient of $\lambda(x_0, t_0, \tau)$. A sharp ridge is characterized by high negative eigenvalues ε of the Hessian matrix. For points on the ridge, the gradient $\nabla\lambda(x_0, t_0, \tau)$ is tangent to the ridge line and perpendicular to the eigenvector ε_{min} corresponding to the smallest eigenvalues ε_{min} of the Hessian, which leads to the condition

$$\Psi = \varepsilon_{min} \nabla\lambda(x_0, t_0, \tau) = 0 \tag{4.22}$$

Ridges are extracted as zero contour lines of the field Ψ. We show in Fig.4-2 backward and forward FTLE ridge computed over gulf of Mexico, attracting LCSs in blue color while red presents repelling ones.

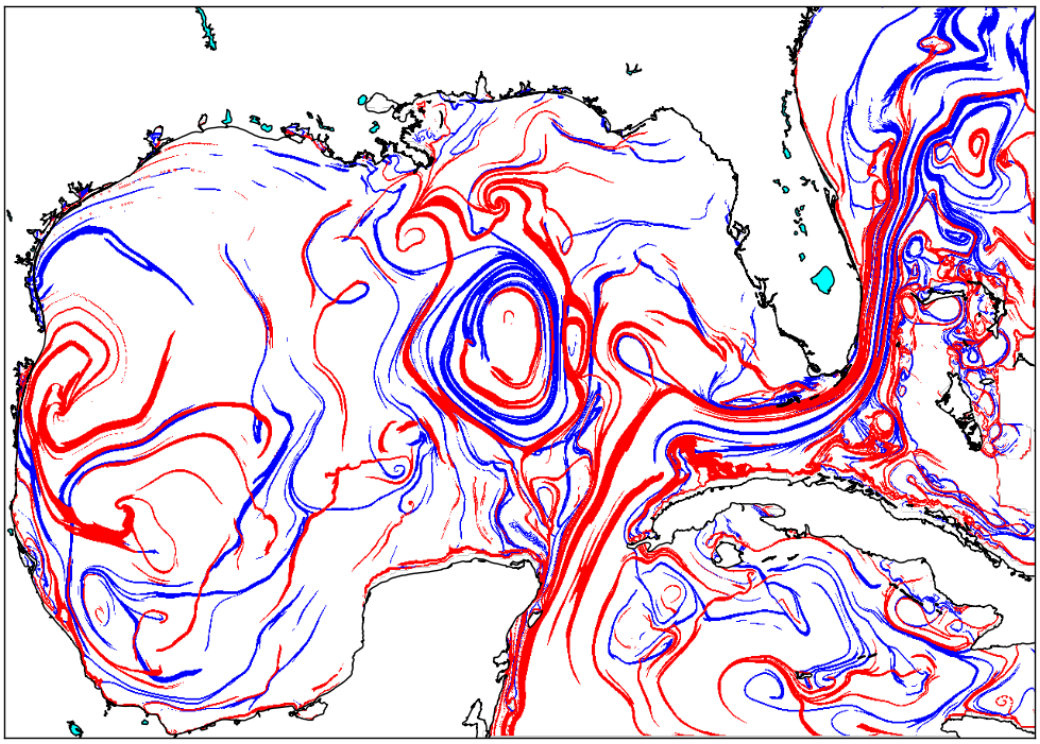

Figure 4-2: Attracting (blue) and repelling (red) LCSs as ridges of high values in the FTLE fields.

4.6 Finite-size Lyapunov Exponents

An alternative assessment of perturbation growth in the flow is provided by the Finite-Size Lyapunov exponent (FSLE). It is also used to extract mixing patterns in unsteady flows [Artale et al., 1997, d'Ovidio et al., 2004, Haza et al., 2010], but instead of fixing a finite time and evaluating the deformation of the fluid after that time, a finite length scale of typical flow structures r is predefined. To define this quantity, we first select an initial separation $\delta_0 > 0$ and a separation factor $r > 1$ of interest. The separation time $\tau(x_0; \delta_0, r)$ is then defined as the minimal time in which the distance between a trajectory starting from x_0 and some neighboring trajectory

starting δ_0-close to x_0 first reaches $r\delta_0$. The FSLE associated with the location x_0 is then defined as [Joseph and Legras, 2002, Aurell et al., 1997, Artale et al., 1997]:

$$\Lambda(x_0; \delta_0, r_0) = \frac{\log r}{\tau(x_0; \delta_0, r)} \tag{4.23}$$

For the computation a small factor r close to unity is chosen, such that $\Lambda(\delta)$ is independent of r. Although r is smaller than 2, it is often called the doubling factor. Many studies make the choice $r = \sqrt{2}$.

Typically, when the integration is stopped after a reasonable time, only a small part of the trajectory pairs have reached the predefined separation. The initial positions of trajectories with the strongest separation rate are located on lines being estimates for the stable manifolds of the unsteady flow. The structure of these lines resembles the structure of ridges of the FTLE field. However, opposed to the FTLE, the FSLE field focuses on separation scales exceeding the threshold r, thus, it can be used for selective structure detection. A further advantage of the FSLE field is that its computation requires no a priory choice of advection time.

By analogy with FTLE ridges, FSLE ridges have also been proposed as indicators of hyperbolic LCSs (see Refs. [Joseph and Legras, 2002, d'Ovidio et al., 2004, Bettencourt et al., 2013]). This analogy is mathematically justified for sharp enough FSLE ridges of nearly constant height. A general correspondence between FSLE and FTLE ridges, however, does not exist [Karrasch and Haller, 2013]. This is because $\Lambda(x_0; \delta_0, r)$ lumps trajectory separation events occurring over different time intervals into the same scalar field, and hence has no general relationship to the single finite-time flow map $F_{t_0}^{t}(x_0)$.

4.7 Other approaches for LCS detection

In order to characterize regions of different mixing patterns in a flow, several methods have been proposed that compute scalar fields from properties of trajectories. These quantities change unexpectedly across stable or unstable manifolds which can be visualized by these methods. Mendoza and Mancho [Mendoza and Mancho, 2010] propose

the arc-length of finite-time trajectories as a scalar field of Lagrangian property that reveals the geometry of transport. In these fields, stable and unstable manifolds appear as thin lines of small values. Since this measure can be interpreted as the Lagrangian velocity averaged along the trajectory, it also serves to distinguish regions of fast trajectories (jet cores) and slow trajectories (vortex cores). [Rypina et al., 2011] use two measures that quantify the complexity of trajectories. These measures are directly linked to the fractal dimension of the trajectory, where the least complex trajectory is a stationary point, and the most complex trajectory is one that fills the whole domain.

Very recent approach was published by Haller [Haller and Beron-Vera, 2012] which aim to find transport barriers in aperiodic two-dimensional flows. With this theory the transport barriers are obtained as hyperstreamlines of the Cauchy-Green strain tensor, whose normal repulsion rate is larger than tangential stretch over backward/forward time intervals. This is a big advantage over methods like the FTLE, where the approximate transport barriers have to be extracted as trenches or ridges in a scalar field. With the new theory it seems to be possible to extract very accurately hyperbolic transport barriers associated with hyperbolic stable and unstable manifolds transport barriers associated with lines of minimal stretching [Haller and Beron-Vera, 2012].

Chapter 5

Surface Mixing and Biological Activity in the North-West African Upwelling

Abstract

Near-shore water along the North-West African margin is one of the world's major upwelling regions. It is associated with physical structures of oceanic fronts which influence the biological productivity. The study of these coherent structures in connection with chlorophyll concentration data is of fundamental importance for understanding the spatial distributions of the plankton. In this chapter, I study the horizontal stirring and mixing in different upwelling areas using Lagrangian coherent structures (LCSs). These LCSs are calculated using the recent geodesic theory of LCSs. I use these LCSs to study the link between the chlorophyll fronts concentrations and surface mixing, based on 10 years of satellite data. These LCSs move with the flow as material lines, thus the horizontal mixing is calculated from the intersection of these LCSs with the finite time Lyapunov exponents (FTLEs) maps. I compare my results with those of a recent study conducted over the same area, but based on Finite Size Lyapunov Exponents (FSLEs) whose output is a plot of scalar distributions [Rossi et al., 2008]. I discuss the differences between FSLE and geodesic theory of LCS. The latter yields analytical solutions of LCSs, while FSLEs can only provide LCSs for sharp enough ridges of nearly constant height.

5.1 Introduction

Oceanography of North-West Upwelling system is forced by the equatorward trade winds [Carr and Kearns, 2003, Benazzouz et al., 2014b]. Wind-driven currents associated with equatorward trade winds are known to exhibit mesoscales instabilities [Allen, 1980, Stommel, 1948]; thus, in addition to upwelled cold intermediate water, significant energy is transferred into submesoscale fronts and vortices in the upper ocean [Capet et al., 2008b, Capet et al., 2008c]. These submesoscale coherent structures arise out of surface frontogenesis; such frontogenesis grows off from upwelled cold filaments that are pulled offshore [Capet et al., 2008a]. Associated with this phenomenon are large vertical vortices and material exchanges between the surface boundary layer and pycnocline [Capet et al., 2008a]. The north-easterly winds not only drive the coastal sea surface temperature through upwelling but are also responsible for inducing the coastal baroclinic upwelling jet. This jet develops in the coastal transition zone (CTZ), located between the shelf and interior oceans [Barton, 1998], and enables communication between adjacent latitudinal upwelling regions [Benazzouz et al., 2014c]. The jet constitutes the actual boundary condition of the subtropical gyre; it can be considered as the easternmost branch of the southward Canary Current, and has been named the Canary Upwelling Current (CUC) [Pelegrí et al., 2005a, Pelegrí et al., 2005b].

Eastern Boundary Upwelling zones include some of the most productive ecosystems in the world [Chavez and Messié, 2009, Carr and Kearns, 2003, Arístegui et al., 2009], particularly the North-West African upwelling which presents one of the world's major upwelling regions. North-West African upwelling is characterized by persistent and variable Upwelling phenomenon almost all around the year [Mittelstaedt, 1983]. Although it represents a small portion of the world's ocean surface, it is considered as one of the most productive regions of the world [Pauly and Christensen, 1995, Ryther, 1969, Fréon et al., 2009, Cushing, 1971] due to its high biological productivity and its impact on commercial fisheries.

Mesoscales filaments and eddies structures are omnipresent in the North-West

African upwelling, they interact with the complex spatial distribution of phytoplankton. These physical oceanic structures are known to affect the plankton community [Mackas et al., 2005, Owen, 1981, Kang et al., 2004]. Indeed, they modulate the biomasses [McGillicuddy Jr et al., 1998, Oschlies and Garcon, 1998] and play an important role in cross-shelf exchanges of water masses [Shanks and Brink, 2005, Dinniman et al., 2003]. Moreover, their manuring role in transporting organic matter to the open ocean has been evidenced [Moore et al., 2007]. The study of these physical oceanic structures and their links with chlorophyll distribution are recognized as a major scientific challenge [Rossi et al., 2008, Rossi et al., 2009, Marchesiello and Estrade, 2009].

Much of oceanic transport is associated with coherent structures [Bettencourt et al., 2017]. The development of Lagrangian diagnostics of transport is firmly gaining ground in the recent literature [Haller, 2015, Haller and Sapsis, 2011, Haller, 2005]. Such approaches come from the field of nonlinear dynamics. They are powerful tools for the identification and the analysis of oceanic transport, since they can be used to extract transport structures underlying raw Eulerian velocity data. Finite Size Lyapunov Exponents (FSLEs) are widely used in the oceanographic community, mainly for their ability to reveal and display oceanic structures that strongly organize fluid motion in the ocean; they are also used to characterize transport in closed areas and are easy to compute [Károlyi et al., 2010]. However, recent mathematically formulated Lagrangian descriptors have also found their place in the oceanographic community. [Haller and Beron-Vera, 2013] introduces a variational principle for coherent material vortices which was applied on eddies. This method was used to study the coherent water transport off the Agulas region [Wang et al., 2015]. The mathematical methods were also used to study the life cycle of a coherent Lagrangian Agulhas ring [Wang et al., 2016]. [Olascoaga et al., 2013] found that drifter motion in the Gulf of Mexico is constrained by altimetric Lagrangian coherent structures. [Beron-Vera et al., 2018] use these Lagrangian methods to illustrate the emergence of coherent Lagrangian swirls among submesoscale motions in the ocean. They were also used to cover the edge of the polar vortex [Serra et al., 2017].

In this chapter, we investigate the relations between horizontal mixing/stirring activity and chlorophyll concentration (considered as a proxy for biological processes). While previous studies analyze the temporal surface mixing and stirring activity using (FSLEs/FTLEs) [Rossi et al., 2008, Rossi et al., 2009, d'Ovidio et al., 2004, Waugh et al., 2012, Lehahn et al., 2007, Lu and Speer, 2010, Bettencourt et al., 2012, d'Ovidio et al., 2009, Kai et al., 2009, d'Ovidio et al., 2010], we address the problem of characterizing mixing and stirring activity, using a recent geodesic theory that allows the localization of coherent structures from mathematically formulated coherence principles [Haller, 2015, Farazmand et al., 2014]. We conduct an experimental study using 10 years of remotely sensed data for the period of time $[2000 - 2010]$; we make use of MODIS weekly chlorophyll datasets and daily interpolated velocity data derived from altimetry. We show that the use of this advanced mathematical formulation of coherence principles shed new light on previous studies about the relationships between mixing and chlorophyll.

This chapter is organized as follows: section II introduces the data and the area of study used throughout this chapter. In section III we describe the methods used for Lagrangian Coherence Structures (LCS) calculation and chlorophyll front extraction. Section IV is devoted a presentation of experimental results. In Section V, we discuss and compare our results with state of the art. We conclude in section VI.

5.2 Area of study and dataset

5.2.1 Area of study

Our work mainly focuses on zones of exchange processes between the shelf and the open ocean. Through these mesoscale processes, filament structures contribute to the offshore export of organic matter; these filament structures play consequently a fertilizing role of the adjacent oligotrophic ocean [Shanks and Brink, 2005, Álvarez-Salgado, 2007]. Recent work has suggested that filaments are responsible for greater offshore transport of carbon [Álvarez-Salgado, 2007, Cravo et al., 2010, García-Muñoz

et al., 2005].

Our study focuses on the North-West African Upwelling. We show in Fig.5-2 a space-time Hovmoller plot of the seasonal and interannual variability over this region of: a) the chlorophyll extension (calculated as the $0.5mg \times m^{-3}$ limit), b) the average chlorophyll concentration (over each latitudinal step within the $0.5mg \times m^{-3}$ limit) ,c) the chlorophyll index defined as the chlorophyll average multiplied by its extension, d) the eddy kinetic energy (EKE) as it is estimated from sea level anomalies from the merged mapped product AVISO using measures of Topex-Poseidon and ERS during the period 2003-2010. The Hovmoller plots show a high spatio-temporal definition of the patterns of upwelling variability in term of extension, intensity and EKE, with well defined seasonal transitions, generally associated to Capes (Cape Ghir, Cape Juby/Cape Bojdor, Cape Blanc and Cape Verde). EKE is the energy associated with fluctuations in the currents, and is a direct measure of the variability associated with eddies. Progressing south, EKE clearly increases alongshore from $0.75m^2/s^2$ $(17°N)$ to $1m^2/s^2$ $(12°N - 15°N)$. The values of EKE in the central part of the system are among the largest in the north-west African region, corresponding to high chlorophyll index, extension and average. This is principally associated with the southward propagation of large mesoscales structures, in addition to oceanic turbulence. In this work [**El Aouni** et al., 2019, El Aouni et al., 2018d], we mainly consider four regions with particular hydrodynamical process have been considered according to the intensity and seasonal upwelling variability and the mesoscales structures activities as depicted from satellite data and modeling approach. These four regions are listed as follows:

- 1) Cape Ghir (red box in Fig.5-1) located between $(9.°W, 29.97°N$ and $13.21°W, 32.56°N)$ where the upwelling occurs during summer [Benazzouz et al., 2014b].
- 2) The region between Cape Juby and Cape Bojador (blue box in Fig.5-1) located between $(11.91°W, 26.30°$ and $16.81°W, 28.°N)$ where maximum filament intensity occurs [Nieto et al., 2012].
- 3) The region between the latitudes $(15.23°W, 19.06°$ and $20.35°W, 22.43°N)$ (orange box in Fig.5-1) where the giant filament of Cape Blanco appears up to

$450km$ of extension [Marcello et al., 2011].

- 4) The region with winter upwelling [Benazzouz et al., 2014b] around Cape Verde (green box in Fig.5-1), located between ($15.21°W, 13.26°$ and $20.51°W, 15.87°N$).

Fig.5-1 shows these areas delimited by colorful boxes. We use the full geographical area shown in Fig.5-1 for the numerical computations of the Lagrangian Coherent Structures, considering the fact that particles may get advected out of the analysis areas.

5.2.2 Data

Velocity field

We use global weekly $1/4°$ ($25km$) resolution products of surface currents[1] , obtained from the Copernicus Marine Environment Monitoring Service (CMEMS[2]) and corresponding to the period of time between March 2000 to March 2010. Velocity data is derived from satellite acquired surface height (altimetry) under the geostrophic approximation, in which the sea surface height $\eta(\phi, \theta, t)$ serves as a non-canonical Hamiltonian for surface velocities in the longitude/latitude (ϕ, θ) coordinate system [Strub and James, 2000]. From these data, daily surface currents are generated with a $0.01°$ of spatial resolution using temporal linear interpolation [Haller et al., 2016, Rossi et al., 2009].

Chlorophyll Data

Weekly level 3 of chlorophyll product are obtained from MODIS (Moderate Resolution Imaging Spectroradiometer) instrument operating on board the polar-orbiting Terra spacecraft. These data are generated by the NASA Goddard Earth Science (GES) and obtained from the NASA's Oceancolor website[3] with a spatial resolution of $4 \times 4km$.

[1]The surface geostrophic velocities of the products we use, are the same as the ones produced by Ssalto/duacs multimission sea level products provided by CLS/Archiving, Validation, and Interpretation of Satellite Oceanographic data (AVISO), with support from CNES (http://www.aviso.oceanobs.com/duacs/).

[2]http://marine.copernicus.eu/

[3]https://oceancolor.gsfc.nasa.gov/

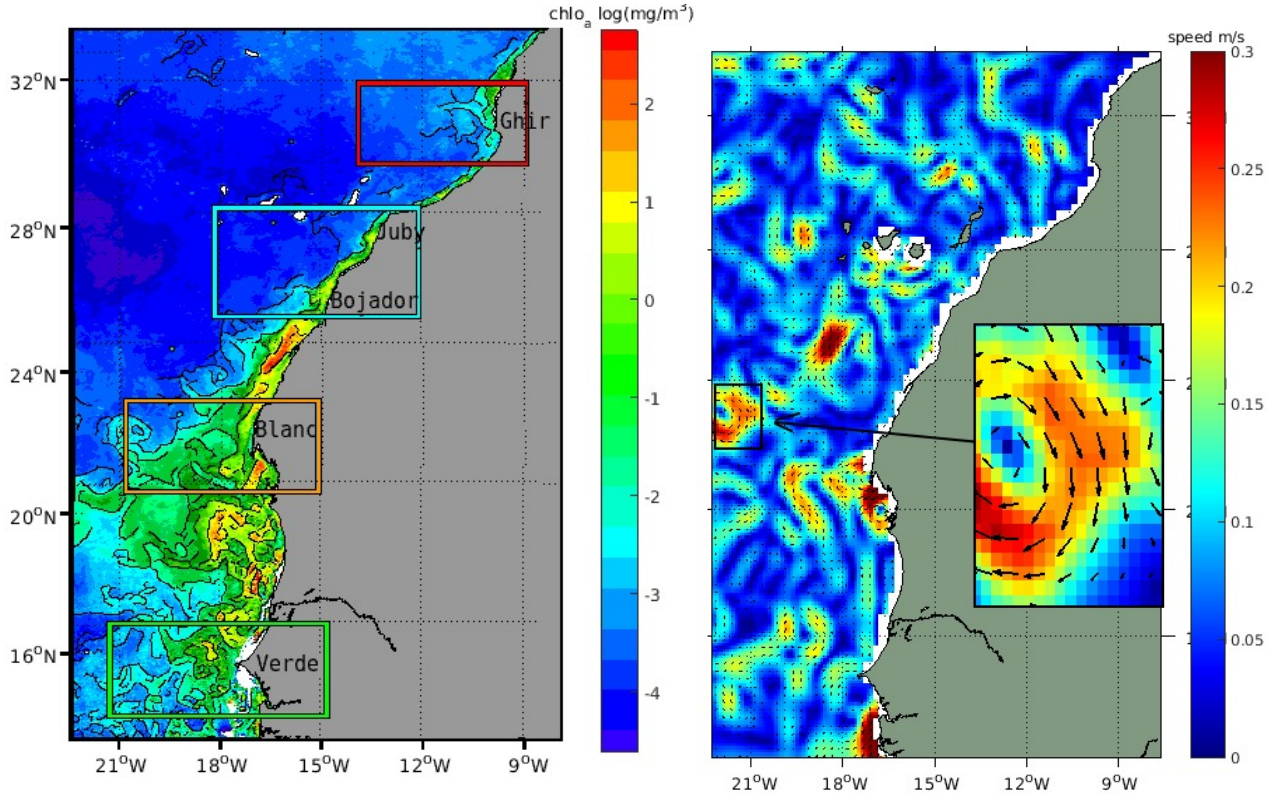

(a) (b)

Figure 5-1: a) Chlorophyll image with MSM fronts overlaid on top, b) Surface velocity and direction. Both at the same date (01-March-2003).

The data used in this study correspond to the period of time between March 2000 to March 2010 (10 years).

5.3 Method

The basic ingredients of our study are satellite data of chlorophyll concentration and ocean surface velocity field. We quantify the horizontal mixing processes based on the geodesic theory of Lagrangian Coherent structures [Haller, 2015, Farazmand et al., 2014, Haller and Beron-Vera, 2013]. This theory is a collection of global variational principles for material surfaces that form the centerpieces of coherent, time-evolving tracer patterns [Haller, 2015]. Hyperbolic LCSs act as repelling or attracting neighboring material elements with locally the highest rate over a given finite-time interval. Parabolic LCSs serve as generalized jet cores. Elliptic LCSs serve

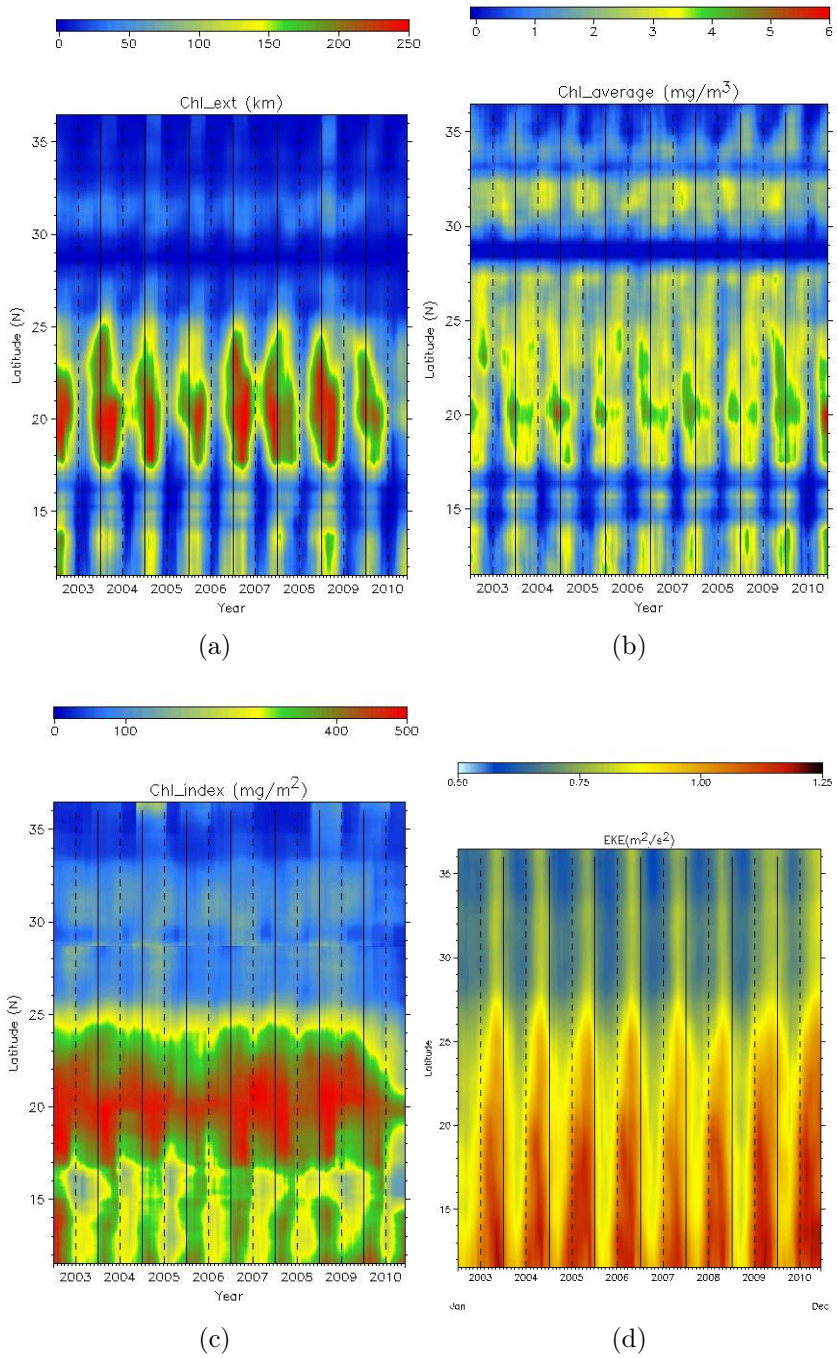

Figure 5-2: Space-time Hovmoller plot of the seasonal and interannual variability a) Upwelling extension (Chl_{ext}) calculated as $0.5mg \times m^{-3}$ limit, b) Chlorophyll averaged over the Upwelling area (Chl_{avg}), c) Upwelling index (Chl_i) computed as the chlorophyll average multiplied by its extension, d) the eddy kinetic energy (EKE) calculated for the period of time between [2003-2010].

as generalized coherent vortex boundaries in finite-time unsteady flows. Geodesic LCS theory is objective, and it is expressible through the invariants of the right Cauchy-Green strain tensor. In this work, we calculate surface mixing based on hyperbolic (attracting) and parabolic LCSs as they have a clear interpretation as fronts of passive scalars driven by the flow [d'Ovidio et al., 2004, Rossi et al., 2008, Rossi et al., 2008, Haller, 2015]. More details are given in section 3.2.

Chlorophyll data are acquisitions of a complex natural phenomenon, with missing data and acquisition artifacts. The determination of accurate fronts in such complex natural data is challenging. For that matter, we will make use of advanced complex system approaches based on unpredictability to extract the pixels fronts in the chlorophyll datasets. This is described in the next subsection.

5.3.1 Chlorophyll fronts extraction

Chlorophyll data show coherent structures generated by oceanic turbulence. However, the datasets might contain missing data in the form of a cloud mask. The spatial resolution of chlorophyll data is $4 \times 4km$, corresponding to large submesoscale. The coherent structures acquired at such resolution are the result of cascading processes associated with turbulence [Frisch, 1995]. Consequently, and following the study presented in [Turiel et al., 2008], multiscale signal processing techniques for the extraction of pixels fronts in such data (identified as transition fronts in [Maji and Yahia, 2014]) are more suitable than classical differential operators of image processing. In this study, we determine the pixel fronts through the calculation of singularity exponents in a microcanonical formulation of the Most Singular Manifold (MSM) [Maji and Yahia, 2014]. The singularity exponents $h(\mathbf{x})$ ($\mathbf{x}$ is pixel location) are determined through logarithmic fitting of the chlorophyll signal's gradient.

Denoting r_0 the smallest scale in the signal, μ the measure associated to the signal's gradient, Ψ a positive wavelet and $\mathcal{T}_\Psi \mu(\mathbf{x}, r)$ the wavelet projection of measure μ at

point $\mathbf{x}$ and scale r, a singularity exponents $h(\mathbf{x})$ is computed as:

$$h(\mathbf{x}) = \frac{\log \mathcal{T}_\Psi \mu(\mathbf{x}, r_0) / \langle \mathcal{T}_\Psi \mu(0, r_0) \rangle}{\log r_0} \tag{5.1}$$

$\langle \cdot \rangle$ denoting spatial average.

The MSM is the set

$$\mathcal{E}_{\text{MSM}} = \bigcup_{h_\infty \leq h \leq 0} \mathcal{F}_h \tag{5.2}$$

h_∞ being the minimal singularity exponent, $\mathcal{F}_h$ the set of points $\mathbf{x}$ such that $h(\mathbf{x}) = h$

Practical algorithmic implementation is provided in [Pont et al., 2013, Maji and Yahia, 2014]. Once pixels fronts are extracted and MSM computed, chlorophyll concentration is calculated as the mean spatial average of chlorophyll concentration over the MSM.

5.3.2 Surface Mixing and Stirring

We consider a time-dependent smooth vector field:

$$\mathbf{v}(\mathbf{x}, t), \quad \mathbf{x} \in \mathbb{R}^2, \quad t \in [\alpha, \beta] \tag{5.3}$$

and its associated ordinary differential equation:

$$\dot{\mathbf{x}} = \mathbf{v}(\mathbf{x}, t), \quad \mathbf{x} \in \mathbb{R}^2, \quad t \in [\alpha, \beta] \tag{5.4}$$

Let $\mathbf{F}_{t_0}^t : \mathbb{R}^2 \to \mathbb{R}^2$ be the associated map of the vector field $\mathbf{v}$, i.e the map which takes a particle located at $\mathbf{x}_0$ at time t_0 to its location $\mathbf{x}_t$ at time t:

$$\mathbf{F}_{t_0}^t(\mathbf{x}_0) := \mathbf{x}(t, t_0, \mathbf{x_0}), \quad \alpha \leq t_0 \leq t \leq \beta \tag{5.5}$$

with $t \mapsto \mathbf{x}(t, t_0, \mathbf{x}_0)$ being the unique Lagrangian trajectory of vector field $\mathbf{v}$ which passes through $\mathbf{x}_0$ a time t_0. A common way to quantify the stretching is by means

of the standard Lyapunov exponents such as Finite Size/Time Lyapunov Exponent (FSLE/FTLE). They are defined as the exponential rate of separation of fluid parcels infinitesimally separated at t_0 by infinitesimal perturbation $\delta\mathbf{x}_0$: $|\delta\mathbf{x}(t)| \approx e^{\lambda}\delta\mathbf{x}_0$. However, these exponent outputs are in the form of a scalar field, whose maxima are expected to highlight coherent structures. FSLEs ridges have been proposed as indicators of hyperbolic LCSs [Joseph and Legras, 2002]. However, FSLE approach to LCSs detection is heuristic, and it is mathematically justified only for sharp enough FSLEs ridges of nearly constant height [Karrasch and Haller, 2013]. In our work we calculate the surface mixing and stirring from hyperbolic (attracting) and parabolic LCSs captured by the geodesic theory of LCS [Haller, 2015]

Let $\nabla\mathbf{F}_{t_0}^{t}(\mathbf{x}_0)$ be the Jacobian of $\mathbf{F}_{t_0}^{t}(\mathbf{x}_0)$ at location $\mathbf{x}_0$. Given an infinitesimal spatial perturbation $\delta\mathbf{x}(t_0) \in \mathbb{R}^2$ at time t_0, the evolution of that perturbation is given by:

$$\delta\mathbf{x}(t) = \nabla\mathbf{F}_{t_0}^{t}(\mathbf{x}_0)\delta\mathbf{x}(t_0) \tag{5.6}$$

Let $\mathcal{M}(t_0)$ be a material line defined at time t_0, its image under Lagrangian advection at time t is defined in term of the flow map as $\mathbf{F}_{t_0}^{t}(\mathcal{M}(t_0))$. The perturbations $\delta\mathbf{x}(t)$ are related to the local deformation of $\mathbf{F}_{t_0}^{t}(\mathcal{M}(t_0))$.

Let $\mathbf{C}_{t_0}^{t_f}(\mathbf{x}_0)$ be the Cauchy-Green strain tensor field

$$\mathbf{C}_{t_0}^{t_f}(\mathbf{x}_0) = [\nabla\mathbf{F}_{t_0}^{t_f}(\mathbf{x}_0)]^T\nabla\mathbf{F}_{t_0}^{t_f}(\mathbf{x}_0) \tag{5.7}$$

with t_0 and t_f respectively the initial and final time, T denoting transposition.

$\mathbf{C}_{t_0}^{t_f}(\mathbf{x}_0)$ is a symmetric and positive tensor, consequently it is diagonalizable in an orthogonal basis, hence its eigenvalues $\lambda_i(\mathbf{x}_0)$ and eigenvectors $\boldsymbol{\xi}_i(\mathbf{x}_0)$ $(i = 1, 2)$ satisfy:

$$\mathbf{C}_{t_0}^{t_f}(\mathbf{x}_0)\boldsymbol{\xi}_i(\mathbf{x}_0) = \lambda_i(\mathbf{x}_0)\boldsymbol{\xi}_i(\mathbf{x}_0), \quad |\boldsymbol{\xi}_i(\mathbf{x}_0)| = 1, \quad i = 1, 2,$$
$$0 < \lambda_1(\mathbf{x}_0) < \lambda_2(\mathbf{x}_0), \quad \boldsymbol{\xi}_1(\mathbf{x}_0) \perp \boldsymbol{\xi}_2(\mathbf{x}_0).$$

Moreover, in the case of incompressible flow, we have $\lambda_1(\mathbf{x}_0)\lambda_2(\mathbf{x}_0) = 1$ [Arnol'd, 2013].

Shearless LCSs are a material curves whom average Lagrangian shears show no leading-order variations when comparing them to nearby C^1-close material lines. *Farazmand et al*[Farazmand et al., 2014] show that shearless LCSs coincide with null-geodesics of the metric tensor:

$$D_{t_0}^{t_f} = \frac{1}{2}[C_{t_0}^{t_f}(x_0)\Omega - \Omega C_{t_0}^{t_f}(x_0)], \quad \Omega = \left(\begin{smallmatrix} 0 & -1 \\ 1 & 0 \end{smallmatrix}\right) \tag{5.8}$$

The tensor $D_{t_0}^{t_f}$ is Lorentzian wherever $\lambda_1(x_0) \neq \lambda_2(x_0)$. All null-geodesics of $D_{t_0}^{t_f}$ are found to be trajectories of one of the two line fields.

$$x_0' = \xi_j(x_0), \quad j = 1, 2 \tag{5.9}$$

Stretch lines are defined as trajectories of Eq.5.9 with $j = 2$. Thus, attracting LCSs are special stretch lines that start from local minima of $\lambda_1(x_0)$.

On the other hand, parabolic LCSs, are smooth, alternating chains of shrink and stretch lines that connect tensorline singularities (more details are given in [Farazmand et al., 2014]).

For computing geodesic LCSs, we use the MATLAB code developed in [Onu et al., 2015]. We follow the trajectories of equation (4) for $T = 60$ days using a standard fourth-order Runge-Kutta scheme with an integration time step of $dt = 1$ day. We use trilinear interpolation for the spatiotemporal interpolation of the velocity field. Each point of the material line $\mathcal{M}(t_f)$ contains the separation rate $log(\lambda_2(\mathbf{x}_0, t_0, t_f))$ averaged by a finite time as:

$$\sigma = \frac{1}{2T}\log(\lambda_2(\mathbf{x}_0, t_0, t_f)) \tag{5.10}$$

σ presents the FSLEs field. For each integration time step of $dt = 1$ day, each point of these material lines updates its position and separation rate.

5.3.3 Comparing FSLE to the geodesic theory of LCSs

Finite-Size Lyapunov exponent is considered as a Lagrangian diagnostic scalar fields which has been proposed for material coherence detection in the literature. It is calculated by defining a separation time $\tau(x_0; \delta_0, r)$ as the minimal time in which the distance between a trajectory starting from x_0 and some neighboring trajectory starting δ_0-close to x_0 first reaches $r\delta_0$, with $\delta_0 > 0$ and $r > 1$ are respectively the initial separation and rate of separation. Thus, FSLE is not linked directly to the flow map between times t_0 and t_f. Indeed, its scalar field includes local separation exponents for each initial condition x_0 over a different time interval of length $\tau(x_0; \delta_0, r)$. Thus, it highlights structures arising over different time intervals.

The FSLE ridges as in indicator of LCSs is shown to be heuristic [Hadjighasem et al., 2017], and only justified for sharp enough FSLE ridges of nearly constant height [Karrasch and Haller, 2013]. On the other hand, geodesic theory of LCSs identify the exact location of LCSs.

In term of surface mixing calculation, FSLE leaves several unaddressed issues:

- FSLE's output is a scalar field, when averaging its separation rate over a given area, we are not calculating separation rate of lines of maximum compression but also from other structures that are less of interest in this study. On the other hand, the geodesic theory of LCS guaranties that only lines of maximal convergence are included.

- FSLE structures arise from different time intervals. On the other hand, geodesic theory of LCSs extract LCSs arising over the same time interval which is more convenient and natural when comparing the surface mixing to the chlorophyll concentrations.

5.4 Results

LCSs are computed for each day of the 10 years database presented in section 2.1. Following [Rossi et al., 2009], for each sub-region, we calculate the mixing quantity by

averaging hyperbolic (attracting) and parabolic LCSs over each one of the boxes in Fig.5-1. Fig.5-3 shows an example of these LCSs corresponding to the time t_0=March 01/2000, with time advection $t_f = t_0 - 60$ days.

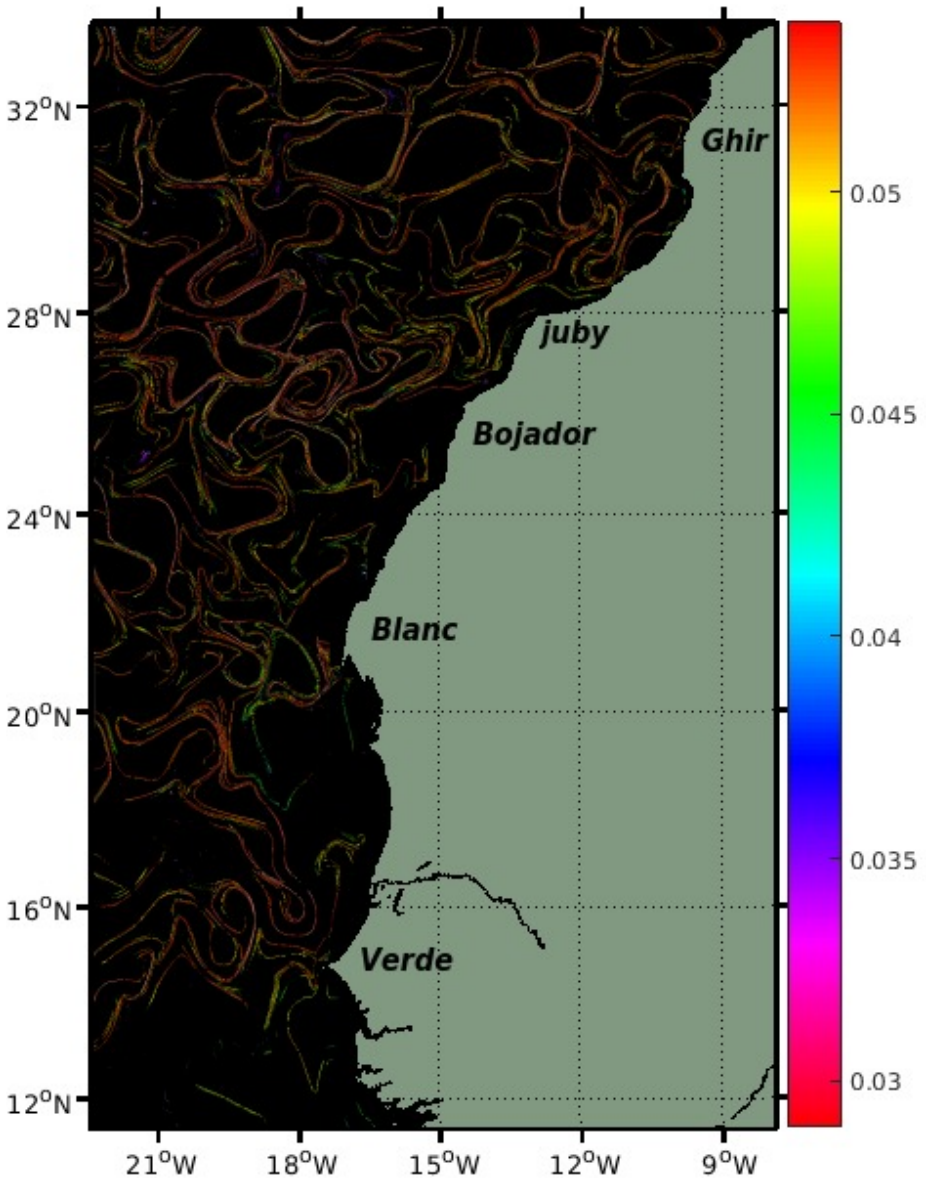

Figure 5-3: Lagrangian Coherent Structures at time t_0=March 01/2000.

5.4.1 Biological Activity: Surface mixing vs Chlorophyll average

We study here the relationship between the horizontal mixing and the chlorophyll fronts concentrations. The determination of fronts is described in subsection 3.1, and we show in Fig. 5-1 (a) the chlorophyll fronts extracted for the date: March 01 2000. We proceed as follows: for each image, pixels fronts are extracted, then for each sub-region we compute the average of chlorophyll concentration over the set of fronts inside its corresponding box.

Fig.5-4 shows on each image the spatial averages of chlorophyll fronts concentration (blue color, range scale on the right) versus the spatial averages of the surface mixing (red color, range scale on the left). It is calculated from hyperbolic (attracting) and parabolic LCSs, during the period from March 01/2000 to March 01/2010.

In Cape Ghir region (red box in Fig.5-1), high chlorophyll concentration takes place during summer for most of the years and decreases at the end of each year. Same remark for surface mixing. Thus, both surface mixing and chlorophyll concentrations tend to have a similar interannual variation. Increase of mixing is followed by increase of chlorophyll except for 2008/2009. The period of [2003 2006] records intensity decrease of both mixing and chlorophyll.

In Cape Verde (green box in Fig.5-1), high mixing intensity takes place during summer for most of the years, while high chlorophyll concentration takes place during winter from 2000 to 2004, then in the summer for the rest of the years. For most of the years, increase of mixing intensity is followed by increase of chlorophyll concentration, especially for the period of [2007 2010]. Thus, both chlorophyll concentrations and mixing show similar variation for the most of the years. We note that both regions are affected by seasonal upwelling, Cape Ghir in summer (red box in Fig.5-1) while Cape Verde in winter (green box in Fig.5-1) following the seasonal movement of the Intertropical Convergence Zone [Wooster et al., 1976].

Cape Blanco (orange box in Fig.5-1) with quasi-permanent upwelling and highest chlorophyll concentrations (over $1.5 mg/m^3$ all over the years) shows no global signif-

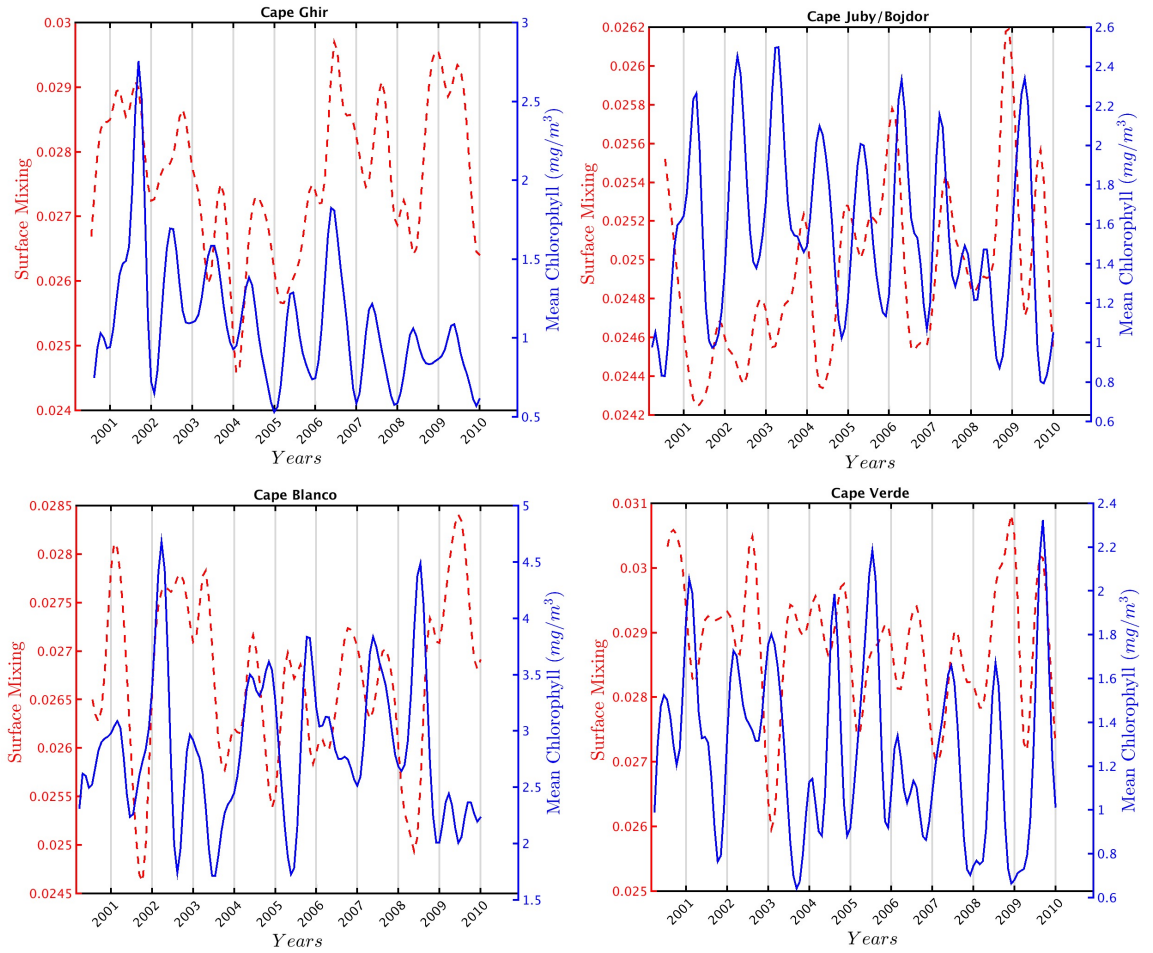

Figure 5-4: Interannual variation of the surface mixing versus the fronts chlorophyll concentrations. Red axis for the mexing and the blue one is for the cholorophyll concentrations (monthly-mean).

icant relation between chlorophyll and surface mixing. In the period of 2000/2002, both chlorophyll and surface mixing tend to be matched, both decrease and increase in similar way, this relation is delayed for the year 2003, and followed by negative relation starting from mid-2004.

The region between Cape Juby and Bojador (blue box in Fig.5-1) exhibits high chlorophyll concentration during summer and decreases at the end of each year. This region records no clear global relation between both chlorophyll and surface mixing. Increase of mixing is followed by decrease of chlorophyll except for the period between mid-2005 and mid-2007.

We have studied 4 areas belonging to the same upwelling ecosystem. These later

show different behaviors, a region with slightly significant correlation ($r = 0.58$) and others with no significant relationship between the surface mixing and the chlorophyll concentrations. We now proceed to analyze the seasonal relationship between these two quantities.

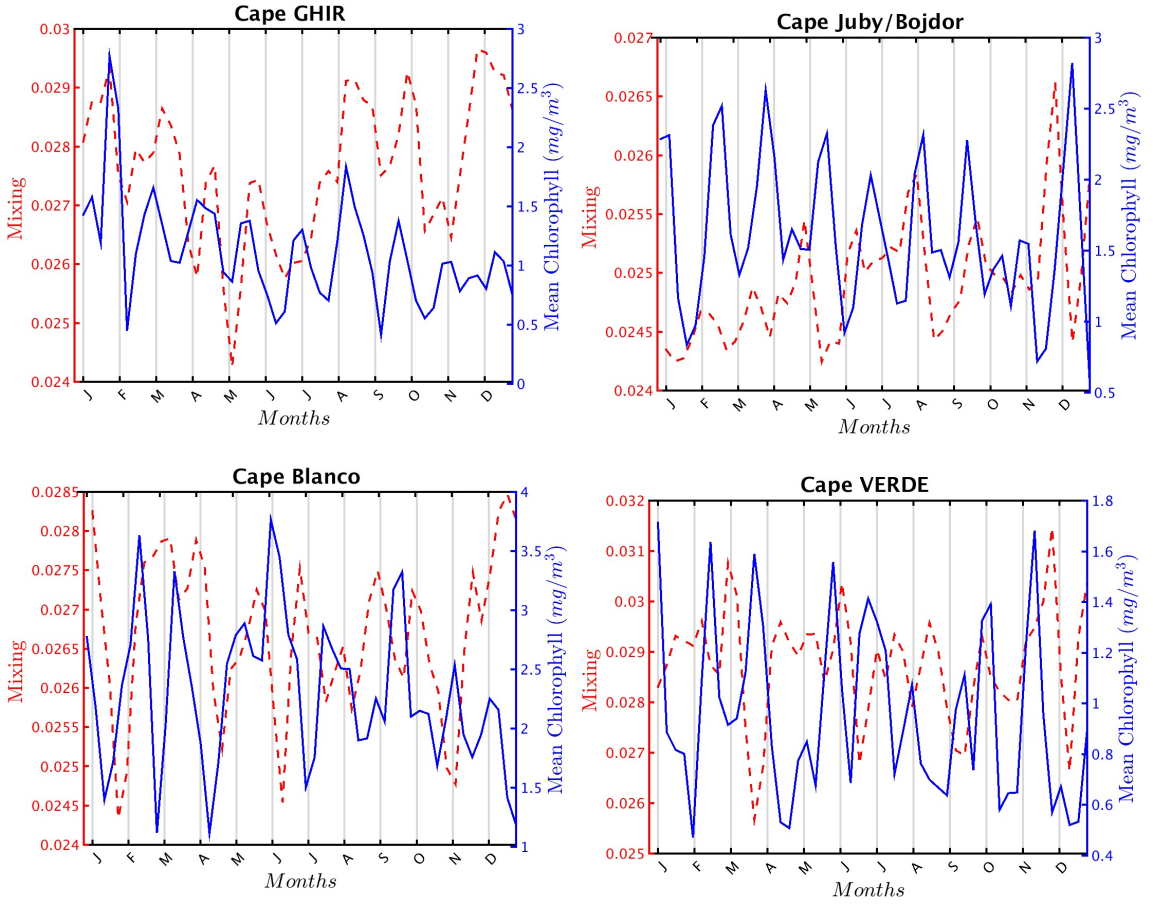

Figure 5-5: Seasonal climatology of the surface mixing versus the fronts chlorophyll concentrations. Red axis for the mixing and the blue one is for the cholorophyll concentrations (monthly-mean).

Fig.5-5 shows on each image the seasonal climatology of chlorophyll fronts concentration (blue color, range scale on the right) versus the seasonal climatology of the mixing calculated from LCSs (red color, range scale on the left). We observe a monthly variation of the front chlorophyll concentration over the four sub-regions, as well as the mixing. Regions of Cape Ghir shows similar variations between chlo-a and mixing for most of the months. This relationship seems to changed for Cape Verde; decreasing of mixing is followed by increasing of chlorophyll concentration for

the most months. Region of Cape Blanco and region between Juby/Bojdor show no clear relation between mixing and cholrophyll concentration for most months.

5.4.2 Biological Activity: Surface mixing vs coastal jet

Along the studied area, the winds change with the season, being upwelling favorable only from late fall to late spring when they oppose the northward flowing Mauritania Current [Castellanos et al., 2013, Nykjær and Van Camp, 1994, Hernández-Guerra and Nykjaer, 1997, Demarcq and FAURE, 2000, Lázaro et al., 2005, Peña-Izquierdo et al., 2012]. Near Cape Blanc, the hydrodynamical process is dominated by intense coastal convergence and offshore export of coastal waters, typically not related to the local wind regime [Pastor et al., 2008, Peña-Izquierdo et al., 2012, Castellanos et al., 2013] which explain the absent relationship between mixing and chlorophyll average in some areas. The north-easterly winds not only drive the coastal upwelling but are also responsible for inducing the coastal baroclinic upwelling jet. This jet develops in the coastal transition zone (CTZ), located between the shelf and interior oceans [Barton et al., 1998], and enables communication between adjacent latitudinal upwelling regions. In some locations, the alongshore jet feeds from the interior eastern boundary ocean: input takes place between the Strait of Gibraltar and Cape Ghir, as the presence of the Strait breaks down the possibility of upstream flow [Pelegrí et al., 2005a, Pelegrí et al., 2006, Mason et al., 2014, Mason et al., 2012], and output occurs at the Cape Verde frontal zone (CVFZ), where the subtropical upwelled waters are diverted offshore as they encounter tropical waters from the south [Pastor et al., 2008, Peña-Izquierdo et al., 2012]. This can widely explain the positive correlation observed in both two areas (Cap Ghir and Cape Verde). The jet constitutes the actual boundary condition of the subtropical gyre and enhance locally the mixing of subsurface layers and consequently enhance biological productivity. Both inertia and upstream conditions introduce temporal and spatial memory to the system [Benazzouz et al., 2014c]. The alongshore wind drives the alongshore coastal jet which, in turns, experiences internal friction and mixing that limits its growth. As the wind ceases or weakens, friction will progressively reduce the alongshore motion, the larger

the momentum (greater inertia) the longer it will take to fully stop. It is the Coriolis force associated with the alongshore jet that induces the offshore and southward motion and mixing. Because of the coastal constraint, this offshore motion creates a cross-shore pressure gradient which opposes the Coriolis force, eventually limiting the size of the cross-shore transport; the cross-shore motion will only decrease when the alongshore jet weakens. The alongshore motion is influenced by the recent history of local forcing but it is also affected by what was taking place sometime before in the neighboring areas [Benazzouz et al., 2014a]. As a consequence, the areas under consideration display different behaviors with slightly significant correlation (Cap Ghir and Cap Verde) and others with no significant correlation between the surface mixing and the chlorophyll concentrations (Cap Juby-Cap Blanc). Thus, a further study is needed to explore the relations between chlorophyll concentrations separately with attracting LCSs repelling LCSs taking into account the importance of connections between adjacent coastal regions and between the coastal and offshore oceans. Last but not least, the upwelling vertical structure will decrease only if the winds cease all along the coast for a sufficient amount of time. Some of these ideas were endorsed by [Gill and Clarke, 1974] when they stated that upwelling depends *"not just on local forcing"* but on the forcing that the flow experienced *"at earlier times as it moved along the coast to the region under consideration."* [Gill and Clarke, 1974] were thinking about propagating waves but the same is true for the geostrophic coastal jet.

5.5 Discussion

Hyperbolic (attracting) and parabolic LCSs, computed over 10 years from satellite velocity data derived from altimetry, allowed us to compute surface mixing and stirring of four majors areas of the North-West African Upwelling Ecosystem. According to previous studies [Falkowski et al., 1991, Benitez-Nelson et al., 2007, McGillicuddy Jr et al., 1998], meso and sub-mesoscale processes can enhance biological production in the ocean. The effect of these oceanic structures enhancing biological produc-

tivity is thought to be more pronounced in low-nutrient environments [Oschlies and Garcon, 1998, McGillicuddy et al., 2007]. This idea of mesoscale structures generally enhancing biological productivity has been challenged by new studies suggesting that these oceanic structures could reduce primary production in the Eastern Boundary Upwelling Systems (EBUS) [Rossi et al., 2008, Rossi et al., 2009, Gruber et al., 2011]. This suggestion emerged from analyzing the correlation between surface mixing calculated using FSLEs, and chlorophyll concentration taken as proxy of biological productivity.

In our work, we focused on the North-West African Upwelling. Our approach to studying the links between biological productivity and surface mixing is different from the previous ones. Instead of using the whole system as in [Rossi et al., 2009], we choose to divide the system into sub-regions with different upwelling properties. Our approach to calculate surface mixing differs as well from previous studies; indeed our mixing calculation is based on a mathematically formulated theory which gives the exact location of Lagrangian coherent structures. Moreover, based on the following considerations:

- There is an increasing evidence suggesting that the distribution of species at different trophic levels is influenced by this oceanic structures; most of this evidence is related to phytoplankton community [Lehahn et al., 2007, d'Ovidio et al., 2010].

- Marine top predators are related to mesoscale fronts as well; [Kai et al., 2009, De Monte et al., 2012] provides evidence that top predators such us seabirds track precisely these oceanic structures to locate food patches.

Thus, we choose to calculate the chlorophyll concentration only over fronts extracted from chlorophyll maps.

In this work we found that Cape Ghir which is characterized by seasonal upwelling, exhibits positive correlation between the mixing activity and the chlorophyll concentrations; this finding is in line with the suggestion of mesoscale processes enhancing biological productivity [Oschlies and Garcon, 1998, McGillicuddy et al., 2007]. But

our work challenges the finding of reducing effect due to mesoscale structures [Rossi et al., 2009]. On the other hand, [Gruber et al., 2011] find negative correlation between eddy-kinetic energy (EKE) and net primary production in the EBUS systems; this negative correlation becomes less significant in most of the EBUS systems when they are analyzed separately. We must note that here, our sub-regions we have tightened our studied areas to associate each area of study with specific upwelling properties (upwelling seasonality). Thus, this could explain the positive correlation found in Cape Ghir, and raise the question about how reliable is studying this relationship over the whole system at once. Another factor which may explain these results is the method used to calculate the mixing; only detects line of maximal compression; contrary to the FTLEs which produce scalar field that contains separation of maximal compressing lines and other structures of less interest. Thus, the key to understand our results may lies in vertical movement: as shown in [Lehahn et al., 2007], lines of high FSLE are more precisely located close to the vertical motions associated with eddies. [Rossi et al., 2008] found that regions of high FSLE indicate occurrence of vertical movements which weakens and decreases nutrients toward the surface. On the other hand, and unlike the previous studies, no significant relationship between surface mixing and chlorophyll concentration is recorded in the other regions of the studied area. An explanation to this could be the upwelling seasonality; Region of Cape blanco, Cape Juby and Bojador are affected by quasi-permanent upwelling due to the trade winds which affect these regions most of the year [Benazzouz et al., 2014b], resulting in Ekman drift associated with vertical movements which dominates over other mesoscale structures; thus, nutrients of upwelled deeper water are important for sea surface fertilization in these areas.

5.6 Conclusion

In this chapter, we have used 10 years of remotely sensed velocity field derived from altimetry and chlorophyll concentrations to address the problem of the relationships between surface mixing and chlorophyll concentrations. Averaged Chlorophyll concen-

tration is calculated from the Most Singular Manifold computed in a microcanonical formulation for fronts extraction. We have used, for the first time for this type of problem, the mathematically formulated geodesic theory of LCSs to address stirring and mixing process. Our results shed new light on the previous studies addressing mixing using FSLEs. Consequently, further work should investigate the relationship found in this upwelling ecosystem systems when examining LCSs versus production. However, the distributions of plankton community in interplay between the nonlinear processes of plankton ecology and their turbulent medium are complex. This study is in the wake of understanding the complex behaviors of the plankton community.

Chapter 6

Defining coherent vortices from particles trajectories

Abstract

In this chapter, I study the transport properties of mesoscale eddies (i.e. vortices of 100 $\sim$ 200 kms in diameter) over a finite time duration. While these oceanic structures are well known to stir and mix surrounding water masses by their swirling motion, they can also carry and transport organic matter as coherent structures. In this chapter, I am interested in dynamic transport properties of these coherent structures, which have chaotic and mixing properties on large time scales. Present techniques to analyze fluid coherent vortices rely on classical geometric theory of the Cauchy-Green's invariants; vortices are related to closed orbits of their field. Others define coherent vortices from vorticity, by calculating its averaged deviation. In this chapter, I take a very different approach, based on a rigorous analysis of particles trajectories. My method identifies coherent vortices and their centers in automatic manner. I illustrate my new method on several two-dimensional flows.

6.1 Introduction

Lagrangian coherent structures (LCSs) are exceptional material surfaces that shape finite-time observed tracer patterns in fluid flows [Peacock and Haller, 2013]. Tracer patterns in the ocean, such as sea surface temperature, chlorophyll concentration and salinity suggest the emergence of coherence even in the ocean, typically with fluxes dominated by advective transport over diffusion. Mesoscale eddies are known

to govern advective transport in the ocean, with typical horizontal scales $\mathcal{O}(100kms)$ and timescales of $\mathcal{O}(weeks)$. These oceanic structures are omnipresent in the ocean and usually exhibit different properties to their surroundings. They are known to stir and mix surroundings water masses as well as by their ability to trap and carry fluid properties in coherent manner. For example, long-lived propagating eddies such as Agulhas eddies are known to transport water properties associated with the Indian ocean far into the South Atlantic [Ruijter et al., 1999]. In this work, we focus on those that remain coherent despite the chaotic nature of their environment. These mesoscale eddies are also known by their important role in climate change, which arises from their influence on the circulation by transporting temperature and salinity, extracting potential energy from the mean flow and exchanging momentum with it. They are also known to help to maintain the extra-tropical climate by contributing to the meridional transport of heat from the tropics to the poles [Farneti et al., 2010].

As the effect of these mesoscale eddies on the global circulation is remarkable, the systematic and accurate detection of eddies has received considerable interest over the last two decades [Karrasch et al., 2015, Froyland et al., 2010, Haller and Beron-Vera, 2013, Haller et al., 2016]. In the literature, several definitions of vortices have been introduced together with their automatic detection [Zhang et al., 2014, Sahner et al., 2007, Herrmann, 2005], most of these formulations are of Eulerian nature. These latter's approaches make use of instantaneous velocity field to detect vortices boundaries. These vortices boundaries fail to coherently carry and transport their encircled water masses, instead, they stretch, deform and develop filaments. As for example, the angular velocity which is defined as the time rate of change of particle's angular displacement $\omega = \frac{d\phi}{dt}$ is considered as Eulerian approach to define vortices boundaries. Fig.6-1(a) shows vortices boundaries extracted from ocean surface velocities derived from satellite altimetry, using the angular velocity. Fig.6-1(b) shows their final position under Lagrangian advection over three months. None of these vortices remains coherent, indeed they all stretch and filament. The complete advection sequence over the time interval $[0, 90]$ is illustrated in the movie M1.

On the other hand, Lagrangian methods are powerful tools to coherent vortices'

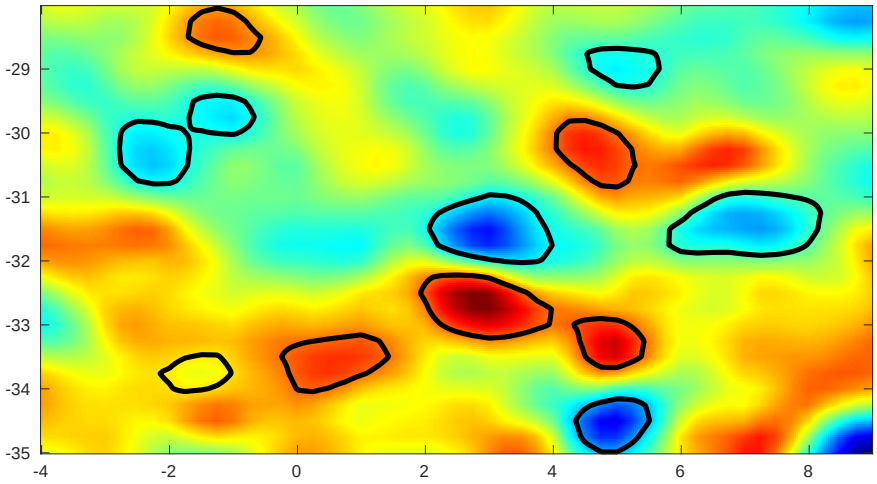

(a)

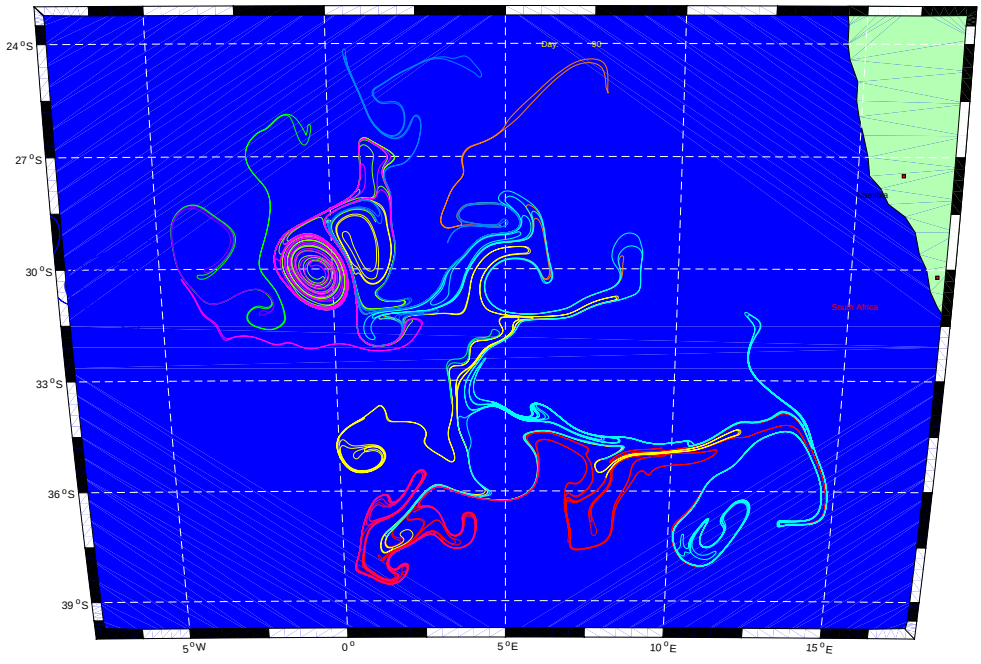

(b)

Figure 6-1: a) Eulerian vortices defined as outermost closed contours of the angular velocity's extrema. b) Their final positions under Lagrangian advection over three months. (See the supplemental movie M1 for the complete advection sequence of these vortices boundaries)

detection due to the fact that they take into account the evolution of particles trajectories [Haller, 2005, Haller et al., 2016, Haller and Beron-Vera, 2013]. A variety of dynamical systems techniques have been introduced to define a Lagrangian characterization of the transport of nonautonomous chaotic dynamical systems. These techniques typically fall into different classes. The first class contains probabilistic approaches, which study the evolution of probability densities and almost-invariant sets [Froyland et al., 2010, Froyland, 2013, Froyland et al., 2012]. For example, lines of constant sea surface height are commonly used to determine locations of eddies and gyres [Crawford et al., 2007], while the maximum gradients of potential vorticity are used to determine the vortices' boundaries [Sobel et al., 1997, Nash et al., 1996]. The second class contains geometric approaches, which use invariant manifolds. For example, In [Haller and Beron-Vera, 2013] authors introduce a variational principle for coherent material vortices, where vortices' boundaries are sought as elliptic LCSs, i.e. exceptional material barriers that exhibit no appreciable stretching or folding over a finite time interval. This method has been reformulated such that it can be solved via the variational level set methodology [Hadjighasem and Haller, 2016]. Another method has been proposed which seeks vortices' boundaries as maximal material tubes in which material elements complete the same polar rotation over a given finite-time interval [Farazmand and Haller, 2016]. However, these stretching-based variational methods rely on a precise computation of Cauchy-green tensor and its invariants, which requires accurate differentiation of particles trajectories with respect to their initial positions. Moreover, they only detect the most coherent elliptic LCSs and ignore those with non-uniform stretching. Most importantly, these methods have no link between material vortices and the expected spinning motion, a defining feature of observed vortices. A clustering approach has been developed by [Hadjighasem et al., 2016], which uses the spectral clustering algorithm to identify coherent structures by grouping Lagrangian particles into coherent and incoherent. This has been done by defining coherent structures as a set of Lagrangian trajectories that maintain short distances among themselves relative to the others outside the structure. This method is simple to implement and requires no differentiation of particles trajectories with

respect to their initial positions. However, it does require a well defined eigengap and it is costly in computation in case for large number of trajectories [Hadjighasem et al., 2017]. [Haller et al., 2016] use the Lagrangian-Averaged Vorticity Deviation to identify Lagrangian coherent vortices. This has been done based on a unique decomposition of gradient deformation into product of two deformation gradients; one for pure strain and other for pure rotation [Haller, 2016]. This approach as well, does not require differentiation of the flow map with respect to initial conditions, and is it simple and low in computation cost. However, it relies on derivatives of the velocity field, and requires large computational domain for spatial mean of vorticity.

Our approach is based on a decomposition of particle trajectory into two parts: closed curves which give information about uniformly rotating flow, and one that describes the mean displacement. The former part yields an objective measure of material rotation. As in [Haller et al., 2016], we define Lagrangian coherent vortex as closed material lines in which fluid parcels complete the same polar rotation. This turns out to be filled with outward-increasing closed contours of the Lagrangian Averaged Closed Curve Length ($\mathcal{LACCL}$). Additionally, $\mathcal{LACCL}-$based vortex's center is defined as the innermost member of $\mathcal{LACCL}$. Our method is based on observed vortex's trajectory, and it has several important features:

- Our method is naturally related to vortex feature and defines vortices based on their observed trajectories [El Aouni et al., 2019a, El Aouni et al., 2018b].
- Material $\mathcal{LACCL}$-vortices guarantee the revolving movement of all particles within vortices' boundaries. At least, all particles rotate 360° around the observed center.
- Our method does not require differentiation of flow map with respect to initial conditions.
- The images produced by $\mathcal{LACCL}$ map itself gives insight into the qualitative evolution of different trajectories' classes without having to explicitly integrate and compare the behavior of trajectories.

- It is suitable to applications to float data, based on the fact that trajectories arch-length can be computed without any reliance on a velocity field.

- $\mathcal{LACCL}$ is generic, it can be adapted with the finite-size notion. The method can be set up to be more selective, where we can require particles' trajectories to complete a certain number of closed curves (the finite-size in question, is then the number of the closed curves). Thus, it could lump vortices boundaries occurring over different time intervals into the same scalar field.

6.2 Related work

A variety of dynamical systems techniques have been introduced to define a Lagrangian characterization of the transport of nonautonomous chaotic dynamical systems. These techniques typically fall into different classes. Probabilistic approaches, which study the evolution of probability densities and almost-invariant sets [Froyland et al., 2010, Froyland, 2013, Froyland et al., 2012]. For example, lines of constant sea surface height are commonly used to determine locations of eddies and gyres [Crawford et al., 2007], while the maximum gradients of potential vorticity are used to determine the vortices' boundaries [Sobel et al., 1997, Nash et al., 1996]. Geometric approaches which use invariant manifolds. [Haller and Beron-Vera, 2013] introduce a variational principle for coherent material vortices, where vortices' boundaries are sought as elliptic LCSs, i.e. exceptional material barriers that exhibit no appreciable stretching or folding over a finite time interval. This method has been reformulated such that it can be solved via the variational level set methodology [Hadjighasem and Haller, 2016]. Another method has been proposed which seeks vortices' boundaries as maximal material tubes in which material elements complete the same polar rotation over a given finite-time interval [Farazmand and Haller, 2016]. However, these stretching-based variational methods rely on a precise computation of Cauchy-green tensor and its invariants, which requires accurate differentiation of particles

[1] http://www.aviso.oceanobs.com/duacs/

trajectories with respect to their initial positions. Moreover, they only detect the most coherent elliptic LCSs and ignore those with non-uniform stretching. Most importantly, these methods have no link between material vortices and the expected spinning motion, a defining feature of observed vortices. A clustering approach has been developed by [Hadjighasem et al., 2016], which uses the spectral clustering algorithm to identify coherent structures by grouping Lagrangian particles into coherent and incoherent. This has been done by defining coherent structures as a set of Lagrangian trajectories that maintain short distances among themselves relative to the others outside the structure. This method is simple to implement and requires no differentiation of particles trajectories with respect to their initial positions. However, it does require a well-defined eigengap and it is costly in computation in case for large number of trajectories [Hadjighasem et al., 2017].

So far, the most accurate method and naturally related to such coherent material cores was proposed by [Haller et al., 2016]. They used the Lagrangian-Averaged Vorticity Deviation to identify Lagrangian coherent vortices. This has been done based on a unique decomposition of gradient deformation into product of two deformation gradients; one for pure strain and other for pure rotation [Haller, 2016]. The detailed method is discussed in the following section.

6.2.1 Lagrangian-Averaged Vorticity Deviation

In [Haller et al., 2016], authors define Lagrangian vortex as a set of material line in which fluid elements complete the same intrinsic dynamic rotation. Solution to this vortex definition turns out to be foliated by outward decreasing tubular level sets of the Lagrangian-averaged vorticity deviation (LAVD). The LAVD is defined as the trajectory-averaged, normed deviation of the vorticity from its spatial mean:

$$LAVD_{t_0}^{t_f} = \int_{t_0}^{t_f} \|\omega(\mathbf{x}(s;\mathbf{x}_0),s) - \bar{\omega}(s)\|\, ds, \tag{6.1}$$

where $\bar{\omega} = \frac{\int_{U(t)} \omega(\mathbf{x},t) dS}{Sur(U(t))}$ is the spatial mean of the vorticity $\omega = \nabla \times \mathbf{v}$, with $Sur(.)$ denotes the area for two-dimensional flows. Accordingly, dS refers to the area element

in $\mathbf{U}(t)$. The time t_0 positions of LAVD-based coherent Lagrangian vortex are defined as evolving material domain $\mathbf{V}(t) \subset \mathbb{R}^2 \times [t_0, t_f]$ such that $\mathbf{V}(t_0) \subset \mathbb{R}^2$ is filled with a nested family of closed contours of $LAVD_{t_0}^{t_f}(\mathbf{x}_0)$ with outward-decreasing $LAVD$ values. Its corresponding boundary $\mathbf{B}(t) \subset \mathbb{R}^2 \times [t_0, t_f]$ of $\mathbf{V}(t)$ is the outermost convex closed contours of $LAVD_{t_0}^{t_f}(\mathbf{x}_0)$ in $\mathbf{V}(t_0)$. The center $\mathbf{C}(t) \subset \mathbb{R} \times [t_0, t_f]$ of $\mathbf{V}(t)$ is defined as the innermost (minimum) member of $LAVD_{t_0}^{t_f}(\mathbf{x}_0)$ in $\mathbf{V}(t_0)$. LAVD-vortices, their boundaries and centers are material objects by definition [Haller et al., 2016]. Thus, their time t position is uniquely determined by Lagrangian advection of their initial positions:

$$\mathbf{V}(t) = \mathbf{F}_{t_0}^{t}(\mathbf{U}(t_0)), \quad \mathbf{B}(t) = \mathbf{F}_{t_0}^{t}(\mathbf{B}(t_0)) \quad \mathbf{C}(t) = \mathbf{F}_{t_0}^{t}(\mathbf{C}(t_0)), \quad t \in [t_0, t_f] \tag{6.2}$$

Where $\mathbf{F}_{t_0}^{t}(\mathbf{x}_0) := \mathbf{x}(t, t_0, \mathbf{x}_0)$ is the flow map that associates times t_0 and t positions of fluid particles which evolve according to:

$$\frac{d\mathbf{x}}{dt} = \mathbf{v}(\mathbf{x}, t) \tag{6.3}$$

where $\mathbf{v}(\mathbf{x}, t)$ is a two-dimensional velocity field. Contrary to the stretching-based variational approaches [Serra and Haller, 2017, Haller and Beron-Vera, 2013], the LAVD-based definition of a rotational LCS may display tangential material filamentation, but any developing filament necessarily rotate together with the vortex without global breakaway [Haller et al., 2016]. This approach as well, does not require differentiation of the flow map with respect to initial conditions, and is it simple and low in computation cost. However, it relies on derivatives of the velocity field, and requires large computational domain for spatial mean of vorticity.

[1]http://www.aviso.oceanobs.com/duacs/

6.3 Set-up

We consider a time-dependent smooth vector field:

$$\mathbf{v}(\mathbf{x}, t), \quad \mathbf{x} \in \mathbb{R}^2, \quad t \in [\alpha, \beta] \tag{6.4}$$

and its associated ordinary differential equation:

$$\dot{\mathbf{x}} = \mathbf{v}(\mathbf{x}, t), \quad \mathbf{x} \in \mathbb{R}^2, \quad t \in [\alpha, \beta] \tag{6.5}$$

where $\mathbf{v}$ a smooth velocity field defined on a domain:

$$\mathbf{U}(t) \subset \mathbb{R}^2, \quad \mathbf{U} = \bigcup_{t \in [\alpha,\beta]} \mathbf{U}(t) \subset \mathbb{R}^2 \times [\alpha, \beta] \tag{6.6}$$

The flow map is defined as the map that takes a particle from its initial location $\mathbf{x}_0$ at time t_0 to its location $\mathbf{x}_t$ at time t:

$$\mathbf{F}_{t_0}^{t}(\mathbf{x}_0) := \mathbf{x}(t, t_0, \mathbf{x}_0), \quad \alpha \leq t_0 \leq t \leq \beta, \tag{6.7}$$

$\mathbf{x}(t, t_0, \mathbf{x}_0)$ denoting the trajectory of Eq.6.5 passing through a point $\mathbf{x}_0$ at time t_0.

Consider a material line (a curve defined by a set of fluid particles) $\mathcal{M}(t_0)$ advected by the flow. Its image at time t can be expressed in term of the flow map as $\mathcal{M}(t) = \mathbf{F}_{t_0}^{t}(\mathcal{M}(t_0))$.

We write the trajectory's arc-length of a given particle $\mathbf{x}_0$ traveling in the flow in the time interval $[t_0, t_f]$ as:

$$\mathcal{L}(\mathbf{x}(t_f, t_0, \mathbf{x}_0)) = \int_{t_0}^{t_f} \|\mathbf{v}(\mathbf{x}_0, t)\| \, dt \tag{6.8}$$

The arc-length of this trajectory can be approximated in term of flow map as:

$$\mathcal{L}(\mathbf{x}(t_f, t_0, \mathbf{x}_0)) = \sum_{i=1}^{f} \left\| \mathbf{F}_{t_0}^{t_i}(\mathbf{x}_0) - \mathbf{F}_{t_0}^{t_{i-1}}(\mathbf{x}_0) \right\| \tag{6.9}$$

With $\left\|(\mathbf{F}_{t_0}^{t_i}(\mathbf{x}_0) - \mathbf{F}_{t_0}^{t_{i-1}}(\mathbf{x}_0))\right\|$ a line segment of a given particle $\mathbf{x}_0$ traveling between the time interval $[t_{i-1}, t_i]$.

6.4 Particles Trajectory in Vortex Boundary

Particle trajectory produced by integrating the velocity vector field in a vortex boundary result into a loopy curve which intersects itself. Fig.6-2(a,b,c) show examples of trajectories of particles initialized in vortices boundaries.

[Dong et al., 2011] propose a scheme to identify loops from trajectories of oceanic surface drifters; particles inside vortices must exhibit self-crossing trajectories. Thus, a possible way to identify Lagrangian coherent vortices is by computing the number of closed curves in particles' trajectories. That is the number n of times when a given particle $\mathbf{x}$'s trajectory crosses itself at $t_i + \tau_i$ $\mathbf{x}(t_i + \tau_i) = \mathbf{x}(t_i)$ and creates a closed curve such as:

$$\mathbf{x}(t_i + \tau_i) = \mathbf{x}(t_i), \quad \tau_i > 0 \quad \text{with} \quad i = 1 \cdots n \quad (a)$$

$$t_i \in]t_0 \; t_f[, \quad t_{i+1} \notin [t_i \; t_i + \tau_i[\quad (b) \tag{6.10}$$

and

$$\mathbf{x}(t_{i+1}) \notin]\mathbf{x}(t_i) \; \mathbf{x}(t_i + \tau_i)[\quad (c)$$

Where τ_i, the period of time for a particle starting at t_i takes to cross its trajectory. Fig.6-2 displays different particles' trajectories; Fig.6-2(a,b,c) displays 3 different scenarios of particles initialized in vortices boundaries, closed curves satisfying conditions in eq.6 are highlighted in red color. First closed curve (in blue) of the trajectory in Fig.6-2(b) does not satisfy condition (c) of eq.6. Fig.6-2(b) shows particle trajectory displaying accumulation phenomenon, where none of its closed curves satisfies the conditions in eq.6.

Computing the number of closed curves for all particles may give an idea of potential vortices' location. Such idea can identify vortices as homogeneous regions where

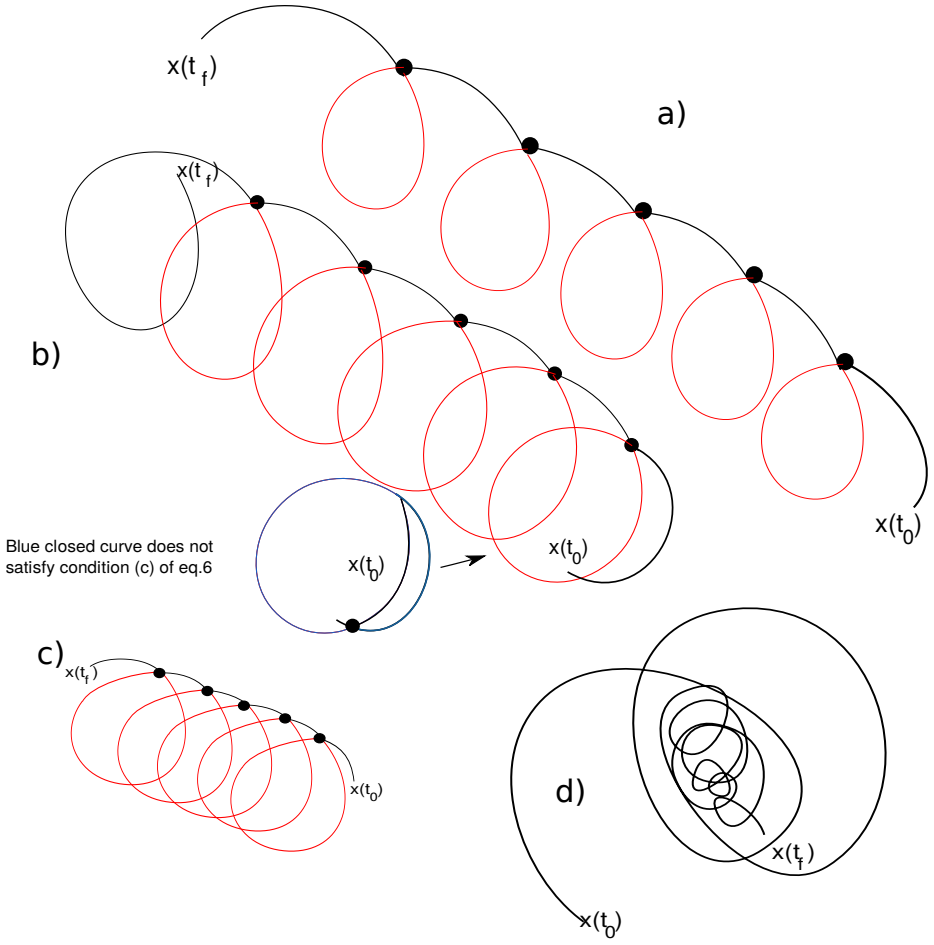

Figure 6-2: a,b and c) 3 particles' trajectories with different angular velocities; closed curves satisfying eq.6 are highlighted in red color. d) Particle trajectory displaying accumulation phenomenon (none of its closed curve satisfy the criteria of Eq.6)

the number of closed curves increases toward their centers and decreases in inverse proportion to the distance from the centers. However, this picture won't give a precise location of vortices boundaries due to the fact particles trajectories of vortex boundary won't have the same number of closed curves due to their initial location and finite-time advection. Fig.6-3(a) shows two trajectories of two particles within the same vortex boundary and advected for the same time interval $[t_0\ t_f]$: one exhibits 5 closed curves while the other has 6 closed curves.

Particles within vortex will exhibit spinning movement resulting in higher trajectories' length compared their pure displacement. Fig.6-3(b) shows two particles' trajectories compared to their pure displacement; both have almost same pure dis-

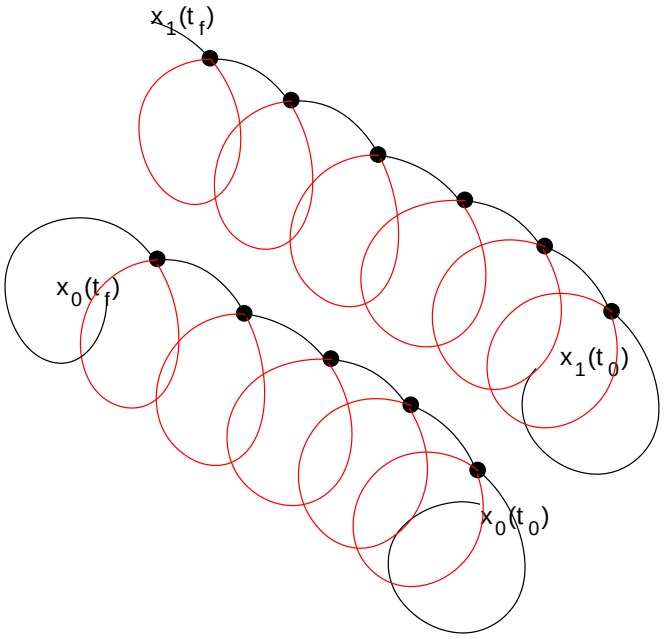

(a)

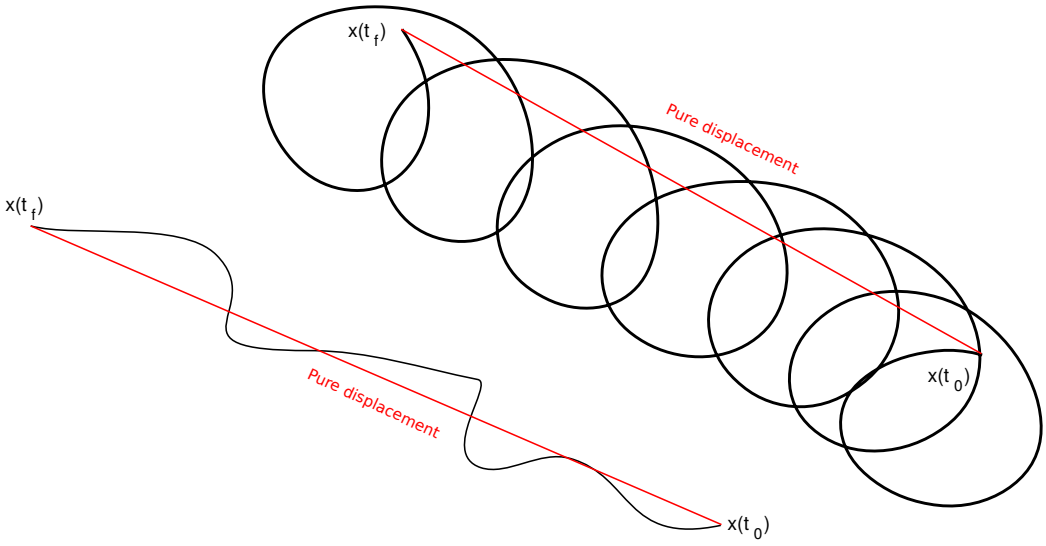

(b)

Figure 6-3: a) Trajectory of two particles within the same vortex boundary and advected for the same period of time; both have different number of closed curves. b) Trajectories of two particles compared to their pure displacement; one within a vortex boundary while the other is outside. Both particles are advected for the same period of time

placement but different trajectories. Thus, another idea we propose to identify Lagrangian coherent structures is by computing the difference between the arc-length of particles' trajectories and their displacement ($\mathcal{ALD}$):

$$\begin{aligned}\mathcal{ALD}_{t_0}^{t_f}(x_0) &= \int_{t_0}^{t_f} \|\mathbf{v}(\mathbf{x}_0,t)\|\,dt - \|\mathbf{x}(t_f,t_0,\mathbf{x}_0) - \mathbf{x}_{t_0}\| \\ &= \sum_{i=1}^{f} \left\|\mathbf{F}_{t_0}^{t_i}(\mathbf{x}_0) - \mathbf{F}_{t_0}^{t_{i-1}}(\mathbf{x}_0)\right\| - \left\|\mathbf{F}_{t_0}^{t_0}(\mathbf{x}_0) - \mathbf{F}_{t_0}^{t_f}(\mathbf{x}_0)\right\|\end{aligned} \tag{6.11}$$

$\mathcal{ALD}$ values of particles within vortex decrease toward its center and increases in inverse. Contrary to the map of the number of closed curves, $\mathcal{ALD}$ is smoother. Thus, we can define a Lagrangian coherent vortex as an evolving material domain $\mathbf{U}(t) \subset \mathbb{R}^2 \times [t_0, t_f]$ such that $\mathbf{U}(t_0) \subset \mathbb{R}^2$ is filled with a nested family of closed contours of $\mathcal{ALD}_{t_0}^{t_f}(\mathbf{x}_0)$ with outward-increasing $\mathcal{ALD}$ values. We define the boundary $\mathbf{B}(t) \subset \mathbb{R}^2 \times [t_0, t_f]$ of $\mathbf{U}(t)$ as outermost closed contours of $\mathcal{ALD}_{t_0}^{t_f}(\mathbf{x}_0)$ in $\mathbf{U}(t_0)$. Its center $\mathbf{C}(t) \subset \mathbb{R}\times[t_0, t_f]$ is defined as the innermost (minimum) member of $\mathcal{ALD}_{t_0}^{t_f}(\mathbf{x}_0)$ in $\mathbf{U}(t_0)$. However, the use of $\mathcal{ALD}$ also leaves several challenges unaddressed:

- $\mathcal{ALD}$ only highlights regions where particles exhibit high spinning compared to their pure displacement.

- It doesn't take into consideration if particles contain closed curve or not. For example, in a chaotic system, a particle might travel in a certain domain and goes back nearby its initial position will eventually have high $\mathcal{ALD}$ value.

We show in Fig.6-4 an example of three particles: (a) particle trajectory within a vortex exhibiting low spinning compared to its displacement, (b) and (c) two particles within the same vortex boundary, both advected for the same period of time but have different number of closed curves.

$\mathcal{ALD}$ is defined as the difference between the arch-length of a particle's trajectory and its pure displacement, thus particle (a) would have a low $\mathcal{ALD}$. Particles b) and c) are within the same vortex boundary, still they would have different $\mathcal{ALD}$ values (similar arch-length but different displacement values). $\mathcal{ALD}$ does not take into

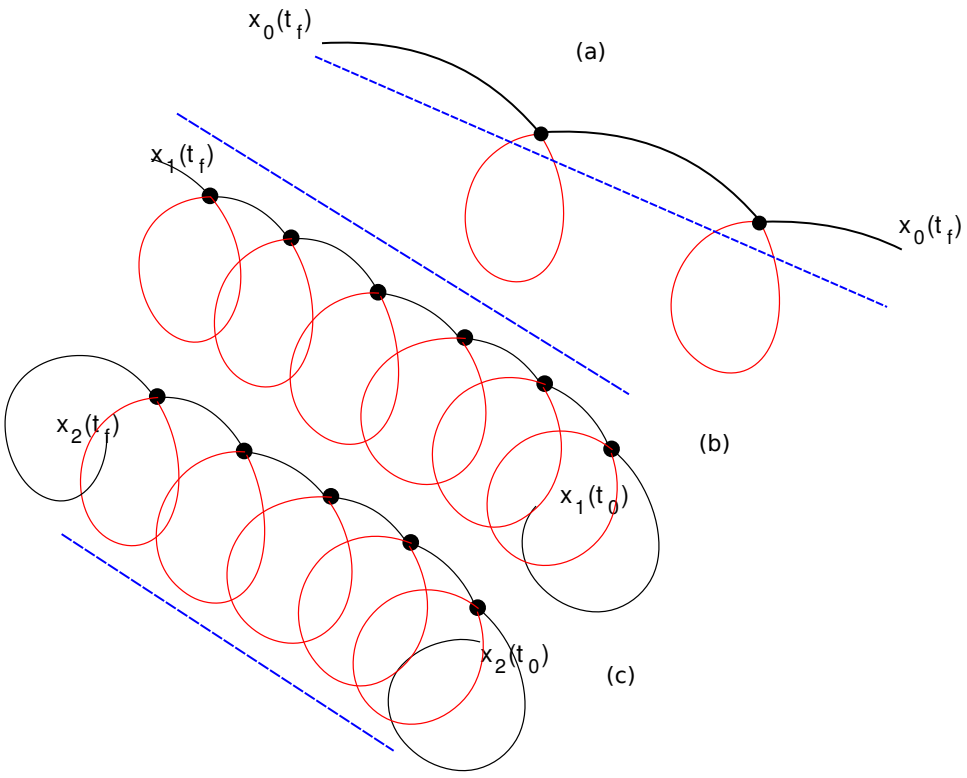

Figure 6-4: a) particle trajectory within vortex exhibiting low spinning compared to its displacement. b) and c) Trajectory of two particles within the same vortex boundary, both are advected for the same period of time; both have different number of closed curves. Blue lines present pure displacement of these particles.

consideration if particles contain closed curve or not. We show in Fig.6-5 two nearby particles: one within vortex boundary and the other outside. These two particles have the same $\mathcal{ALD}$ value, but different trajectories type. Based on $\mathcal{ALD}$, these two particles belong to the same physical structure, which is incorrect. Moreover, particles within different vortices but with the same diameter would have different $\mathcal{ALD}$ values, due to their initial locations and components associated with vortical structure and transfer. An objective identification of vortices is only by considering closed curves part of the trajectory, which is not the case in the $\mathcal{ALD}$ approach.

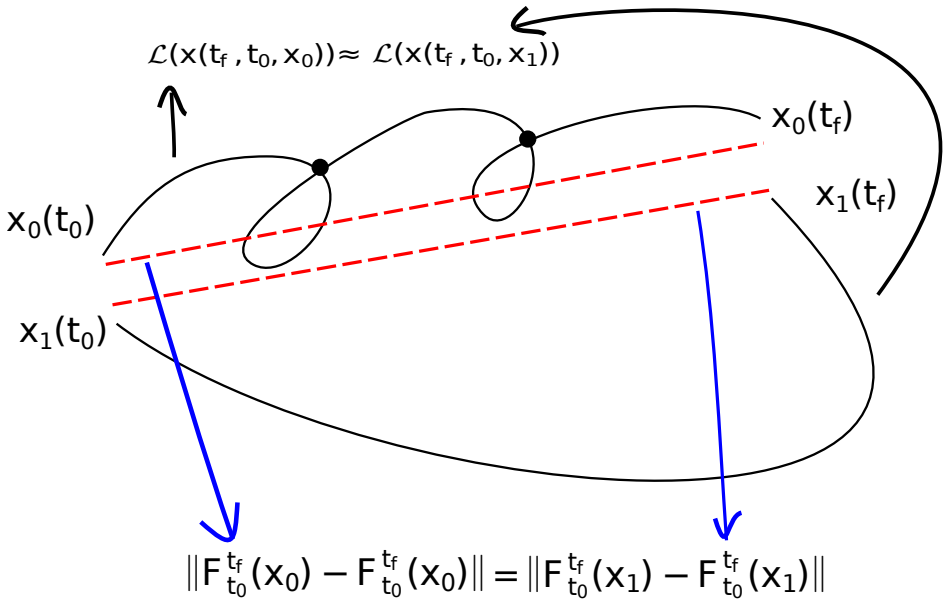

Figure 6-5: Two different trajectories with similar arch-length and displacement.

6.5 Defining Vortex Boundary from Particles Trajectory

We seek to identify Lagrangian coherent vortices as closed material lines along which particles exhibit similar rotations around the same axis, and over a finite time interval.

Particles within the same vortex boundary, will undergo a very similar trajectory, with different trajectory shifts due to their initial position, but not necessarily the same number of closed curves, mainly due to their initial position and the advection time interval. Instead of concentrating on particles trajectories themselves, we only want to study more significant segments of these latter, which are more related to

vortices nature.

Particle trajectory can further be divided into two parts; closed curves which give information about uniformly rotating flow, and one that describes the mean displacement. Based on the fact that fluid parcels along vortex boundary exhibit the same polar rotation, we only consider the first part which gives closed curves of particle trajectory. In this way, we only analyze particles that undergo loopy movement, thus we avoid all the challenges mentioned in $\mathcal{ALD}$ approach.

We define the Lagrangian Averaged Closed Curve Length metric ($\mathcal{LACCL}$) as:

$$\mathcal{LACCL}(\mathbf{x}(t_f, t_0, \mathbf{x}_0)) = \sum_{i=1}^{n} \frac{\int_{t_i}^{t_i+\tau_i} \|\mathbf{v}(\mathbf{x}_0, t)\| \, dt}{n} \tag{6.12}$$

such as

$$\begin{gathered} \mathbf{x}(t_i + \tau_i) = \mathbf{x}(t_i), \quad \tau_i > 0 \quad \text{with} \quad i = 1 \cdots n \\ , \\ t_i \in]t_0 \; t_f[, \quad t_{i+1} \notin [t_i \; t_i + \tau_i[\\ \text{and} \\ \mathbf{x}(t_{i+1}) \notin]\mathbf{x}(t_i) \; \mathbf{x}(t_i + \tau_i)[\end{gathered} \tag{6.13}$$

With n, the number of segments of the particle $\mathbf{x}$ trajectory satisfying $\mathbf{x}(t_i + \tau_i) = \mathbf{x}(t_i)$. Where τ_i is the period of time for a particle initialized at t_i to return to the same point at $t_i + \tau_i$. Fig.6-6(a) shows an example of particle trajectory and its segments satisfying the eq.8.2, while Fig.6-6(b) shows the geometric view of the $\mathcal{LACCL}$ calculation for two particles initialized in a given vortex boundary. In similar way, we show the geometric view of the $\mathcal{LACCL}$ method applied on a particle trajectory within a vortex with a radial flow where all particles converge toward its attracting center in Fig.6-7. For a parcel fluid starting from $\mathbf{x}_0$, the $\mathcal{LACCL}_{t_0}^{t}(\mathbf{x}_0)$ field is dynamically consistent measure of the mean material rotation.

We now use the $\mathcal{LACCL}$ to identify closed convex curve along which fluid parcels experience the same rotation over a time interval $[t_0 \; t_f]$. Time t_0 positions of such closed convex curves are closed contours of the function $\mathcal{LACCL}_{t_0}^{t_f}$. The inner-most

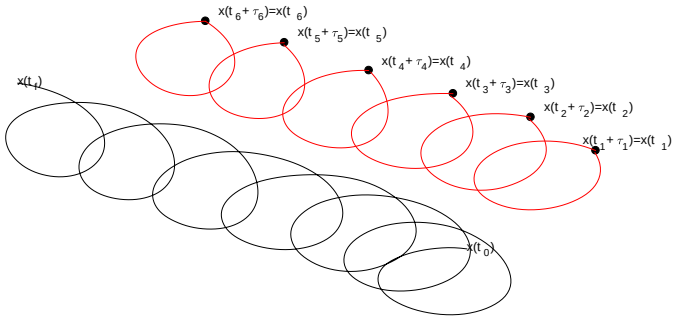

(a)

$$\mathcal{LACCL}(\mathbf{x}(t_f, t_0, \mathbf{x_1})) = \sum_{i=1}^{6} \frac{\int_{t_i}^{t_i+\tau_i} \|\mathbf{v}(\mathbf{x_1}, t)\|\, dt}{6}$$

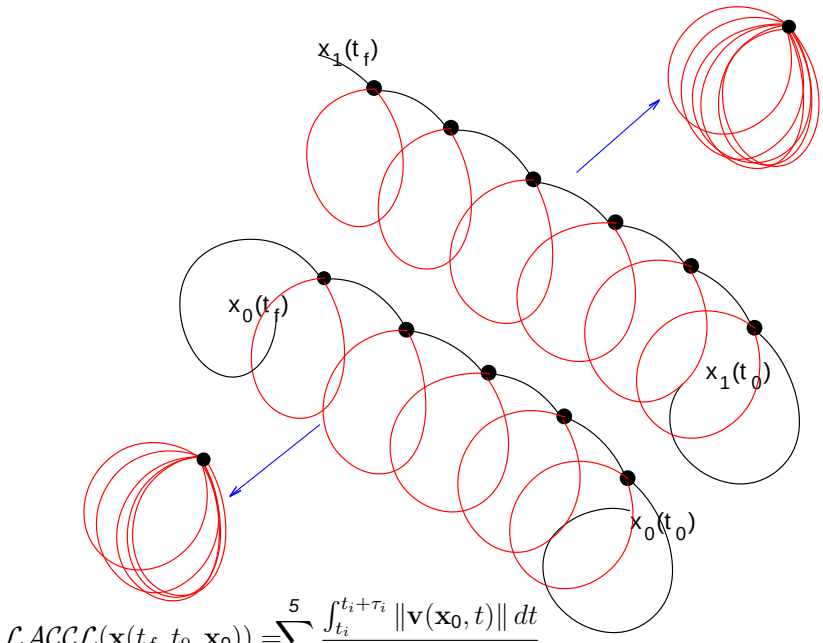

$$\mathcal{LACCL}(\mathbf{x}(t_f, t_0, \mathbf{x_0})) = \sum_{i=1}^{5} \frac{\int_{t_i}^{t_i+\tau_i} \|\mathbf{v}(\mathbf{x_0}, t)\|\, dt}{5}$$

(b)

Figure 6-6: a) (black) Trajectory of particle within vortex boundary, (red) segments satisfying equation 8.2. b) Example of $\mathcal{LACCL}_{t_0}^{t_f}$ calculation of two particles within the same vortex boundary.

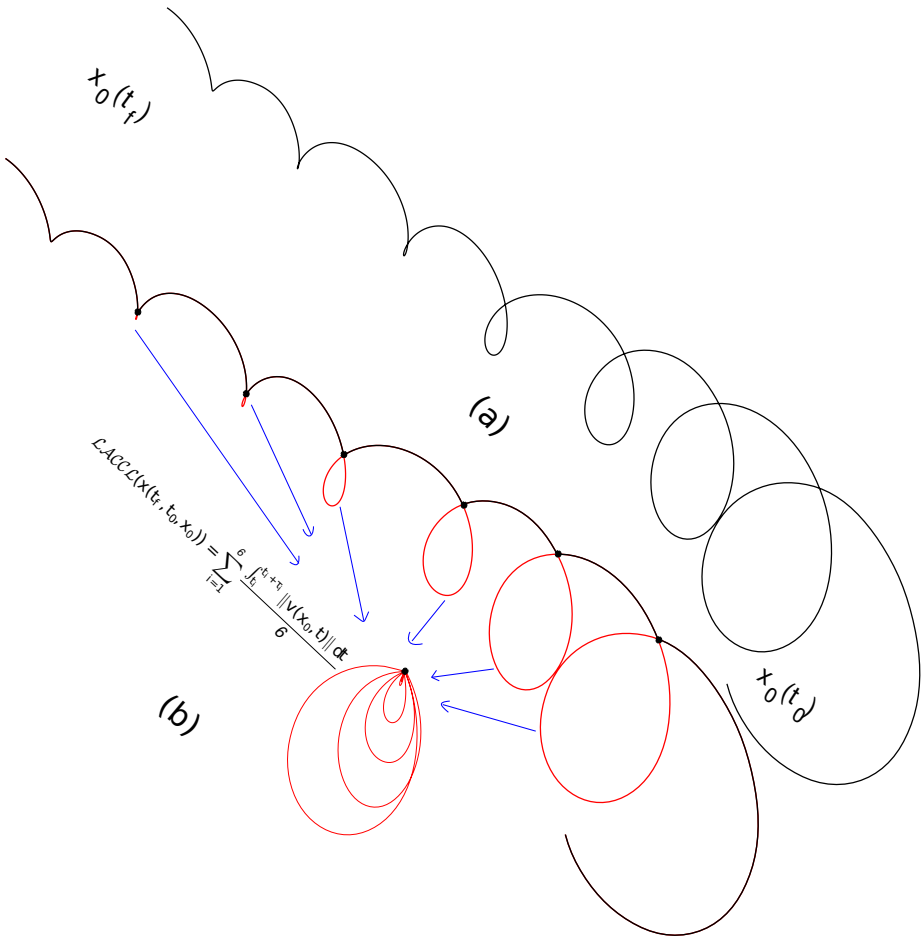

Figure 6-7: (black) Trajectory of particle within a vortex with a radial flow where the particles trajectories converge, (red) segments satisfying equation 8.2. b) Example of $\mathcal{LACCL}_{t_0}^{t_f}$ calculation of this converging trajectory.

member of such a nested sequence of closed contours, with inward decreasing $\mathcal{LACCL}$ values, allows us to define Lagrangian vortex center. Similarly, the largest closed convex curve of such a nested contour family defines the boundary of Lagrangian vortex. At least all particles within a vortex boundary have to complete at least one polar rotation to allow their identification. We summarize the $\mathcal{LACCL}$-based vortex identification in the following definition:

Definition 1. *For a given time interval* $[t_0, t_f]$*:*

- *1) Lagrangian coherent vortex is an evolving material domain* $\mathbf{U} = \bigcup_{t\in[t_0,t_f]} \mathbf{U}(t) \subset \mathbb{R}^2 \times [t_0, t_f]$ *such that* $\mathbf{U}(t_0) \subset \mathbb{R}^2$ *is filled with a nested family of closed contours of* $\mathcal{LACCL}_{t_0}^{t_f}(\mathbf{x}_0)$ *with outward-increasing* $\mathcal{LACCL}$ *values.*

- *2) The boundary* $\mathbf{B} = \bigcup_{t\in[t_0,t_f]} \mathbf{B}(t) \subset \mathbb{R}^2 \times [t_0, t_f]$ *of* $\mathbf{U}$ *is the outermost convex closed contours of* $\mathcal{LACCL}_{t_0}^{t_f}(\mathbf{x}_0)$ *in* $\mathbf{U}(t_0)$.

- *3) The center* $\mathbf{C} = \bigcup_{t\in[t_0,t_f]} \mathbf{C}(t) \subset \mathbb{R}^2 \times [t_0, t_f]$ *of* $\mathbf{U}$ *is defined as the innermost (minimum) member of* $\mathcal{LACCL}_{t_0}^{t_f}(\mathbf{x}_0)$ *in* $\mathbf{U}(t_0)$.

The above definitions extract Lagrangian vortices with the simplest geometry at the initial time t_0. That is by setting a maximal convexity deficiency parameter, which allows capturing filamented parts that rotate together with the vortices without a global breakaway.

Lagrangian vortices, as well as their boundaries and centers, are materials objects [Haller et al., 2016]. Thus, their position at a given time t is only determined by Lagrangian advection:

$$\begin{gathered} \mathbf{U}(t) = \mathbf{F}_{t_0}^{t}(\mathbf{U}(t_0)), \quad \mathbf{B}(t) = \mathbf{F}_{t_0}^{t}(\mathbf{B}(t_0)) \\ \mathbf{C}(t) = \mathbf{F}_{t_0}^{t}(\mathbf{C}(t_0)), \quad t \in [t_0, t_f] \end{gathered} \tag{6.14}$$

The $\mathcal{LACCL}$-vortex approach differs from the previous definitions, it does define vortex based on its observed particles' trajectory, more precisely closed-curves segments of particles' trajectory. As no differentiation of particles trajectories with respect to their initial positions is required, our approach does not require advection of high-density grids. $\mathcal{LACCL}$-vortex may show material filament, but by definition, these filamented parts will rotate together with the vortex without breaking away. An interesting feature of our approach is its ability to include the notion of finite-size by requiring particles' trajectory to complete a certain number closed-curves. In this case, our method could lump vortices boundaries occurring over different time intervals into the same scalar field. This could be interesting in geophysical flows applications having different eddies with different lifetimes in the same scalar field could for instance give an idea about the effect of vortices on each other.

6.6 Experiments

Here we present numerical results that confirm our theoretical predictions regarding the identification of coherent vortices.

6.6.1 Direct numerical simulation of two-dimensional turbulence

We solve numerically the Navier-Stokes PDE model for the time evolution of 2 components of the velocity, $u : \mathcal{D} \to \mathbb{R}^2$ of an incompressible fluid on a torus, $\mathcal{D} = [0, 2\pi] \times [0, 2\pi]$. This can be expressed in spherical coordinates as:

$$\begin{aligned} \partial u_t + u \cdot \nabla u &= -\nabla p + \nu \Delta u + f, && (x,t) \in \mathcal{D} \times [a,b], \\ \nabla \cdot u &= 0, && (x,t) \in \mathcal{D} \times [a,b], \\ \int u^j dx &= 0, && (x,t) \in \mathcal{D} \times [a,b], j = 1,2, \\ u &= u^*, && (x,t) \in \mathcal{D} \times \{0\} \end{aligned} \tag{6.15}$$

Where $\Delta := \left[\frac{\partial^2}{\partial x_1^2} + \frac{\partial^2}{\partial x_2^2}\right]$ is the Laplacian operator such that $\Delta u = (u^{(1)}_{x_1 x_1} + u^{(1)}_{x_2 x_2}, u^{(2)}_{x_1 x_1} + u^{(2)}_{x_2 x_2})$, and $\nabla := \left[\frac{\partial}{\partial x_1} + \frac{\partial}{\partial x_2}\right]$ is the gradient operator such that $\nabla u = (u^{(1)}_{x_1} + u^{(1)}_{x_2}, u^{(2)}_{x_1} + u^{(2)}_{x_2})$. We further assume periodic boundary conditions and use a standard pseudo-spectral method with 256 modes in each direction and 2/3 dealiasing to solve the above Navier-Stokes equation with viscosity $\nu = 10^{-4}$ on the time interval $t \in [0, 1600]$. The initial condition u_0 is the velocity field of two adjacent vortices perturbed by a random uniform distribution. The flow integration is then carried out over the interval $t \in [400, 1600]$, in which the turbulent flow has fully developed, by a fourth-order Runge-Kutta method with variable step-size.

Fig.6-8 shows forward simulated velocity field, obtained at four distinct time points by the Navier-Stokes model 6.15, over two spatial dimensions: the angle of the inner ring (horizontal axis) and outer ring (vertical axis) of a two-dimensional torus. The complete sequence of this simulated velocity field is illustrated in the movie M2.

To construct the $\mathcal{ALD}^{t_f}_{t_0}$ and $\mathcal{LACCL}^{t_f}_{t_0}$ fields, we consider an initial grid of $512 \times$

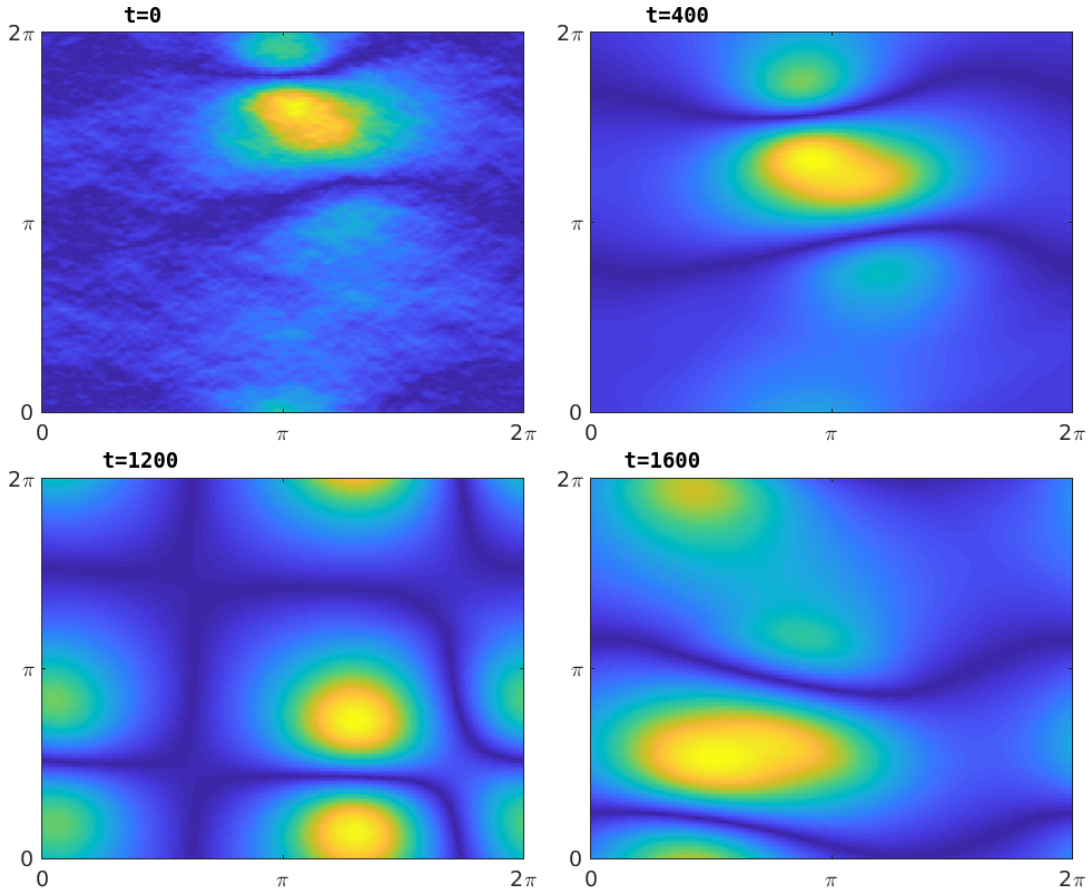

Figure 6-8: Time evolution a simulated realization of fluid velocity, governed by the Navier-Stokes model 6.15, over two spatial dimensions: the angle of the inner ring (horizontal axis) and outer ring (vertical axis) of a two dimensional torus. Angles are expressed in radians. Velocities are evaluated at times t = (0, 400, 1200, 1600). (See the supplemental movie M2 for the complete sequence of this velocity field.)

512 points and integrate the simulated velocity field over the time interval $[t_0 = 400, t_f = 1600]$ using the eq.6.5. Fig.6-9 shows simultaneously (a) the number the closed curves of particles trajectories and (b) the $\mathcal{ALD}_{t_0}^{t_f}(\mathbf{x}_0)$ computed from the simulated realization of fluid velocity governed by the Navier-Stokes model 6.15. None of these maps is smooth enough to allow the detection coherent vortices. A discontinuity within the expected vortices boundaries is observed in both maps. This is due to their initial position and finite-time advection.

Fig.6-10(a) shows coherent vortices and their centers extracted from the $\mathcal{LACCL}_{t_0}^{t_f}(\mathbf{x}_0)$ map applied on the simulated realization of fluid velocity of the model 6.15. Fig. 6-

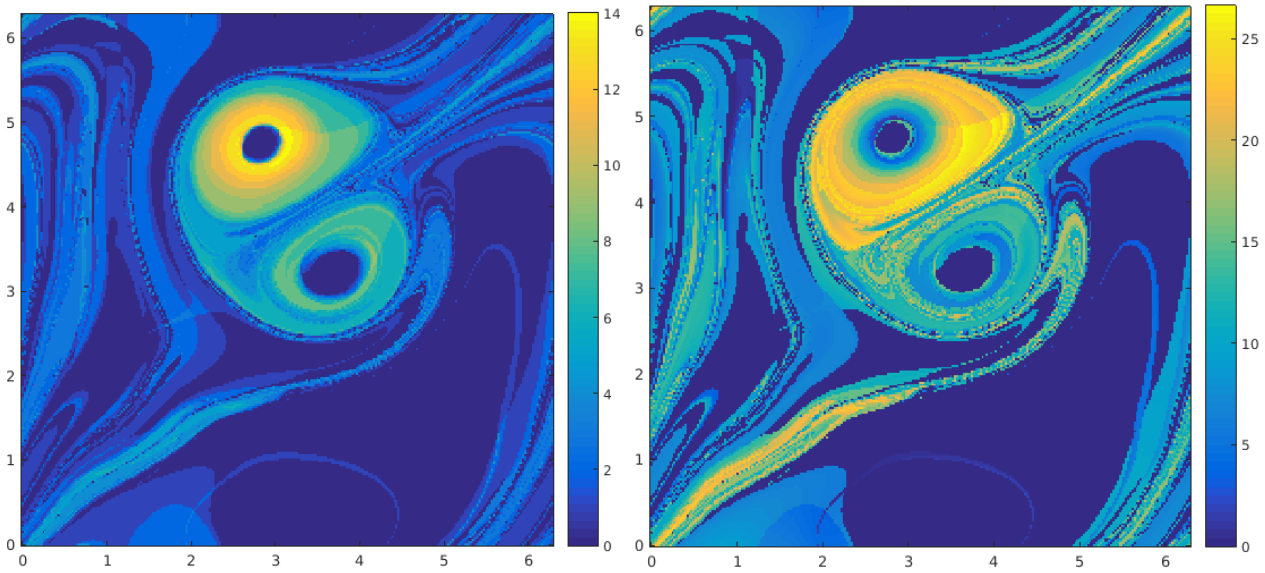

(a) (b)

Figure 6-9: a) Regions of potential vortices: number of closed curves in each particle trajectory, b) $\mathcal{ALCD}_{t_0}^{t_f}(\mathbf{x}_0)$ applied on the simulated realization of fluid velocity, governed by the Navier-Stokes model.

10(b) shows their final position as well as their centers' trajectories under Lagrangian advection. These vortices remain coherent, their boundaries don't stretch or fold. The complete advection sequence over the time interval [0, 1200] is illustrated in the movie M3.

6.6.2 Two-dimensional eddies in satellite altimetry

Here, we use sea surface velocity data to illustrate the detection of Lagrangian vortices. This velocity data is derived from satellite altimetry under the geostrophic approximation where sea-surface height $\eta(\varphi, \theta, t)$ serves as a non-canonical Hamiltonian for surface velocities in the (φ, θ) longitude-latitude coordinate system. The evolution of fluid particles satisfies:

$$\begin{aligned} \dot{\varphi}(\varphi, \theta, t) &= -\frac{g}{R^2 f(\theta) \cos\theta} \partial_\theta \eta(\varphi, \theta, t) \\ \dot{\theta}(\varphi, \theta, t) &= \frac{g}{R^2 f(\theta) \cos\theta} \partial_\varphi \eta(\varphi, \theta, t) \end{aligned} \tag{6.16}$$

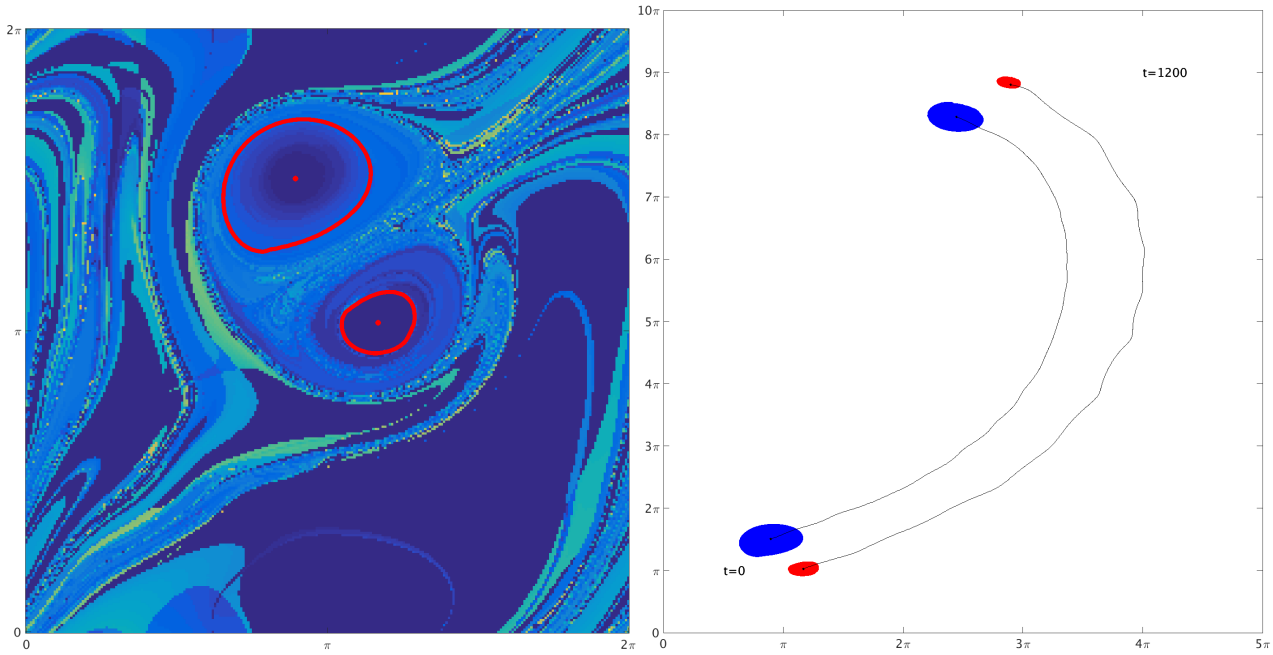

(a) (b)

Figure 6-10: a) Coherent vortices and their centers at time t_0 extracted from the velocity field generated by Navier-Stokes model 6.5 using definition.1 with the $\mathcal{LACCL}_{t_0}^{t_f}(\mathbf{x}_0)$ map shown in background . b) Their initial and final positions under Lagrangian advection. (See the supplemental movie M3 for the complete advection sequence of these vortices.)

where g is the constant of gravity, R is the mean radius of the Earth and $f(\theta) = 2\Omega \sin\theta$ is the Coriolis effect, with Ω denoting the Earth's mean angular velocity. This data is produced by Ssalto/duacs multi-mission sea level products provided by AVISO (CLS/Archiving, Validation, and Interpretation of Satellite Oceanographic data)[1] with a spatial resolution of $1/4°$ and temporal resolution of 7 days. We chose the region of the Agulhas leakage in the Southern Ocean, spans from $[-28°N, -4°W]$ and $[-35°N, 9°W]$. This region is well known for its long-lived propagating eddies that carry water properties from the Indian ocean far into the South Atlantic [Ruijter et al., 1999]. In this study, we chose the time period between 11/11/2006 and 11/1/2007. We integrate the AVISO data set (eq.7.12) over the period of time between $t_0 = 11$ November 2006 and $t_f = t_0 + 90$ days over an initial grid of particles with step size $\Delta x_0 = 1/50°$. We show in Fig.6-11 the number the closed curves of particles trajectories integrated from the satellite velocity field. This image highlight

regions of vortices but it is not smooth enough to enable their exact identification. Fig.6-12(a) shows coherent eddies and their centers extracted from the $\mathcal{ALD}_{t_0}^{t_f}(\mathbf{x}_0)$

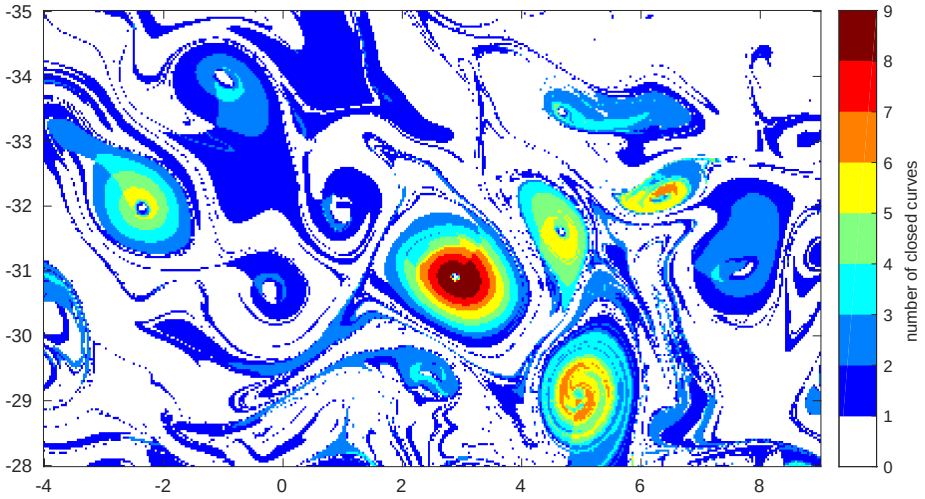

Figure 6-11: Regions of potential vortices: number of closed curves in each particle trajectory.

map, while Fig. 6-12(b) shows their final position under Lagrangian advection. These eddies remain coherent, their boundaries don't stretch or fold. The complete advection sequence over the time interval [0, 90] is illustrated in the movie M4. On the other hand, we show in Fig.6-13(a) $\mathcal{LACCL}_{t_0}^{t_f}(\mathbf{x}_0)$ map computed from the satellite velocity field (eq.7.12). At the same image, we show coherent eddies' boundaries and their centers as they were extracted from the $\mathcal{LACCL}$ map. In Fig.6-13(b), we show their initial and final position as well as their centers' trajectories under Lagrangian advection. These eddies remain coherent, their boundaries don't stretch or fold. The complete advection sequence over the time interval [0, 90] is illustrated in the movie M5. The $\mathcal{ALD}$ approach captured the same Lagrangian vortices region as the $\mathcal{LACCL}$ approach, but it yields tighter vortex boundaries. The outermost boundaries of these vortices are not smooth enough in the $\mathcal{ALD}$ to allow their identification.

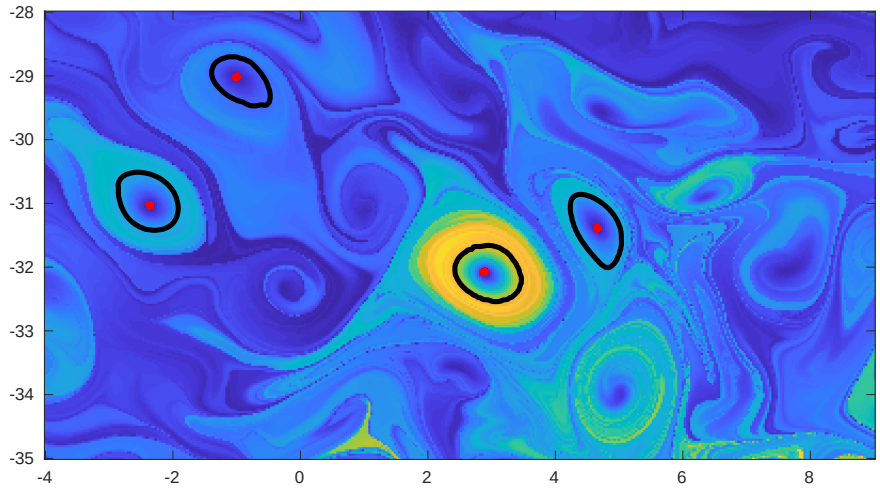

(a)

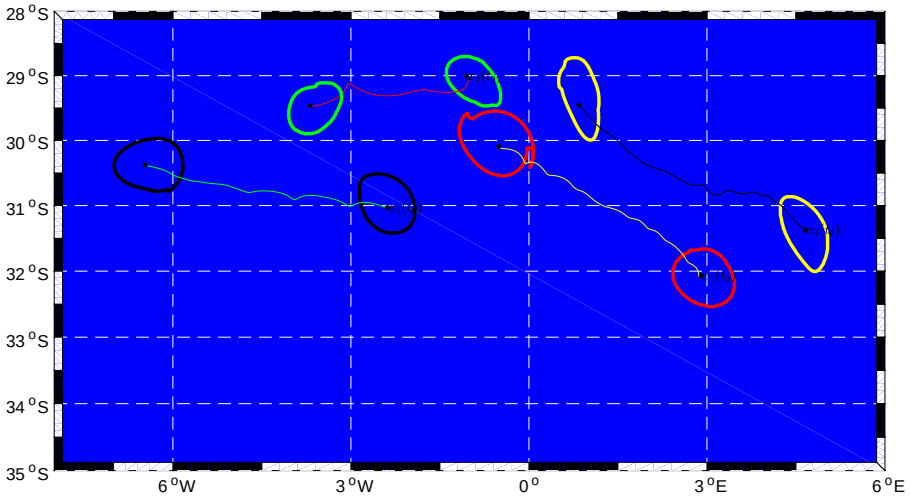

(b)

Figure 6-12: a) Coherent vortices and their centers at time t_0 with the $\mathcal{ALD}_{t_0}^{t_f}(\mathbf{x}_0)$ map shown in background, with $t_f = 90$ days. b) Their initial and final positions under Lagrangian advection. (See the supplemental movie M4 for the complete advection sequence of these vortices.)

6.7 Inertial particles geostrophic Lagrangian vortices

Consider a small spherical particle of radius r_0 and density ρ_{part} in a geostrophic flow of density ρ and viscosity ν. Under the β-plane approximation, let f denote

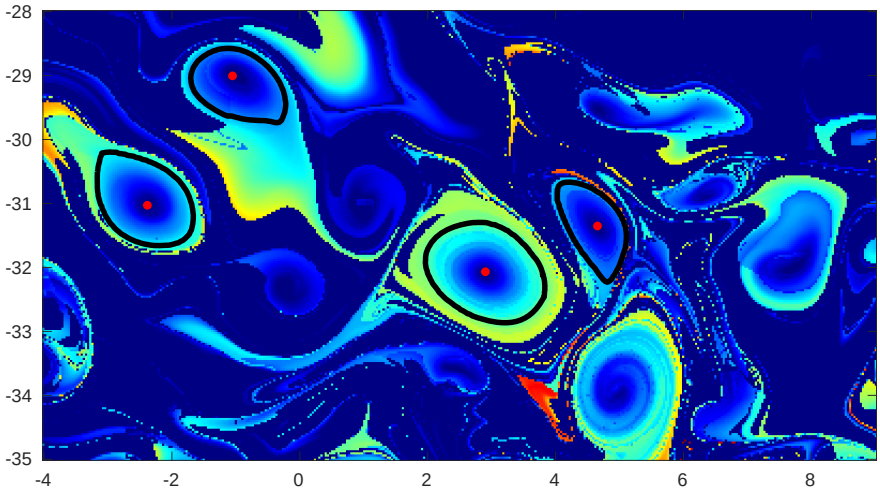

(a)

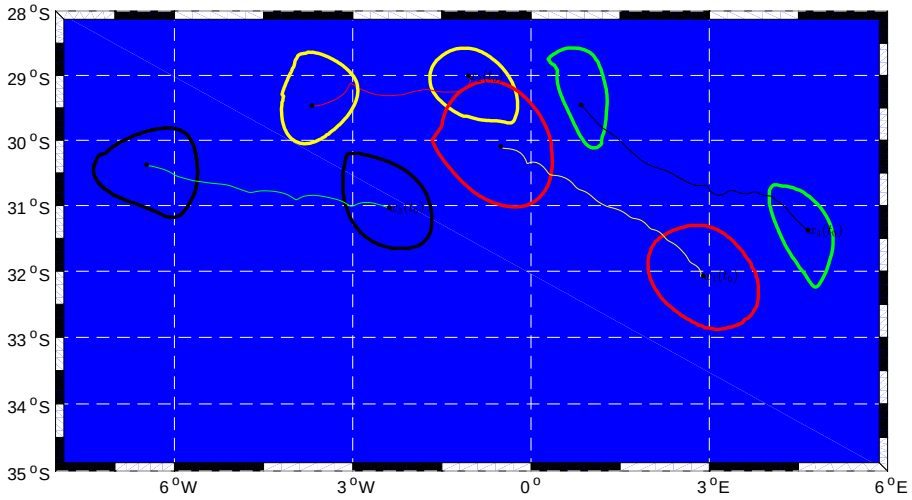

(b)

Figure 6-13: a) Coherent vortices and their centers at time t_0 extracted using definition.1 with the $\mathcal{LACC}\mathcal{L}_{t_0}^{t_f}(\mathbf{x}_0)$ map shown in background . b) Their initial and final positions under Lagrangian advection. (See the supplemental movie M5 for the complete advection sequence of these vortices.)

the Coriolis parameter (twice the local vertical component of the angular velocity of the Earth). By applying a slow-manifold reduction to the Maxey-Riley equations [Maxey and Riley, 1983] in the limit of small Rossby numbers, it has been shown by

[Beron-Vera et al., 2015] that the inertial particle motion satisfies:

$$\dot{\mathbf{x}} = \mathbf{v}(\mathbf{x},t) + \tau(\delta-1)f\mathbf{J}\mathbf{v} + \mathcal{O}(\tau^2), \quad \begin{pmatrix} 0 & -1 \\ 1 & 0 \end{pmatrix}, \quad \mathbf{x} \in \mathbb{R}^2, \quad t \in [\alpha, \beta] \tag{6.17}$$

where

$$\delta = \frac{\rho}{\rho_{part}}, \quad \tau := \frac{2r_0^2}{9\nu\delta} \tag{6.18}$$

Remarkably, in the limit of vanishing Rossby numbers, cyclonic attractors for light particles ($\delta > 1$) and anticyclonic attractors for heavy particles ($\delta < 1$) in (eq.6.17). We select the computational domain in the longitudinal range $[2°W, 4°W]$ and the latitudinal range $[-30°N, -32°N]$, which falls inside the region of the Agulhas leakage in the Southern Ocean.

We consider the AVISO data set ranging from the initial time $t_0 = 11$ November 2006 to the final time $t_f = t_0 + 90$ days. We integrate this satellite velocity data (7.12) using the Maxey-Riley the equation.6.17. Inertial particles were assumed to have $r_0 = 0.25m$, which is a realistic radius value for commonly employed spherical drifting buoys. Both light and heavy particles were considered, with $\delta = 1.1$ and 0.9, respectively. Here, we illustrate our method over a different scenario: a vortex with a radial flow where the particles' trajectory converge toward its attracting center. We show in Fig.6-14(a) an example of this vortex and its center extracted from the $\mathcal{LACCL}_{t_0}^{t_f}(\mathbf{x}_0)$ map. Fig. 6-14(b) shows its initial and final position under Lagrangian advection. This confirms that its boundary does not fold or filament under Lagrangian advection even when it shrinks by time. This also shows that the $\mathcal{LACCL}$-based vortex center acts as an attractor for heavy particles released in an anticyclonic eddy. The complete advection sequence over the time interval [0, 90] is illustrated in the movie M6.

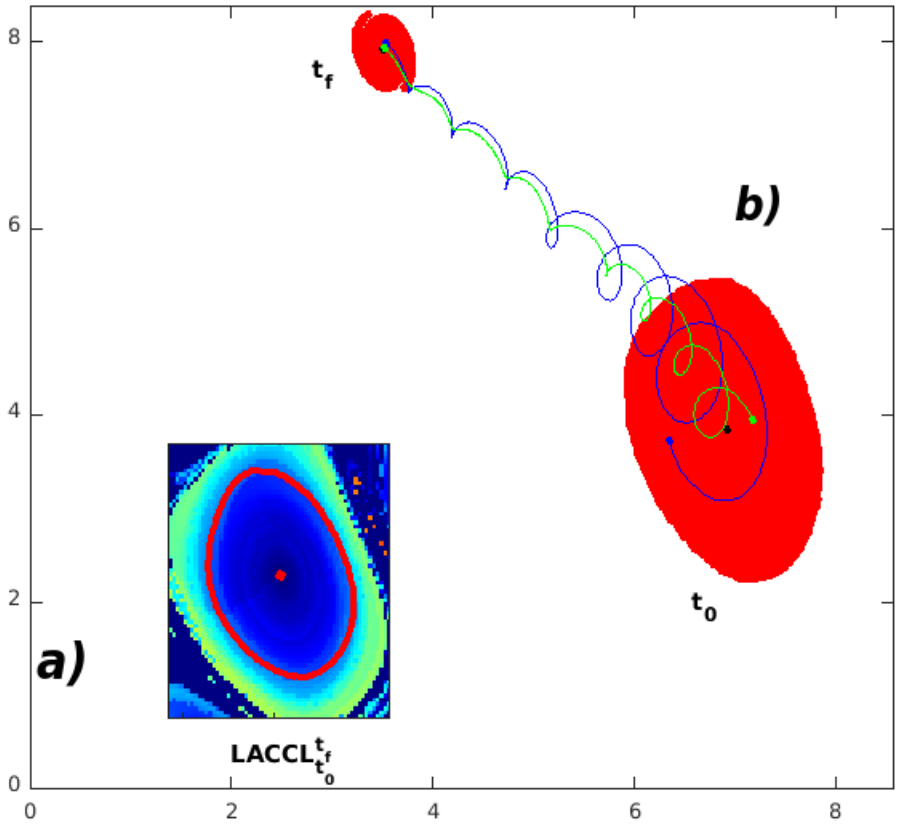

Figure 6-14: a) Coherent vortex and its center at time t_0 extracted using definition.1 with the $\mathcal{LACCL}^{t_f}_{t_0}(\mathbf{x}_0)$ map shown in background . b) Its initial and final positions under Lagrangian advection. (See the supplemental movie M6 for the complete advection sequence of this vortices.).

6.8 Conclusion

We proposed an objective definition of Lagrangian vortices from particles trajectory. We defined these vortices as closed material lines in which fluid parcels exhibit similar rotation. These closed material lines are obtained based on particles' trajectory decomposition. We expressed vortices boundaries as closed convex curves of the Lagrangian Averaged Closed Curve Length ($\mathcal{LACCL}$). Our method enables the identification of vortex center as the most-inner member of $\mathcal{LACCL}$. We illustrated our new method on several two-dimensional flows including ocean surface velocities derived from satellite altimetry, over the region of Agulhas leakage in the Southern Ocean. In this region, such Lagrangian analysis of coherent mesoscale eddies is important, due to their noticeable effect on global circulation and climate [Beal et al., 2011]. Our

results show that vortices boundaries and their centers obtained are sharply defined, do not fold or filament. Our method has the advantage of not requiring high-grids advection of fluid parcels. It is suitable to applications to float data. Moreover, it can be adapted to select vortices boundaries occurring over different time interval.

Chapter 7

A Fourier approach to Lagrangian coherent vortices detection

Abstract

This chapter is a follow-up of the previous chapter. Here, I study the transport properties of coherent vortices over a finite time duration and show that such vortices can be identified based on frequency-domain representation of Lagrangian trajectories. Fourier analysis is used to convert particles' trajectories from their time domain into a representation in the frequency domain. Coherent vortices are identified and extracted as material surfaces along which particles' trajectories share similar frequencies. The method identifies all coherent vortices in an automatic manner, showing high vortices' monitoring capacity. I illustrate the new method by identifying and extracting coherent Lagrangian vortices in different two- and three-dimensional flows.

7.1 Introduction

It has long been acknowledged that even unsteady flows with aperiodic time dependence admit coherent structures, such patterns are mostly in the shape of vortices that remain coherent over time exceeding typical time scales in the flow. In the previous chapter, I proposed a geometrical approach to identify and extract such coherent vortices from the analysis of particles' trajectories. The present chapter is also devoted to studying Lagrangian coherent vortices. Here, I propose a different approach based on frequency-domain analysis of Lagrangian particle trajectories. I represent

particles' trajectory in their frequency domain in the form of sinusoids. Each sinusoid is characterized by an amplitude which gives information about vortex's diameter and frequency, the latter measures the vortex-turn-over in time. The latter part yields an objective measure of material rotation. I define a Lagrangian coherent vortex as a closed material surface in which fluid parcels complete the same rotation. In the frequency domain, this turns out to be filled with outward-increasing tubular level-sets of particle trajectories' frequencies.

7.2 Set-up

We consider a time-dependent smooth vector field:

$$\mathbf{v}(\mathbf{x}, t), \quad \mathbf{x} \in \mathbb{R}^3, \quad t \in [\alpha, \beta] \tag{7.1}$$

and its associated ordinary differential equation:

$$\dot{\mathbf{x}} = \mathbf{v}(\mathbf{x}, t), \quad \mathbf{x} \in \mathbb{R}^3, \quad t \in [\alpha, \beta] \tag{7.2}$$

where $\mathbf{v}$ a smooth velocity field defined on a domain:

$$\mathbf{U}(t) \subset \mathbb{R}^3, \quad \mathbf{U} = \bigcup_{t \in [\alpha, \beta]} \mathbf{U}(t) \subset \mathbb{R}^3 \times [\alpha, \beta] \tag{7.3}$$

The flow map is defined as the map that takes a particle from its initial location $\mathbf{x}_0$ at time t_0 to its location $\mathbf{x}_t$ at time t:

$$\mathbf{F}_{t_0}^{t}(\mathbf{x}_0) := \mathbf{x}(t, t_0, \mathbf{x}_0), \quad \alpha \leq t_0 \leq t \leq \beta, \tag{7.4}$$

$\mathbf{x}(t, t_0, \mathbf{x}_0)$ denoting the trajectory of Eq.7.2 passing through a point $\mathbf{x}_0$ at time t_0.

Consider a material domain (defined by a set of fluid particles) $\mathcal{M}(t_0)$ advected by the flow. Its image at time t can be expressed in term of the flow map as $\mathcal{M}(t) = \mathbf{F}_{t_0}^{t}(\mathcal{M}(t_0))$.

7.3 Method

The general outline of the proposed method is as follows. We produce particle trajectories by solving the ordinary differential equation 7.2. Next we apply the Fourier transform over each particle trajectory to represent them in the frequency domain. Finally, we seek coherent vortices as material surfaces along which particles' trajectories share similar frequencies' components.

7.3.1 Frequency-domain analysis and Fourier transform

Frequency-domain analysis is a cornerstone of signal and system analysis. While time-domain analysis shows how a mathematical function or a signal changes over time, frequency-domain analysis shows how their energies are distributed over a domain of frequencies. Furthermore, observing a given system from frequency point of view usually gives an intuitive interpretation of the qualitative behavior of the system. A given signal contains frequency information that can be computed using the Fourier transform which is recalled below.

If $x(t)$ is any signal, either integrable or of finite energy, the Fourier transform of x, $\mathcal{F}(x)(\xi)$, measures, at each frequency ξ, the amount of periodic information contained in x, by simply evaluating $< x \mid e^{-i\xi} >$ through an integral computation:

$$\mathcal{F}(x)(\xi) = \int_{\mathbb{R}} x(t) e^{-it\xi} dt \tag{7.5}$$

with the frequency spectrum defined as the mapping $\xi \mapsto |\mathcal{F}(\xi)|^2$.

If $x(t)$ is absolutely integrable on $]-\infty, +\infty[$, then $\mathcal{F}(\xi)$ is continuous, $\mathcal{F}(\xi) \to 0$ as $\xi \to \pm\infty$, and

$$|\mathcal{F}(\xi)| \leq \int_{-\infty}^{+\infty} |x(t)| dt \tag{7.6}$$

In present scenario, continuous signals are sampled and quantized to get a discrete domain signal. This approach helps employing a variety of digital signal processing operations. In signal processing field, the Fourier transform is mostly computed using

the Fast Fourier Transform algorithm (FFT).

7.4 Vortex trajectory in time domain

Various studies have addressed the problem of coherent vortex identification based on their observed trajectories. In [Mancho et al., 2013] authors use trajectory length to reveal the time t_0 positions of geometrical structures of different dynamics. This method is supposed to display an imprint of Lagrangian coherent structures as shown in [Mancho et al., 2013]. However, no existing mathematical link between that method's features and material coherent structures [Hadjighasem et al., 2017]. Moreover, the scalar field does not allow the identification and extraction of coherent vortices to allow their tracking and monitoring. Another method which make use of particles' trajectories to identify coherent structures is presented in [Hadjighasem et al., 2016]. This has been done by classifying fluid particles into coherent and incoherent classes. In their work, a coherent structure is described as a set of Lagrangian trajectories that keep minimum distances between themselves with respect to others outside the structure. This method is simple to implement but it has no link between material vortices and the expected spinning motion [Hadjighasem et al., 2017].

Particle trajectory produced by integrating the velocity vector field in a vortex results into a loopy curve as shown in Fig.7-1, this figure shows trajectories' examples of particles initialized within a given vortex. Thus, a natural way to identify vortex is by locating particle trajectories which exhibit spinning motion. By neglecting the vertical components, particles' trajectories in Fig.7-1 result in continuous curves which intersects themselves and create closed-curves segments each time a particle returns to one of its former positions after some time such as in Fig.7-1. Based on this idea, authors in [Dong et al., 2011] proposed a scheme to identify loops from trajectories of oceanic surface drifters. Such method indeed does identify the existence of eddies, but it does not identify vortices' cores or boundaries. Moreover this method leaves several unaddressed vortices cases where particle trajectories don't intersect themselves; for example, given a vortex with zero-translating speed and radial flow

where the particles' trajectories converge according to inflow.

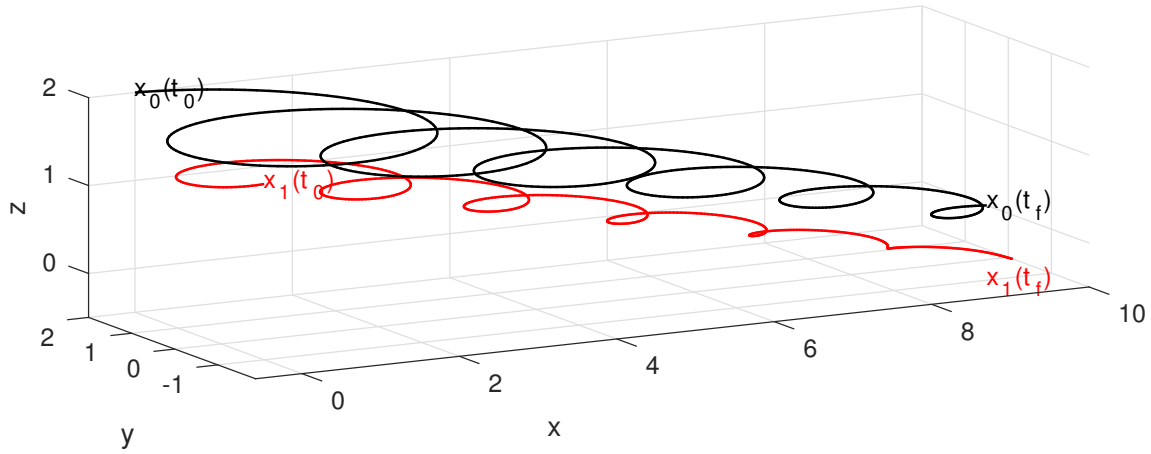

(a)

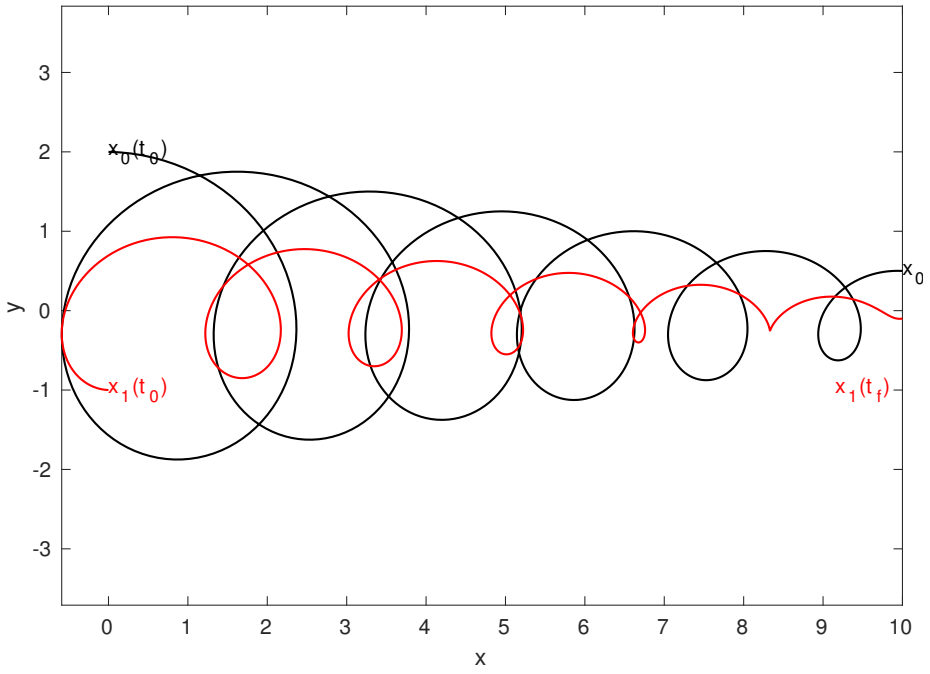

(b)

Figure 7-1: a) Two particle trajectories within the same vortex: particle within the vortex boundary is presented in black while red color refers to a particle near by the vortex center. b) Their projection on the (x, y) coordinates.

7.5 Particle trajectory in frequency domain

In spatial domain, particle's trajectory coordinates are represented by the Euclidean components x, y and z, where they refer to their spatial position. In this domain, a particle trajectory within a vortex results into a loopy curve as shown in Fig.7-1. Its time projection over each of the spatial direction results into three components responsible for plane and vertical movement as shown in Fig.7-2. The x and y components of this particle trajectory show the emergence of an attractor associated with vortical motion. They display periodic motions characterized by a frequency presenting the vortex-turn-over time and an amplitude referring to the vortex radius.

In frequency domain, particle trajectory coordinates refer to frequencies ξ_x, ξ_y and ξ_w in each of the spatial directions. Fig.7-3 shows the frequency-domain representation of particles' trajectories in the Fig.7-1 after excluding the drift effect. Both red and black trajectories share the same frequency but have different amplitudes. Here we see that analyzing such trajectories in their frequency domain representation is more easier than analyzing their general shapes.

7.6 Defining vortices from their frequency components

We seek to identify Lagrangian coherent vortices as closed material surfaces along which particles exhibit similar rotations around the same axis, and over a finite time interval. In the frequency domain representation, we seek Lagrangian coherent vortices as closed material surfaces along which particle trajectories share similar frequencies' components [El Aouni et al., 2019d]. In this domain, a particle trajectory can further be divided into two components; frequency which gives information about uniformly rotating flow, and the amplitude that describes the radius of a rotating particle. Based on the fact that fluid particles along vortex boundary exhibit the same polar rotation, we only consider the first part which gives information about the frequency of particle trajectory.

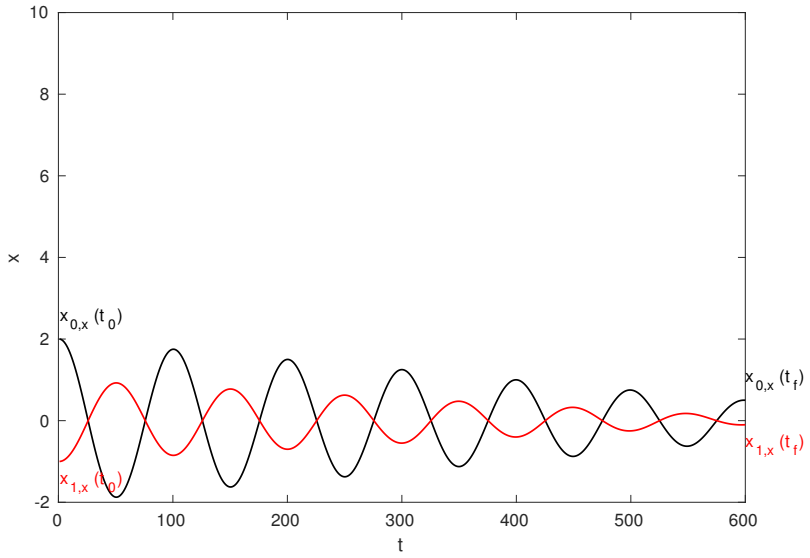

(a)

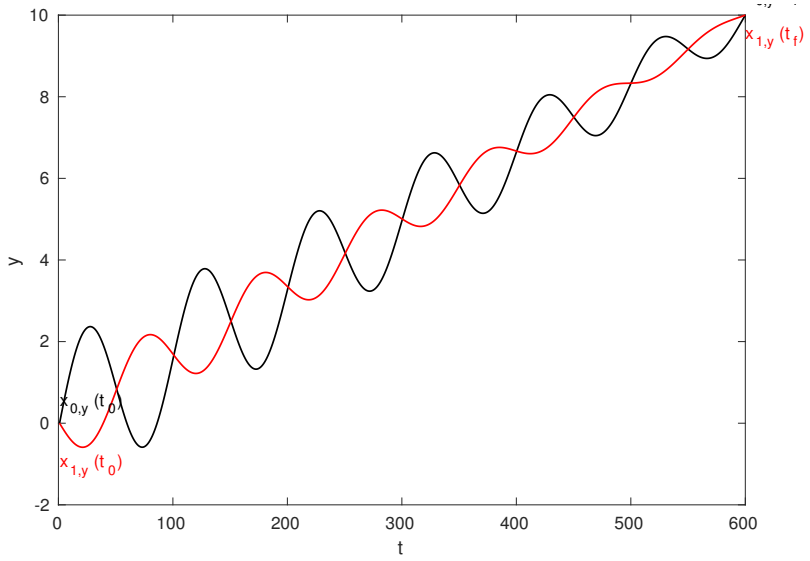

(b)

Figure 7-2: Two particle trajectories within the same vortex: particle within the vortex boundary is presented in black while red color refers to a particle near by the vortex center.

We define Lagrangian Trajectory Frequency $\mathcal{LTF}$ as:

$$\mathcal{LTF}^{\xi}(\mathbf{x}(\cdot, t_0, \mathbf{x}_0)) := \int_{t_0}^{t_n} \mathbf{x}(t, \mathbf{x}_0) e^{-it\xi} dt, \qquad \xi = (\xi_1, \xi_2, \dots \xi_n) \tag{7.7}$$

where $\xi = (\xi_1, \xi_2, \dots \xi_n)$ presents a vector of n frequencies of a given particle tra-

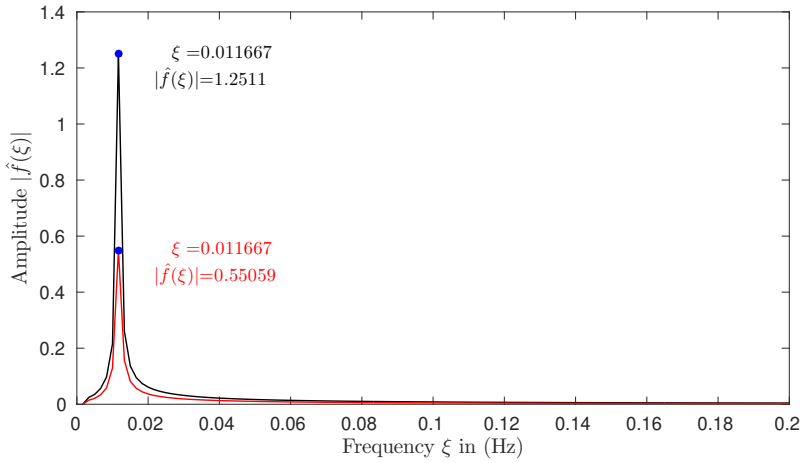

(a)

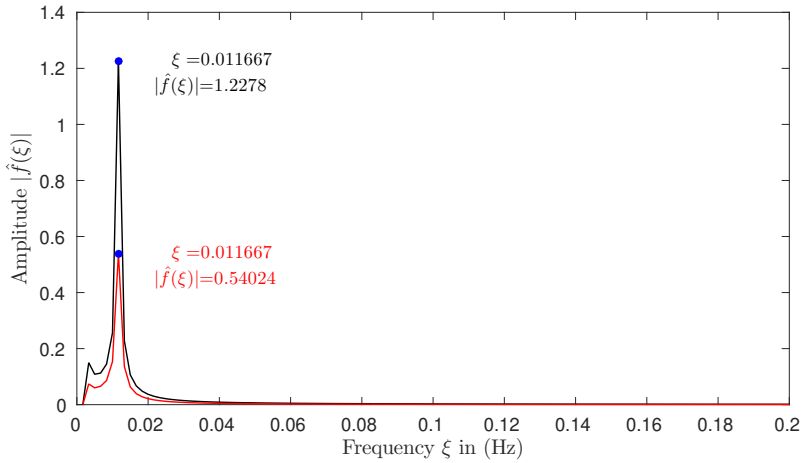

(b)

Figure 7-3: Frequency-domain representation of the particles' trajectories in Fig.7-1, red an black trajectories have the same frequency but different amplitudes: a) within x-direction, b) within y-direction.

jectory. With that, we are computing n points of a one-dimensional Fourier transform. For a particle fluid starting from $\mathbf{x}_0$, the $\mathcal{LTF}^{\xi}(\mathbf{x_0})$ vector field is a dynamically consistent measure of material rotation; the average frequency weighted by the frequency spectrum:

$$\overline{\xi} = \frac{\int_{\xi_0}^{\xi_n} \xi d\xi |\mathcal{LTF}^{\xi}|^2}{\int_{\xi_0}^{\xi_n} d\xi |\mathcal{LTF}^{\xi}|^2} \tag{7.8}$$

gives a consistent measure of particle rotation, whereas, the mean average of the magnitude $\overline{|\mathcal{LTF}^{\xi}(\mathbf{x_0})|}$ is a consistent measure of particle rotation radius.

We now use the $\mathcal{LTF}$ to identify closed material surface along which fluid parcels

experience the same rotation over a time interval $[t_0\ t_f]$. Time t_0 positions of such material tubes are tubular level (a convex contour in two dimensions, and a convex cylindrical or cone-shaped set in three dimensions) surfaces of the scalar $\overline{\xi}$, with $\xi \mapsto |\mathcal{LTF}^{\xi}(\mathbf{x}_0)|^2$. By definition, the $\overline{|\mathcal{LTF}^{\xi}(\mathbf{x_0})|}$ map allows the identification of vortex' center as inner most member of the vortex with the minimal rotation radius.

We summarize the $\mathcal{LTF}$-based vortex identification in the following definition, with its geometry illustrated in Fig.7-4-a.

Definition 2. *For a given time interval* $[t_0, t_f]$*:*

- *1) Lagrangian coherent vortex is an evolving material domain* $\mathbf{U} = \bigcup_{t\in[t_0,t_f]} \mathbf{U}(t) \subset \mathbb{R}^3 \times [t_0, t_f]$ *such that* $\mathbf{U}(t_0) \subset \mathbb{R}^3$ *is filled with a nested family of tubular level surfaces of* $\overline{\xi} = \frac{\int_{\xi_0}^{\xi_n} \xi d\xi |\mathcal{LTF}^{\xi}|^2}{\int_{\xi_0}^{\xi_n} d\xi |\mathcal{LTF}^{\xi}|^2}$.
- *2) The boundary* $\mathbf{B} = \bigcup_{t\in[t_0,t_f]} \mathbf{B}(t) \subset \mathbb{R}^3 \times [t_0, t_f]$ *of* $\mathbf{U}$ *is the outermost closed material surface of* $\overline{\xi}$ *in* $\mathbf{U}(t_0)$.

In the computational world, we relax the convexity strictness for closed material surface of $\overline{\xi}$. The first reason for this convexity relaxation consists of allowing small tangential filamentation even at time t_0 of vortices' boundaries (Fig.7-4-b-1). The second reason consists of the nature of multi-scale data, such data shows the presence of small-scale vortices nearby the boundaries of big-scale vortices (Fig.7-4-b-2). The third reason consists of the representation of vortices' boundaries by discrete polygons (Fig.7-4-b-3). At the initial time t_0, the definition 1 identify Lagrangian coherent vortices with a simple geometry, that is by defining a parameter of maximal convexity deficiency d_{max} to allow the relaxation of convexity strictness. This enables capturing filamented parts that rotate together with the vortices without a global breakaway. The aforementioned definition allows the identification of vortex boundary $\mathbf{B}(\mathbf{t_0})$ which has convexity deficiency less than the maximal limit d_{max}. We define the convexity deficiency of a closed curve in the plane as the ratio of the area difference between the curve and its convex hull to the area enclosed by the curve as: $d = \frac{A(Conv(\mathbf{B}(\mathbf{t_0})))-A(\mathbf{B}(\mathbf{t_0}))}{A(\mathbf{B}(\mathbf{t_0}))}$. Fig.7-4-b shows the geometrical view of the convexity deficiency

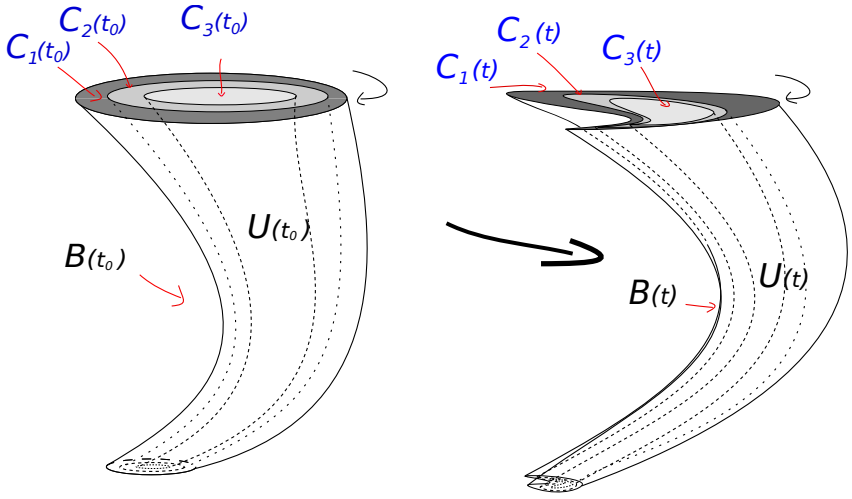

(a)

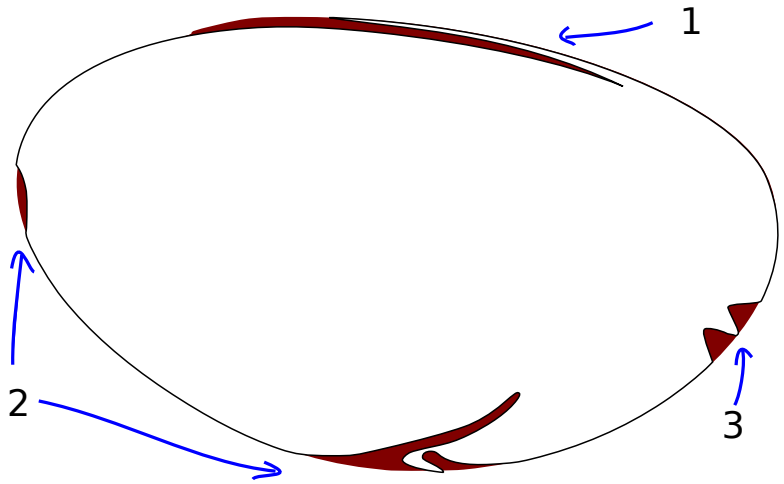

(b)

Figure 7-4: a) Initial and time t positions of a coherent Lagrangian vortex $\mathbf{U}(t)$ and a Lagrangian vortex boundary $\mathbf{B}(t)$. Also shown within $\mathbf{U}(t)$ are different vortex cores $\mathbf{C}(t)$ along which particles' trajectories share different frequencies over the time interval $[t_0, t]$. b) An example of a closed material line which profits from the relaxation of convexity to small convexity deficiency. Dark red area indicates the area difference between the closed material line and its convex hull: (1) minor tangential filamentation, (2) deformation by smaller-scale vortices, (3) discrete approximation of a convexity.

parameter, the dark red color refers to the difference between the curve (in white) and its convex hull.

Lagrangian vortices, as well as their boundaries are materials objects [Haller et al., 2016]. Thus, their position at a given time t is only determined by Lagrangian

advection:

$$\begin{gathered}\mathbf{U}(t) = \mathbf{F}_{t_0}^{t}(\mathbf{U}(t_0)), \quad \mathbf{B}(t) = \mathbf{F}_{t_0}^{t}(\mathbf{B}(t_0)), \\ t \in [t_0, t_f]\end{gathered} \tag{7.9}$$

The $\mathcal{LTF}$-vortex approach differs from the previous definitions, it does define vortex based on the frequency domain representation of their trajectories; more precisely, it defines vortices as closed material surfaces along which particles share similar frequencies. Our method does not require differentiation of particles trajectories with respect to their initial positions, thus, it does not require advection of high-density grids. $\mathcal{LTF}$-vortex might show material filament, but by definition, they will all rotate together with the vortex without breaking away.

7.7 Experiments

Here we present numerical results that confirm our theoretical predictions regarding the identification of coherent vortices.

7.7.1 Two-dimensional examples

Direct numerical simulation of two-dimensional turbulence

We solve numerically the Navier-Stokes PDE model for the time evolution of 2 components of the velocity, $u : \mathcal{D} \to \mathbb{R}^2$ of an incompressible fluid on a torus, $\mathcal{D} = [0, 2\pi] \times [0, 2\pi]$. This can be expressed as:

$$\begin{aligned}
\partial u_t + u \cdot \nabla u &= -\nabla p + \frac{1}{Re}\Delta u + f, && (x,t) \in \mathcal{D} \times [a,b], \\
\nabla \cdot u &= 0, && (x,t) \in \mathcal{D} \times [a,b], \\
\int u^j dx &= 0, && (x,t) \in \mathcal{D} \times [a,b], j = 1,2, \\
u &= u^*, && (x,t) \in \mathcal{D} \times \{0\}
\end{aligned} \tag{7.10}$$

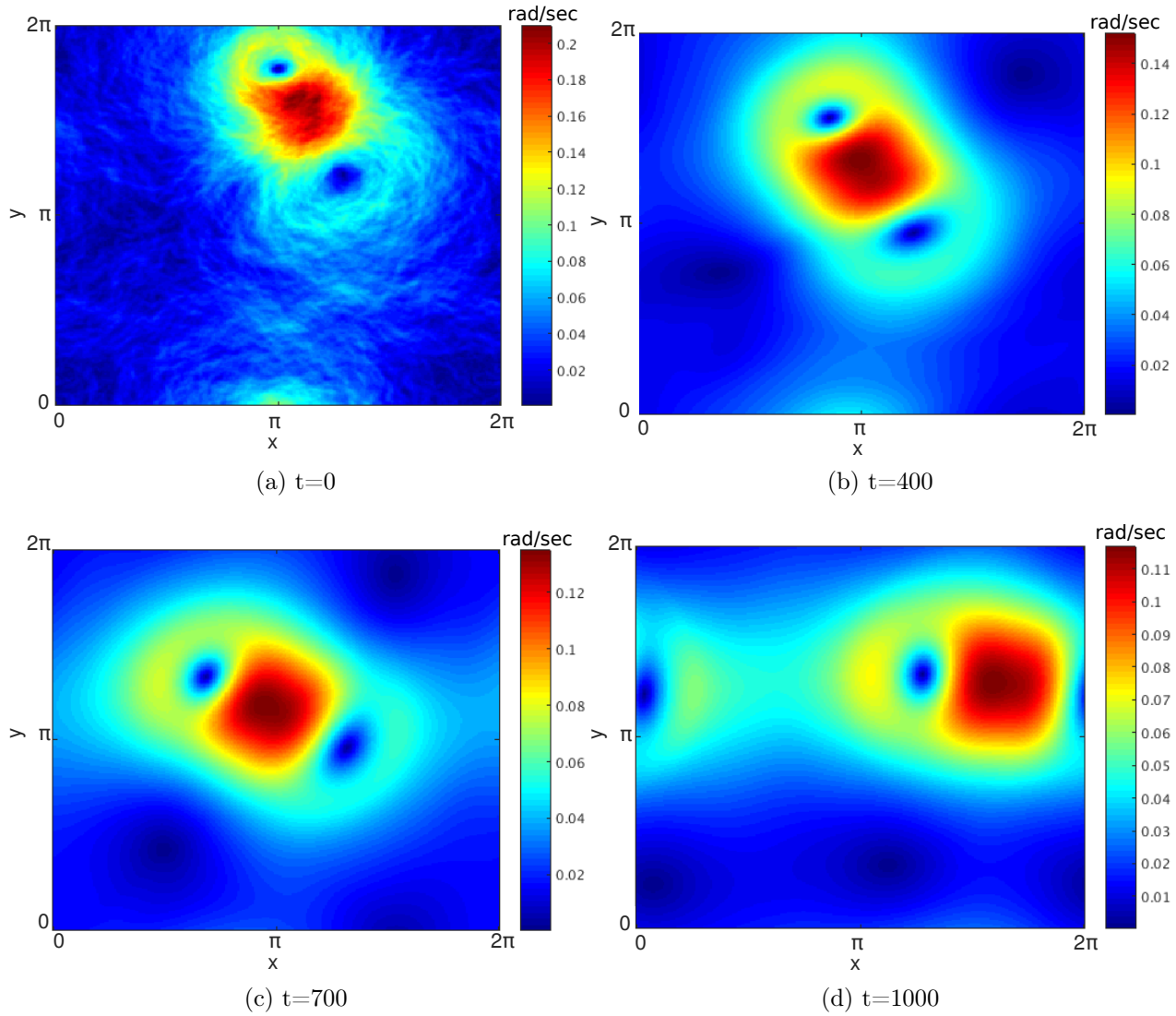

(a) t=0 (b) t=400

(c) t=700 (d) t=1000

Figure 7-5: Time evolution of the magnitude of fluid velocity, governed by the Navier-Stokes model 7.10, over two spatial dimensions: the angle of the inner ring (horizontal axis) and outer ring (vertical axis) of a two dimensional torus. Angles are expressed in radians. Velocities are evaluated at times t = (0, 400, 700, 1000).

Where $u \cdot \nabla u$ is the inertial term which characterizes Navier-Stokes equation, and is responsible for the transfer of kinetic energy in the turbulent cascade. ∇p is the pressure gradients which guarantee the incompressibility of the flow, and $\frac{1}{Re}\Delta u$ is the the dissipative viscous term. We further assume periodic boundary conditions and use a standard pseudo-spectral method with 512 modes in each direction and 2/3 dealiasing to solve the above Navier-Stokes equation with Reynolds number $Re = 10^4$ on the time interval $t \in [0, 1000]$. The model is parametrized by the pressure function

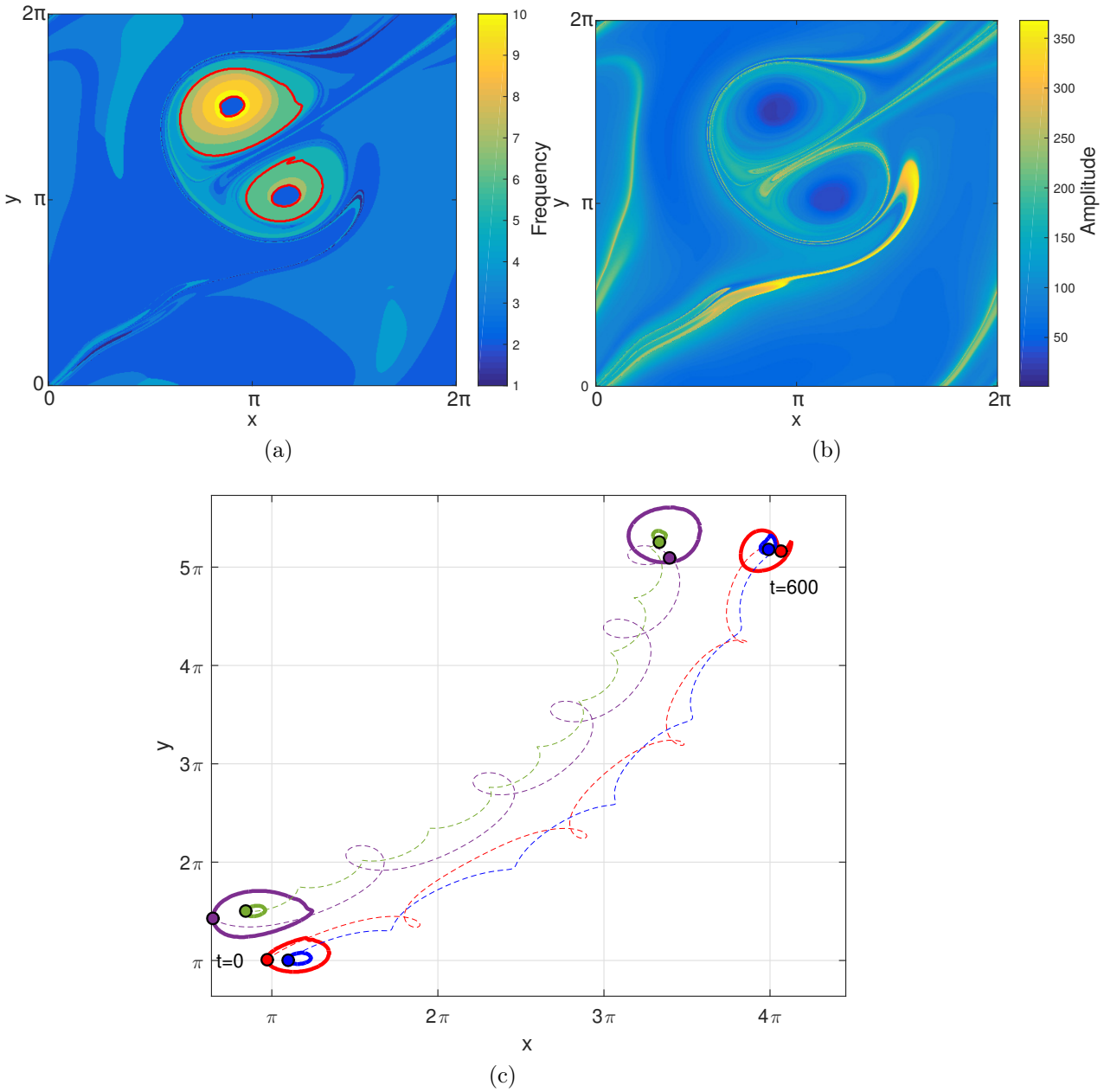

Figure 7-6: a) Lagrangian coherent vortices at time t_0 extracted from the velocity field generated by Navier-Stokes model 7.10 using definition.1 with the $\overline{\xi}$ map shown in background, with $\xi \mapsto |\mathcal{LTF}^{\xi}(\mathbf{x}_0)|^2$. b) The mean-average magnitude $\overline{|\mathcal{LTF}^{\xi}(\mathbf{x}_0)|}$ highlighting areas of spinning movement. c) Their initial and final positions under Lagrangian advection as well as different particles initialized within their boundaries and their trajectories in Dashed line. (See the supplemental movie M7 for the complete advection sequence of these vortices.)

$p : D \times [a, b] \to \mathbb{R}$, with no external forcing ($f = 0$). We initialize the system with

the vorticity of two adjacent vortices perturbed by a random uniform distribution:

$$\overline{\omega}|_{t_0} = exp(\frac{(x-\pi)^2 + (y-2\pi-\pi/4)^2}{0.2}) - exp(\frac{(x-\pi-\pi/4)^2 + (y-\pi-\pi/4)^2}{0.8}) \quad (7.11)$$

We use the vorticity stream formulation [Spotz and Carey, 1995] for implementation and get back velocity and pressure from the stream function. The flow integration is then carried out over the interval $t \in [400, 1000]$, in which the turbulent flow is under fully developed turbulence, by a fourth-order Runge-Kutta method with variable step-size.

Fig.7-5 shows the forward simulated velocity field, obtained at four distinct time points by the Navier-Stokes model 7.10, over two-dimensional plane defined by: the angle of the inner and outer rings of a two dimensional torus.

To construct the $\mathcal{LTF}^{\xi}$ vector field, we consider an initial grid of 512×512 points and integrate the simulated velocity field over the time interval $[t_0 = 400, t_f = 1000]$ using the eq.7.2.

Fig.7-6(a) shows coherent vortices extracted from the $\overline{\xi}$ map computed from the simulated realization of fluid velocity of the model 7.10, with $d_{max} = 10^{-3}$. For each vortex we extract the inner- and outer-most cores. Fig. 7-6(c) shows their final position under Lagrangian advection as well as trajectories of particles initialized on their boundaries. These Lagrangian vortices maintain their coherency, they don't stretch or fold. The complete advection sequence over the time interval $[t_0 = 400, t_f = 1000]$ is illustrated in the movie M7.

7.7.2 Two-dimensional eddies in satellite altimetry

Here, we use sea surface velocity data to illustrate the detection of Lagrangian vortices. This velocity data is derived from satellite altimetry under the geostrophic approximation where sea-surface height $\eta(\varphi, \theta, t)$ serves as a non-canonical Hamiltonian for surface velocities in the (φ, θ) longitude-latitude coordinate system. The

evolution of fluid particles satisfies

$$\begin{aligned}\dot{\varphi}(\varphi,\theta,t) &= -\frac{g}{R^2 f(\theta)\cos\theta}\partial_\theta \eta(\varphi,\theta,t)\\ \dot{\theta}(\varphi,\theta,t) &= \frac{g}{R^2 f(\theta)\cos\theta}\partial_\varphi \eta(\varphi,\theta,t)\end{aligned} \tag{7.12}$$

where g is the constant of gravity, R is the mean radius of the Earth and $f(\theta) = 2\Omega\sin\theta$ is the Coriolis effect, with Ω denoting the Earth's mean angular velocity. This data is produced by Ssalto/duacs multi-mission sea level products provided by AVISO (CLS/Archiving, Validation, and Interpretation of Satellite Oceanographic data)[1] with a spatial resolution of $1/4°$ and temporal resolution of 7 days.

We chose the region of the Agulhas leakage in the Southern Ocean, spans from $[-28°N, -4°W]$ and $[-35°N, 9°W]$. This region is well known for its long-lived propagating eddies that carry water properties from the Indian ocean far into the South Atlantic [Ruijter et al., 1999]. In this study, we chose the time period between 11/11/2006 and 11/1/2007.

We integrate the AVISO data set (eq.7.12) over the period of time between $t_0 = 11$ November 2006 and $t_f = t_0 + 90$ days over an initial grid of particles with step size $\Delta x_0 = 1/50°$. We show in Fig.7-7(a) $\overline{\xi}$ map computed from the satellite velocity field (eq.7.12). In the same image, we show coherent eddies' boundaries as they are extracted from the $\overline{\xi}$ map, with $d_{max} = 10^{-3}$. In Fig.7-7(c), we show their initial and final position under Lagrangian advection as well as trajectories of particles initialized on their boundaries. These eddies remain coherent. The complete advection sequence over the time interval [0, 90] is illustrated in the movie M8.

Three-dimensional Agulhas eddies in a data-assimilating circulation model

Here, we apply $\mathcal{LTF}$-based vortex extraction to a three-dimensional unsteady velocity field set obtained from the Southern Ocean state estimation (SOSE) model [Mazloff et al., 2010]. The domain of the data set lies in the area of the Agulhas leakage in the Southern Ocean.

[1] http://www.aviso.oceanobs.com/duacs/

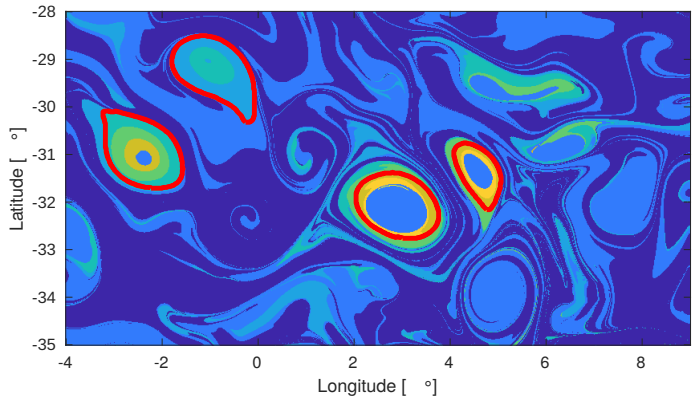

(a)

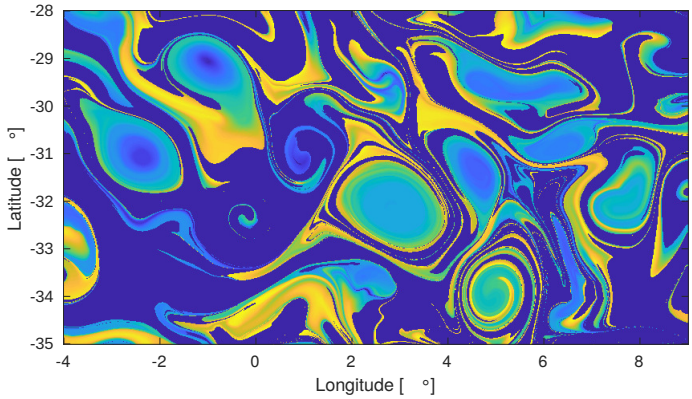

(b)

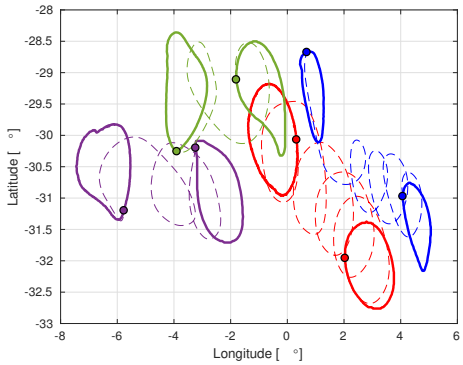

(c)

Figure 7-7: a) Coherent eddies at time t_0 extracted using definition.1 with the $\overline{\xi}$ map shown in background, with $\xi \mapsto |\mathcal{LTF}^{\xi}(\mathbf{x}_0)|^2$. b) The mean-average magnitude $\overline{|\mathcal{LTF}^{\xi}(\mathbf{x}_0)|}$ highlighting areas of spinning movement. c) Their initial and final positions under Lagrangian advection as well as different particles initialized within their boundaries and their trajectories in Dashed line. (See the supplemental movie M8 for the complete advection sequence of these vortices.)

Our Lagrangian study covers a period of $T = 30$ days, ranging from $t_0 = 15$ May 2006 to $t = 15$ june 2006. As in [Haller et al., 2016], we select the computational domain bounded by longitudes $[11°E, 16°E]$, latitudes $[37°S, 33°S]$ and depths $[7, 2000]$ m. We compute the $\mathcal{LTF}$ vector field over a uniform grid of $150 \times 160 \times 60$ points, and identify a Lagrangian coherent eddy.

Fig.7-8(a) shows the three-dimensional field of the $\overline{\xi}$, $\xi \mapsto |\mathcal{LTF}^{\xi}(\mathbf{x}_0)|^2$ with the eddy's inner- and outer-most cores enclosed with red color. Particles belonging to these two cores have different frequencies. Fig.7-8(b) shows the initial position of a coherent Lagrangian eddy boundary (dark red), extracted as level sets of $\overline{\xi}$. Also shown is a nearby $\overline{|\mathcal{LTF}^{\xi}|}$ level surface outside the eddy boundary, illustrating the complexity of the near-surface mixing region enclosing the eddy. Fig.7-8(c) gives a full view of the Lagrangian eddy. Fig.7-8(d) shows the initial and the materially advected position of the eddy at the final time $t_f = t_0 + 30$ days, whereas, Fig.7-8(e) shows the initial and final position of different eddy's layers presented in different colors. As anticipated there is moderate tangential filamentation in the material eddy boundary, but precisely no breakaway from the rotating eddy core. This high degree of material coherence in the presence of the complex surrounding material mixing demonstrates the efficiency of $\mathcal{LTF}$-based vortex detection.

7.8 Conclusion

We have presented an objective (completely observer-independent) frequency-domain definition of Lagrangian coherent vortices as closed material surfaces along which fluid parcels exhibit the same intrinsic rotation. This coherent material is obtained from the frequency-domain representation of their trajectories. This intrinsic rotating material is expressible as material tube characterized by a given frequency. We illustrated our new method on different two- and three-dimensional flows. Our results show that vortices boundaries obtained are sharply defined. Our approach does not require advection of high-density material grids, a generally an expensive computational procedure in Lagrangian coherence calculations. Moreover, it is suitable to applications

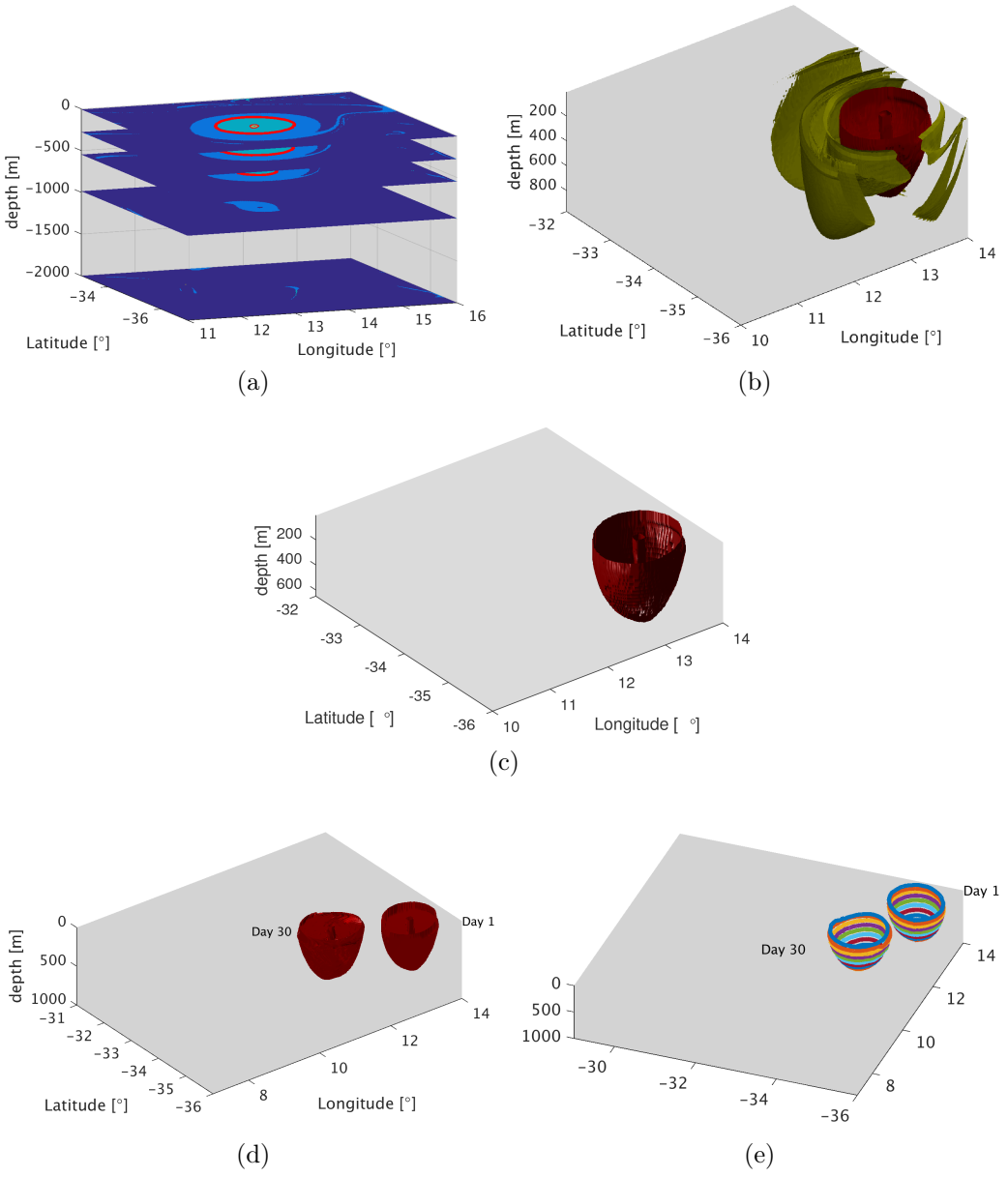

Figure 7-8: a) A three-dimensional field of the $\overline{\xi}$, with $\xi \mapsto |\mathcal{LTF}^{\xi}(\mathbf{x}_0)|^2$. b) Representative level surfaces of $\overline{\xi}$. The dark red surface is extracted using the definition.1, marking the vortex boundary for a mesoscale coherent Lagrangian eddy, extending from 7 m down to 600 m in depth. The green surface is a nearby level surface of $\overline{|\mathcal{LTF}^{\xi}|}$ outside the Lagrangian eddy region. c) Full view of the Lagrangian eddy boundary. d) The initial and the advected eddy boundary 30 days later, whereas e) shows initial and the advected images of different layers of the eddy. (See the supplemental movie M9 and M10 for the complete advection sequence of these vortices.)

to float data.

Chapter 8

Coherent water transport off the North-West African Upwelling

Abstract

In this chapter, I explore the impact of the NWA upwelling system over the open ocean. I do this by exploring the role played by mesoscale eddies off the Canary archipelago in carrying coherent waters from the upwelling regions and pouring them into the open ocean. I use the method I proposed in the previous chapter to extract coherent mesoscale eddies from a 24 years dataset of sea surface velocity field derived from satellite surface altimetry. I investigate their lifespan, create a sequence of consistent fluid transport, and assess the significance of the achieved transport estimations. I use these mesoscale eddies to compute coherent fluid transport off Canary Islands, which I prove to be lower (by about one order of magnitude) than previous transport estimates.

8.1 Introduction

Eastern Boundary Upwelling zones (EBUZ) include some of the most productive ecosystems in the world, particularly the Canary Current Upwelling System (CCUS) which presents one of the world's major Upwelling regions. Unlike the other (EBUZ), CCUS includes a source of mesoscale eddies; the existence of the Canary Island archipelago which act as a barrier perturbing the southwestward flowing Canary Current [Arístegui et al., 1997, Arístegui et al., 1994], along with the mechanism played

by the wind shear at the islands wake which permits eddy shedding at relatively low intensities of the Canary Current. Thus, in addition to upwelled cold and nutrient-rich deep waters, significant energy is transferred into oceanic mesoscale eddies that are almost continuously spun off by the archipelago. This can play a significant role in carrying water properties from the cold nutrient-rich Upwelling in the direction of the open ocean which can have a relevant impact on the global and regional distribution of the biological and physical water properties.

Oceanic eddies generated at the Canary Islands have been intensively investigated over the last two decades [Arístegui et al., 1994, Sangrà et al., 2005, Sangrà et al., 2009]. Their first observations were from remote sensing [La Violette, 1974, Hernández-Guerra, 1990, Hernández-Guerra et al., 1993]. They were identified as cold (warm) core cyclonic (anticyclonic) eddies from thermal images. Later, their principal characteristics such as diameter and depth were revealed from *in situ* data [Arístegui et al., 1994]. Afterwards, the focus of researchers shifted towards understanding their biological effects [Arístegui et al., 1997, Barton et al., 1998, Arístegui and Montero, 2005, Alonso-González et al., 2013, Lasternas et al., 2013] as well as determining their generation mechanisms [Piedeleu et al., 2009]. Other studies focused on their Lagrangian evolution [Sangrà et al., 2005, Sangrà et al., 2007]. [Sangrà et al., 2005] studied an eddy off Canary Islands based on the use of buoys together with thermal satellite images. Results show that the eddy remain coherent up to 200 days while traveling southwestward up to 500 km. Based on wavelet technique, [Sangrà et al., 2015] tracked Canary's eddies from surface geostrophy velocity fields. The finding shows that the impact of these eddies may be felt far from the islands, affecting the whole northeastern subtropical Atlantic region as they can extend as far as the Mid-Atlantic Ridge (MAR). They estimated the westward transport made by Canary Eddy Corridor to be higher than quarter of the southward transport made by the Canary Current. However, this long-term transport view on Canary's eddies can be questioned by the key characteristic of other structures of transport such as filaments [Wang et al., 2015, Haller et al., 2016]. Thus, it needs to be evaluated using a recent Lagrangian method designed to structure the shape of interest as it has been

done in other regions of the planet [Wang et al., 2015, Wang et al., 2016, Abernathey and Haller, 2018]. Indeed, Such Lagrangian descriptors have found their place in the oceanographic community. For example, [Haller and Beron-Vera, 2013] introduces a variational principle for coherent material vortices which was applied on eddies. This method was used to study the fluid transport off the Agulas region [Wang et al., 2015], which yield to be at least 2 orders of magnitude smaller than earlier transport estimation. A reexamination study made by [Wang et al., 2016] also used this Lagrangian method to investigate the life process of a coherent Agulhas ring. Their study inspected and reported a separate 2-years long-lived Agulas eddy, and conclude that their earlier finding was likely an underestimation of water transport made by Agulhas eddies. [Abernathey and Haller, 2018] use one of these methods to identify coherent eddies in the eastern Pacific and quantify their meridional transport which shows up to be below 0.1% compared to the meridional dispersion in their studied area. [Beron-Vera et al., 2018] use these Lagrangian methods to illustrate the development of coherent swirls in the ocean.

In the present work [El Aouni et al., 2019c, El Aouni et al., 2018c], we aim to present a more accurate estimation of water transport made by coherent eddies off the Canary Island archipelago using a recent Lagrangian method made for eddy's detection. We extract coherent mesoscale eddies from a 24 years dataset of sea surface velocity field derived from satellite surface altimetry. We investigate their lifespan, create a sequence of consistent fluid transport, and assess the significance of the achieved transport estimations. We extract coherent eddies using the method developed in the previous chapter. Free of the reference coordinate system, this technique enables the identification of coherent eddies and their tracking, in forward time until they vanish and in backward time until the moment of their genesis.

8.2 Methods

We use the method we proposed in the previous chapter in order to identify coherent eddies. Coherent eddies detection and tracking are implemented as follows:

(*i*) We start by fixing an area U and time interval $[t_0, t_f]$ over which we seek for coherent eddies. (*ii*) Within U, we set a grid G_U of introductory conditions over the period of time $[t_0, t_f]$. (*iii*) For each particle $\mathbf{x}_0 \in G_U$, simultaneously integrate equation 6.3 and solve the following equation from t_0 to t_f:

$$\mathcal{LACCL}(\mathbf{x}(t_f, t_0, \mathbf{x}_0)) = \sum_{i=1}^{n} \frac{\int_{t_i}^{t_i+\tau_i} \|\mathbf{v}(\mathbf{x}_0, t)\|\, dt}{n} \tag{8.1}$$

such as

$$\begin{gathered} \mathbf{x}(t_i + \tau_i) = \mathbf{x}(t_i), \quad \tau_i > 0 \quad \text{with} \quad i = 1 \cdots n \\ , \\ t_i \in]t_0\ t_f[, \quad t_{i+1} \notin [t_i\ t_i + \tau_i[\\ \text{and} \\ \mathbf{x}(t_{i+1}) \notin]\mathbf{x}(t_i)\ \mathbf{x}(t_i + \tau_i)[\end{gathered} \tag{8.2}$$

(*iv*) We start by determining local minima of LACCL fields, then identify eddies as outermost closed LACCL level curves. (*v*) Finally, passively advect the detected eddies boundaries to track their motion.

The velocity field considered here is derived from satellite acquired surface height (altimetry) under the geostrophic approximation $\mathbf{v}(\phi, \theta, t) = gf^{-1}\nabla^{\perp}\eta(\phi, \theta, t)$, with g being the gravity's acceleration constant, f presents the Coriolis coefficient, $\eta(\phi, \theta, t)$ is the sea surface height (SSH) and $\perp$ stands for a 90° anticlockwise rotation. These velocity data are provided daily on 1/4° ($25km$) resolution longitude-latitude grid. These data are collected from the Copernicus Marine Environment Monitoring Service ($CMEMS$) and corresponding to a period of 24 years, between January 1993 to December 2016. Here, 6 hours surface currents are generated using temporal linear interpolation which reduces trajectory overshooting. We chose $U = [21°N, 10°W] \times [32°N, 23°W]$ (indicated by a gray box in Fig.8-1). This Domain lies on the NWA Upwelling, a region distinguished by the existence of the Canary archipelago which led to permanent long-lived eddies off the islands. We set the advection time $t_f - t_0$ each time equal to 90, 180, 270 and 360 days which results in detecting eddies with different

lifetimes and maximum diameters diminishing from about 142 km to 38 km. Eddies' diameters hold out stable about 96% to 81%. 90 days eddies lose about 4% of their diameter while 360 days' ones lose about 19%. Eddies detection is carried out over 1993-2016 in a manner that U is packed with new coherent eddies at each time t_0, by that means avoiding redundant eddies' counting. We set G_U to be regular with square elements of 0.01° of spatial resolution. We use bilinear interpolation method with a step-size-adapting fourth-order Runge-Kutta to carry out all particles' integration.

8.3 Results

As we outlined the approach to determine and extract Lagrangian eddies, we now shift to the fundamental point of our study: the role of coherent eddies in westward transport.

8.3.1 Characteristics of canary's coherent eddies

Here we describe different characteristics related to coherent eddies of the Canary archipelago. Fig.8-1 shows charts of diameters, average speeds of mesoscale eddies off Canary Islands and their trajectories. These eddies were identified from integration with T = 90, 180, 270 and 360 days from top to bottom respectively. A total of 74 (47), 17 (6), 6 (0), and 2 (0) anticyclonic (cyclonic) eddies are extracted over the period of time between $[1993 - 2016]$ (We exclude from this analysis 105 (77), 2 (3), 1 (1), and 0 (0) anticyclones (cyclones) which pursue southward directions. The latter are not of important purposes in our study). We observe a predominance of anticyclones over cyclones. This is linked to anticipation of their longer lifespan. Stable anticyclones might rotate twice quicker than cyclones [Sangrà et al., 2007]. We must note here that 180, 270 and 360-day eddies appear inside the bounds of 90-day eddies, i.e., they do not form unalike eddies but truly form different closed-contour whitin the 90-day coherent eddies. In fact, eddies' boundaries extracted with a given period of time T usually lie nearby some closed-contour of $LACCL_{t_0}^{t_0+T}$ that fill eddies detected with a shorter T. We clearly observe while inspecting Fig.8-1 that

the number of cyclone decreases and vanishes with T increasing from 90 to 360 days.

Another obvious observation is that trajectories' lengths increases on average roughly from 452, 932 to 1684, 2480 km with T increasing from 90, 180 to 270, 360 days. This is followed by contraction in eddies' size; their diameter decreases on average from 60 to 30 km. Mean eddies' speeds stay fairly stable about 5 km/day for T=90, 180 days and 6.5 km/day for T=270, 360.

8.3.2 Transport by Canary's coherent eddies

Here, we carry on estimating the transport made by Canary's coherent eddies. Following [Wang et al., 2015], we fix a curve $\mathcal{C}$ (green curve in the bottom of Fig.8-1) which suppose to separate the offshore water (left of $\mathcal{C}$) from the Upwelling area (right of the blue curve) and the transition zone associated with it (between the green and blue curves). We assume that these eddies occasionally traverse $\mathcal{C}$ in westward direction. We estimate coherent transport off Canary Island by computing the quantity of the water transported by these mesoscale eddies across $\mathcal{C}$. This estimation is given by a succession of bars chart with diverse magnitudes presenting areas of the eddies crossing $\mathcal{C}$. We must note that in case where more than one eddy is caught at the same date, the bar box presents the sum of their areas.

Fig.8-2 illustrates the estimation of coherent transport over the period of time between 1993-2016 obtained by considering a) 90, b) 180, c) 270 and d) 360-days eddies which traverse $\mathcal{C}$ in westward direction. We note that the eddies are identified from two-dimensional data, thus, we describe the 3D transport measured in Sverdrup (Sv) ($10^6 m^3 s^-1$). We obtain this by multiplying the 2D transport values by 300 m [Sangrà et al., 2009, Alonso-González et al., 2009, Hernández-Guerra et al., 2005]. Blue, green and yellow bar portions in Fig.8-2 refer to transport of fluid captured in the interior eddies respectively from Upwelling region, transition zone and the offshore. Results show that 63 90-days eddies crossed the curve $\mathcal{C}$, 15 of 180-days eddies, 6 of 270-days eddies and 2 of 360-days ones. 90-days eddies are more dominant and hence are the most significant to compute the transport. A differentiating aspect of the 90-days eddies' time series is a large variability, both intra and inter-annual.

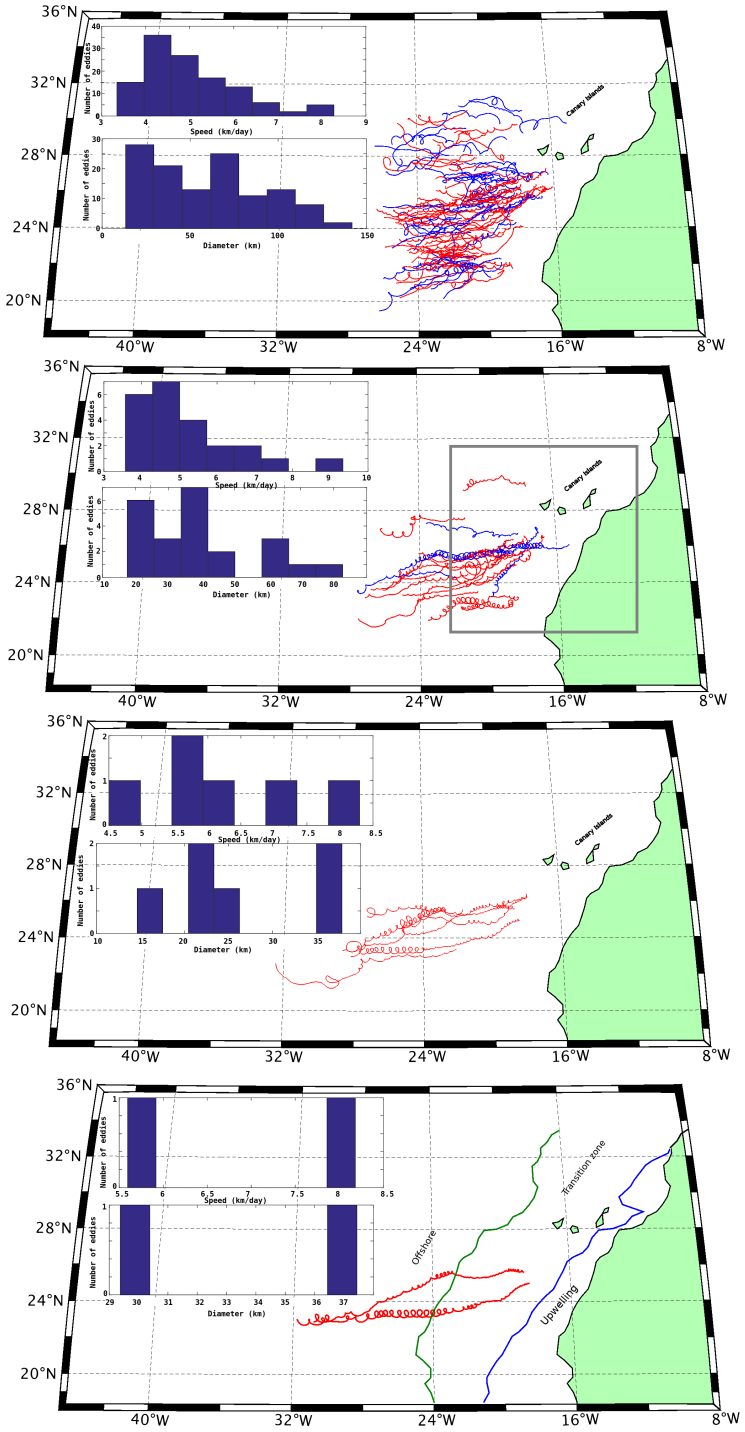

Figure 8-1: Trajectories, diameters and average speeds of the identified coherent mesoscale eddies off the Canary Islands. These eddies are extracted over 1993-2016 with lifetimes from top to bottom: 90, 180, 270 and 360 days. Red color presents trajectories of anticyclone while the blue stands for cyclones.

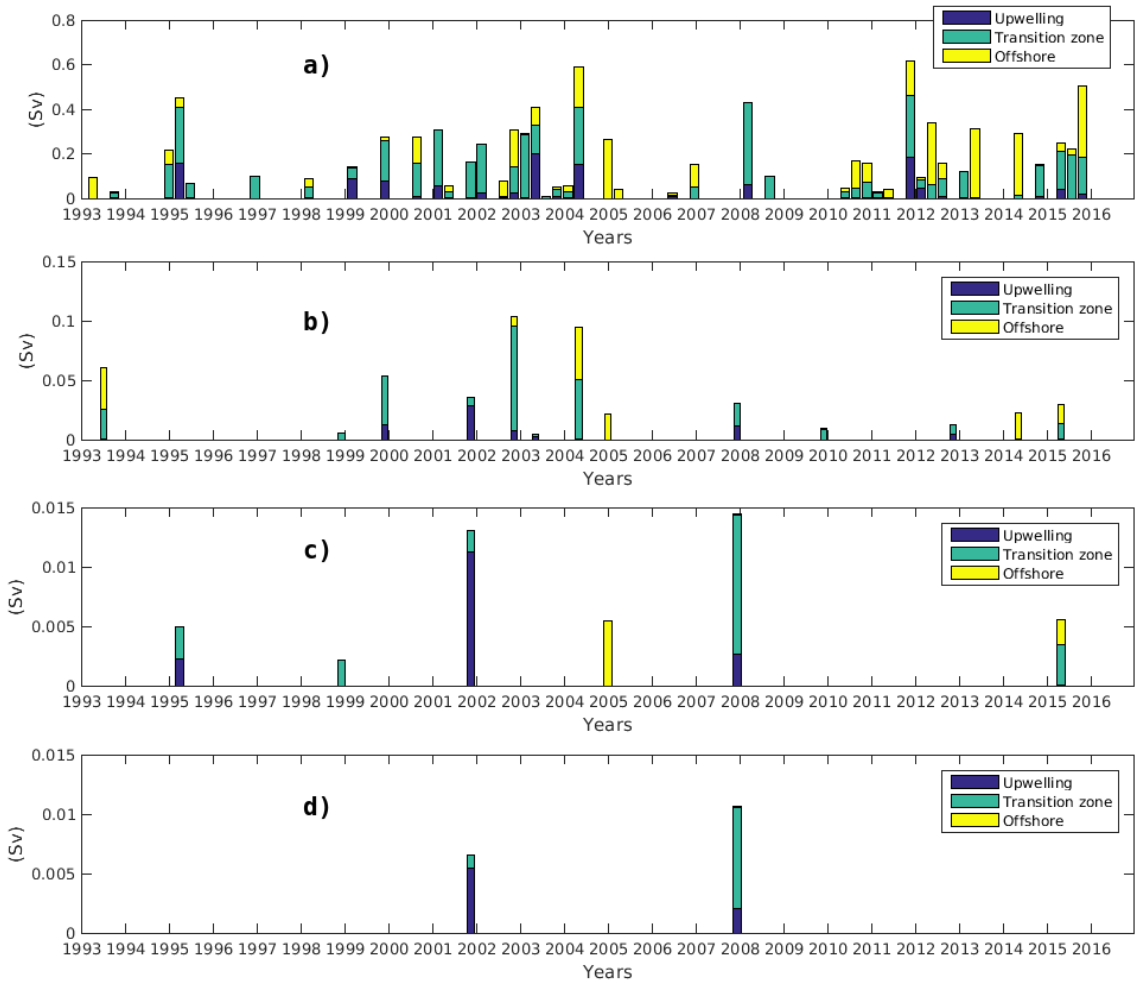

Figure 8-2: Instantaneous time series of transport produced by a) 90, b) 180, c) 270 and d) 360-day coherent eddies crossing the green curve indicated in Fig.8-1. Blue bar portions correspond to transport of Upwelling water carried inside the coherent eddies. Green bars correspond to the water coming from Transition zone trapped inside the eddies. Yellow bars correspond to the water coming from offshore trapped inside the eddies.

The eddies' detection rate is quite irregular. About one to 4 eddies cross $\mathcal{C}$ per year, mainly, all years except 1997, 2007, 2009, and 2016 where left without eddies. However, two 180-days eddies crossed the curve $\mathcal{C}$ in 2007 and 2009, which lefts only 1997 and 2016 with no eddies crossing $\mathcal{C}$. Eddies' transport estimations vary roughly about 0.1 to 0.8 Sv. The variation of transport estimations are mainly associated to ranging eddies' sizes. Scattered zero eddies' transport breaks last approximately from about a month to a year. The yearly $1 \sim 4$ eddies generated off the Canary Islands

contribute to a westward mass and volume transport of TrM=$3.7 \times 10^8 kgs^{-1}$ and TrV=0.37 Sv($10^6 m^3 s^{-1}$). Canary Islands eddies' participate roughly about 4.5% to the southward transport by the Canary Current (approximated as 4.5Sv [Hernández-Guerra et al., 2005]). Our estimation is one order of magnitude smaller than the previous finding of [Sangrà et al., 2009] where they estimate the yearly transport to be TrV=1.3 Sv, and it is about half of the estimation of [Hernández-Guerra et al., 2005] where they find a yearly value of TrV=0.7. This significant difference may be decreased if a substantial southward extent for the eddies is taken. [Sangrà et al., 2009] find a yearly average of 17 eddies compared to 3 eddies per year found in our study.

Our result are in line with the recent works of [Wang et al., 2015, Abernathey and Haller, 2018] which use recent Lagrangian methods to estimate the water transport in different regions. [Wang et al., 2015] used a stretching based method to estimate coherent water transport in the Agulas region. Their finding is at least 2 orders of magnitude lowed than the earlier finding based on Eulerian vortices tracking. On the other hand, [Abernathey and Haller, 2018] used the LACCL method to quantify water transport made by coherent eddies in the eastern Pacific. Their study shows that 30-days eddies water transport is less by one order of magnitude than the earlier Eulerian estimation. For the 90-days eddies, the water transport is even lower. Their finding is in contradiction with the previous finding of [Dong et al., 2014]. The outcome of this is: despise the studied area, using Lagrangian method casts doubt on the previous finding based on Eulerian tracking. The cause of this important conflict resides in the fact that those previous estimates essentially assume that those eddies can remain coherent for long term. This cannot be promised by Eulerian tools applied on satellite SSH or the analysis of in situ, satellite-tracked float and drifter, which drove to the early transport estimations.

Now we process to analyze the origin of water portion enclosed within these eddies. This is predestined by advecting theses eddies in reverse time till at least 100% of time-reversibility is achieved by the 90,180-days eddies and 60% for the 270,360-days eddies. The Upwelling water contained in these eddies is estimated by computing the

fraction of the trapped water found east of the blue curve (bottom of Fig.8-1). In the same way, we estimate the water coming from the Upwelling transition zone as the portion of water found in the region between the green and blue curves indicated in Fig.8-1. Eddies are found in this way to transport on mean around 10% of water coming from the Upwelling zone. As a result, yearly average transport of Upwelling water enclosed inner the eddies is estimated to be about 0.05 Sv. The water from the Upwelling transition zone carried by these eddies is estimated on average about 49%. Accordingly, yearly average transport of Upwelling transition water enclosed inside the eddies is estimated to be around 0.19 Sv.

8.3.3 Evolution of Canary's long-lived eddies

Here, we discuss the evolution of the long-lived coherent eddies detected off Canary Islands. We first, focus on the very unique 360-day eddies as they consist the most insistent cores of all the extracted eddies. Fig.8-3 shows a snapshot of the progress of a 360-day eddy detected here (Video M11 including 10-days snapshots is supplied as supporting information). The time series evolution is made by passively advecting particles enclosed by the eddy's boundary at detection time t_0 in onward time (further off its theoretical coherence time) and in reverse time (considering to reach 60% of reversibility). Such coherent material eddy is characterized by a small diameter (38km), and it was formed by merge of two anticyclones that exited south off the islands at $26°N$. This genesis picture found here is more coherent with those from previous finding [Sangrà et al., 2009]. The eddy is formed from water which belong mainly to fluid traceable into the transition zone of the canary Upwelling and a minor portion of fluid that resides in the Upwelling areas. The detected 360-days eddy remains coherent for 500 days (Fig.8-3 (d)) traveling southward through advection by the Canary Current, and westward up to 1600 km by self advection due to the β-effect (gradient of the local rotating rate [Cushman-Roisin and Manga, 1995, van Leeuwen, 2007]). Finally, the eddy lose its coherence, and its content is mingled with the open ocean in the neighborhood of the Mid-Atlantic Ridge.

In similar way, we turn to analyze the evolution of the 90-days long-lived coherent

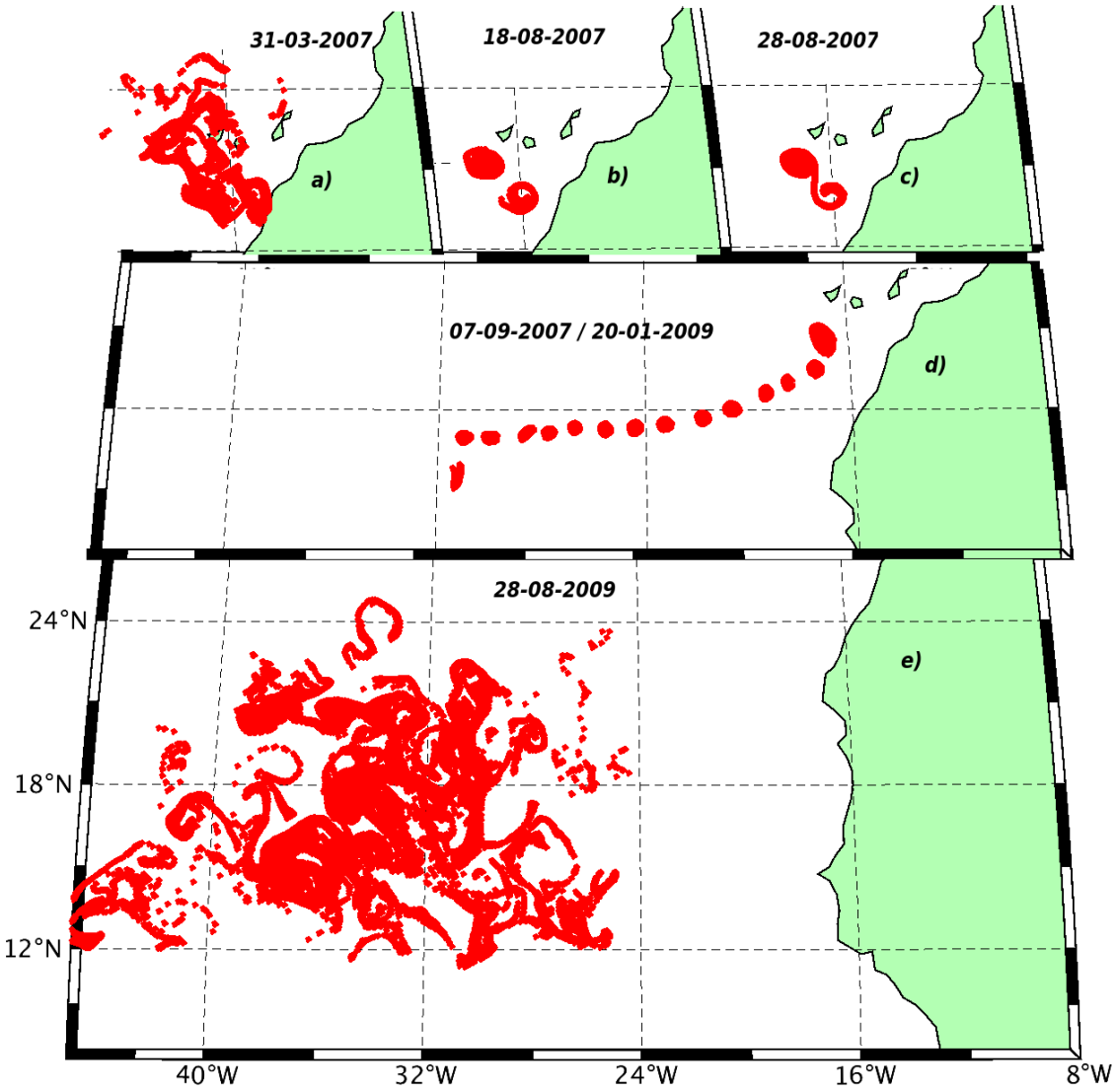

Figure 8-3: Snapshot of the lifelong progress of a 360-day mesoscale eddy off the Canary Islands: a) passive tracer which completely fill this eddy during its creation. b) and c) the genesis of the eddy. d) The eddy while it remains coherent is indicated. e) passive tracer poured by the eddy after losing its coherence. (See the supplemental movie M11 for the entire advection evolution of this 360-day eddy.)

eddies as they are more dominant. Fig.8-4 shows a snapshot of the evolution of two eddies (cyclone in blue and anticyclone in red color) detected here (Video M12 including 10-days snapshots is supplied as supporting information). These coherent eddies are characterized by larger diameters. Similar to the 360-days cores, the 90-days cores are formed from fluid traceable south and west the islands. The detected 90-days eddies remain coherent for 300 days (anticyclone) and 270 days (cyclone) and

propagating up to 880 km westward. During their propagation, the cyclone follows similar path of the anticyclone before it loses its stability and from rotating fluid around the anticyclone before. Finally, they mix their content together west 24°N (see supporting information Movie M12). Out of the 121 detected eddies, 63 adhere to this picture (their emergence, demise and trajectory).

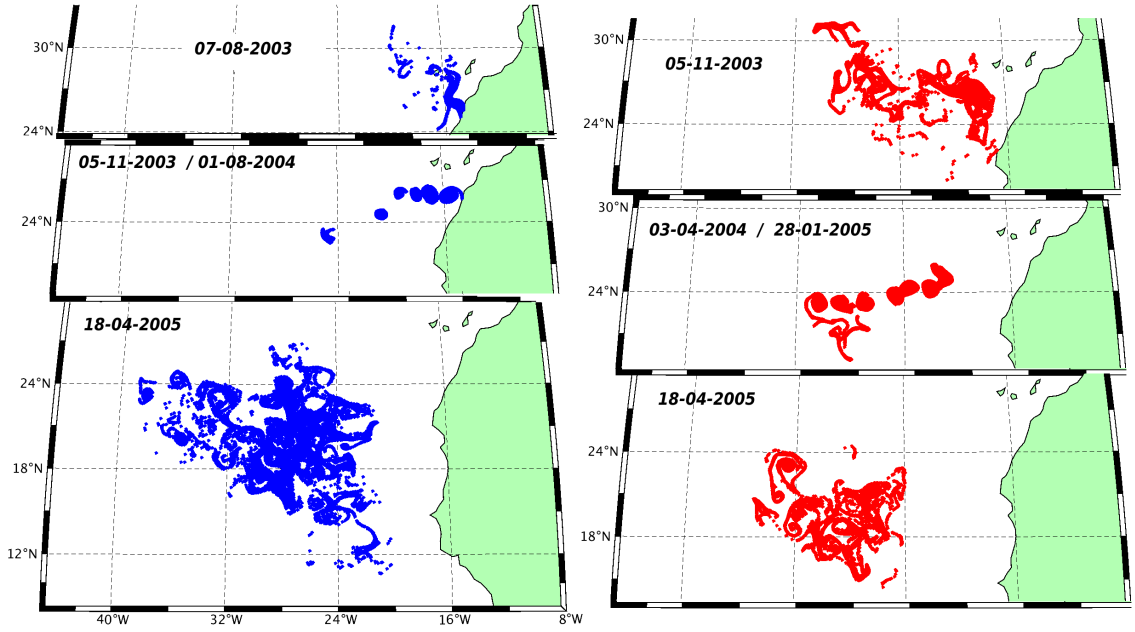

Figure 8-4: Snapshotof the lifelong progress of two 90-day mesoscale eddies off the Canary Islands: blue) anticyclone, red) cyclone. (See the supplemental movie M12 for the entire advection evolution of these two 90-day eddies.)

8.4 Conclusion

Using a recent Lagrangian method, we have reported coherent transport signal off Canary Islands from a 24 years dataset of geostrophic velocities derived from satellite altimetry. This approach allows precise identification of coherent eddies which remain coherent up to one year. We identified cyclones and anticyclones of different diameters and lifetime ranging from 90-days up to 360. We used these coherent mesoscale eddies to compute transport off Canary Islands, which shown to be smaller (by about one order of magnitude) than previous transport estimates. This is in line with the finding of [Wang et al., 2015, Abernathey and Haller, 2018] which also used Lagrangian

tools to estimate the water transport in their studied areas. Our finding suggests a diminished role of Canary's eddies in transporting coherent water off the islands. The main reason behind this conflict is that previous transport estimations used Eulerian footsteps in satellite altimetry to identify coherent mesoscale eddies. We also computed the annual portions of water coming from the Upwelling region and the transition zone associated to it which are trapped inside the mesoscale eddies. Our finding confirms the theoretical concept in which Canary's eddies shed from the islands archipelago as result of the barrier-role played by the latter and the existence of the canary current along with the trade wind. Most of these mesoscale eddies are formed in this manner. About 50% (63 out of 121) of eddies were found to pour their content in the ambient water.

Chapter 9

Conclusion and Outlook

Abstract

Eastern Boundary Upwelling zones (EBUZ) include some of the most productive ecosystems in the world, particularly the Canary Current Upwelling System (CCUS) which presents one of the world's major Upwelling regions. The focus of this thesis was to establish an interdisciplinary study of the coastal upwelling system covering different spheres: the problem of the upwelling detection, monitoring the spatio-temporal variation of its dynamics, studying its bio-physical interaction and ending by exploring its impact on the open ocean.

In this chapter, the main results of this analysis will be summarised by answering the research questions raised in the introduction. Finally, an outlook about further research objectives is included.

9.1 Conclusion

Why do previous automatic upwelling detection methods only function on the southern part of the system? I addressed this question in chapter 2. I reviewed earlier methods which were developed to extract the Moroccan upwelling regions. These methods generally start by applying a clustering algorithm over SST images with a number of clusters $c = 2$ in order to separate the upwelling cold waters from the warmer ones offshore, then labeling the cluster with the minimal centroid as upwelling waters. Later on, a region-growing algorithm to remove noisy structures in the offshore water is applied based on the fact that all pixels belonging to the upwelling region must have connectivity with the coastline. However, these methods

were only tested over the southern part of the system. Once they were applied over the whole Moroccan upwelling system, these methods fail to properly identify the upwelling regions in the northern part. I showed that the main reason behind this failure lies in the concept itself along with the high variability of the latitudinal distribution of temperatures. As the whole system receives uneven solar energy, northern offshore temperatures can be close to the southern upwelling temperatures. Knowing that simple clustering algorithm doesn't take into consideration the location of pixels, but only their temperature, this causes these clustering algorithms to label offshore temperature in the northern part as upwelling water. For this problem I have proposed two approaches to identify and extract upwelling regions over the whole Moroccan Atlantic coast. The first method is basically inspired by the Ekman transport theory; if the wind blows parallel to the coast in the Northern hemisphere (such as along the coast of Morocco, where the wind blows South), Ekman transport can produce a net movement of surface water 90° to the left which might result in coastal upwelling. Thus, in order to identify the upwelling, I proposed to naturally compare the temperature of the inshore water with offshore water within a perpendicular direction to the coast. In other words, I propose a latitudinal normalization by offshore temperatures; I partitioned each image to R radials which are perpendicular to the coast. Then, each of these radials R is normalized by its maximum temperature in the offshore. Once the normalized image is produced, one can easily apply a clustering algorithm to separate the maximal gradient in the upwelling areas from the minimal gradient in the offshore water. The second method considers a region-dependent clustering approach. That method is performed in two main stages: the first one with the goal to break-down the SST images into homogeneous regions, and the second step develops the simple algorithm that chooses and merges groups of pixels which best reproduce the shape of upwelling areas. This method not only successfully delineates upwelling regions from SST images along the whole Moroccan Atlantic coast, but also extracts in similar manner the upwelling region from CHLa images.

How to automatically delineating the upwelling can serve us to study its spatio-temporal dynamics? I addressed this question in chapter 3. I used the

upwelling segmentation methods developed in chapter 2 to improve the computation of the classical coastal upwelling index, which is defined as a simple thermal difference between coastal and offshore temperatures at the same latitude $I^r = T^r_{max} - T^r_{min}$. Various locations have been proposed in the literature for both T^r_{min} and T^r_{max}. In most of the methods in the literature, T^r_{min} is defined as the minimum temperature recorded in the coastal band from the coast up to the continental slope. T^r_{max} should be chosen as the offshore temperature where the influence of the Upwelling is expected to be negligible. On the other hand, note that by definition, T^r_{min} necessarily belongs to the Upwelling region. Thus, given that I have developed an upwelling segmentation method which shows a very good accuracy, I naturally defined T^r_{min} as the minimal temperature recorded within the extracted Upwelling area. In similar manner I defined T^r_{max} as the maximal temperature outside of the upwelling segmented area. I used this proposed method to carry out a 30 years historical study of the spatio-temporal variation of the upwelling intensity. The proposed upwelling segmentation method used to compute the $\mathrm{CHL_a}$ index, and to monitor and characterize the spatio-temporal variation of the upwelling extension form biological and physical satellite observation.

What are the atmospheric drivers of the Moroccan upwelling system? I addressed this question in chapter 3. I carried out a statistical study of the upwelling spatio-temporal variation in terms of intensity, $\mathrm{CHL_a}$ concentration, spatial extension with focus on its relationship to atmospheric variables (wind stress, NAO). I showed that the relationship between upwelling spatial extension and the atmospheric variables differ somewhat in the two regions. However, the pattern of the upwelling intensity generally reflect the common atmospheric pattern favoring upwelling: Cross-shore Ekman. On the other hand NAO index plays role only in extreme events.

How do physical and biological processes interact with each other in the Moroccan upwelling system? I addressed this question in chapter 5. I explored the relationship between physical structures of oceanic fronts and the biological activity. In this regard, I proposed a new concept of studying the nonlinear relationship between surface mixing/stirring and chlorophyll concentration. I have used 10 years

of remotely sensed velocity field derived from altimetry and chlorophyll concentrations to address the problem of the relationships between surface mixing and chlorophyll concentrations. I computed the surface mixing/stirring based on a recent geodesic theory of Lagrangian coherent structures (LCSs). I used these LCSs to study the link between surface mixing/stirring and chlorophyll-a (CHL_a) fronts concentration that I extracted through the calculation of singularity exponents in a microcanonical formulation of the Most Singular Manifold (MSM). I compared my results with those of a recent study conducted over the same area, but based on finite size Lyapunov exponents (FSLEs), whose output is a plot of scalar distributions. I discussed the differences between FSLE and geodesic theory of LCS, then showed how this concept shed new light on the previous studies addressing mixing using FSLEs.

How does the Moroccan upwelling system contribute and impact the open ocean? I addressed this question in chapter 7. I explored the impact of NWA upwelling over the open ocean throughout the roles played by mesoscale eddies off the Canary archipelago in carrying coherent waters from upwelling regions and pouring them into the open ocean. First, I proposed in chapter 6 an objective definition of coherent Lagrangian vortices along with their automatic identification method. I did this by decomposing particle trajectory into two parts: closed curves which give information about uniformly rotating flow, and one that describes the mean displacement. The former part yields an objective measure of material rotation. The method I proposed defines a Lagrangian coherent vortex as closed material lines in which fluid parcels complete the same polar rotation. I used this method to extract coherent mesoscale eddies from a 24 years dataset of sea surface velocity field derived from satellite surface altimetry. I investigate their lifespan, create a sequence of consistent fluid transport, and assess the significance of the achieved transport estimations. I detect a yearly up to 4 coherent mesoscale eddies characterized by diameters varying from 25 to 140 km. An overall of 63 coherent eddies of about 40 km in diameter among about 59% of their contents resides in the Upwelling and its transition. I also used these mesoscale eddies to compute coherent fluid transport off Canary Islands, which I prove to be lower (by about one order of magnitude) than previous transport

estimates.

9.2 Outlook

This thesis shed some light on several questions regarding the NWA upwelling system. As perspectives and follow-up to this work, several lines of research are identified to deepen the characterization and analysis of the Moroccan upwelling phenomenon.

The Moroccan Atlantic continental shelf is part of the Canary Current ecosystem, and constitutes an area of high biological productivity and intensive fisheries' activity. This productive area sustains an important fishing industry which represents an important economic activity for the bordering countries. It would be very interesting to detect and discriminate the different thermal structures composing Moroccan upwelling (ie fronts, filaments, jets) as well as their properties and their differences compared to other upwelling systems. It would also be very useful to highlight the activity of upwelling through the frequency analysis of thermal fronts to identify areas with high marine productivity. It is also necessary to study the relationship between the upwelling variability in terms of plankton communities and their relation with the annual fisheries of different species. In addition, these results can be linked to fishing statistics to evaluate the impact of upwelling variability on the fluctuations of the fishing resources in order to predict their evolution.

The region north of $33°N$ is argued whether it is characterized by the upwelling phenomenon or not. While studying the spatial extension of the Moroccan upwelling from physical and biological observation, we have observed that the upwelling is CHL_a detected within CHL_a images but not in SST images in that precise region. It will be interesting to study source of the chlorophyll detected in that region. A combination between model and satellite data, along with recent Lagrangian tools designed to extract structures flow that organize fluid trajectories is necessary is that region.

It will be interesting to study the mesoscale eddies off the Canary archipelago throughout three-dimensional velocity field issued from model. Such study will allow the identification of their three-dimensional physical structures, their depth and

to establish a more accurate estimate of their coherent water transport. It is also interesting to combine these data with other three-dimensional model data such as temperature, salinity and other biological parameters in order to have a more insight view of the impact of these coherent in transporting physical and biological water properties to the open ocean.

Appendix A

A.1 North Atlantic Oscillations

One of the Northern Hemisphere's most important teleconnection indices (NAO) has been obtained from the National Center of Environmental Prediction (NCEP) at monthly time scales from 2003 to 2016. This mode has shown to be the most prevalent pattern on the eastern North Atlantic region. It is made up of a north-south dipole of geopotential anomalies with a center located in Iceland and another one spanning between $35°N$ and $40°N$ in the central North Atlantic. A positive phase on this index is an augmentation in the pressure differences, as results, frequency and strength of winter storms increase across the Atlantic Ocean that typically take a more northerly track [Alvarez et al., 2010][Gomez-Gesteira et al., 2008]. The negative phase represents a reduced pressure gradient resulting in a weak and small amount of winter storms across Europe, which travel on a more west-east pathway. Research has identified the NAO index as the local manifestation of the more global pattern of the Arctic Oscillation during the winter [Thompson et al., 2000].

A.2 Region-Growing

Region-growing algorithm aims to group a set of pixels according to the criteria of homogeneity and adjacency. It analyzes neighboring pixels of initial points and decides if the adjacent pixel must be added to the region. The pixels belonging to the same region are labeled by the same index and the pixels in other regions are labeled

by a different index.

A.3 Particle Swarm Optimization

Particle swarm optimization (PSO) is a stochastic optimization method inspired by birds' social behavior in a flock [Kennedy, 2011][Kennedy et al., 2001]. It works by having a group of candidate solutions called particles. Each of these particles flies through the space of search according to a few simple formula over the position and velocity of particles. Their movements are influenced by their own best-known position in the space of search called $p$best, and best-known position of the whole group called $g$best [Shi and Eberhart, 1998]. After each iteration, each particle's velocity and positions is recomputed with following equation:

$$v_i(t+1) = \omega v_i(t) + c_1 r_1(t)(p_i(t) - x_i(t)) + c_2 r_2(t)(\hat{p}(t) - x_i(t)) \tag{A.1}$$

$$x_i(t+1) = x_i(t) + v_i(t+1) \tag{A.2}$$

ω presents the inertia weight, which controls the influence of the previous velocity; a large inertia weight favors exploration, while a small inertia weight favors exploitation [Shi and Eberhart, 1998]. c_1 and c_2 present constants of acceleration, v_i is the particle's velocity, $x_i(t)$ is the particle's time-position, $p_i(t)$ and $\hat{p}_i(t)$ are the $p$best and $g$best as stated before. r_1 and r_2 are vectors with their elements sampled from a uniform distribution $U(0,1)$

The cognitive component $p_i(t) - x_i(t)$ serves as a memory of previous particles' best positions, while the social component $\hat{y}(t) - x_i(t)$ gives the whole group's belief as to where the best solution is.

PSO's efficiency is sensitive to the parameters ω, c_1 and c_2. While several suggestions (based on empirical studies) for good values can be found in the literature, such as in [Van Den Bergh, 2006][Van Den Bergh, 2006] where the PSO exhibits convergent behavior if the following condition is satisfied:

$$\omega > \frac{1}{2}(c_1 + c_2), \quad \omega < 1 \tag{A.3}$$

if not the PSO exhibits cyclic or divergent behavior.

A.3.1 PSO Clustering algorithm

Within the framework of pixels clustering, each particle x_i is structured as $x_i = (m_{i1}, ..., m_{ij}, ..., m_{iNc})$ where m_{ij} is the jth cluster centroid vector of the ith particle. Thus, a swarm reflects a number of candidate pixels clusterings. The fitness function is used to evaluate each particle as:

$$f(x_i, Z_i) = \omega_1 \bar{d}_{max}(Z_i, x_i) + \omega_2(z_{max} - d_{min}(x_i)) \tag{A.4}$$

where z_{max} is the highest value in the image; Z_i is the matrix which assigns each pixel to clusters of particle i. Each element z_{ijp} decides if a pixel z_p belongs to a cluster C_{ij} of a particle i. The constants ω_1 and ω_2 are user-defined constants.

$$\bar{d}_{max}(Z_i, x_i) = \max_{j=1,....N_c} \left\{ \sum_{\forall z_p \in C_{ij}} \frac{d(z_p, m_{ij})}{|C_{ij}|} \right\} \tag{A.5}$$

presents the highest average Euclidean distance between all classes and their associated particles, with $|C_{ij}|$ presents the cardinality of the set C_{ij}.

$$d_{min}(x_i) = \min_{\forall j_1, j_2, j_1 \neq j_2} \{d(m_{ij_1}, d_{ij_2})\} \tag{A.6}$$

presents the lowest Euclidean distance between any pair of centroids.

This fitness function is multiobjective and it is designed to:

- reduce the distance between cluster centroid and its associate pixels, as quantified by $\bar{d}_{max}(Zi, xi)$
- increase the distance between any pair of centroids, as quantified by $d_{min}(x_i)$.

The PSO-based clustering method can be summarized as:

Compared to the FCM algorithm, this approach minimizes the impact of initial conditions. Moreover, an advantage of this method is that an optimal clustering search is performed in parallel.

Algorithm 1: PSO clustering algorithm.

Data: Initialize the parameters ω, ω_1, ω_2.

- Initialize each particle to contain N_c randomly selected cluster means.
- Initialize the particles velocities and accelerations.

for $t = 1$ *to* $t = tmax$ **do**
  for *each particle* i **do**
    for *each pixel* Z_p **do**
      - calculate $d(z_p, m_{ij})$ for all clusters C_{ij}
      - assign z_p to C_{ij} where $d(z_p, m_{ij}) = \min_{\forall c=1...N_c} \{d(z_p, m_{ic})\}$

    end
    Calculate the fitness, $f(x_i(t), Z_i)$
  end
  - Find the global best solution $\hat{p}(t)$
  - Update the cluster centroids using equations. (1) and (2)

end

Algorithm 2: Divide to sub-regions.

for *each step of* $90km$ **do**
  calculate the cardinality of the first cluster $G(1)$, and label it as upwelling region if it presents less than 15% of cardinality of the sub-region;
  i=2;
  while $\frac{G(i)}{\Sigma_{j=1}^{j=i} G(j)} \leq 0.5$ *and* $i < 6$ **do**
    label the ist cluster as upwelling region.
  end
end

A.4 Region-based algorithm

A.5 Fuzzy c means

FCM algorithm attempts to partition a finite collection of n pixels $X = \{x_1, ..., x_n\}$ into a collection of c fuzzy clusters with respect to some given criterion. Given a finite set of pixels, the algorithm returns a list of c cluster centers $C = \{c_1, ..., c_c\}$ and a fuzzy partition matrix, which presents the degree of belonging for each pixel x_k to a given cluster c_i. The FCM algorithm is applied to minimize an objective function

called c-means functional:

$$J_m(X;U,V) = \sum_{k=1}^{n}\sum_{i=1}^{c}(\mu_{ik})^m \left\|x_k - v_i\right\|^2 \tag{A.7}$$

where n is the length of the vector X presenting pixels of a given SST image. $V = \{v_1, v_2, ..., v_n\}$ is the vector of cluster prototypes and $U = [\mu_{ik}]$ is the fuzzy partition matrix which presents the degree of belonging for each pixel x_k to a given cluster c_i. The weighting exponent m controls the fuzziness of membership values, which vary in the interval $[1, \infty[$. An increase of m lead to an increase of fuzziness partitions.

The objective function (Eq.A.7) can be seen as a measure of the total variance of x_k from v_i. The minimization of the objective function (Eq.A.7) represents a nonlinear optimization problem that can be solved by using respectively the following cluster centroids and membership functions:

$$v_i = \frac{\sum_{k=1}^{n}(\mu_{ik}^m)x_k}{\sum_{k=1}^{n}(\mu_{ik}^m)}, 1 \leq i \leq c \tag{A.8}$$

$$\mu_{ik} = \frac{1}{\sum_{j=1}^{c}(\frac{\left\|x_k - v_i\right\|}{\left\|x_k - v_j\right\|})^{\frac{2}{(m-1)}}}, 1 \leq i \leq c, 1 \leq k \leq n \tag{A.9}$$

The goal here is to iteratively improve a sequence of sets of fuzzy clusters through those equations until no further improvement is possible for the objective function.

List of publications

Journal Articles

1. Anass El Aouni, Khalid Daoudi, Hussein Yahia, Khalid Minaoui, and Aïssa Benazzouz. *Surface mixing and biological activity in the northwest african upwelling.* Chaos: An Interdisciplinary Journal of Nonlinear Science, 29(1):011104, 2019 `https://doi.org/10.1063/1.5067253`.

2. Anass El Aouni, Hussein Yahia, Khalid Daoudi, and Khalid Minaoui. *A fourier approach to lagrangian vortex detection.* Chaos: An Interdisciplinary Journal of Nonlinear Science, 29(9):093106, 2019 `https://doi.org/10.1063/1.5115996`.

3. Anass El Aouni, Veronique Garçon, Sudre Joel, Hussein Yahia, Khalid Daoudi, and Khalid Minaoui. Segmentation, quantification and dynamics of coastal upwelling using sst satellite images. IEEE Transaction on Geoscience and Remote Sensing, Accepted, 2019

Under review manuscripts

4. Anass El Aouni, Khalid Daoudi, Hussein Yahia, and Khalid Minaoui. *Defining coherent vortices from particles trajectories.* Fluid Dynamics Research, Undergoing minor revision, 2019

5. Anass El Aouni, Khalid Daoudi, Khalid Minaoui, and Hussein Yahia. *Segmentation, quantification and dynamics of coastal upwelling using sst satellite images.* Submited to: Ocean Dynamics, Under review, 2018

6. Anass El Aouni, Khalid Minaoui, Khalid Daoudi, and Hussein Yahia. Transport by lagrangian eddies off the north-west african upwelling. Submited to: Scientific reports, 2019

International Peer-Reviewed Conferences

7. Anass El Aouni, Khalid Daoudi, Hussein Yahia, and Khalid Minaoui. *Surface mixing and biological activity in the north african upwelling.* In AGU Ocean Sciences Meeting 2018, 2018

8. Anass El Aouni, Khalid Daoudi, Hussein Yahia, and Khalid Minaoui. *Coherent vortex detection from particles trajectories analysis.* In 2018 SIAM Conference on Nonlinear Waves and Coherent Structures, 2018

9. Anass El Aouni, Khalid Daoudi, Hussein Yahia, and Khalid Minaoui. *The contribution and influence of coherent mesoscale eddies off the north-west african upwelling on the open ocean.* In 2018 SIAM Conference on Mathematics of Planet Earth, 2018

10. Anass El Aouni, Khalid Minaoui, Khalid Daoudi, and Hussein Yahia. *North-west african upwelling dynamics from physical and biological satellite observations.* In Report of the 4th GEO Blue Planet Symposium, 2018

11. Anass El Aouni, Khalid Minaoui, Ayoub Tamim, Khalid Daoudi, and Hussein Yahia. *An improved method for accurate computation of coastal upwelling index using sea surface temperature images.* In 2018 9th International Symposium on Signal, Image, Video and Communications (ISIVC), pages 76-81. IEEE, 2018

12. Anass El Aouni, Khalid Minaoui, Ayoub Tamim, Khalid Daoudi, Hussein Yahia, Abderrahman Atillah, and Driss Aboutajdine. *Detection of moroccan coastal upwelling using sea surface chlorophyll concentration.* In Computer Systems and Applications (AICCSA), 2015 ACS International Conference on, pages 1-4. IEEE, 2015

Bibliography

[Aagaard et al., 1985] Aagaard, K., Swift, J., and Carmack, E. (1985). Thermohaline circulation in the arctic mediterranean seas. *Journal of Geophysical Research: Oceans*, 90(C3):4833–4846.

[Abernathey and Haller, 2018] Abernathey, R. and Haller, G. (2018). Transport by lagrangian vortices in the eastern pacific. *Journal of Physical Oceanography*, 48(3):667–685.

[Acharya and Ray, 2005] Acharya, T. and Ray, A. K. (2005). *Image processing: principles and applications*. John Wiley & Sons.

[Al-Amri et al., 2010] Al-Amri, S. S., Kalyankar, N., and Khamitkar, S. (2010). Image segmentation by using edge detection. *International journal on computer science and engineering*, 2(3):804–807.

[Alexander and Fairbridge, 1999] Alexander, D. E. and Fairbridge, R. W. (1999). *Encyclopedia of environmental science*. Springer Science & Business Media.

[Allen, 1980] Allen, J. (1980). Models of wind-driven currents on the continental shelf. *Annual Review of Fluid Mechanics*, 12(1):389–433.

[Allen, 1973] Allen, J. S. (1973). Upwelling and coastal jets in a continuously stratified ocean. *Journal of Physical Oceanography*, 3(3):245–257.

[Alonso-González et al., 2009] Alonso-González, I., Arístegui, J., Vilas, J., and Hernández-Guerra, A. (2009). Lateral poc transport and consumption in surface and deep waters of the canary current region: A box model study. *Global Biogeochemical Cycles*, 23(2).

[Alonso-González et al., 2013] Alonso-González, I. J., Arístegui, J., Lee, C., Sanchez-Vidal, A., Calafat, A., Fabrés, J., Sangrá, P., and Mason, E. (2013). Carbon dynamics within cyclonic eddies: insights from a biomarker study. *PloS one*, 8(12):e82447.

[Alvarez et al., 2010] Alvarez, I., Gomez-Gesteira, M., Gomez-Gesteira, J., Dias, J., et al. (2010). Summer upwelling frequency along the western cantabrian coast from 1967 to 2007. *Journal of Marine Systems*, 79(1):218–226.

[Álvarez-Salgado, 2007] Álvarez-Salgado, X. (2007). Contribution of upwelling filaments to offshore carbon export in the subtropical northeast atlantic ocean. *Limnology and Oceanography*, 52(3):1287–1292.

[Anderson et al., 2009] Anderson, R., Ali, S., Bradtmiller, L., Nielsen, S., Fleisher, M., Anderson, B., and Burckle, L. (2009). Wind-driven upwelling in the southern ocean and the deglacial rise in atmospheric co2. *science*, 323(5920):1443–1448.

[Andrews and Hutchings, 1980] Andrews, W. and Hutchings, L. (1980). Upwelling in the southern benguela current. *Progress in Oceanography*, 9(1):1–81.

[Aref, 1984] Aref, H. (1984). Stirring by chaotic advection. *Journal of fluid mechanics*, 143:1–21.

[Aref, 1990] Aref, H. (1990). Chaotic advection of fluid particles. *Phil. Trans. R. Soc. Lond. A*, 333(1631):273–288.

[Aref, 2002] Aref, H. (2002). The development of chaotic advection. *Physics of Fluids*, 14(4):1315–1325.

[Arístegui et al., 2006] Arístegui, J., Alvarez-Salgado, X. A., Barton, E. D., Figueiras, F. G., Hernandez-Leon, S., Roy, C., and Santos, A. (2006). Oceanography and fisheries of the canary current/iberian region of the eastern north atlantic (18a, e). *The global coastal ocean: interdisciplinary regional studies and syntheses*, 14:879.

[Arístegui et al., 2009] Arístegui, J., Barton, E. D., Álvarez-Salgado, X. A., Santos, A. M. P., Figueiras, F. G., Kifani, S., Hernández-León, S., Mason, E., Machú, E., and Demarcq, H. (2009). Sub-regional ecosystem variability in the canary current upwelling. *Progress in Oceanography*, 83(1):33–48.

[Arístegui and Montero, 2005] Arístegui, J. and Montero, M. F. (2005). Temporal and spatial changes in plankton respiration and biomass in the canary islands region: the effect of mesoscale variability. *Journal of Marine Systems*, 54(1-4):65–82.

[Arístegui et al., 1994] Arístegui, J., Sangrá, P., Hernández-León, S., Cantón, M., Hernández-Guerra, A., and Kerling, J. (1994). Island-induced eddies in the canary islands. *Deep Sea Research Part I: Oceanographic Research Papers*, 41(10):1509–1525.

[Arístegui et al., 1997] Arístegui, J., Tett, P., Hernández-Guerra, A., Basterretxea, G., Montero, M. F., Wild, K., Sangrá, P., Hernández-León, S., Cantón, M., García-Braun, J., et al. (1997). The influence of island-generated eddies on chlorophyll distribution: a study of mesoscale variation around gran canaria. *Deep Sea Research Part I: Oceanographic Research Papers*, 44(1):71–96.

[Arnol'd, 2013] Arnol'd, V. I. (2013). *Mathematical methods of classical mechanics*, volume 60. Springer Science & Business Media.

[Arrowsmith and Place, 1990] Arrowsmith, D. K. and Place, C. M. (1990). *An introduction to dynamical systems*. Cambridge university press.

[Artale et al., 1997] Artale, V., Boffetta, G., Celani, A., Cencini, M., and Vulpiani, A. (1997). Dispersion of passive tracers in closed basins: Beyond the diffusion coefficient. *Physics of Fluids*, 9(11):3162–3171.

[Aurell et al., 1997] Aurell, E., Boffetta, G., Crisanti, A., Paladin, G., and Vulpiani, A. (1997). Predictability in the large: an extension of the concept of lyapunov exponent. *Journal of Physics A: Mathematical and General*, 30(1):1.

[Backer and Jain, 1981] Backer, E. and Jain, A. K. (1981). A clustering performance measure based on fuzzy set decomposition. *IEEE Transactions on Pattern Analysis & Machine Intelligence*, (1):66–75.

[Baker et al., 1996] Baker, G. L., Baker, G. L., and Gollub, J. P. (1996). *Chaotic dynamics: an introduction*. Cambridge University Press.

[Bakun, 1990] Bakun, A. (1990). Global climate change and intensification of coastal ocean upwelling. *Science*, 247(4939):198–201.

[Barghout and Lee, 2004] Barghout, L. and Lee, L. (2004). Perceptual information processing system. US Patent App. 10/618,543.

[Barrow and Tenenbaum, 1981] Barrow, H. G. and Tenenbaum, J. M. (1981). Interpreting line drawings as three-dimensional surfaces. *Artificial intelligence*, 17(1-3):75–116.

[Barton et al., 1998] Barton, E., Arıstegui, J., Tett, P., Cantón, M., Garcıa-Braun, J., Hernández-León, S., Nykjaer, L., Almeida, C., Almunia, J., Ballesteros, S., et al. (1998). The transition zone of the canary current upwelling region. *Progress in Oceanography*, 41(4):455–504.

[Barton, 1998] Barton, E. D. (1998). Eastern boundary of the north atlantic: northwest africa and iberia. *The Sea.*

[Beal et al., 2011] Beal, L. M., De Ruijter, W. P., Biastoch, A., Zahn, R., Cronin, M., Hermes, J., Lutjeharms, J., Quartly, G., Tozuka, T., Baker-Yeboah, S., et al. (2011). On the role of the agulhas system in ocean circulation and climate. *Nature*, 472(7344):429.

[Benazzouz et al., 2014a] Benazzouz, A., Mamad, O., Abedi, P., Bouali-Benazzouz, R., and Chetrit, J. (2014a). Involvement of dopamine loss in extrastriatal basal ganglia nuclei in the pathophysiology of parkinson's disease. *Frontiers in aging neuroscience*, 6:87.

[Benazzouz et al., 2014b] Benazzouz, A., Mordane, S., Orbi, A., Chagdali, M., Hilmi, K., Atillah, A., Pelegrí, J. L., and Hervé, D. (2014b). An improved coastal upwelling index from sea surface temperature using satellite-based approach–the case of the canary current upwelling system. *Continental Shelf Research*, 81:38–54.

[Benazzouz et al., 2014c] Benazzouz, A., Pelegrí, J. L., Demarcq, H., Machín, F., Mason, E., Orbi, A., Peña-Izquierdo, J., and Soumia, M. (2014c). On the temporal memory of coastal upwelling off nw africa. *Journal of Geophysical Research: Oceans*, 119(9):6356–6380.

[Benitez-Nelson et al., 2007] Benitez-Nelson, C. R., Bidigare, R. R., Dickey, T. D., Landry, M. R., Leonard, C. L., Brown, S. L., Nencioli, F., Rii, Y. M., Maiti, K., Becker, J. W., et al. (2007). Mesoscale eddies drive increased silica export in the subtropical pacific ocean. *Science*, 316(5827):1017–1021.

[Beron-Vera et al., 2018] Beron-Vera, F., Hadjighasem, A., Xia, Q., Olascoaga, M., and Haller, G. (2018). Coherent lagrangian swirls among submesoscale motions. *Proceedings of the National Academy of Sciences*, page 201701392.

[Beron-Vera et al., 2015] Beron-Vera, F. J., Olascoaga, M. J., Haller, G., Farazmand, M., Triñanes, J., and Wang, Y. (2015). Dissipative inertial transport patterns near coherent lagrangian eddies in the ocean. *Chaos: An Interdisciplinary Journal of Nonlinear Science*, 25(8):087412.

[Bettencourt et al., 2012] Bettencourt, J. H., López, C., and Hernández-García, E. (2012). Oceanic three-dimensional lagrangian coherent structures: A study of a mesoscale eddy in the benguela upwelling region. *Ocean Modelling*, 51:73–83.

[Bettencourt et al., 2013] Bettencourt, J. H., López, C., and Hernández-García, E. (2013). Characterization of coherent structures in three-dimensional turbulent flows using the finite-size lyapunov exponent. *Journal of Physics A: Mathematical and Theoretical*, 46(25):254022.

[Bettencourt et al., 2017] Bettencourt, J. H., Rossi, V., Hernández-García, E., Marta-Almeida, M., and López, C. (2017). Characterization of the structure and cross-shore transport properties of a coastal upwelling filament using three-dimensional finite-size lyapunov exponents. *Journal of Geophysical Research: Oceans*.

[Binet et al., 1998] Binet, D., Samb, B., Taleb Sidi, M., Levenez, J.-J., and Servain, J. (1998). Sardine and other pelagic fisheries changes associated with multi-year trade wind increases in the southern canary current.

[Boyd, 2005] Boyd, D. (2005). Physical basis of remote sensing. *Journal of Geoinformatics*, 1:67–81.

[Branicki and Wiggins, 2009] Branicki, M. and Wiggins, S. (2009). Finite-time lagrangian transport analysis: stable and unstable manifolds of hyperbolic trajectories and finite-time lyapunov exponents. *arXiv preprint arXiv:0908.1129*.

[Capet et al., 2008a] Capet, X., McWilliams, J. C., Molemaker, M. J., and Shchepetkin, A. (2008a). Mesoscale to submesoscale transition in the california current system. part i: Flow structure, eddy flux, and observational tests. *Journal of Physical Oceanography*, 38(1):29–43.

[Capet et al., 2008b] Capet, X., McWilliams, J. C., Molemaker, M. J., and Shchepetkin, A. (2008b). Mesoscale to submesoscale transition in the california current system. part ii: Frontal processes. *Journal of Physical Oceanography*, 38(1):44–64.

[Capet et al., 2008c] Capet, X., McWilliams, J. C., Molemaker, M. J., and Shchepetkin, A. (2008c). Mesoscale to submesoscale transition in the california current system. part iii: Energy balance and flux. *Journal of Physical Oceanography*, 38(10):2256–2269.

[Carder et al., 2004] Carder, K., Chen, F., Cannizzaro, J., Campbell, J., and Mitchell, B. (2004). Performance of the modis semi-analytical ocean color algorithm for chlorophyll-a. *Advances in Space Research*, 33(7):1152–1159.

[Carr and Kearns, 2003] Carr, M.-E. and Kearns, E. J. (2003). Production regimes in four eastern boundary current systems. *Deep Sea Research Part II: Topical Studies in Oceanography*, 50(22):3199–3221.

[Castellanos et al., 2013] Castellanos, P., Pelegrí, J. L., and Benazzouz, A. (2013). Wind-driven surface circulation in the cape blanc region. *Continental Shelf Research*, 60:87–103.

[Cayula and Cornillon, 1992] Cayula, J.-F. and Cornillon, P. (1992). Edge detection algorithm for sst images. *Journal of Atmospheric and Oceanic Technology*, 9(1):67–80.

[Cayula et al., 1991] Cayula, J.-F., Cornillon, P., Holyer, R., and Peckinpaugh, S. (1991). Comparative study of two recent edge-detection algorithms designed to process sea-surface temperature fields. *IEEE transactions on geoscience and remote sensing*, 29(1):175–177.

[Chan and Vese, 2001] Chan, T. F. and Vese, L. A. (2001). Active contours without edges. *IEEE Transactions on image processing*, 10(2):266–277.

[Chandra et al., 1998] Chandra, S., Ziemke, J., Min, W., and Read, W. (1998). Effects of 1997–1998 el nino on tropospheric ozone and water vapor. *Geophysical Research Letters*, 25(20):3867–3870.

[Chang and Li, 1994] Chang, Y.-L. and Li, X. (1994). Adaptive image region-growing. *Image Processing, IEEE Transactions on*, 3(6):868–872.

[Charnock, 1955] Charnock, H. (1955). Wind stress on a water surface. *Quarterly Journal of the Royal Meteorological Society*, 81(350):639–640.

[Chavez and Messié, 2009] Chavez, F. P. and Messié, M. (2009). A comparison of eastern boundary upwelling ecosystems. *Progress in Oceanography*, 83(1):80–96.

[Chelton et al., 2001] Chelton, D. B., Ries, J. C., Haines, B. J., Fu, L.-L., and Callahan, P. S. (2001). Satellite altimetry. In *International geophysics*, volume 69, pages 1–ii. Elsevier.

[Cohen et al., 2010] Cohen, J., Foster, J., Barlow, M., Saito, K., and Jones, J. (2010). Winter 2009–2010: A case study of an extreme arctic oscillation event. *Geophysical Research Letters*, 37(17).

[Cravo et al., 2010] Cravo, A., Relvas, P., Cardeira, S., Rita, F., Madureira, M., and Sánchez, R. (2010). An upwelling filament off southwest iberia: Effect on the chlorophyll a and nutrient export. *Continental Shelf Research*, 30(15):1601–1613.

[Crawford et al., 2007] Crawford, W. R., Brickley, P. J., and Thomas, A. C. (2007). Mesoscale eddies dominate surface phytoplankton in northern gulf of alaska. *Progress in Oceanography*, 75(2):287–303.

[Csanady, 1967] Csanady, G. (1967). On the "resistance law" of a turbulent ekman layer. *journal of the Atmospheric Sciences*, 24(5):467–471.

[Cury and Roy, 1989] Cury, P. and Roy, C. (1989). Optimal environmental window and pelagic fish recruitment success in upwelling areas. *Canadian Journal of Fisheries and Aquatic Sciences*, 46(4):670–680.

[Cushing, 1971] Cushing, D. H. (1971). Upwelling and the production of fish. *Advances in marine biology*, 9:255–334.

[Cushman-Roisin and Manga, 1995] Cushman-Roisin, B. and Manga, M. (1995). Introduction to geophysical fluid dynamics. *Pure and Applied Geophysics*, 144(1):177–178.

[De Monte et al., 2012] De Monte, S., Cotté, C., d'Ovidio, F., Lévy, M., Le Corre, M., and Weimerskirch, H. (2012). Frigatebird behaviour at the ocean–atmosphere interface: integrating animal behaviour with multi-satellite data. *Journal of the Royal Society Interface*, 9(77):3351–3358.

[Demarcq and FAURE, 2000] Demarcq, H. and FAURE, V. (2000). Coastal upwelling and associated retention indices derived from satellite sst. application to octopus vulgaris recruitment. *Oceanologica Acta*, 23(4):391–408.

[Dinniman et al., 2003] Dinniman, M. S., Klinck, J. M., and Smith, W. O. (2003). Cross-shelf exchange in a model of the ross sea circulation and biogeochemistry. *Deep Sea Research Part II: Topical Studies in Oceanography*, 50(22):3103–3120.

[Dong et al., 2011] Dong, C., Liu, Y., Lumpkin, R., Lankhorst, M., Chen, D., McWilliams, J. C., and Guan, Y. (2011). A scheme to identify loops from trajectories of oceanic surface drifters: an application in the kuroshio extension region. *Journal of Atmospheric and Oceanic Technology*, 28(9):1167–1176.

[Dong et al., 2014] Dong, C., McWilliams, J. C., Liu, Y., and Chen, D. (2014). Global heat and salt transports by eddy movement. *Nature communications*, 5:3294.

[d'Ovidio et al., 2004] d'Ovidio, F., Fernández, V., Hernández-García, E., and López, C. (2004). Mixing structures in the mediterranean sea from finite-size lyapunov exponents. *Geophysical Research Letters*, 31(17).

[Durand et al., 1998] Durand, M.-H., Cury, P., Mendelssohn, R., Roy, C., Bakun, A., and Pauly, D. (1998). *Global versus local changes in upwelling systems*.

[d'Ovidio et al., 2010] d'Ovidio, F., De Monte, S., Alvain, S., Dandonneau, Y., and Lévy, M. (2010). Fluid dynamical niches of phytoplankton types. *Proceedings of the National Academy of Sciences*, 107(43):18366–18370.

[d'Ovidio et al., 2009] d'Ovidio, F., Isern-Fontanet, J., López, C., Hernández-García, E., and García-Ladona, E. (2009). Comparison between eulerian diagnostics and finite-size lyapunov exponents computed from altimetry in the algerian basin. *Deep Sea Research Part I: Oceanographic Research Papers*, 56(1):15–31.

[Ebuchi et al., 2002] Ebuchi, N., Graber, H. C., and Caruso, M. J. (2002). Evaluation of wind vectors observed by quikscat/seawinds using ocean buoy data. *Journal of Atmospheric and Oceanic Technology*, 19(12):2049–2062.

[Ekman, 1905] Ekman, V. W. (1905). On the influence of the earth\'s rotation on ocean currents. *Ark. Mat. Astron. Fys.*, 2:1–53.

[El Aouni et al., 2018a] El Aouni, A., Daoudi, K., Minaoui, K., and Yahia, H. (2018a). Segmentation, quantification and dynamics of coastal upwelling using sst satellite images. *Submited to: Ocean Dynamics*, page Under review.

[El Aouni et al., 2018b] El Aouni, A., Daoudi, K., Yahia, H., and Minaoui, K. (2018b). Coherent vortex detection from particles trajectories analysis. In *2018 SIAM Conference on Nonlinear Waves and Coherent Structures*.

[El Aouni et al., 2018c] El Aouni, A., Daoudi, K., Yahia, H., and Minaoui, K. (2018c). The contribution and influence of coherent mesoscale eddies off the northwest african upwelling on the open ocean. In *2018 SIAM Conference on Mathematics of Planet Earth*.

[El Aouni et al., 2018d] El Aouni, A., Daoudi, K., Yahia, H., and Minaoui, K. (2018d). Surface mixing and biological activity in the north african upwelling. In *AGU Ocean Sciences Meeting 2018*.

[El Aouni et al., 2019a] El Aouni, A., Daoudi, K., Yahia, H., and Minaoui, K. (2019a). Defining coherent vortices from particles trajectories. *Fluid Dynamics Research*, page Undergoing minor revision.

[El Aouni et al., 2019b] El Aouni, A., Garçon, V., Joel, S., Yahia, H., Daoudi, K., and Minaoui, K. (2019b). Segmentation, quantification and dynamics of coastal upwelling using sst satellite images. *Transaction on Geoscience and Remote Sensing*, page accepted.

[El Aouni et al., 2018e] El Aouni, A., Minaoui, K., Daoudi, K., and Yahia, H. (2018e). North-west african upwelling dynamics from physical and biological satellite observations. In *Report of the 4th GEO Blue Planet Symposium*.

[El Aouni et al., 2019c] El Aouni, A., Minaoui, K., Daoudi, K., and Yahia, H. (2019c). Transport by lagrangian eddies off the north-west african upwelling. *Submited to: Scientific reports*.

[El Aouni et al., 2018f] El Aouni, A., Minaoui, K., Tamim, A., Daoudi, K., and Yahia, H. (2018f). An improved method for accurate computation of coastal upwelling index using sea surface temperature images. In *2018 9th International Symposium on Signal, Image, Video and Communications (ISIVC)*, pages 76–81. IEEE.

[El Aouni et al., 2015] El Aouni, A., Minaoui, K., Tamim, A., Daoudi, K., Yahia, H., Atillah, A., and Aboutajdine, D. (2015). Detection of moroccan coastal upwelling using sea surface chlorophyll concentration. In *Computer Systems and Applications (AICCSA), 2015 ACS International Conference on*, pages 1–4. IEEE.

[El Aouni et al., 2019d] El Aouni, A., Yahia, H., Daoudi, K., and Minaoui, K. (2019d). A fourier approach to lagrangian vortex detection. *Chaos: An Interdisciplinary Journal of Nonlinear Science*, 29(9):093106.

[Elias, 2006] Elias, S. (2006). *Encyclopedia of Quaternary science*. Elsevier.

[Ellabban et al., 2014] Ellabban, O., Abu-Rub, H., and Blaabjerg, F. (2014). Renewable energy resources: Current status, future prospects and their enabling technology. *Renewable and Sustainable Energy Reviews*, 39:748–764.

[Fairbanks, 1989] Fairbanks, R. G. (1989). A 17,000-year glacio-eustatic sea level record: influence of glacial melting rates on the younger dryas event and deep-ocean circulation. *Nature*, 342(6250):637.

[Falkowski et al., 1991] Falkowski, P. G., Ziemann, D., Kolber, Z., and Bienfang, P. K. (1991). Role of eddy pumping in enhancing primary production in the ocean. *Nature*, 352(6330):55.

[Farazmand et al., 2014] Farazmand, M., Blazevski, D., and Haller, G. (2014). Shearless transport barriers in unsteady two-dimensional flows and maps. *Physica D: Nonlinear Phenomena*, 278:44–57.

[Farazmand and Haller, 2016] Farazmand, M. and Haller, G. (2016). Polar rotation angle identifies elliptic islands in unsteady dynamical systems. *Physica D: Nonlinear Phenomena*, 315:1–12.

[Farneti et al., 2010] Farneti, R., Delworth, T. L., Rosati, A. J., Griffies, S. M., and Zeng, F. (2010). The role of mesoscale eddies in the rectification of the southern ocean response to climate change. *Journal of Physical Oceanography*, 40(7):1539–1557.

[Feely et al., 2008] Feely, R. A., Sabine, C. L., Hernandez-Ayon, J. M., Ianson, D., and Hales, B. (2008). Evidence for upwelling of corrosive" acidified" water onto the continental shelf. *science*, 320(5882):1490–1492.

[Flather, 2000] Flather, R. A. (2000). Existing operational oceanography. *Coastal Engineering*, 41(1-3):13–40.

[Fréon et al., 2009] Fréon, P., Barange, M., and Aristegui, J. (2009). Eastern boundary upwelling ecosystems: integrative and comparative approaches.

[Frigui and Krishnapuram, 1996] Frigui, H. and Krishnapuram, R. (1996). A robust algorithm for automatic extraction of an unknown number of clusters from noisy data. *Pattern Recognition Letters*, 17(12):1223–1232.

[Frisch, 1995] Frisch, U. (1995). Turbulence (cambridge).

[Froyland, 2013] Froyland, G. (2013). An analytic framework for identifying finite-time coherent sets in time-dependent dynamical systems. *Physica D: Nonlinear Phenomena*, 250:1–19.

[Froyland et al., 2012] Froyland, G., Horenkamp, C., Rossi, V., Santitissadeekorn, N., and Gupta, A. S. (2012). Three-dimensional characterization and tracking of an agulhas ring. *Ocean Modelling*, 52:69–75.

[Froyland et al., 2010] Froyland, G., Santitissadeekorn, N., and Monahan, A. (2010). Transport in time-dependent dynamical systems: Finite-time coherent sets. *Chaos: An Interdisciplinary Journal of Nonlinear Science*, 20(4):043116.

[García-Muñoz et al., 2005] García-Muñoz, M., Arístegui, J., Pelegrí, J. L., Antoranz, A., Ojeda, A., and Torres, M. (2005). Exchange of carbon by an upwelling filament off cape ghir (nw africa). *Journal of Marine Systems*, 54(1-4):83–95.

[Garric and Parent, 2013] Garric, G. and Parent, L. (2013). Quality information document. *Change*, 2:14.

[Garric et al., 2017] Garric, G., Parent, L., Greiner, E., Drévillon, M., Hamon, M., Lellouche, J.-M., Régnier, C., Desportes, C., Le Galloudec, O., Bricaud, C., et al. (2017). Performance and quality assessment of the global ocean eddy-permitting physical reanalysis glorys2v4. In *EGU General Assembly Conference Abstracts*, volume 19, page 18776.

[Gill and Clarke, 1974] Gill, A. and Clarke, A. (1974). Wind-induced upwelling, coastal currents and sea-level changes. In *Deep Sea Research and Oceanographic Abstracts*, volume 21, pages 325–345. Elsevier.

[Glazman et al., 1996] Glazman, R., Fabrikant, A., and Greysukh, A. (1996). Statistics of spatial-temporal variations of sea surface height based on topex altimeter measurements. *Remote Sensing*, 17(13):2647–2666.

[Gomez-Gesteira et al., 2008] Gomez-Gesteira, M., Lorenzo, M., Alvarez, I., Crespo, A., et al. (2008). Influence of atmospheric modes on coastal upwelling along the western coast of the iberian peninsula, 1985 to 2005. *Climate Research*, 36(2):169–179.

[Gonzalez et al., 2004] Gonzalez, R. C., Woods, R. E., Eddins, S. L., et al. (2004). *Digital image processing using MATLAB.*, volume 624. Pearson-Prentice-Hall Upper Saddle River, New Jersey.

[Griffa et al., 2007] Griffa, A., Kirwan Jr, A., Mariano, A. J., Özgökmen, T., and Rossby, H. T. (2007). *Lagrangian analysis and prediction of coastal and ocean dynamics*. Cambridge University Press.

[Gruber et al., 2011] Gruber, N., Lachkar, Z., Frenzel, H., Marchesiello, P., Münnich, M., McWilliams, J. C., Nagai, T., and Plattner, G.-K. (2011). Eddy-induced reduction of biological production in eastern boundary upwelling systems. *Nature geoscience*, 4(11):787.

[Hadjighasem et al., 2017] Hadjighasem, A., Farazmand, M., Blazevski, D., Froyland, G., and Haller, G. (2017). A critical comparison of lagrangian methods for coherent structure detection. *Chaos: An Interdisciplinary Journal of Nonlinear Science*, 27(5):053104.

[Hadjighasem and Haller, 2016] Hadjighasem, A. and Haller, G. (2016). Level set formulation of two-dimensional lagrangian vortex detection methods. *Chaos: An Interdisciplinary Journal of Nonlinear Science*, 26(10):103102.

[Hadjighasem et al., 2016] Hadjighasem, A., Karrasch, D., Teramoto, H., and Haller, G. (2016). Spectral-clustering approach to lagrangian vortex detection. *Physical Review E*, 93(6):063107.

[Hadley et al., 1735] Hadley, G. et al. (1735). Vi. concerning the cause of the general trade-winds. *Philosophical Transactions*, 39(437):58–62.

[Haller, 2005] Haller, G. (2005). An objective definition of a vortex. *Journal of fluid mechanics*, 525:1–26.

[Haller, 2015] Haller, G. (2015). Lagrangian coherent structures. *Annual Review of Fluid Mechanics*, 47:137–162.

[Haller, 2016] Haller, G. (2016). Dynamic rotation and stretch tensors from a dynamic polar decomposition. *Journal of the Mechanics and Physics of Solids*, 86:70–93.

[Haller and Beron-Vera, 2012] Haller, G. and Beron-Vera, F. J. (2012). Geodesic theory of transport barriers in two-dimensional flows. *Physica D: Nonlinear Phenomena*, 241(20):1680–1702.

[Haller and Beron-Vera, 2013] Haller, G. and Beron-Vera, F. J. (2013). Coherent lagrangian vortices: The black holes of turbulence. *Journal of Fluid Mechanics*, 731.

[Haller et al., 2016] Haller, G., Hadjighasem, A., Farazmand, M., and Huhn, F. (2016). Defining coherent vortices objectively from the vorticity. *Journal of Fluid Mechanics*, 795:136–173.

[Haller and Sapsis, 2011] Haller, G. and Sapsis, T. (2011). Lagrangian coherent structures and the smallest finite-time lyapunov exponent. *Chaos: An Interdisciplinary Journal of Nonlinear Science*, 21(2):023115.

[Haller and Yuan, 2000] Haller, G. and Yuan, G. (2000). Lagrangian coherent structures and mixing in two-dimensional turbulence. *Physica D: Nonlinear Phenomena*, 147(3-4):352–370.

[Haszpra and Tél, 2011] Haszpra, T. and Tél, T. (2011). Volcanic ash in the free atmosphere: A dynamical systems approach. In *Journal of Physics: Conference Series*, volume 333, page 012008. IOP Publishing.

[Haza et al., 2010] Haza, A. C., Özgökmen, T. M., Griffa, A., Molcard, A., Poulain, P.-M., and Peggion, G. (2010). Transport properties in small-scale coastal flows: relative dispersion from vhf radar measurements in the gulf of la spezia. *Ocean Dynamics*, 60(4):861–882.

[Heileman and Tanstad, 2008] Heileman, S. and Tanstad, M. (2008). I-3 canary current: Lme# 27. *The UNEP Large Marine Ecosystem Report: A Perspective on Changing Conditions in LMEs of the World's Regional Seas. UNEP Regional Seas Report and Studies*, (182):131–142.

[Hernández-Guerra, 1990] Hernández-Guerra, A. (1990). *Estructuras oceanográficas observadas en las aguas que rodean las Islas Canarias mediante escenas de los sensores AVHRR y CZCS*.

[Hernández-Guerra et al., 1993] Hernández-Guerra, A., Arístegui, J., Cantón, M., and Nykjaer, L. (1993). Phytoplankton pigment patterns in the canary islands area as determined using coastal zone colour scanner data. *International Journal of Remote Sensing*, 14(7):1431–1437.

[Hernández-Guerra et al., 2005] Hernández-Guerra, A., Fraile-Nuez, E., López-Laatzen, F., Martínez, A., Parrilla, G., and Vélez-Belchí, P. (2005). Canary current and north equatorial current from an inverse box model. *Journal of Geophysical Research: Oceans*, 110(C12).

[Hernández-Guerra and Nykjaer, 1997] Hernández-Guerra, A. and Nykjaer, L. (1997). Sea surface temperature variability off north-west africa: 1981-1989. *International Journal of Remote Sensing*, 18(12):2539–2558.

[Herrmann, 2005] Herrmann, M. (2005). A eulerian level set/vortex sheet method for two-phase interface dynamics. *Journal of Computational Physics*, 203(2):539–571.

[Holyer and Peckinpaugh, 1989] Holyer, R. J. and Peckinpaugh, S. H. (1989). Edge detection applied to satellite imagery of the oceans. *IEEE transactions on geoscience and remote sensing*, 27(1):46–56.

[Hueckel, 1973] Hueckel, M. H. (1973). A local visual operator which recognizes edges and lines. *Journal of the ACM (JACM)*, 20(4):634–647.

[Huhn et al., 2012] Huhn, F., von Kameke, A., Allen-Perkins, S., Montero, P., Venancio, A., and Perez-Munuzuri, V. (2012). Horizontal lagrangian transport in a tidal-driven estuary—transport barriers attached to prominent coastal boundaries. *Continental Shelf Research*, 39:1–13.

[Huyer, 1983] Huyer, A. (1983). Coastal upwelling in the california current system. *Progress in oceanography*, 12(3):259–284.

[Ide et al., 1997] Ide, K., Courtier, P., Ghil, M., and Lorenc, A. C. (1997). Unified notation for data assimilation: Operational, sequential and variational (gtspecial issueltdata assimilation in meteology and oceanography: Theory and practice). *Journal of the Meteorological Society of Japan. Ser. II*, 75(1B):181–189.

[Jain and Dubes, 1978] Jain, A. K. and Dubes, R. (1978). Feature definition in pattern recognition with small sample size. *Pattern Recognition*, 10(2):85–97.

[Jain and Dubes, 1988] Jain, A. K. and Dubes, R. C. (1988). *Algorithms for clustering data*. Prentice-Hall, Inc.

[Jennings et al., 2009] Jennings, S., Kaiser, M., and Reynolds, J. D. (2009). *Marine fisheries ecology*. John Wiley & Sons.

[Jensen and Lulla, 1987] Jensen, J. R. and Lulla, K. (1987). Introductory digital image processing: a remote sensing perspective.

[Joseph and Legras, 2002] Joseph, B. and Legras, B. (2002). Relation between kinematic boundaries, stirring, and barriers for the antarctic polar vortex. *Journal of the Atmospheric Sciences*, 59(7):1198–1212.

[Justice et al., 2002] Justice, C., Giglio, L., Korontzi, S., Owens, J., Morisette, J., Roy, D., Descloitres, J., Alleaume, S., Petitcolin, F., and Kaufman, Y. (2002). The modis fire products. *Remote Sensing of Environment*, 83(1-2):244–262.

[Kai et al., 2009] Kai, E. T., Rossi, V., Sudre, J., Weimerskirch, H., Lopez, C., Hernandez-Garcia, E., Marsac, F., and Garçon, V. (2009). Top marine predators track lagrangian coherent structures. *Proceedings of the National Academy of Sciences*, 106(20):8245–8250.

[Kämpf and Chapman, 2016] Kämpf, J. and Chapman, P. (2016). *Upwelling systems of the world: A scientific journey to the most productive marine ecosystems*. Springer.

[Kang et al., 2004] Kang, J.-H., Kim, W.-S., Chang, K.-I., and Noh, J.-H. (2004). Distribution of plankton related to the mesoscale physical structure within the surface mixed layer in the southwestern east sea, korea. *Journal of plankton research*, 26(12):1515–1528.

[Károlyi et al., 2010] Károlyi, G., Pattantyús-Ábrahám, M., Krámer, T., Józsa, J., and Tél, T. (2010). Finite-size lyapunov exponents: A new tool for lake dynamics. *Proceedings of the Institution of Civil Engineers-Engineering and Computational Mechanics*, 163(4):251–259.

[Karrasch and Haller, 2013] Karrasch, D. and Haller, G. (2013). Do finite-size lyapunov exponents detect coherent structures? *Chaos: An Interdisciplinary Journal of Nonlinear Science*, 23(4):043126.

[Karrasch et al., 2015] Karrasch, D., Huhn, F., and Haller, G. (2015). Automated detection of coherent lagrangian vortices in two-dimensional unsteady flows. In *Proc. R. Soc. A*, volume 471, page 20140639. The Royal Society.

[Kaymak and Setnes, 2002] Kaymak, U. and Setnes, M. (2002). Fuzzy clustering with volume prototypes and adaptive cluster merging. *IEEE Transactions on Fuzzy Systems*, 10(6):705–712.

[Kennedy, 2011] Kennedy, J. (2011). Particle swarm optimization. In *Encyclopedia of machine learning*, pages 760–766. Springer.

[Kennedy et al., 2001] Kennedy, J., Kennedy, J. F., Eberhart, R. C., and Shi, Y. (2001). *Swarm intelligence*. Morgan Kaufmann.

[Klein and Lapeyre, 2009] Klein, P. and Lapeyre, G. (2009). The oceanic vertical pump induced by mesoscale and submesoscale turbulence. *Annual review of marine science*, 1:351–375.

[Knauss and Garfield, 2016] Knauss, J. A. and Garfield, N. (2016). *Introduction to physical oceanography*. Waveland Press.

[Kostianoy and Zatsepin, 1996] Kostianoy, A. and Zatsepin, A. (1996). The west african coastal upwelling filaments and cross-frontal water exchange conditioned by them. *Journal of Marine Systems*, 7(2-4):349–359.

[Kundu, 1976] Kundu, P. K. (1976). Ekman veering observed near the ocean bottom. *Journal of Physical Oceanography*, 6(2):238–242.

[La Violette, 1974] La Violette, P. E. (1974). A satellite-aircraft thermal study of the upwelled waters off spanish sahara. *Journal of Physical Oceanography*, 4(4):676–684.

[Lagerloef et al., 1999] Lagerloef, G. S., Mitchum, G. T., Lukas, R. B., and Niiler, P. P. (1999). Tropical pacific near-surface currents estimated from altimeter, wind, and drifter data. *Journal of Geophysical Research: Oceans*, 104(C10):23313–23326.

[Lasternas et al., 2013] Lasternas, S., Piedeleu, M., Sangrà, P., Duarte, C. M., and Agustí, S. (2013). Forcing of dissolved organic carbon release by phytoplankton by anticyclonic mesoscale eddies in the subtropical ne atlantic ocean. *Biogeosciences*, 10(3):2129–2143.

[Lathuilière et al., 2008] Lathuilière, C., Echevin, V., and Lévy, M. (2008). Seasonal and intraseasonal surface chlorophyll-a variability along the northwest african coast. *Journal of Geophysical Research: Oceans*, 113(C5).

[Lázaro et al., 2005] Lázaro, C., Fernandes, M. J., Santos, A. M. P., and Oliveira, P. (2005). Seasonal and interannual variability of surface circulation in the cape verde region from 8 years of merged t/p and ers-2 altimeter data. *Remote sensing of environment*, 98(1):45–62.

[Lehahn et al., 2007] Lehahn, Y., d'Ovidio, F., Lévy, M., and Heifetz, E. (2007). Stirring of the northeast atlantic spring bloom: A lagrangian analysis based on multisatellite data. *Journal of Geophysical Research: Oceans*, 112(C8).

[Lillesand et al., 2014] Lillesand, T., Kiefer, R. W., and Chipman, J. (2014). *Remote sensing and image interpretation*. John Wiley & Sons.

[Lindeberg, 2001] Lindeberg, T. (2001). Scale-space theory. *Encyclopaedia of Mathematics*.

[Liu, 2002] Liu, W. T. (2002). Progress in scatterometer application. *Journal of Oceanography*, 58(1):121–136.

[Looney, 1999] Looney, C. G. (1999). A fuzzy clustering and fuzzy merging algorithm. *Reno, NV*.

[Loubere, 2012] Loubere, P. (2012). The global climate system.

[Lu and Speer, 2010] Lu, J. and Speer, K. (2010). Topography, jets, and eddy mixing in the southern ocean. *Journal of Marine Research*, 68(3-1):479–502.

[Machu et al., 2009] Machu, E., Ettahiri, O., Kifani, S., Benazzouz, A., Makaoui, A., and Demarcq, H. (2009). Environmental control of the recruitment of sardines (sardina pilchardus) over the western saharan shelf between 1995 and 2002: a coupled physical/biogeochemical modelling experiment. *Fisheries Oceanography*, 18(5):287–300.

[Mackas et al., 2005] Mackas, D., Tsurumi, M., Galbraith, M., and Yelland, D. (2005). Zooplankton distribution and dynamics in a north pacific eddy of coastal origin: Ii. mechanisms of eddy colonization by and retention of offshore species. *Deep Sea Research Part II: Topical Studies in Oceanography*, 52(7):1011–1035.

[Madec et al., 2015] Madec, G. et al. (2015). Nemo ocean engine.

[Mahadevan and Tandon, 2006] Mahadevan, A. and Tandon, A. (2006). An analysis of mechanisms for submesoscale vertical motion at ocean fronts. *Ocean Modelling*, 14(3-4):241–256.

[Maini and Aggarwal, 2009] Maini, R. and Aggarwal, H. (2009). Study and comparison of various image edge detection techniques. *International journal of image processing (IJIP)*, 3(1):1–11.

[Maji and Yahia, 2014] Maji, S. K. and Yahia, H. M. (2014). Edges, transitions and criticality. *Pattern Recognition*, 47(6):2104–2115.

[Mancho et al., 2006] Mancho, A. M., Small, D., and Wiggins, S. (2006). A tutorial on dynamical systems concepts applied to lagrangian transport in oceanic flows defined as finite time data sets: Theoretical and computational issues. *Physics Reports*, 437(3-4):55–124.

[Mancho et al., 2013] Mancho, A. M., Wiggins, S., Curbelo, J., and Mendoza, C. (2013). Lagrangian descriptors: A method for revealing phase space structures of general time dependent dynamical systems. *Communications in Nonlinear Science and Numerical Simulation*, 18(12):3530–3557.

[Marcello et al., 2011] Marcello, J., Hernandez-Guerra, A., Eugenio, F., and Fonte, A. (2011). Seasonal and temporal study of the northwest african upwelling system. *International Journal of Remote Sensing*, 32(7):1843–1859.

[Marcello et al., 2005] Marcello, J., Marqués, F., and Eugenio, F. (2005). Automatic tool for the precise detection of upwelling and filaments in remote sensing imagery. *Geoscience and Remote Sensing, IEEE Transactions on*, 43(7):1605–1616.

[Marchesiello and Estrade, 2009] Marchesiello, P. and Estrade, P. (2009). Eddy activity and mixing in upwelling systems: a comparative study of northwest africa and california regions. *International Journal of Earth Sciences*, 98(2):299–308.

[Margalef, 1978] Margalef, R. (1978). Phytoplankton communities in upwelling areas. the example of nw africa. *Oecologia aquatica*, 3(3).

[Marlow et al., 2000] Marlow, J. R., Lange, C. B., Wefer, G., and Rosell-Melé, A. (2000). Upwelling intensification as part of the pliocene-pleistocene climate transition. *Science*, 290(5500):2288–2291.

[Mason et al., 2014] Mason, E., Pascual, A., and McWilliams, J. C. (2014). A new sea surface height–based code for oceanic mesoscale eddy tracking. *Journal of Atmospheric and Oceanic Technology*, 31(5):1181–1188.

[Mason et al., 2012] Mason, R. P., Choi, A. L., Fitzgerald, W. F., Hammerschmidt, C. R., Lamborg, C. H., Soerensen, A. L., and Sunderland, E. M. (2012). Mercury biogeochemical cycling in the ocean and policy implications. *Environmental research*, 119:101–117.

[Matano et al., 2010] Matano, R., Palma, E. D., and Piola, A. R. (2010). The influence of the brazil and malvinas currents on the southwestern atlantic shelf circulation.

[Matheron, 1975] Matheron, G. (1975). Random sets and integral geometry.

[Maxey and Riley, 1983] Maxey, M. R. and Riley, J. J. (1983). Equation of motion for a small rigid sphere in a nonuniform flow. *The Physics of Fluids*, 26(4):883–889.

[Mazloff et al., 2010] Mazloff, M. R., Heimbach, P., and Wunsch, C. (2010). An eddy-permitting southern ocean state estimate. *Journal of Physical Oceanography*, 40(5):880–899.

[McGillicuddy et al., 2007] McGillicuddy, D. J., Anderson, L. A., Bates, N. R., Bibby, T., Buesseler, K. O., Carlson, C. A., Davis, C. S., Ewart, C., Falkowski, P. G., Goldthwait, S. A., et al. (2007). Eddy/wind interactions stimulate extraordinary mid-ocean plankton blooms. *Science*, 316(5827):1021–1026.

[McGillicuddy Jr et al., 1998] McGillicuddy Jr, D. J., Robinson, A., Siegel, D., Jannasch, H., et al. (1998). Influence of mesoscale eddies on new production in the sargasso sea. *Nature*, 394(6690):263.

[McPhaden, 1999] McPhaden, M. J. (1999). Genesis and evolution of the 1997-98 el niño. *Science*, 283(5404):950–954.

[Mendoza and Mancho, 2010] Mendoza, C. and Mancho, A. M. (2010). Hidden geometry of ocean flows. *Physical review letters*, 105(3):038501.

[Minnett et al., 2004] Minnett, P. J., Brown, O. B., Evans, R. H., Key, E. L., Kearns, E. J., Kilpatrick, K., Kumar, A., Maillet, K. A., and Szczodrak, G. (2004). Sea-surface temperature measurements from the moderate-resolution imaging spectroradiometer (modis) on aqua and terra. In *Geoscience and Remote Sensing Symposium, 2004. IGARSS'04. Proceedings. 2004 IEEE International*, volume 7, pages 4576–4579. Ieee.

[Mittelstaedt, 1983] Mittelstaedt, E. (1983). The upwelling area off northwest africa—a description of phenomena related to coastal upwelling. *Progress in Oceanography*, 12(3):307–331.

[Moore et al., 2007] Moore, T. S., Matear, R. J., Marra, J., and Clementson, L. (2007). Phytoplankton variability off the western australian coast: Mesoscale eddies and their role in cross-shelf exchange. *Deep Sea Research Part II: Topical Studies in Oceanography*, 54(8):943–960.

[Nascimento and Franco, 2009a] Nascimento, S. and Franco, P. (2009a). Segmentation of upwelling regions in sea surface temperature images via unsupervised fuzzy clustering. In *International Conference on Intelligent Data Engineering and Automated Learning*, pages 543–553. Springer.

[Nascimento and Franco, 2009b] Nascimento, S. and Franco, P. (2009b). Unsupervised fuzzy clustering for the segmentation and annotation of upwelling regions in sea surface temperature images. In *International Conference on Discovery Science*, pages 212–226. Springer.

[Nash et al., 1996] Nash, E. R., Newman, P. A., Rosenfield, J. E., and Schoeberl, M. R. (1996). An objective determination of the polar vortex using ertel's potential vorticity. *Journal of Geophysical Research: Atmospheres*, 101(D5):9471–9478.

[Nieto et al., 2012] Nieto, K., Demarcq, H., and McClatchie, S. (2012). Mesoscale frontal structures in the canary upwelling system: New front and filament detection algorithms applied to spatial and temporal patterns. *Remote Sensing of Environment*, 123:339–346.

[Nykjær and Van Camp, 1994] Nykjær, L. and Van Camp, L. (1994). Seasonal and interannual variability of coastal upwelling along northwest africa and portugal from 1981 to 1991. *Journal of Geophysical Research: Oceans*, 99(C7):14197–14207.

[Nykjaer and Vancamp, 1992] Nykjaer, L. and Vancamp, L. (1992). Seasonal sst and upwelling indices along the northwest african coast. *ESA, Environment Observation and Climate Modelling Through International Space Projects.*, 1.

[Olascoaga et al., 2013] Olascoaga, M., Beron-Vera, F., Haller, G., Trinanes, J., Iskandarani, M., Coelho, E., Haus, B., Huntley, H., Jacobs, G., Kirwan, A., et al. (2013). Drifter motion in the gulf of mexico constrained by altimetric lagrangian coherent structures. *Geophysical Research Letters*, 40(23):6171–6175.

[Olascoaga and Haller, 2012] Olascoaga, M. J. and Haller, G. (2012). Forecasting sudden changes in environmental pollution patterns. *Proceedings of the National Academy of Sciences*.

[Olson et al., 1988] Olson, D. B., Podesta, G. P., Evans, R. H., and Brown, O. B. (1988). Temporal variations in the separation of brazil and malvinas currents. *Deep Sea Research Part A. Oceanographic Research Papers*, 35(12):1971–1990.

[Onu et al., 2015] Onu, K., Huhn, F., and Haller, G. (2015). Lcs tool: A computational platform for lagrangian coherent structures. *Journal of Computational Science*, 7:26–36.

[Osborn, 2011] Osborn, T. J. (2011). Winter 2009/2010 temperatures and a record-breaking north atlantic oscillation index. *Weather*, 66(1):19–21.

[Oschlies and Garcon, 1998] Oschlies, A. and Garcon, V. (1998). Eddy-induced enhancement of primary production in a model of the north atlantic ocean. *Nature*, 394(6690):266.

[Ott, 2002] Ott, E. (2002). *Chaos in dynamical systems*. Cambridge university press.

[Ottino, 1989] Ottino, J. M. (1989). *The kinematics of mixing: stretching, chaos, and transport*, volume 3. Cambridge university press.

[Owen, 1981] Owen, R. W. (1981). Fronts and eddies in the sea: mechanisms, interactions and biological effects. *Analysis of marine ecosystems*, pages 197–233.

[Pastor et al., 2008] Pastor, M. V., Pelegrí, J. L., Hernández-Guerra, A., Font, J., Salat, J., and Emelianov, M. (2008). Water and nutrient fluxes off northwest africa. *Continental Shelf Research*, 28(7):915–936.

[Pauly and Christensen, 1995] Pauly, D. and Christensen, V. (1995). Primary production required to sustain global fisheries. *Nature*, 374(6519):255.

[Peacock and Dabiri, 2010] Peacock, T. and Dabiri, J. (2010). Introduction to focus issue: Lagrangian coherent structures.

[Peacock and Haller, 2013] Peacock, T. and Haller, G. (2013). Lagrangian coherent structures: The hidden skeleton of fluid flows. *Physics today*, 66(2):41.

[Pelegrí et al., 2005a] Pelegrí, J., Arístegui, J., Cana, L., González-Dávila, M., Hernández-Guerra, A., Hernández-León, S., Marrero-Díaz, A., Montero, M., Sangrà, P., and Santana-Casiano, M. (2005a). Coupling between the open ocean and the coastal upwelling region off northwest africa: water recirculation and offshore pumping of organic matter. *Journal of Marine Systems*, 54(1-4):3–37.

[Pelegrí et al., 2005b] Pelegrí, J., Marrero-Díaz, A., Ratsimandresy, A., Antoranz, A., Cisneros-Aguirre, J., Gordo, C., Grisolía, D., Hernández-Guerra, A., Láiz, I., Martínez, A., et al. (2005b). Hydrographic cruises off northwest africa: the canary current and the cape ghir region. *Journal of Marine Systems*, 54(1-4):39–63.

[Pelegrí et al., 2006] Pelegrí, J. L., Marrero-Díaz, A., and Ratsimandresy, A. (2006). Nutrient irrigation of the north atlantic. *Progress in Oceanography*, 70(2-4):366–406.

[Peña-Izquierdo et al., 2012] Peña-Izquierdo, J., Pelegrí, J. L., Pastor, M. V., Castellanos, P., Emelianov, M., Gasser, M., Salvador, J., and Vázquez-Domínguez, E. (2012). The continental slope current system between cape verde and the canary islands. *Scientia Marina*, 76(S1):65–78.

[Picaut, 1983] Picaut, J. (1983). Propagation of the seasonal upwelling in the eastern equatorial atlantic. *Journal of Physical Oceanography*, 13(1):18–37.

[Piedeleu et al., 2009] Piedeleu, M., Sangrà, P., Sánchez-Vidal, A., Fabrés, J., Gordo, C., and Calafat, A. (2009). An observational study of oceanic eddy generation mechanisms by tall deep-water islands (gran canaria). *Geophysical Research Letters*, 36(14).

[Pierrehumbert, 1994] Pierrehumbert, R. (1994). Tracer microstructure in the large-eddy dominated regime. *Chaos, Solitons & Fractals*, 4(6):1091–1110.

[Pont et al., 2013] Pont, O., Turiel, A., and Yahia, H. (2013). Singularity analysis of digital signals through the evaluation of their unpredictable point manifold. *International Journal of Computer Mathematics*, 90(8):1693–1707.

[Pottier, 2006] Pottier, C. (2006). *Combinaison multi-capteurs de données de couleur de l'eau : application en océanographie opérationnelle*. PhD thesis, Université Paul Sabatier.

[Price et al., 1987] Price, J. F., Weller, R. A., and Schudlich, R. R. (1987). Wind-driven ocean currents and ekman transport. *Science*, 238(4833):1534–1538.

[Pvamanarhan et al., 1989] Pvamanarhan, V., Barksrrom, B. R., and Harrison, E. F. (1989). Climate and the earth's radiation budget. *Physics Today*, page 20.

[Rayner et al., 2003] Rayner, N., Parker, D. E., Horton, E., Folland, C. K., Alexander, L. V., Rowell, D., Kent, E., and Kaplan, A. (2003). Global analyses of sea surface temperature, sea ice, and night marine air temperature since the late nineteenth century. *Journal of Geophysical Research: Atmospheres*, 108(D14).

[Rhines and Young, 1982] Rhines, P. B. and Young, W. R. (1982). A theory of the wind-driven circulation. i. mid-ocean gyres. *J. Mar. Res*, 40(3):559–596.

[Richards, 2013] Richards, J. A. (2013). Clustering and unsupervised classification. In *Remote Sensing Digital Image Analysis*, pages 319–341. Springer.

[Risien and Chelton, 2008] Risien, C. M. and Chelton, D. B. (2008). A global climatology of surface wind and wind stress fields from eight years of quikscat scatterometer data. *Journal of Physical Oceanography*, 38(11):2379–2413.

[Rossi et al., 2009] Rossi, V., López, C., Hernández-García, E., Sudre, J., Garçon, V., and Morel, Y. (2009). Surface mixing and biological activity in the four eastern boundary upwelling systems. *arXiv preprint arXiv:0909.0115*.

[Rossi et al., 2008] Rossi, V., López, C., Sudre, J., Hernández-Garcia, E., and Garçon, V. (2008). Comparative study of mixing and biological activity of the benguela and canary upwelling systems. *Geophysical Research Letters*, 35(11).

[Ruijter et al., 1999] Ruijter, W. d., Biastoch, A., Drijfhout, S., Lutjeharms, J., Matano, R., Pichevin, T., Leeuwen, P. v., and Weijer, W. (1999). Indian-atlantic interocean exchange: Dynamics, estimation and impact. *Journal of Geophysical Research: Oceans*, 104(C9):20885–20910.

[Rypina et al., 2011] Rypina, I. I., Scott, S., Pratt, L. J., and Brown, M. G. (2011). Investigating the connection between complexity of isolated trajectories and lagrangian coherent structures. *Nonlinear Processes in Geophysics*, 18(6):977–987.

[Ryther, 1969] Ryther, J. H. (1969). Photosynthesis and fish production in the sea. *Science*, 166(3901):72–76.

[Sahner et al., 2007] Sahner, J., Weinkauf, T., Teuber, N., and Hege, H.-C. (2007). Vortex and strain skeletons in eulerian and lagrangian frames. *IEEE Transactions on Visualization and Computer Graphics*, 13(5).

[Samelson and Wiggins, 2006] Samelson, R. M. and Wiggins, S. (2006). *Lagrangian transport in geophysical jets and waves: The dynamical systems approach*, volume 31. Springer Science & Business Media.

[Sangrà et al., 2007] Sangrà, P., Auladell, M., Marrero-Díaz, A., Pelegrí, J. L., Fraile-Nuez, E., Rodríguez-Santana, A., Martín, J., Mason, E., and Hernández-Guerra, A. (2007). On the nature of oceanic eddies shed by the island of gran canaria. *Deep Sea Research Part I: Oceanographic Research Papers*, 54(5):687–709.

[Sangrà et al., 2009] Sangrà, P., Pascual, A., Rodríguez-Santana, Á., Machín, F., Mason, E., McWilliams, J. C., Pelegrí, J. L., Dong, C., Rubio, A., Arístegui, J., et al. (2009). The canary eddy corridor: A major pathway for long-lived eddies in the subtropical north atlantic. *Deep Sea Research Part I: Oceanographic Research Papers*, 56(12):2100–2114.

[Sangrà et al., 2005] Sangrà, P., Pelegrí, J. L., Hernández-Guerra, A., Arregui, I., Martín, J., Marrero-Díaz, A., Martínez, A., Ratsimandresy, A., and Rodríguez-Santana, A. (2005). Life history of an anticyclonic eddy. *Journal of Geophysical Research: Oceans*, 110(C3).

[Sangrà et al., 2015] Sangrà, P., Troupin, C., Barreiro-González, B., Desmond Barton, E., Orbi, A., and Arístegui, J. (2015). The cape ghir filament system in august 2009 (nw africa). *Journal of Geophysical Research: Oceans*, 120(6):4516–4533.

[Santos et al., 2005] Santos, A. M. P., Kazmin, A. S., and Peliz, A. (2005). Decadal changes in the canary upwelling system as revealed by satellite observations: their impact on productivity. *Journal of Marine Research*, 63(2):359–379.

[Savtchenko et al., 2004] Savtchenko, A., Ouzounov, D., Ahmad, S., Acker, J., Leptoukh, G., Koziana, J., and Nickless, D. (2004). Terra and aqua modis products available from nasa ges daac. *Advances in Space Research*, 34(4):710–714.

[Schowengerdt, 2006] Schowengerdt, R. A. (2006). *Remote sensing: models and methods for image processing*. Elsevier.

[Seager et al., 2010] Seager, R., Kushnir, Y., Nakamura, J., Ting, M., and Naik, N. (2010). Northern hemisphere winter snow anomalies: Enso, nao and the winter of 2009/10. *Geophysical research letters*, 37(14).

[Serra, 1983] Serra, J. (1983). *Image analysis and mathematical morphology*. Academic Press, Inc.

[Serra and Haller, 2017] Serra, M. and Haller, G. (2017). Efficient computation of null geodesics with applications to coherent vortex detection. In *Proc. R. Soc. A*, volume 473, page 20160807. The Royal Society.

[Serra et al., 2017] Serra, M., Sathe, P., Beron-Vera, F., and Haller, G. (2017). Uncovering the edge of the polar vortex. *Journal of the Atmospheric Sciences*, 74(11):3871–3885.

[Shadden et al., 2005] Shadden, S. C., Lekien, F., and Marsden, J. E. (2005). Definition and properties of lagrangian coherent structures from finite-time lyapunov exponents in two-dimensional aperiodic flows. *Physica D: Nonlinear Phenomena*, 212(3-4):271–304.

[Shanks and Brink, 2005] Shanks, A. L. and Brink, L. (2005). Upwelling, downwelling, and cross-shelf transport of bivalve larvae: test of a hypothesis. *Marine Ecology Progress Series*, 302:1–12.

[Shapiro and Stockman, 2001] Shapiro, L. and Stockman, G. C. (2001). Computer vision. 2001. *ed: Prentice Hall*.

[Shi and Eberhart, 1998] Shi, Y. and Eberhart, R. C. (1998). Parameter selection in particle swarm optimization. In *International Conference on Evolutionary Programming*, pages 591–600. Springer.

[Sobel et al., 1997] Sobel, A., Plumb, R., and Waugh, D. (1997). Methods of calculating transport across the polar vortex edge. *Journal of the atmospheric sciences*, 54(18):2241–2260.

[Sousa et al., 2008] Sousa, F. M., Nascimento, S., Casimiro, H., and Boutov, D. (2008). Identification of upwelling areas on sea surface temperature images using fuzzy clustering. *Remote Sensing of Environment*, 112(6):2817–2823.

[Spotz and Carey, 1995] Spotz, W. and Carey, G. (1995). High-order compact scheme for the steady stream-function vorticity equations. *International Journal for Numerical Methods in Engineering*, 38(20):3497–3512.

[Steininger and Horning, 2007] Steininger, M. and Horning, N. (2007). The basics of remote sensing. *Sourcebook on Remote Sensing and Biodiversity Indicators, Technical Series*, (32):201.

[Stewart, 2000] Stewart, R. H. (2000). Introduction to physical oceanography.

[Stoffelen and Anderson, 1997] Stoffelen, A. and Anderson, D. (1997). Scatterometer data interpretation: Estimation and validation of the transfer function cmod4. *Journal of Geophysical Research: Oceans*, 102(C3):5767–5780.

[Stommel, 1948] Stommel, H. (1948). The westward intensification of wind-driven ocean currents. *Eos, Transactions American Geophysical Union*, 29(2):202–206.

[Stommel and Arons, 1959] Stommel, H. and Arons, A. (1959). On the abyssal circulation of the world ocean—i. stationary planetary flow patterns on a sphere. *Deep Sea Research (1953)*, 6:140–154.

[Strass, 1992] Strass, V. H. (1992). Chlorophyll patchiness caused by mesoscale upwelling at fronts. *Deep Sea Research Part A. Oceanographic Research Papers*, 39(1):75–96.

[Strub and James, 2000] Strub, P. T. and James, C. (2000). Altimeter-derived variability of surface velocities in the california current system: 2. seasonal circulation and eddy statistics. *Deep Sea Research Part II: Topical Studies in Oceanography*, 47(5-6):831–870.

[Sudre et al., 2013] Sudre, J., Maes, C., and Garçon, V. (2013). On the global estimates of geostrophic and ekman surface currents. *Limnology and Oceanography: Fluids and Environments*, 3(1):1–20.

[Sverdrup, 1947] Sverdrup, H. U. (1947). Wind-driven currents in a baroclinic ocean; with application to the equatorial currents of the eastern pacific. *Proceedings of the National Academy of Sciences*, 33(11):318–326.

[Tamim, 2015] Tamim, A. (2015). *Segmentation et classification des images satellitaires: application à la détection des zones d'upwelling côtier marocain et mise en place d'un logiciel de suivi spatiotemporel.* PhD thesis, UNIVERSITÉ MOHAMMED V FACULTÉ DES SCIENCES Rabat.

[Tamim et al., 2014a] Tamim, A., Minaoui, K., Daoudi, K., Atillah, A., and Aboutajdine, D. (2014a). On detectability of moroccan coastal upwelling in sea surface temperature satellite images. In *International Symposium on Visual Computing*, pages 386–395. Springer.

[Tamim et al., 2014b] Tamim, A., Minaoui, K., Daoudi, K., Atillah, A., Yahia, H., and Aboutajdine, D. (2014b). Upwelling detection in sst images using fuzzy clustering with adaptive cluster merging. In *ISIVC 2014*.

[Tamim et al., 2015] Tamim, A., Minaoui, K., Daoudi, K., Yahia, H., Atillah, A., and Aboutajdine, D. (2015). An efficient tool for automatic delimitation of moroccan coastal upwelling using sst images. *Geoscience and Remote Sensing Letters, IEEE*, 12(4):875–879.

[Tamim et al., 2013] Tamim, A., Minaoui, K., Daoudi, K., Yahia, H., Atillah, A., Smiej, M. F., and Aboutajdine, D. (2013). A simple and efficient approach for coarse segmentation of moroccan coastal upwelling. In *Signal Processing Conference (EUSIPCO), 2013 Proceedings of the 21st European*, pages 1–5. IEEE.

[**El Aouni** et al., 2019] **El Aouni**, t., Daoudi, K., Yahia, H., Minaoui, K., and Benazzouz, A. (2019). Surface mixing and biological activity in the north-west african upwelling. *Chaos: An Interdisciplinary Journal of Nonlinear Science*, 29(1):011104.

[Thompson et al., 2000] Thompson, D. W., Wallace, J. M., and Hegerl, G. C. (2000). Annular modes in the extratropical circulation. part ii: Trends. *Journal of climate*, 13(5):1018–1036.

[Torre and Poggio, 1986] Torre, V. and Poggio, T. A. (1986). On edge detection. *IEEE Transactions on Pattern Analysis and Machine Intelligence*, (2):147–163.

[Trenberth et al., 1990] Trenberth, K. E., Large, W. G., and Olson, J. G. (1990). The mean annual cycle in global ocean wind stress. *Journal of Physical Oceanography*, 20(11):1742–1760.

[Tsang et al., 1985] Tsang, L., Kong, J. A., and Shin, R. T. (1985). Theory of microwave remote sensing.

[Turiel et al., 2008] Turiel, A., Yahia, H., and Pérez-Vicente, C. J. (2008). Microcanonical multifractal formalism—a geometrical approach to multifractal systems: Part i. singularity analysis. *Journal of Physics A: Mathematical and Theoretical*, 41(1):015501.

[Ulloa et al., 2001] Ulloa, O., Escribano, R., Hormazabal, S., Quinones, R. A., González, R. R., and Ramos, M. (2001). Evolution and biological effects of the 1997–98 el nino in the upwelling ecosystem off northern chile. *Geophysical Research Letters*, 28(8):1591–1594.

[Van Camp et al., 1991] Van Camp, L., Nykjaer, L., Mittelstaedt, E., and Schlittenhardt, P. (1991). Upwelling and boundary circulation off northwest africa as depicted by infrared and visible satellite observations. *Progress in Oceanography*, 26(4):357–402.

[Van Den Bergh, 2006] Van Den Bergh, F. (2006). *An analysis of particle swarm optimizers*. PhD thesis, University of Pretoria.

[van Leeuwen, 2007] van Leeuwen, P. J. (2007). The propagation mechanism of a vortex on the β plane. *Journal of Physical Oceanography*, 37(9):2316–2330.

[Van Vliet et al., 1989] Van Vliet, L. J., Young, I. T., and Beckers, G. L. (1989). A nonlinear laplace operator as edge detector in noisy images. *Computer vision, graphics, and image processing*, 45(2):167–195.

[Vidard et al., 2009] Vidard, A., Balmaseda, M., and Anderson, D. (2009). Assimilation of altimeter data in the ecmwf ocean analysis system 3. *Monthly Weather Review*, 137(4):1393–1408.

[Wang et al., 2014] Wang, M., Liu, X., Jiang, L., Son, S., Sun, J., Shi, W., Tan, L., Naik, P., Mikelsons, K., Wang, X., et al. (2014). Evaluation of viirs ocean color products. In *Ocean Remote Sensing and Monitoring from Space*, volume 9261, page 92610E. International Society for Optics and Photonics.

[Wang et al., 2016] Wang, Y., Beron-Vera, F., and Olascoaga, M. (2016). The life cycle of a coherent lagrangian agulhas ring. *Journal of Geophysical Research: Oceans*, 121(6):3944–3954.

[Wang et al., 2015] Wang, Y., Olascoaga, M., and Beron-Vera, F. (2015). Coherent water transport across the south atlantic. *Geophysical Research Letters*, 42(10):4072–4079.

[Waugh et al., 2012] Waugh, D. W., Keating, S. R., and Chen, M.-L. (2012). Diagnosing ocean stirring: Comparison of relative dispersion and finite-time lyapunov exponents. *Journal of Physical Oceanography*, 42(7):1173–1185.

[Wentz et al., 1992] Wentz, F. J. et al. (1992). Measurement of oceanic wind vector using satellite microwave radiometers. *IEEE Transactions on Geoscience and Remote Sensing*, 30(5):960–972.

[Wiggins, 2005] Wiggins, S. (2005). The dynamical systems approach to lagrangian transport in oceanic flows. *Annu. Rev. Fluid Mech.*, 37:295–328.

[Williamson et al., 2000] Williamson, G. B., Laurance, W. F., Oliveira, A. A., Delamonica, P., Gascon, C., Lovejoy, T. E., and Pohl, L. (2000). Amazonian tree mortality during the 1997 el nino drought. *Conservation Biology*, 14(5):1538–1542.

[Wooster et al., 1976] Wooster, W. S., Bakun, A., and McLain, D. R. (1976). Seasonal upwelling cycle along the eastern boundary of the north atlantic. *Journal of Marine Research*, 34(2):131–141.

[Wyrtki, 1981] Wyrtki, K. (1981). An estimate of equatorial upwelling in the pacific. *Journal of Physical Oceanography*, 11(9):1205–1214.

[Yelland and Taylor, 1996] Yelland, M. and Taylor, P. K. (1996). Wind stress measurements from the open ocean. *Journal of Physical Oceanography*, 26(4):541–558.

[Zhang et al., 2014] Zhang, L., Deng, Q., Machiraju, R., Rangarajan, A., Thompson, D., Walters, D. K., and Shen, H.-W. (2014). Boosting techniques for physics-based vortex detection. In *Computer Graphics Forum*, volume 33, pages 282–293. Wiley Online Library.